Study on Compressible Low-Reynolds-Number Flow over a Sphere

著者	TAKAYUKI NAGATA
学位授与機関	Tohoku University
学位授与番号	11301甲第19228号
URL	http://hdl.handle.net/10097/00130541

Doctoral Thesis

Thesis Title

Study on Compressible Low-Reynolds-Number Flow over a Sphere

Department of Aerospace Engineering
Graduate school of Engineering,
TOHOKU UNIVERSITY

TAKAYUKI NAGATA

(ID No. B7TD1610)

指導教員	野々村 拓　准教授
研究指導教員	
審査委員 (○印は主査)	○　浅井 圭介　教授 1　大西 直文　教授　　2　早瀬 敏幸 教授 3　野々村 拓　准教授

TOHOKU UNIVERSITY

Graduate School of Engineering

Study on Compressible Low-Reynolds-Number Flow over a Sphere
（球周りの圧縮性低 Reynolds 数流れに関する研究）

A dissertation submitted for the degree of Doctor of Philosophy (Engineering)

Department of Aerospace Engineering

by

Takayuki NAGATA

January 14, 2020

Study on Compressible Low-Reynolds-Number Flow over a Sphere

Takayuki NAGATA

Abstract

Multiphase flow models are basically based on the knowledge of the flow over a sphere at low-Reynolds-number conditions. In the case of high-speed multiphase flows, the flow over particles becomes the compressible low-Reynolds-number condition, particularly when the particles pass the shock waves, shear layer, and turbulence. However, there are few studies on the flow over a sphere in the compressible low-Reynolds-number condition. The objective of the present study is to investigate the fundamental characteristics of the compressible low-Reynolds-number flow over a sphere toward the construction of the accurate compressible multiphase flow model. The numerical and experimental studies were conducted in a wide range of Reynolds numbers.

In the numerical studies, the uniform flow over a stationary adiabatic, stationary isothermal, and rotating adiabatic spheres and linear-shear flow over a stationary adiabatic sphere were investigated by the direct numerical simulation of the three-dimensional compressible Navier–Stokes equations. The Navier–Stokes equations were solved on the body-fitted grid by using the high-order schemes. In the experimental studies, the free-flight and shock-sphere interaction experiments were carried out by using a ballistic range and a shock tube, respectively.

The uniform flow over a stationary adiabatic sphere was investigated at the Reynolds number ranging from 50 to 1,000 and the Mach number ranging from 0.3 to 2.0. It was clarified that the wake of the sphere is significantly stabilized as the Mach number increases, particularly at the Mach number of greater than or equal to 0.95. However, the turbulent kinetic energy in the wake at higher Mach numbers is higher than that at the lower Mach numbers with a similar flow regime. Also, a rapid extension of the length of the recirculation region was observed around the transitional Mach number which unsteady flows become steady by compressibility effects. The drag coefficient increases as the Mach number increases mainly in the transonic regime and its increment is almost due to the increment of the pressure component. In addition, the increment in the drag coefficient in the continuum regime is approximately the function of the Mach number and is regardless of the Reynolds number despite the low-Reynolds-number condition. Moreover, the effect of the Mach and Reynolds numbers on the flow properties such as the drag coefficient and flow regime can approximately be characterized by the position of the separation point.

The uniform flow over a stationary isothermal sphere was computed and investigated the effect of the surface temperature of the sphere. The Reynolds number was set to be between 100 and 300, the Mach number was set to be between 0.3 and 2.0, and the temperature ratio based on the freestream temperature and the sphere surface temperature was set to be between 0.5 and 2.0. It was clarified that the unsteady vortex shedding is promoted and suppressed for the heated and cooled spheres, respectively. This trend implies that the unsteadiness of the flowfield becomes strong and weak depending on the surface temperature of the sphere. It is due to the change in the kinematic viscosity coefficient in the vicinity of the sphere. A similar effect can be seen in the flow geometry and drag coefficient. In particular, the drag coefficient decreases and increases when the temperature ratio increases and decreases. However, the previous drag model cannot predict the effect of the surface temperature on the drag coefficient. The effect of the surface temperature on the flow geometry and the drag coefficient can be characterized by the position of the separation point because the kinematic viscosity coefficient in the boundary layer has a significant effect on the separation. In addition, the difference in the Nusselt number predicted by the previously proposed models and present DNS becomes large as the temperature difference or Mach number increases.

The effect of the rotation was investigated at the Reynolds number ranging from 100 to 300, the Mach number ranging from 0.3 to 2.0, and the non-dimensional rotation rate based on the surface velocity at the equator of the sphere and the freestream velocity ranging from 0 to 1.0. In the case of the high-rotation rate, the wake is stabilized due to the compressibility effect even though the Mach number of 0.3. At the supersonic flow, the rotation-induced lift is reduced. It is due to the influence of the strong compression and deceleration of the fluid caused by the detached shock wave. Because of those effects, the pressure at the region where the low-pressure is generated under the shock-free flow becomes increases at the transonic and supersonic flows. The pitching moment in the opposite direction to the rotation of the sphere at the same rotation rate increases as the Mach number increases.

The linear-shear flow over a stationary adiabatic sphere was calculated. The Reynolds number was set to be between 50 and 300, the Mach number was set to be between 0.3 and 1.5, and the non-dimensional shear rate based on the radius of the sphere and the velocity of the freestream was fixed at 0.1. The flow structure at the low-subsonic condition appears to be similar to that of the incompressible flow. At the high-subsonic and transonic conditions, the expansion wave and detached shock wave are formed only on the high-speed side due to the difference in the local Mach number of the mainstream. Hence, the recirculation region in the supersonic conditions is skewed into the low-speed side which is opposite to the incompressible cases in the investigated Reynolds number range. Also, the negative shear-induced lift at the compressible flow is larger than that at the incompressible flow, and it increases as the Reynolds number decreases. This trend is caused by the change in the pressure distribution in the upstream side of the high-speed side of the sphere surface due to the compressibility effect which is described by the Prandtl–Glauert transformation and the detached shock wave.

The free-flight experiment of the sphere was conducted, and the time-resolved schlieren images of the flow over a small sphere (the minimum diameter of 1.5 mm) were acquired at the low-pressure condition. The flow condition around the sphere was the Mach number between 0.9 and 1.6 and the Reynolds number between 3.9×10^3 and 3.8×10^5. The images of the time-averaged flowfield were produced and compared with the numerical results at the Reynolds number between 50 and 1,000. Also, the time-series schlieren images were analyzed by the singular value decomposition, and the wake structure was extracted even if the data with low-signal-to-noise ratio. The Mach and Reynolds numbers effects on the structures of the shock waves, the length of the recirculation region, and the wake vortices were clarified at the Reynolds number of $O(10^3)$–$O(10^5)$ under transonic and supersonic flows. The instantaneous schlieren image shows that the oscillation amplitude of the wake was reduced as the Mach number increases. In addition, the width of the wake at the end of the recirculation region on the time-averaged field is reduced by increasing the Mach number. Also, the length of the recirculation region increases as the Reynolds number decreases. This trend is opposite to that at the Reynolds number less than 10^3, and it suggests the possibility of the change in the flow regime occurs around the Reynolds number of $O(10^3)$.

In addition, the flow visualization and drag estimation through the shock-sphere interaction experiment were carried. In the case of the flow visualization, the Mach and Reynolds numbers based on the relative velocity between the sphere and the quantities behind the planar-shock wave were ranging from 0.45 to 1.28 and from 4.0×10^3 to 1.4×10^4, respectively. The experimental scheme to conduct the shock-particle interaction experiment using a single small particle (the minimum diameter of 0.3 mm) was established, and it was succeeded that the flow structure not only the shock waves but also the wake structures formed behind the sphere was visualized. Also, the flow over clustered spheres was visualized and its breakdown process was observed. In addition, the mean drag coefficient was estimated from the time-position data of the sphere at the Reynolds number ranging from 3.0×10^3 to 9.2×10^3 with the Mach number of 0.45. The estimated drag coefficient was higher than that of the drag model in steady-state as same as the previous experimental results.

Acknowledgment

This work is the outcome of the research over six years (from FY2014 to FY2019) including when I studied at Tokai University.

First of all, I wish to thank my chief examiner, Professor Dr. Keisuke Asai of the Department of Aerospace Engineering, Tohoku University. I am honored to have had the opportunity to have graduated under his guidance. Of course, I would like to acknowledge my Supervisor, Associate Professor Dr. Taku Nonomura of the Department of Aerospace Engineering, Tohoku University. He guided me over 6 years since I started my career as a researcher. I had no skills for research when I was an undergraduate student, but he taught me patiently what I need to conduct researches. I have learned how to advance the research from him, and then I could produce a number of results.

I am very grateful to the members of the doctoral committee, Professor Dr. Naofumi Onishi of the Department of Aerospace Engineering, Tohoku University and Professor Dr. Toshiyuki Hayase of the Institute of Fluid Science, Tohoku University. My doctoral thesis has been remarkably improved with their appropriate advice.

I want to express my gratitude to Specially Appointed Associate Professor Dr. Kiyonobu Ohtani of the Institute Fluid Science, Tohoku University for his collaboration in the design and preparation of my experimental studies and valuable comments. Also, I would like to thank Mr. Toshihiro Ogawa who helped in the design and preparation of the experimental setup and execution of the experiments. I never could conduct experimental research without their guidance.

There are several individuals in Tokai University who must be acknowledged. I am grateful to Associate Professor Dr. Kota Fukuda of the Department of Aeronautics and Astronautics who supervised my master thesis at Tokai University and advised my research as one of the collaborators. I would like to acknowledge Associate Professor Dr. Shun Takahashi of the Department of Prime Mover Engineering who advised my research as one of the collaborators.

They also gave me opportunities to work on biomedical research. That experience spread my insight and skills. Also, I would like to acknowledge Mr. Yusuke Mizuno of Course of Science and Technology and Ms. Mayu Yoshida of the Department of Aeronautics and Astronautics who worked with me on the present work.

Professor Dr. Eric Loth of the Department of Mechanical and Aerospace Engineering, the University of Virginia, must be thanked. He accepted my short term internship at the University of Virginia, and he gave me a great opportunity to conduct collaborative work regarding the drag model of the sphere and supersonic vortex generator. He kindly has guided me in collaborative researches during and after finishing my internship.

I would further like to thank Assistant Professor Dr. Yuji Saito for his time in improving my presentation and many helpful comments. His guidance helped me to improve the content and logic of my research. Also, I am grateful to the members of the Mars Wind Tunnel team, Experimental Aerodynamics Laboratory, Department of Aerospace Engineering, Tohoku University. I would like to thank Mr. Akito Noguchi and Mr. Kensuke Kusama who kindly supported my experiments must be acknowledged. They are conducting wonderful works regarding the study on the compressible low-Reynolds-number flow at Mars Wind Tunnel and the knowledge acquired by their works was very helpful for me.

I would like to thank all the members of the Experimental Aerodynamics Laboratory, Department of Aerospace Engineering, Tohoku University. Discussions with them have been a great help to advance my work.

This work was supported by the Japan Society for the Promotion of Science, KAKENHI Grants 18J11205 and Division for Interdisciplinary Advanced Research and Education, Tohoku University. The simulations were implemented on the supercomputer JSS and JSS2 of the Japan Aerospace Exploration Agency.

I am also grateful to my friends and my family, in particular, my father and my mother for support in all these days.

January 14, 2020
Takayuki NAGATA

Contents

List of Figures

List of Tables

Chapter 1

Introduction

List of Symbols

A = Projected area
C_D = Drag coefficient
C_L = Lift coefficient
D = Drag force
E, F, G = x, y, and z components of an inviscid flux
$E_\mathrm{v}, F_\mathrm{v}, G_\mathrm{v}$ = x, y, and z components of an viscous flux
I = Interaction term
Kn = Knudsen number
M = Mach number
Pr = Prandtl number
Q = Conservative variable vector
Q_t = Amount of transferred heat
St = Strouhal number
T = Temperature of gas
Re = Reynolds number
L = Lift force
a = Sound speed
c_p = Specific heat at constant pressure
c_m = Specific heat of the particle material
c_v = Specific heat at constant volume
d = Diameter
e = Total energy per unit volume of the gas phase
f = Drag factor, frequency
g = Gravity
m = Mass of particle
p = Pressure
q = Heat flux
t = Time

u = Velocities of fluid, velocity in x direction

v = Velocities of particle, velocity in y direction

V_d = Volume fraction of the dispersed phase

w = Slip velocities between particle and fluid, velocity in z direction

x, y, z = Cartesian coordinates

ϵ = Eddington epsilon

γ = Specific heat ratio

λ = Mean free path length

μ = Dynamic viscosity coefficient

ν = Kinematic viscosity coefficient

π = The ratio of the circumference of a circle to its diameter

ρ = Density

σ = Number of density

τ = Response time

τ_{ij} = Viscous stress tensor

ω = Rotation vector

Θ = temperature of the solid phase

Ω = Angular velocity, Total energy per unit volume of the solid phase

Ω^* = Nondimensional rotation rate

Subscripts

$_\mathrm{f}$ = Continuum phase, fluid

$_\mathrm{g}$ = Gas phase

$_\mathrm{p}$ = Particle

$_{i,j}$ = Index for Einstein summation convention

1.1 Multiphase Flow

Multiphase flow including dispersed phase appears in various fields, such as biology, engineering, and air pollution. The properties of flows can be significantly influenced by a dispersed phase. This flow is subcategorized into a multicomponent and multiphase flow type. A *component* represents a chemical species such as nitrogen, oxygen, or water. A *phase* denotes the state of the matter such as solid, liquid or gas. Table 1.1 shows an example of single component or multicomponent and multiphase flows.

	Single component	Multicomponent
Singlephase	Water flow Nitrogen flow	Air flow Flow of emulsions
Multiphase	Steam-water flow Freon-Freon vapor flow	Air-water flow Slurry flow

TABLE 1.1: Example of single and multicomponent, multiphase flows (Crowe et al., 2011).

The flow of air is an example of a single-phase multicomponent flow because air is composed of nitrogen, oxygen, and so on. A single-phase flow of the mixture fluid is commonly treated as a single component flow with a viscosity coefficient and a thermal conductivity which represents the mixture. This assumption works except that the major components of the fluid have significantly different molecular weights or extremely high- and low-temperature conditions where dissociation or condense out.

Single-component multiphase flows are typically the flow of a liquid with its vapor. The flow of water with a stream is an example of a single-component and multiphase flow. Steam-water flow is very common, for example in the industrial field and daily life. If the flow of air including solid particles or water droplets, the flow becomes a multiphase multicomponent flow.

Category	Example
Gas-liquid flows	Bubbly flows Separated flows Gas-droplet flows
Gas-solid flows	Gas-particle flows Pneumatic transport Fluidized beds
Liquid-solid flows	Slurry flows Hydrotransport Sediment transport
Three-phase flows	Bubbles in a slurry flow Droplets/particles in gaseous flows

TABLE 1.2: Categories and example of multiphase flows (Crowe et al., 2011).

The single-phase flow has been studied by numerous researchers for a long time. Navier–Stokes equations are well accepted and used as the governing equations for single-phase flows in the continuum regime. Quite a few analytical solutions and numerous numerical simulations have been conducted. The modeling of turbulence is one of the major issues in the dynamics of the flowfield. Researchers and engineers are pursuing an accurate turbulence model. On the other hand, the multiphase flow model is also still in a developing phase and more primitive than turbulent model.

Table 1.2 shows the example of the multiphase flow and its classification. Multiphase flows can be subdivided into four categories, which are gas-liquid, gas-solid, liquid-solid, and three-phase flows. An example of gas-liquid flow is the liquid flow including bubble. In this case, the liquid and gas phases are the continuum and disperse phases, respectively. A gas flow including liquid droplets are also gas-liquid flow, but the continuum phase is the gas and the disperse phase is the liquid in this case. In addition, a separated multiphase flow that both gas and liquid phases are exist as a continuum phase. Gas-particle and liquid-particle flows are gas and liquid flows including solid particles, respectively. For example, particle transportation by gas or liquid flows corresponds to gas-particle and liquid-particle flows. Furthermore, the flow consists of gas, liquid, and solid phases is a three-phase flow. It should be noted that if the particles are not in motion such as flow in a porous medium, the flow is not a gas- or liquid-solid flow.

1.1.1 Fluid Force on Particles

Particles in fluid flows receive a drag and lift forces. Estimations of those fluid forces are essential for prediction of the particle motion. Particularly, the drag force is the dominant force on the motion of the particle in particle-laden flows so that characteristics of the particle drag have been examined by numerous researchers.

Stokes, 1851 was among the first to derive the analytic solution of the Navier–Stokes equations for the uniform flow over a stationary isolated sphere at a low Reynolds number of $Re \ll 1$. Basset, 1888; Boussinesq, 1895; Oseen, 1927 attempt to analyze the motion of a falling sphere in a quiescent fluid. In their honor, the equation of motion for a spherical particle in a fluid at low-Reynolds-number conditions is called the Basset-Boussinesq-Oseen (BBO) equations. Tchen, 1974 studied the effect of nonuniformity and unsteadiness of the flow on the particle motion to extend previous works.

The equation of motion for a small particle in nonuniform, unsteady flow at the low Reynolds number was derived by Maxey and Riley, 1983,

$$
\begin{aligned}
m\frac{\mathrm{d}v_i}{\mathrm{d}t} = {} & \overbrace{mg_i}^{\text{body force}} + \overbrace{V_\mathrm{d}\left(-\frac{\partial p}{\partial x_i}+\frac{\partial \tau_{ij}}{\partial x_j}\right)}^{\text{undisterbed flow}} + \overbrace{3\pi\mu d\left[(u_i-v_i)+\frac{d^2}{24}\nabla^2 u_i\right]}^{\text{steady state drag}} \\
& + \overbrace{\frac{1}{2}\rho_\mathrm{f} V_\mathrm{d}\frac{\mathrm{d}}{\mathrm{d}t}\left[(u_i-v_i)+\frac{d^2}{40}\nabla^2 u_i\right]}^{\text{virtual or apparent mass term}} \\
& + \overbrace{\frac{3}{2}\pi\mu d^2 \int_o^t \left[\frac{\mathrm{d}/\mathrm{d}\tau\left(u_i - v_i + d^2/24\times\nabla^2 u_i\right)}{\pi\nu(t-\tau)^{1/2}}\right] d\tau}^{\text{Basset or history term}}
\end{aligned}
\tag{1.1}
$$

m, v_i, and t indicate the mass of a particle, the velocity of a particle, and the time, respectively. The first term on the right-hand side is the body force due to the gravity acceleration g and others, and other terms on the right-hand side are the fluid dynamic forces. The second term is the force due to undisturbed flow, which is caused by the gradient of the pressure p and the stress tensor τ_{ij}, where V_d and x_i indicates the volume fraction of dispersed phase and the Cartesian coordinates, respectively. The third term represents the steady-state drag force, which acts on the particle in the uniform and the steady relative velocity between the particle and the fluid, where μ, u_i, and v_i denote the viscosity coefficient, and the velocities of the fluid, respectively. The fourth and fifth terms are only for unsteady flows. The fourth term represents the virtual mass force, which is the force related to the acceleration of the fluid caused by the particle motion, where ρ_f is the density of the continuum phase. When a particle accelerated through the fluid, the ambient fluid of the particle is also accelerated and additional work appears. This additional work related to the virtual mass force and it corresponds to the form drag caused by acceleration. The last term indicates the Basset force, which is the force due to temporal delay of the boundary layer development as the relative velocity change with time. This force corresponds to the additional viscous drag due to acceleration. In addition, lift forces or other external forces will be included depending on the problem.

In the present study, we focused on the flow over a sphere in the steady flow so that steady drag and lift forces are introduced in detail below. Figure 1.1 illustrates the schematic diagram of the steady fluid force acting on the sphere, that are the drag force, the rotation-induced lift force, and the shear-induced lift force.

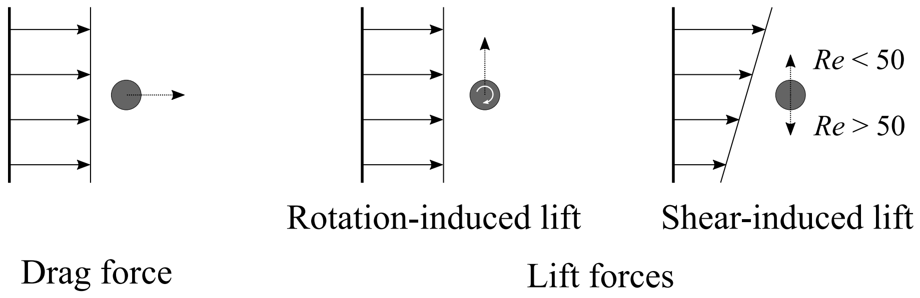

FIGURE 1.1: Fluid forces acting on particles in the steady incompressible low-Reynolds-number flow in the continuum regime.

Steady Drag Force

Steady drag force depending on the relative velocity w_i between the fluid and velocities. The relative velocity is

$$w_i = v_i - u_i, \tag{1.2}$$

and the particle Reynolds number Re_p based on the diameter of a particle, the density of fluid, and the dynamic viscosity is

$$Re_\mathrm{p} = \frac{\rho_\mathrm{f}|w_i|d}{\mu_\mathrm{f}}. \tag{1.3}$$

Stokes, 1851 analytically derived the drag force acting on a stationary isolated sphere in incompressible flows of $Re_\mathrm{p} \ll 1$ and the drag force expressed as follows and known as Stokes' drag law:

$$D_{\mathrm{p},i} = -3\pi d\mu_\mathrm{f} w_i. \tag{1.4}$$

As eq. 1.4, the drag force is proportional to the relative velocity, and this flow regime called the Stokes regime. Also, the drag coefficient in the Stokes regime can be written as follows:

$$C_D = \frac{24}{Re}. \tag{1.5}$$

At the flow regime that the inertial force is dominant, on the other hand, the drag coefficient is proportional to the dynamic pressure.

$$D_{\mathrm{p},i} = -\frac{1}{8}\rho_\mathrm{f}|w_i|w_i C_{Di} d^2. \tag{1.6}$$

Particularly, the drag coefficient at $2.0 \times 10^3 \leq Re \leq 3.0 \times 10^5$ is almost constant for $C_D \approx 0.45$. The drag coefficient in the intermediate regime between the Stokes and Newton regimes can be characterized by Re and the drag factor f is introduced taken into account the inertial effect. Oseen extended the Stokes solution by including first-order inertial effect, and the drag coefficient by the Oseen approximation is described as follows:

$$C_D = \frac{24}{Re}\left(1 + \frac{3}{16}Re\right). \tag{1.7}$$

This expression is valid up to $Re = 5$. In eq. 1.7, the correction function for the inertial effect $\left(1 + \frac{3}{16}Re\right)$ appears. For further high-Re conditions, several correction functions available as a function of Re. The correction function by Schiller and Naumann, 1933 is one of the reasonable one and gives the drag coefficient with less than 5% up to $Re = 800$.

$$C_D = \frac{24}{Re}\left(1 + 0.15Re^{0.687}\right) \tag{1.8}$$

Clift and Gauvin, 1971 proposed a drag model, which can be applied at a wider range of the Reynolds number ($Re < 2.0 \times 10^5$).

$$C_D = \frac{24}{Re}\left(1 + 0.15Re_{\mathrm{p}}^{0.687}\right) + \frac{0.42}{1 + \frac{42{,}500}{Re_{\mathrm{p}}^{1.16}}} \tag{1.9}$$

The first term of this equation is the drag model by Schiller and Naumann, 1933 shown in eq. 1.8. The second term is a term for asymptotic to the drag coefficient in the newton regime.

In high-speed flows, a particle Mach number M_{p} defined as the ratio of the relative velocity to a sound speed a is also important.

$$M_{\mathrm{p},i} = \frac{w_i}{a} \tag{1.10}$$

In the high-speed particle-laden flows such as exhaust gas of rocket engines, relative velocities between particles and fluid become large and compressibility effects are no longer small, particularly when particles through shock waves, shear layer, or turbulence. Furthermore, noncontinuum effects appear in the case of small particles in high-M flows. The parameter characterizing the continuum or non-continuum flows is the Knudsen number Kn_{p} defined as the ratio of the mean free-path length of the gas molecules λ to representative length (particle diameter for the particle Knudsen number), and it can be rewritten as the functions of M and Re (Schaaf and Chambre, 1958),

$$Kn_{\mathrm{p}} = \frac{\lambda}{d} = \sqrt{\frac{\pi\gamma}{2}}\frac{M_{\mathrm{p}}}{Re_{\mathrm{p}}} \tag{1.11}$$

where γ is a specific heat ratio. The flow regime can be subdivided into the continuum flow ($Kn_{\mathrm{p}} \leq 0.01$), the slip flow ($0.01 \leq Kn_{\mathrm{p}} \leq 0.1$), the transitional flow ($0.1 \leq Kn_{\mathrm{p}} \leq 1$), and the free molecular flow as shown in figure 1.2.

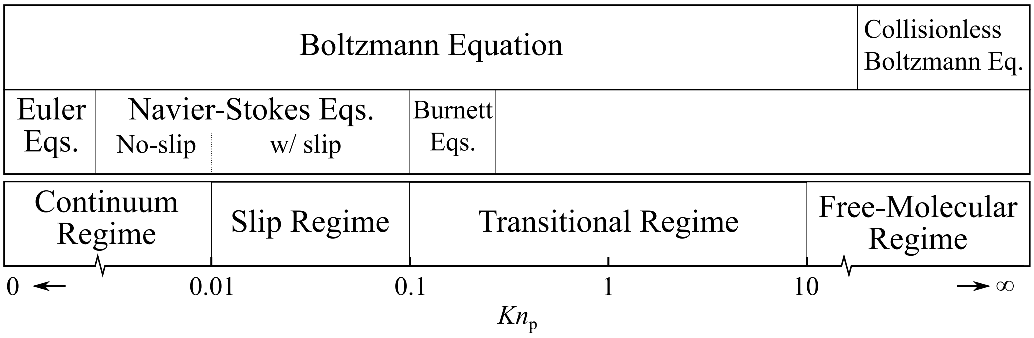

FIGURE 1.2: Flow regime and governing equations.

The effects of M and Kn on the drag coefficient must be considered as well as the Re effect in the compressible and rarefied regimes.

Steady Lift Force

Lift forces acting on an isolated particle in a continuum regime can be subdivided into two types, which are the rotation-induced lift and the shear-induced lift. These lift forces are generally smaller than the drag force, but it has a large impact on the distribution of the particles.

The particle rotation is mainly introduced by the velocity gradient of ambient flow, collision with a wall, and so on. The particle rotation results in the velocity difference between a certain side and its opposite side, and it causes a pressure difference. The rotation-induced lift is called *Magnus lift force*. The Magnus lift force was derived by Rubinow and Keller, 1961 for Re of the order of unity

$$L_{\mathrm{Magnus},i} = \frac{\pi}{8} d^3 \rho_{\mathrm{f}} \{\epsilon_{ijk} \omega_{\mathrm{p},j} (v_k - u_k)\} \tag{1.12}$$

where ϵ is the Eddington epsilon, ω_{p} is the particle rotation vector. If the rotation velocity vector is normal to the relative velocity vector, Magnus lift force becomes as follows:

$$L_{\mathrm{Magnus},j} = \frac{\pi}{8} d^3 \rho_{\mathrm{f}} \omega_{\mathrm{p}} (v_k - u_k). \tag{1.13}$$

The Magnus lift force can be quantified in the form

$$L_{\text{Magnus}} = \frac{1}{2}\rho_{\text{f}} C_{L_{\text{R}}} A|v - u|(v - u), \tag{1.14}$$

where $C_{L_{\text{R}}}$ and A denote the lift coefficient due to particle rotation and the projected area of the particle. The lift coefficient of the Magnus lift force at Re of the order of unity is

$$C_{L_{\text{R}}} = \frac{d\omega_{\text{p}}}{|u - v|} = 2\Omega^* \tag{1.15}$$

where Ω^* is the nondimensional rotation rate defined as

$$\Omega^* = \frac{d\omega_{\text{p}}}{2|u - v|}. \tag{1.16}$$

Tanaka, Yamagata, and Tsuji, 1990 suggested the model of the coefficient of the rotation-induced lift at the higher-Re conditions

$$C_{L_{\text{R}}} = \min(0.5, 0.5\Omega^*) \tag{1.17}$$

which is a ramp function up to 0.5.

The velocity gradient also makes a pressure difference on particles. The pressure in the high-speed side is lower than that of the low-speed side so that the direction of the shear-induced lift is from the low-speed side to high-speed side at sufficiently low- and high-Re conditions. The shear-induced lift was derived by Saffman, 1965 at $Re \ll 1$ by using Oseen approximation. This lift force is called as *Saffman lift force* and he found that the magnitude of the lift force to be

$$L_{\text{Saffman},i} = 1.61\mu d|u_i - v_i|\sqrt{Re_{\text{G}}} \tag{1.18}$$

where Re_{G} is the shear Reynolds number defined as

$$Re_{\text{G}} = \frac{d^2}{\nu}\frac{\mathrm{d}u}{\mathrm{d}y}. \tag{1.19}$$

Here, Re_{G} indicates the Reynolds number based on the velocity difference between the top and bottom of the particle. Saffman's analysis is based on the Oseen approximation with a strong shear rate so that his analysis valid in the condition of $Re_{\text{p}} \ll \sqrt{Re_{\text{G}}} \ll 1$. McLaughlin, 1991 extended Saffman's analysis to include the condition of $Re_{\mathrm{p}} > Re_{\mathrm{G}}$, and his analysis clarified that the shear-induced lift force rapidly decreases as Re_{p} increases. Mei, 1992 proposed the empirical model based on Re_{p} and Re_{G} by modifying the Saffman's analysis.

1.1.2 Numerical Simulation of Particle-Laden Flow

There are a number of ways to solve multiphase flows from the viewpoint of the resolution of the eddies and dispersed phase. The most accurate simulation is the particle-resolved DNS (finite-size particle approach). All scales of eddies in the flowfield are resolved by DNS of the Navier–Stokes equations and the flow around particles are also resolved by the immersed boundary method (IBM). The fluid forces acting on the particles are directly computed by integrating the fluid stress on the surface of each particle. Also, the wake vortices generated by the particles can also be resolved. No turbulence and multiphase flow models are required and all phenomena in the flowfield are directly solved. However, a fine computational grid is required to resolve the flow over the particles. Therefore, the particle-resolved DNS has applied to the limited problem settings with a small physical domain.

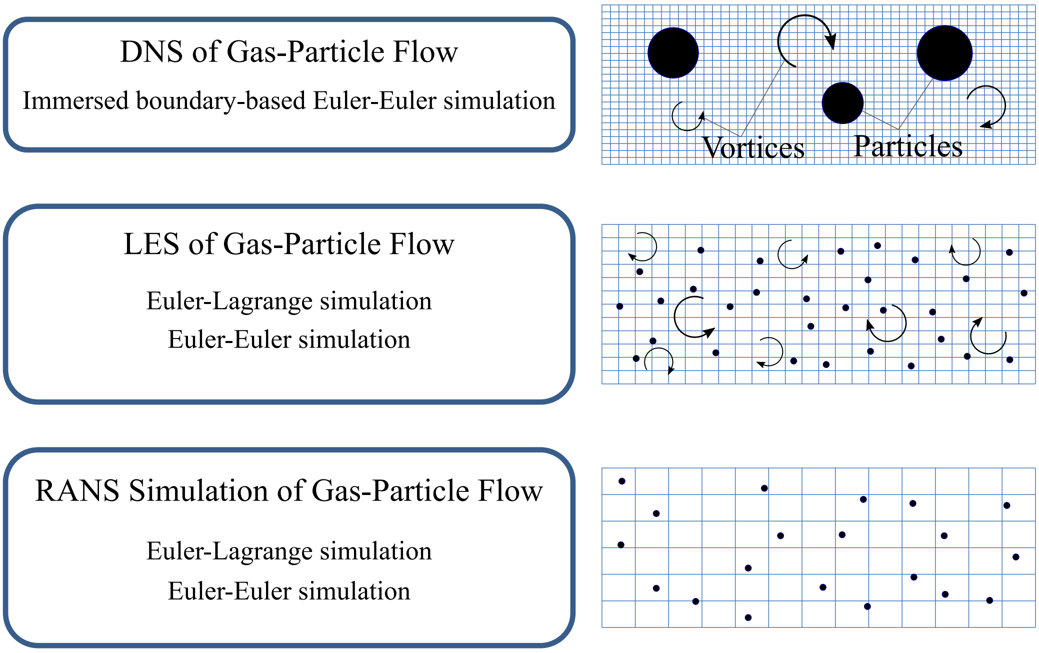

Figure 1.3: Category of gas-particle flow simulations.

More practical methods for the multiphase flow simulation is the point-particle approach combining with large-eddy simulations (LES) or Reynolds-averaged Navier–Stokes (RNAS) simulations. The sub-grid scale eddies or all of the eddies in the flowfield are modeled, and the particles are treated as the mass point. The method to treat the particles can be subdivided into Lagrangian and Eulerian approaches. In any case, the particles are considered to have a sub-grid scale and a particle model giving the particle effect on the flowfield or the interaction effects between the continuum and disperse phases are required, but the simulations of the large-scale problem settings is feasible.

Finite-Size Particle Approach

In the finite-size particle approach, the coupling model obtained by the discrete element method (DEM) (Cundall and Strack, 1979) and computational fluid dynamics (CFD) Chorin, 1968 is widely used. This model, i.e., the DEM-CFD model, was proposed by Tsuji, Tanaka, and Ishida, 1992; Tsuji, Kawaguchi, and Tanaka, 1993. In DEM-CFD coupling, the inter-particle interaction can be taken into account even if the particles are non-circular or non-spherical. However, DEM-CFD a coupling is a one-way coupling on the particle-fluid interaction. In the case of the IBM, the fully-resolved DNS can be realized. In this case, the flow around each particle can be captured. The IBM has been used to simulate of the unsteady viscous flow by Udaykumar, Shyy, and Rao, 1996; Ye et al., 1999 and the derived type such as direct forcing IBM proposed by Uhlmann, 2005. In addition, the IBM is extended to compressible flow simulations by Ghias, Mittal, and Dong, 2007. In addition, Takahashi, Nonomura, and Fukuda, 2014; Luo et al., 2016 and proposed the simplified IBM for compressible viscous flows based on the IBM by Mittal et al., 2008. The immersed boundary-Lattice Boltzmann method (IB-LBM) was proposed by Feng and Michaelides, 2004. The fully-resolved DNS is the most accurate way to simulate the multiphase flows. However, a large scale computational resources are required to compute the particle-laden flow, and thus it is difficult to conduct the flow simulation by the fully-resolved approach with a large scale physical domain. In the case of a point-particle approach, which will describe in the next section, on the other hand, it is capable of the computation of the particle-laden flow with a large physical domain using coarser computational grids. However, the point-particle approach cannot consider the effect of anisotropic in the particle effect. Fukada, Takeuchi, and Kajishima, 2016; Fukada et al., 2018; Fukada, Takeuchi, and Kajishima, 2019 proposed the finite-size particle approach based on the local volume averaging. Their method considers the finite-size particles, and particles are resolved with several grid points. The effect of the particles is considered by the *interaction force* based on the surface stress distribution. They succeeded in the consideration of the influence of the particle with finite-size without computation of the flow over particles.

Point-Particle Approach

A point-particle approach can be subdivided into four types from the point of view of the treatment of fluid-particle interactions. The simplest one is the one-way coupling which considers only the fluid force acting on the particle. In this case, the particles are transported by fluid, but particles do not affect the flowfield around them. This approximation is valid for the case which is the light particle (small Stokes number) with fewer collisions. The second one is the two-way coupling, which considers the interaction between particles and fluid mutually. In this case, the momentum and heat exchanges are considered. Both effect of the particles on the fluid and the effect of fluid on the particles treated as volume average. This approximation is valid for the case which is the relatively heavy particles with fewer collisions. The last one is the four-way coupling which considers both fluid-particle and inter-particle interactions. In this case, the inter-particle collisions between particles are considered by hard-sphere collision models (Hoomans et al., 1996; Crowe et al., 2011) or the other advanced model of hard-sphere (e.g., Kosinski and Hoffmann, 2010) or soft-sphere (e.g., Costa et al., 2015) models, and the collision process are considered.

Multiphase Flow Model based on Point-Particle Approach

The interaction model between particles and fluid are required in finite-size and point-particle approaches or one-way, two-way, or four-way couplings, except particle-resolved simulation using IBM. The particle-resolved simulation using IBM requires the very fine mesh to resolve the flow around the particle so that computational cost becomes extremely expensive for the simulation of the large-scale multiphase flow such as engineering and industrial scale problems.

Therefore, the fluid-particle interaction is typically considered using the particle drag and heat transfer models. As an example, the two-fluid model (Euler-Euler formulation) is shown below. Both fluid and solid phases are expressed as the continuum phase. The fluid phase is expressed by the Navier–Stokes equations, and the solid phase is expressed by the Euler equations.

$$\begin{cases} \dfrac{\partial Q_\mathrm{f}}{\partial t} + \dfrac{\partial E_\mathrm{f}}{\partial x} + \dfrac{\partial F_\mathrm{f}}{\partial y} + \dfrac{\partial G_\mathrm{f}}{\partial z} = \dfrac{\partial E_\mathrm{v}}{\partial x} + \dfrac{\partial F_\mathrm{v}}{\partial y} + \dfrac{\partial G_\mathrm{v}}{\partial z} - I \\ \dfrac{\partial Q_\mathrm{p}}{\partial t} + \dfrac{\partial E_\mathrm{p}}{\partial x} + \dfrac{\partial F_\mathrm{p}}{\partial y} + \dfrac{\partial G_\mathrm{p}}{\partial z} = I \end{cases} \tag{1.20}$$

where subscript f and p indicate the fluid and particle, respectively. The vectors Q contains conservative variables; E, F, and G are the x, y, and z components of the inviscid flux, respectively,

$$Q_\mathrm{g} = \begin{bmatrix} \rho_\mathrm{g} \\ \rho_\mathrm{g} u_\mathrm{g} \\ \rho_\mathrm{g} v_\mathrm{g} \\ \rho_\mathrm{g} w_\mathrm{g} \\ e \end{bmatrix}, E_\mathrm{g} = \begin{bmatrix} \rho_\mathrm{g} u_\mathrm{g} \\ \rho_\mathrm{g} u_\mathrm{g}^2 + p \\ \rho_\mathrm{g} u_\mathrm{g} v_\mathrm{g} \\ \rho_\mathrm{g} u_\mathrm{g} w_\mathrm{g} \\ (e+p) u_\mathrm{f} \end{bmatrix}, F_\mathrm{g} = \begin{bmatrix} \rho_\mathrm{g} v_\mathrm{g} \\ \rho_\mathrm{g} v_\mathrm{g} u_\mathrm{g} \\ \rho_\mathrm{g} v_\mathrm{g}^2 + p \\ \rho_\mathrm{g} v_\mathrm{g} w_\mathrm{g} \\ (e+p) v_\mathrm{g} \end{bmatrix}, G_\mathrm{g} = \begin{bmatrix} \rho_\mathrm{g} w_\mathrm{g} \\ \rho_\mathrm{g} w_\mathrm{g} u_\mathrm{g} \\ \rho_\mathrm{g} w_\mathrm{g} v_\mathrm{g} \\ \rho_\mathrm{g} w_\mathrm{g}^2 + p \\ (e+p) w_\mathrm{g} \end{bmatrix} \tag{1.21}$$

where u, v, and w are the x, y, and z components of the velocity, respectively; and ρ, p, and e are the density, the pressure, and the total energy per unit volume of the gas phase, respectively. It assumes to be the state of the ideal gas,

$$e = \rho_\mathrm{g} \left(c_v T + \frac{1}{2} \rho_\mathrm{g} (u_\mathrm{g}^2 + v_\mathrm{g}^2 + w_\mathrm{g}^2) \right) \tag{1.22}$$

where c_v and T are the specific heat at constant volume and the temperature of gas phase. Also, vectors E_v, F_v, and G_v are the x, y, and z components of the viscous flux, respectively,

$$E_\mathrm{v} = \begin{bmatrix} 0 \\ \tau_{xx} \\ \tau_{xy} \\ \tau_{xz} \\ \beta_x \end{bmatrix}, F_\mathrm{v} = \begin{bmatrix} 0 \\ \tau_{yx} \\ \tau_{yy} \\ \tau_{yz} \\ \beta_y \end{bmatrix}, G_\mathrm{v} = \begin{bmatrix} 0 \\ \tau_{zx} \\ \tau_{zy} \\ \tau_{zz} \\ \beta_z \end{bmatrix} \tag{1.23}$$

$$\begin{cases} \beta_x = \tau_{xx}u_\mathrm{g} + \tau_{xy}v_\mathrm{g} + \tau_{xz}w_\mathrm{g} - q_x \\ \beta_y = \tau_{yx}u_\mathrm{g} + \tau_{yy}v_\mathrm{g} + \tau_{yz}w_\mathrm{g} - q_y \\ \beta_z = \tau_{zx}u_\mathrm{g} + \tau_{zy}v_\mathrm{g} + \tau_{zz}w_\mathrm{g} - q_z \end{cases}$$

where τ and q are the viscous stress and the heat flux, respectively. For the solid phase,

$$Q_\mathrm{p} = \begin{bmatrix} \rho_\mathrm{p} \\ \rho_\mathrm{p}u_\mathrm{p} \\ \rho_\mathrm{p}v_\mathrm{p} \\ \rho_\mathrm{p}w_\mathrm{p} \\ \Omega \end{bmatrix}, E_\mathrm{p} = \begin{bmatrix} \rho_\mathrm{p}u_\mathrm{p} \\ \rho_\mathrm{p}u_\mathrm{p}^2 \\ \rho_\mathrm{p}u_\mathrm{p}v_\mathrm{p} \\ \rho_\mathrm{p}u_\mathrm{p}w_\mathrm{p} \\ \Omega u_\mathrm{p} \end{bmatrix}, F_\mathrm{p} = \begin{bmatrix} \rho_\mathrm{p}v_\mathrm{p} \\ \rho_\mathrm{p}v_\mathrm{p}u_\mathrm{p} \\ \rho_\mathrm{p}v_\mathrm{p}^2 \\ \rho_\mathrm{p}v_\mathrm{p}w_\mathrm{p} \\ \Omega v_\mathrm{p} \end{bmatrix}, G_\mathrm{p} = \begin{bmatrix} \rho_\mathrm{p}w_\mathrm{p} \\ \rho_\mathrm{p}w_\mathrm{p}u_\mathrm{p} \\ \rho_\mathrm{p}w_\mathrm{p}v_\mathrm{p} \\ \rho_\mathrm{p}w_\mathrm{p}^2 \\ \Omega w_\mathrm{p} \end{bmatrix} \tag{1.24}$$

where Ω is the total energy per unit volume of the solid phase as shown below.

$$\Omega = \rho_\mathrm{p}\left\{c_m\Theta + \frac{1}{2}\rho(u_\mathrm{p}^2 + v_\mathrm{p}^2 + w_\mathrm{p}^2)\right\}. \tag{1.25}$$

Variables c_m and Θ are the specific heat of the particle material and the temperature of the solid phase, respectively. In addition, I is the interaction term to couple the solid and gas phases.

$$I = \frac{\sigma}{m}\begin{bmatrix} 0 \\ D_x \\ D_y \\ D_z \\ Q_\mathrm{t} + u_\mathrm{p}D_x + v_\mathrm{p}D_y + w_\mathrm{p}D_z \end{bmatrix} \tag{1.26}$$

$$m = \frac{1}{6}\rho_\mathrm{p}\pi d^3,$$

$$\mathbf{D} = \frac{1}{8}\pi d^2\rho_\mathrm{g}(\mathbf{u}_\mathrm{g} - \mathbf{u}_\mathrm{p})|\mathbf{u}_\mathrm{g} - \mathbf{u}_\mathrm{p}|C_D,$$

$$Q_\mathrm{t} = \frac{\pi d\mu c_p}{\mathrm{Pr}}(T - \Theta)Nu.$$

where σ, m, and d are the number of density, the mass, of particles, and the diameter of particles; and Q_t and D are the amount of transferred heat between particle and gas and the drag force of particles; and μ, c_p, and Pr are the viscosity coefficient, the specific heat at constant pressure, and the Prandtl number. As shown above, the interaction term includes the drag coefficient C_D and the Nusselt number Nu of particles so that particle drag and the Nusselt number models are required to solve the equations of the two-fluid model.

In the case of the incompressible regime, there are numerous researches on the low-Re flow over a sphere (see section 1.2.1), and accurate drag models have been proposed based on that knowledge (e.g., Clift and Gauvin, 1971). The heat transfer between a sphere and fluid has also been modeled (e.g., Ranz and Marshall, 1952).

1.1.3 Compressible Multiphase Flow

Multiphase flow has been investigated in various fields, particularly in the incompressible flow regime. However, the study on the compressible multiphase flow is fewer than that of the incompressible regime. In aerospace engineering, the compressible multiphase flow appears in the exhaust gas of rocket engines, high-speed combustion, and so on.

Exhaust Jets of Rocket Engines

The exhaust jet of rocket engines emits strong acoustic waves and could cause critical damage to the payload in the fairing. Therefore, it is necessary to predict and reduce the acoustic level at liftoff. Traditionally, the acoustic level has been predicted by semi-empirical method using either NASA SP-8072 (Eldred, 1971) or static firing tests of sub-scale models (Ishii et al., 2012). However, NASA-SP8072 is the semi-empirical method based on a large number of launch data obtained in the United States and so is not suitable to design a new launch pad. In recent years, computational fluid dynamics (CFD) have been used in the studies of acoustic level prediction and investigations of acoustic phenomena. Tsutsumi et al., 2008; Tsutsumi et al., 2014 performed simulations of the jet flow and acoustic field including the influence of the flame deflector plate and the launch facility. Nonomura et al., 2014 investigated the influence of the difference in the specific heat ratio of the exhaust gas and the atmosphere. By these studies, acoustic phenomena in the exhaust jet of the rocket engines have been studied with limited accuracy.

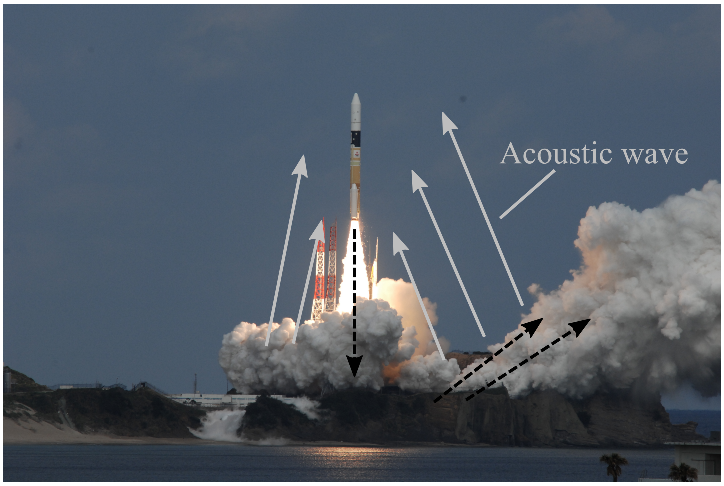

FIGURE 1.4: Exhaust jet of rocket engines.

However, the exhaust jet of the solid rocket motor contains small alumina droplets and alumina particles, and water droplets are also generated because of water injection during the liftoff of large liquid-propellant rockets. Attenuation effects by water droplets in the air have been studied since 1948 (Knudsen, Wilson, and Anderson, 1948). The result of the static firing tests shows the particles included in the jet attenuate acoustic wave. Zoppellari and Juve, 1998 studied the noise suppression of the supersonic jet by injecting up to several times the mass of the water jet. Their result showed that the far-field noise of a supersonic jet decreases approximately 10dB. Krothapalli et al., 2003 investigated the noise suppression of the supersonic jet by water up to 5% mass flow rate of the jet with PIV measurements. The water droplets modified the turbulence structures of the jet and results in the reduction of the fluctuation of the velocity field and turbulent shear stress. (Fukuda et al., 2011) studied the noise suppression by water injections through analytical and numerical investigations. Their result suggested that the effect of the particle is not a simple scattering of the sound. The attenuation effect due to water injection can reasonably be evaluated by the specific parameter based on the gas density and turbulent kinetic energy proposed by them. Ignatius, Sathiyavageeswaran, and Chakravarthy, 2014 conducted the experiment by a 1:100 scaled-down model that exactly replicates a launch vehicle and launchpad for simulating the aeronautic environment at the liftoff of rockets. They investigated the noise suppression effect caused by the water injection on the heated and cooled jets at the single-nozzle free-jet and impinging-jet by changing the various parameters such as the injection point of the water jet, the size of the droplets, and so on. Terakado et al., 2016 conducted the DNS of the temporally evolving compressible turbulent mixing layer including solid particles simulating the shear layer of the atmosphere and the exhaust jet of solid rocket motors by solving the three-dimensional compressible gas-particle-multiphase Navier–Stokes equations in the Euler–Euler formulation. They investigated the effect of the solid particle on the flowfield and pressure wave emitted from the shear layer. They found that the fine-scale turbulent structures are attenuated by the existence of the solid particles, especially for the jet side. Also, the growth rate of the mixing layer becomes small due to the particle effects. Because of the change in the flowfield, the Mach-wave-like structure disappear in the multiphase case. This kind of similar problem setting was also studied by Buchta, Shallcross, and Capecelatro, 2019. They conducted the DNS of the temporally evolving high-speed free-shear-flow turbulence including droplets or particles by Eulerian–Lagrangian simulations. The interaction between the turbulence and particles are considered via the particle drag model and volume displacement, which correspond to the effects of the local slip velocity between phases and the finite-size particles, respectively. Their result showed that the emitted noise from the subsonic jet increases with increasing mass loading, consistent with existing low-Mach-number theory. Conversely, the sound level emitted from the supersonic jet suppressed with increasing mass, consistent with the trend reported by previous experimental and numerical studies.

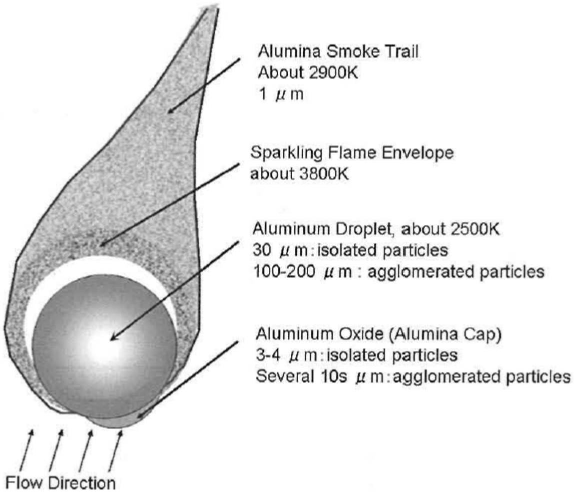

FIGURE 1.5: Sketch of a burning aluminum droplet in solid rocket motor (Shimada, Daimon, and Sekino, 2006).

Toward highly accurate predictions of the acoustic level at the liftoff of the rocket, the influences of the particles to be examined by accurate numerical simulations. The detailed aspects of the complex physics should be taken into account, but the size of the aluminum droplets and alumina particles released from solid rocket motors are approximately 1–200 μm Shimada, Daimon, and Sekino, 2006, and the exhaust jet is supersonic flow. Therefore, the flow over each particle experiences the compressible low-*Re* conditions (e.g., when particles passing through the shock wave or shear layer).

The flow over each particle appears to be compressible low-*Re* flows due to the high-speed flows with small size particles. If the flowfield is uniform, the relative velocity between the particle and fluid eventually becomes zero even though the supersonic flows. However, there are the turbulence, shear layer, and shock wave in the actual flowfield. Those phenomena lead to the velocity difference between the particles and fluid when the particles passed those flow structures. However, the confidence of models to describe particle effects on the compressible multiphase flow is not sufficient because the understanding of the characteristics of the compressible low-*Re* flow over a sphere is limited due to a lack of the experimental study due to the difficulty of the experiment.

Drag Model in Steady Compressible Flow

The particle drag model for the steady compressible flow has been proposed by several researchers. These models are based on the experimental data (see section 1.2.1), theoretical formula, and empirical collections. For example, Carlson and Hoglund, 1964 constructed the particle drag model for the compressible and rarefied regime. His model is based on the Stokes' law (Stokes, 1851) and correction terms which taken into accent the inertia, compressibility, and rarefaction effects. The correction term for the inertia effect is based on the empirical correction by Torobin and Gauvin, 1959. The correction term for the compressibility effect at continuum regime is based on the empirical fit using drag data at compressible high-*Re* flows by Hoerner, 1965. The rarefaction effect at the low-speed regime is considered based on the formula by Millikan, 1923, and the rarefaction effect at the high-speed regime is considered based on the constants determined by the theoretical formula by Stalder and Zurick, 1951. The newer particle drag models for the compressible and rarefied regimes have been proposed by using the similar way with the updated sphere drag database (Crowe, 1967; Henderson, 1976; Hermsen, 1979; Loth, 2008; Parmar, Haselbacher, and Balachandar, 2010). Such drag models can be used in the simulation of the compressible multiphase flows, for example. However, Saito, Marumoto, and Takayama, 2003 pointed out that the result of numerical simulations of the compressible particle-laden flow using the particle drag model is changed depending on the particle drag model used in the simulations.

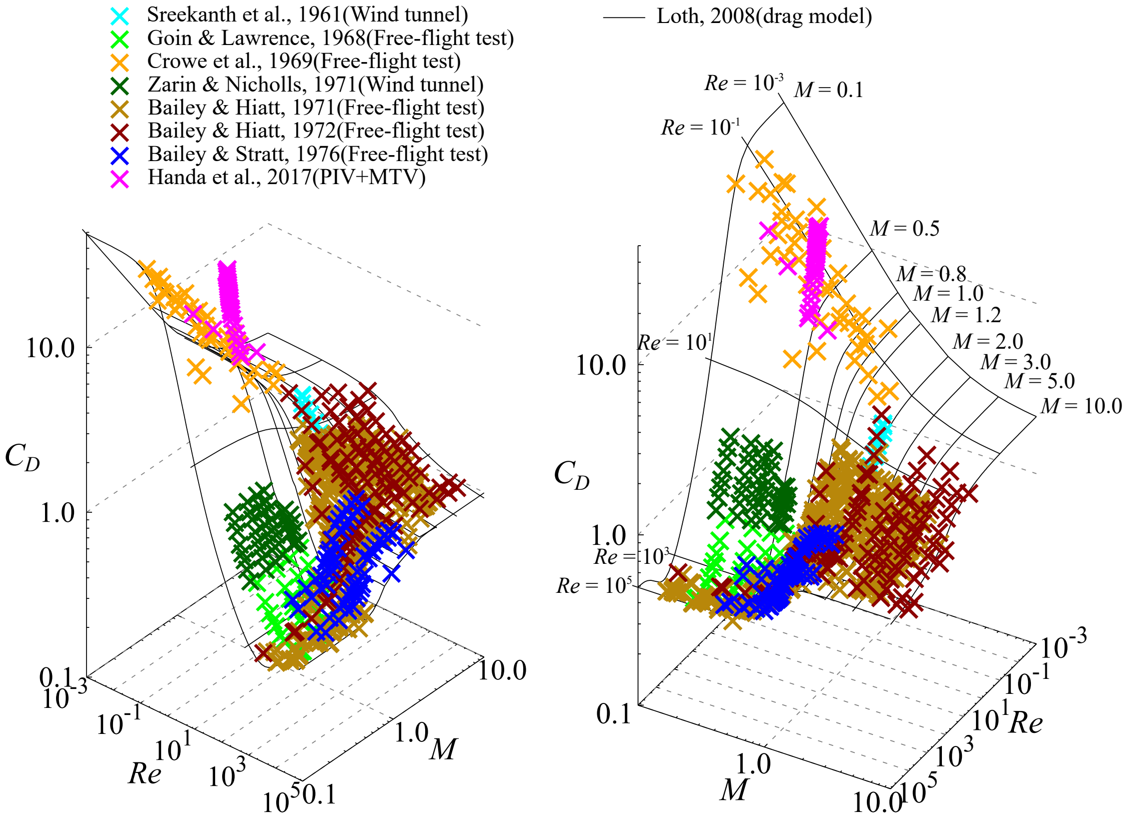

FIGURE 1.6: Map of the drag coefficient of a sphere at compressible low-Reynolds-number flows.

The particle drag model for the compressible flow is used not only for the multiphase flow analysis but also for the correction of the PIV measurement at the compressible flow. When the particles pass the shock, for example, the velocity of the gas instantaneously decreases and the particles do not trace the gas because of its inertia. The slip of the tracer particle has been studied by many researchers (Lang, 2000; Koike et al., 2007; Ragni et al., 2011; Williams et al., 2015; Chen et al., 2017). For example, Williams et al., 2015 examine the effects of compressibility, slip, and fluid inertia on the frequency response of the particle image velocity by solving the equation of quasi-steady drag for solid spherical particles at the supersonic condition. They showed that the frequency response for weak disturbance, such as turbulence, is much lower than obtained from a shock response. This result indicates the particle response frequency is depending on the strength of the disturbance. In addition, Handa, Koike, and Imabayashi, 2017 estimated the drag coefficient of the PIV tracer particle in the compressible and rarefied flows through the measurement of an under expanded jet by PIV and molecular-tagging velocimetry. The estimated drag coefficients were not agree with the predicted value by a well-known empirical model including both compressible and rarefaction effects. The data fit a relation similar to the form of the Stokes drag law rather than the well-known compressible and rarefied models.

1.2 Incompressible and Compressible Low-Reynolds-Number Flow over Blunt Bodies

1.2.1 Flow over a Sphere

Studies of flow over generic bodies such as a flat plate, cylinder, or sphere have contributed to a better understanding of the fundamentals of fluid mechanics and the modeling of complex phenomena. A sphere is the simplest three-dimensional body, but the flowfield is complicated even such a simple body, and the flow over a sphere varies depending on flow conditions. Tiwari et al., 2019a; Tiwari et al., 2019b published excellent review paper for flow over a sphere.

The behaviour of flow over a sphere varies with Re. This has been examined by various researchers experimentally and numerically under incompressible conditions. Taneda, 1956 experimentally examined the wake of a sting-mounted sphere at $5 \leq Re \leq 300$. He determined that the critical Re of the formation of an axisymmetric vortex ring behind a sphere is $Re \approx 24$. Also, he observed a very long period oscillation of the axisymmetric vortex ring when Re reached $Re = 130$. Magarvey and Bishop, 1961 experimentally examined wake structures of a falling liquid droplet in liquid at $0 \leq Re \leq 2,500$. They observed that asymmetry appears in the recirculation region at around $Re > 210$. Nakamura, 1976 also observed asymmetry in a steady recirculation region at $Re > 190$. Taneda, 1978 experimentally examined the wake behind a sphere at Re ranging from $O(10^4)$ to $O(10^6)$ using the surface-oil flow, smoke, and tuft-grid methods. He observed wave motion in the wake at $O(10^4) \leq Re \leq 3.8 \times 10^5$ and noted that it forms a pair of streamwise vortices at $3.8 \times 10^5 \leq Re \leq 10^6$. Sakamoto and Haniu, 1990 experimentally investigated the vortex shedding from a sphere in a uniform flow at $300 \leq Re \leq 4.0 \times 10^4$. They examined the wake of a sphere by hot-wire and flow visualization experiments. They showed that the wake vortices change from laminar to turbulent when Re reached approximately 800. In addition, they found that the higher- and lower-frequency modes of a Strouhal number ($St = fd/u_\infty$) of a vortex shedding frequency f coexist at $800 \leq Re \leq 1.5 \times 10^4$. Johnson and Patel, 1999 experimentally and numerically examined at $20 \leq Re \leq 300$. They numerically identified the critical Re for a steady axisymmetric flow ($Re \leq 210$), steady non-axisymmetric (planar-symmetric) flow ($210 \leq Re \leq 270$), and unsteady (periodic) flow ($Re > 270$) by DNS of the three-dimensional incompressible Navier–Stokes equations. The higher-Re conditions for flows over a sphere were studied by Tomboulides and Orszag, 2000 and Rodriguez et al., 2011 for $25 \leq Re \leq 1,000$ and $Re = 3,700$, respectively.

Kane, 1951 was among the first to investigate the effect of Re on the sphere drag under the compressible flow. He measured the sphere drag at $2.1 \leq M \leq 2.8$ and $15 \leq M \leq 800$ using a low-density supersonic wind tunnel, and Re effect on the drag coefficient has been confirmed. Furthermore, he conducted the flow visualization and the photograph indicated that interaction occurred between the sphere boundary layer and shock wave. May, 1953 measured the drag coefficients by a free-flight experiment using the pressurized Ballistic range. They used steel and aluminum spheres 1/4 to 3/4 inch in diameter. The test condition was $0.8 \leq M \leq 4.7$ and $1.14 \times 10^3 \leq Re \leq 8.4 \times 10^6$, and the sphere drag coefficients were obtained from position-time data. The variation of the drag coefficient was found to be approximately 10% in the range $1.6 < M < 4.7$ and $4.0 \times 10^3 < Re < 1.0 \times 10^6$. May, 1957 obtained the drag coefficient of a sphere at further low-Re conditions in $1.5 < M < 3.0$ and $350 < Re < 3,000$ by free-flight experiments using a ballistic range, and they derived a contour map of the sphere drag in M and Re coordinate by the experimental data. Sreekanth, 1961 measured the drag coefficient of a sting-supported sphere at $M = 2$ and $0.1 < Kn < 0.8$ in a low-density wind tunnel. The influence of support interference on the measured drag force was reported. Goin and Lawrence, 1968; Bailey and Hiatt, 1971; Bailey and Hiatt, 1972; Bailey, 1974; Bailey and Starr, 1976 carried out free-flight experiments using a ballistic range and estimated the drag coefficient of the sphere for a wide range of Re and $M(0.1 \leq M \leq 6$ and $O(10^{-2}) \leq Re \leq O(10^{7}))$. Crowe et al., 1968 calculated the drag coefficients of micron-size particles through subsonic speed free-flight experiments by measuring the deceleration of the flight speed of the particle with a Faraday cage. In addition, Zarin and Nicholls, 1971 conducted wind tunnel experiments with a sphere at $0.1 \leq M \leq 0.57$ and $40 \leq Re \leq 5,000$. They used a one-component magnetic balance and suspension system to subtract the support interference. By their studies, the characteristics of the sphere drag coefficient have been investigated in a wide range of M and Re. However, the data of the sphere drag in this region is still fewer than that in the incompressible flow. Also, because these studies only focused on the drag coefficient, the number of studies on the flowfield, the heat transfer, and the lift coefficient due to the rotation of the sphere and background shear at compressible low-Re flows remains few.

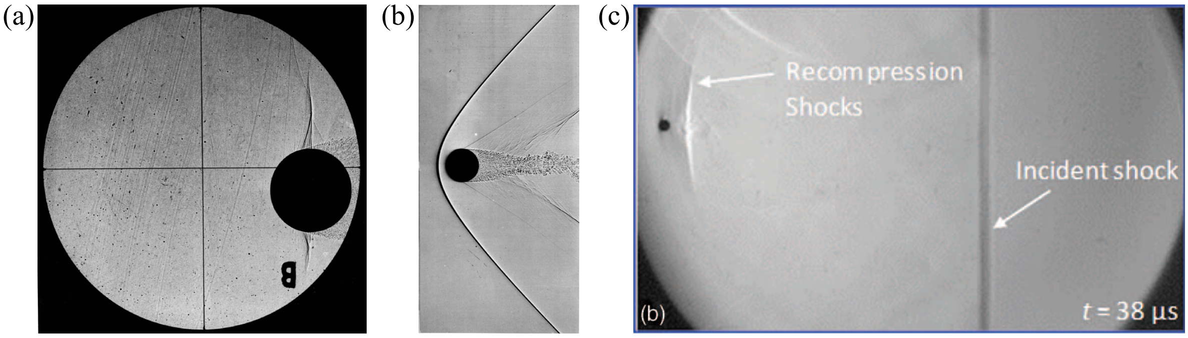

FIGURE 1.7: Visualization image of the flow over a sphere in compressible flows: (a) $M = 0.86$ and $Re = 9.2 \times 10^{5}$ (Dyke, 1982); (b) $M = 1.53$ and $Re \approx 4.4 \times 10^{5}$ (estimated value as standard atmosphere) (Dyke, 1982); (c) $M = 0.99$ and $Re \approx 4.3 \times 10^{4}$(Wagner et al., 2012).

Visualization studies on the compressible low-Re flow are quite difficult because of the small-sized test model and low-density gases to decrease Re. Particularly, the visualization of the wake structure is extremely difficult. A number of beautiful pictures of the flow visualization of the compressible flow over a sphere have been taken. Figures 1.7(a) and (b) are the shadowgraph images of the flow over a sphere in free flight at $Re = O(10^{5})$ in the transonic and supersonic speeds (Dyke, 1982). In this Re range, the shock wave and wake structures can clearly be seen, also even turbulent boundary layer separation. Figure 1.7(c) is the schlieren image of the shock particle interaction process taken by Wagner et al., 2012. The flow condition based on the particle and flow behind the incident shock is $Re \approx 4.3 \times 10^{4}$ at $M = 0.99$. The diameter of the test model in this picture is 1 mm. In this Re range, the visualization image is unclear due to the small size of the model. The outline of the shock structure can be recognized but the wake structure is cannot be confirmed. It should be noted that the purpose of their experiment was not the visualization of the wake.

Numerical examinations of the compressible low-Re in the continuum regime have also been conducted. Meliga, Sipp, and Chomaz, 2010 studied linear dynamics of global eigenmodes in the wake of compressible axisymmetric flows of the sphere at $0 \leq M \leq 0.7$ and $270 \leq Re \leq 285$. They determine the boundary of the stable and unstable region in the M and Re coordinates, and showed that an increase in M yields a destabilization of the flow past the sphere. Recently, the flow over a sphere under compressible low-Re flow have been studied through the fully three-dimensional numerical simulations by us (since 2016), Riahi et al., 2018, and Sansica et al., 2018. Riahi et al., 2018 computed the flow over a sphere at $0.3 \leq M \leq 2.0$ and $50 \leq Re \leq 600$ using the IBM. They found that the wake structure for $M = 0.95$ is unsteady flow with alternating hairpin vortices at $Re = 600$, and the wake at $M = 2.0$ is steady flow up to Re of 600. Sansica et al., 2018 conducted a fully three-dimensional linear stability analysis to investigate the unstable bifurcations of the compressible flow over a sphere with the low-Re condition in the range of $0.1 \leq M \leq 1.2$ and $200 \leq Re \leq 370$. They showed that the flow becomes globally stable and switches to a noise-amplifier system when reached supersonic conditions. In addition, they applied a continuous Gaussian white noise forcing in front of the shock and examine the convective nature of the flow by a Fourier analysis and a dynamic mode decomposition. The transition in the wake does not observe in the chosen Re and forcing amplitude. Mao et al., 2019 carried out the DNS of supersonic turbulent flow over a sphere by the three-dimensional ghost zone IBM with high-order schemes. They showed that the drag coefficient increases as the inflow turbulence intensity increases, and the increment of the drag coefficient is smaller than that of the incompressible cases. In addition, both Kolmogorov and Taylor scales decrease after being compressed by the bow shock, and the both streamwise and transverse Reynolds stress take peak value at the shock location.

In addition, the particle-resolved DNS by finite-size particle approach have been conducted. Mizuno et al., 2015; Mizuno et al., 2016 constructed the simple IBM flow solver. The solver has the capability to solve the three-dimensional compressible particle-laden flow including shock waves, and they investigated flow containing multiple moving particles and the shock wave. They successfully simulate the normal shock-particle interaction by the particle-resolved DNS. Das et al., 2017; Das et al., 2018 also constructed the IBM flow solver which has capability to solve the three-dimensional compressible particle-laden flow including shock waves, and they simulated the interaction of the normal shock and particle cloud. Moreover, they applied machine learning to develop surrogate drag models for shocked particulate flows. Schneiders et al., 2016 examined the interaction between the particles and compressible turbulence. They simulated the modulation of decaying isotropic turbulence by 45,000 spherical particles of Kolmogorov-length-scale size by particle-resolved DNS using the cut-cell method. By using the cut-cell method, the exchange of the momentum and energy through the fluid-particle interface is strictly conserved. Their results showed that the particles absorb energy from the large scales component of the gas-phase while the motion of small-scale turbulence is determined by the particle dynamics. The level of dissipation increases locally because of the intense strain rate generated near the particle surfaces caused by the crossing-trajectory effect. Hosseinzadeh-Nik, Subramaniam, and Regele, 2018 conducted the particle-resolved DNS of the normal shock-particle interactions. They studied the unsteady interaction of the wave-wave and wake-wake interactions, the interaction of the planar-shock with a particle cloud, and the intensity of the incident wave from the compression wave to impulsive shock wave. Osnes et al., 2019 investigated the Re effects on the shock-induced flow using ensemble-averaged results from particle-resolved LES. They showed that the shock-particle cloud interaction produces a reflected shock wave and its strength increases with a decreasing of particle Re.

1.2.2 Flow over a Circular Cylinder

A circular cylinder is one of the simplest geometry, but the flow field around the circular cylinder is complex and changes depending on Re. The incompressible flow over a circular cylinder has been investigated numerically and experimentally for a wide range of Re.

Taneda, 1956 conducted a flow visualization experiment and investigated the flow structure around a circular cylinder at $0.1 \leq Re \leq 2,000$. He showed that the flow over a circular cylinder is fully attached at $Re \leq 5$. The separation occurs at $Re = 5$, then the length of the recirculation region increases as Re increases, and becomes asymmetric recirculation approximately at $Re = 45$. Dennis and Chang, 1970 conducted numerical simulations of the wake of a circular cylinder at $5 \leq Re \leq 100$ using the finite difference method. Their results showed that the length of the recirculation region approximately linearly increases as Re increases. Coutanceau and Bouard, 1977 visualized the wake of a circular cylinder at $5 < Re < 40$ and showed that the length of the recirculation region increases linearly with increasing Re.

For $Re > 47$, periodic laminar vortex shedding occurs. The Re effect on the St of the vortex shedding in the unsteady regime was also studied. Roshko, 1954 measured the vortex shedding frequency of a circular cylinder at $40 < Re < 10,000$. He showed that the St of vortex shedding increases as Re increases. On the other hand, the St of vortex shedding is independent from Re at $300 < Re < 10,000$. Williamson, 1988a; Williamson, 1988b; Behara and Mittal, 2010 investigated the three-dimensional effects on the St of vortex shedding and the wake structures. The three-dimensionality in the wake firstly observed at around $Re = 64$. There is a discontinuity in the St of the vortex shedding in the spanwise direction, and the lower frequency was observed in the region near the sidewall. The frequency spectra of the vortex shedding make a single and sharp peak at around $64 < Re < 180$ (oblique shedding). In this regime, wake vortices have a slant angle. As Re increases, the discontinuity on the Re–St curve and the streamwise vortices appear at around $Re = 180$. The St of vortex shedding discontinuously decreases due to the vortex dislocation, and this mode is retained at $180 < Re < 230$ (mode-A). As Re further increases, a second discontinuity on the Re–St curve appears, and the St of vortex shedding discontinuously increases at around $Re = 230$ (mode-B). In addition, the steady and unsteady aerodynamic force measurements were conducted over a range of Re from the onset of the two-dimensional oscillation and the conditions that the boundary layer becomes turbulent (Delany and Sorensen, 1953; Tritton, 1959; Gerrard, 1961; Norberg, 2001).

In the case of the incompressible flows over a circular cylinder, the flow dynamics can be characterized by Re. In the case of the compressible flows over a circular cylinder, there is the effects of M on the flow properties as well as Re. Lindsey, 1938 was among the first to investigate the effect of Re under the compressible flow. He measured the drag force of a circular cylinder at $840 \leq Re \leq 3.1 \times 10^5$ and $0.05 \leq M \leq 0.65$ and demonstrated the M and Re dependence of the drag coefficient through a wind tunnel experiment. Gowen and Perkins, 1953 measured the pressure distribution around a circular cylinder in the subsonic and supersonic flows and measured the drag coefficients in the range of $5.0 \times 10^4 \leq Re \leq 1.0 \times 10^6$ and $0.3 \leq M \leq 2.9$. They clarified that there is no Re effect on the drag coefficient under the supersonic conditions that they investigated. McCarthy and Kubota, 1964 investigated the flow field behind a circular cylinder at $M = 5.7$ and $4,500 \leq Re \leq 66,500$ by measuring the Pitot pressure, static pressure, and total temperature in the wake. They determined the transition from laminar to turbulent flow based on the velocity profiles and correlated with the result of mass-diffusion and hot-wire fluctuation measurements. Murthy and Rose, 1978 investigated the vortex shedding frequencies of a circular cylinder at $Re = 3.0 \times 10^4$, 1.66×10^5 and 5.0×10^5 and $0.25 \leq M \leq 1.2$ by wind tunnel experiments. They showed that the St of vortex shedding at $O(10^4) \leq Re \leq O(10^5)$ is approximately 0.18 at $M < 0.9$ and that there is no detectable vortex shedding at $M > 0.9$. Rodriguez, 1984 investigated flow over a circular cylinder at $1.7 \times 10^5 \leq Re \leq 3.4 \times 10^5$ and $0.4 < M < 0.8$ by the high-speed flow visualization synchronized with unsteady surface-pressure measurements. They clarified the relationship between the distribution of the surface pressure and the flow patterns in the near wake.

Numerical studies have also been conducted. Canuto and Taira, 2015 performed a two-dimensional direct numerical simulation (DNS) of the compressible flow over a circular cylinder at $20 \leq Re \leq 100$ and $0 \leq M \leq 0.5$. They found that the compressibility effects reduce the growth rate and dominant frequency in the linear growth stage. Xu, Chen, and Lu, 2009 investigated the flow around a circular cylinder at $Re = 2.0 \times 10^5$ and $0.85 \leq M \leq 0.95$ through a detached-eddy simulation. They showed that the flow at $M < 0.9$ is an unsteady flow characterized by moving shock waves interacting with the turbulent wake in the near region of the circular cylinder and that the flow at $M > 0.9$ is a quasi-steady flow with nearly stationary shock waves formed in the near wake. Xia et al., 2016 computed the compressible flow past a circular cylinder at $Re = 4.0 \times 10^4$ and 1.0×10^6 and $0.5 \leq M \leq 0.95$ through a constrained large-eddy simulation approach. They analyzed the effect of M on the flow pattern and some flow quantities such as the drag coefficient and pressure coefficient distribution. They showed that flowfield and flow properties dramatically changed around the high-subsonic and transonic flows.

Figure 1.8 shows a map of the condition investigated in the previous studies. The experimental and numerical studies on the compressible flow over a circular cylinder have been conducted at $O(10^1) \leq Re \leq O(10^2)$ and $O(10^4) \leq Re \leq O(10^6)$. Because it is difficult to investigate this region through either computation or visualization due to the large computational cost or the small test model and low-density conditions, respectively, there are few studies at around $Re = O(10^3)$, particularly flow visualization studies.

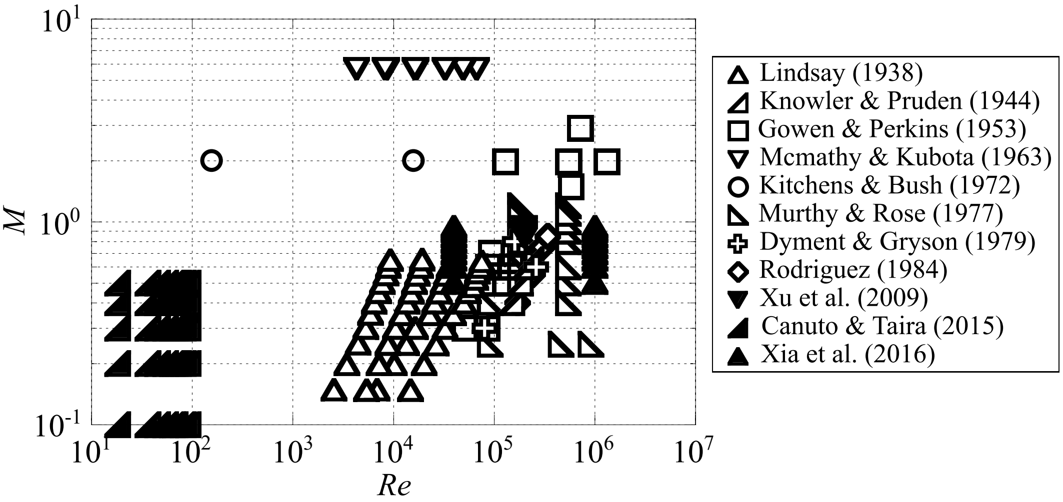

FIGURE 1.8: Map of the conditions of published studies for a circular cylinder at compressible low-*Re* flows. Lindsey, 1938 (exp., drag measurement); Knowler and Pruden, 1944 (exp., drag and pressure measurement); Gowen and Perkins, 1953 (exp., drag and pressure measurement, shadowgraph); McCarthy and Kubota, 1964 (exp., pitot-pressure, static pressure, and total temperature measurements, schlieren); Kitchens and Bush, 1972 (exp., hot-wire measurement, shadowgraph); Murthy and Rose, 1978 (exp., pressure and skin friction measurement); Dyment and Gryson, 1979 (exp., shadowgraph and schlieren); Rodriguez, 1984 (exp., shadowgraph and unsteady pressure measurement); Xu, Chen, and Lu, 2009 (CFD, DES); Canuto and Taira, 2015 (CFD, DNS); Xia et al., 2016 (CFD, CLES)

1.3 Contributions and Outline

In the present study, the characteristics of the compressible low-*Re* flow over an isolated sphere are investigated toward the modeling of the compressible multiphase flows. The flow over a sphere is investigated by the direct numerical simulation of the Navier–Stokes equations, the free-flight experiments, and the shock-sphere interaction experiment. The outline of the present study is shown in figure 1.9.

In chapter 3, the uniform flow over a stationary adiabatic sphere is investigated by the direct numerical simulation of the three-dimensional compressible Navier–Stokes equations at $50 \leq Re \leq 1{,}000$ and $0.3 \leq M \leq 2.0$. The effects of M and Re on the flow regime, flow geometry, aerodynamic force coefficients are provided.

In chapter 4, the uniform flow over a stationary isothermal sphere is investigated by the direct numerical simulation of the three-dimensional compressible Navier–Stokes equations at $100 \leq Re \leq 300$ and $0.3 \leq M \leq 2.0$. The temperature difference between the freestream and the surface of the sphere is varied in the range from 0.5 to 2.0, and the effects of the surface temperature on the flow properties are provided.

In chapter 5, the uniform flow over a rotating adiabatic sphere and the linear shear flow over a stationary adiabatic sphere are investigated by the direct numerical simulation of the three-dimensional compressible Navier–Stokes equations. The flow condition for the rotating sphere is $100 \leq Re \leq 300$ and $0.3 \leq M \leq 2.0$. The normalized rotation rate based on the freestream velocity and the surface velocity at the equator of the sphere is varied in the range from 0 to 1.0, and the effects of the rotation on the flow properties are provided. The flow condition for the rotating sphere is $100 \leq Re \leq 300$ and $0.3 \leq M \leq 1.5$. The normalized dimensional shear rate normalized by the freestream velocity and the radius of the sphere is fixed at 0.1, and the effects of the background shear on the flow properties are provided. In chapter 6, the flow over an isolated sphere is investigated by the free-flight and shock-sphere interaction experiments. The flow condition for the free-flight experiment is $3.7 \times 10^3 \leq Re \leq 3.8 \times 10^5$ and $0.9 \leq M \leq 1.6$. The small sphere is launched into the low-pressurized test section by a single-stage light gas gun, and the flowfield is visualized by the schlieren technique. The effects of M and Re on the wake structure and flow geometry are provided. The flow conditions for the shock-sphere interaction experiment based on the shock behind quantities is $1.8 \times 10^3 \leq Re \leq 1.4 \times 10^4$ and $0.4 \leq M \leq 1.3$. The sphere drop-off system is constructed and applied to the experiment. The small sphere is released from the upper wall of the shock tube and interacts with the planar-shock wave. The flowfield acquired by the schlieren technique and the drag coefficient estimated from the position-time data of the sphere are provided.

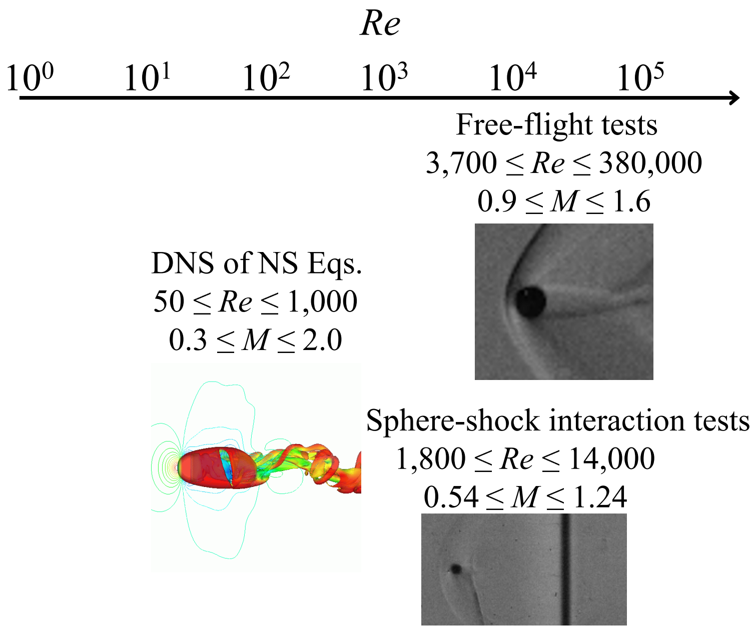

FIGURE 1.9: Outline of the present study.

Chapter 2

Methodologies

List of Symbols

a = sound speed

E, F, G = x, y, and z components of an inviscid flux

$E_\mathrm{v}, F_\mathrm{v}, G_\mathrm{v}$ = x, y, and z components of an viscous flux

L = Length

J = Transformation Jacobian

Q = Conservative variable vector ξ, η, ζ directions

R = Gas constant

T = Temperature

U, V, W = Contravariant velocities in

c_p = Specific heat at constant pressure

e = Total energy per unit volume of the gas phase

h = Heat transfer coefficient

k = Thermal conductivity

p = Pressure

q = Heat flux

t = Time

u, v, w = Velocity in x, y, and z directions

x, y, z = Cartesian coordinates

$\delta_i.j$ = Kronecker delta

γ = Specific heat ratio

λ = Second viscosity coefficient

μ = Dynamic viscosity coefficient

ρ = Density

τ_{ij} = Viscous stress tensor

ξ, η, ζ, τ = Curvilinear coordinates

Subscripts

cg = center of gravity

∞ = Freestream

2.1 Numerical Methods

2.1.1 Navier–Stokes Equations

Navier–Stokes Equations in Cartesian Coordinate System

The three-dimensional compressible Navier–Stokes equations were employed as governing equations. These equations in the Cartesian coordinate system are as follows:

$$\frac{\partial Q}{\partial t}+\frac{\partial E}{\partial x}+\frac{\partial F}{\partial y}+\frac{\partial G}{\partial z}=\frac{\partial E_{\mathrm{v}}}{\partial x}+\frac{\partial F_{\mathrm{v}}}{\partial y}+\frac{\partial G_{\mathrm{v}}}{\partial z} \tag{2.1}$$

where Q contains conservative variables; E, F, and G are the x, y, and z components of an inviscid flux, respectively; and E_{v}, F_{v}, and G_{v} are the x, y, and z components of a viscous flux, respectively.

$$Q=\begin{bmatrix}\rho\\ \rho u\\ \rho v\\ \rho w\\ e\end{bmatrix}, E=\begin{bmatrix}\rho u\\ \rho u^2+p\\ \rho uv\\ \rho uw\\ (e+p)u\end{bmatrix}, F=\begin{bmatrix}\rho v\\ \rho vu\\ \rho v^2+p\\ \rho vw\\ (e+p)v\end{bmatrix}, G=\begin{bmatrix}\rho w\\ \rho wu\\ \rho wv\\ \rho w^2+p\\ (e+p)w\end{bmatrix} \tag{2.2}$$

$$E_{\mathrm{v}}=\begin{bmatrix}0\\ \tau_{xx}\\ \tau_{xy}\\ \tau_{xz}\\ \beta_x\end{bmatrix}, F_{\mathrm{v}}=\begin{bmatrix}0\\ \tau_{yx}\\ \tau_{yy}\\ \tau_{yz}\\ \beta_y\end{bmatrix}, G_{\mathrm{v}}=\begin{bmatrix}0\\ \tau_{zx}\\ \tau_{zy}\\ \tau_{zz}\\ \beta_z\end{bmatrix} \tag{2.3}$$

$$\begin{cases}\beta_x=\tau_{xx}u+\tau_{xy}v+\tau_{xz}w-q_x\\ \beta_y=\tau_{yx}u+\tau_{yy}v+\tau_{yz}w-q_y\\ \beta_z=\tau_{zx}u+\tau_{zy}v+\tau_{zz}w-q_z\end{cases}$$

where q and tau denote the heat flux and viscous stress. Moreover, e is the total energy per unit volume and assume to be the state of the ideal gas,

$$e = \frac{p}{\gamma - 1} + \frac{1}{2}\rho(u^2 + v^2 + w^2) \tag{2.4}$$

where γ denotes the specific heat ratio and it was set to be 1.4 for the air. We assume that the stress tensor is a linear function of the rate of the strain tensor. The viscous stress tensor $\tau_{i,j}$ for a Newtonian fluid is based on the temperature T and velocity,

$$\tau_{i,j} = \mu(T)\left(\frac{\partial u_i}{\partial x_j} + \frac{\partial u_j}{\partial x_i}\right) + \delta_{ij}\lambda\frac{\partial u_k}{\partial x_k}\frac{p}{\gamma - 1} + \frac{1}{2}\rho(u^2 + v^2 + w^2) \tag{2.5}$$

where the Einstein summation convention is used. The sum of the diagonal component of τ becomes

$$\sum \tau_{i,i} = (3\lambda + 2\mu)\frac{\partial u_i}{\partial x_i}. \tag{2.6}$$

The second viscosity coefficient λ is determined as this value becomes zero and its average value is

$$\frac{\sum \tau_{i,i}}{3} = (\lambda + \frac{2}{3}\mu)\frac{\partial u_i}{\partial x_i} \tag{2.7}$$

where the coefficient $\lambda + \frac{2}{3}\mu$ is called the bulk viscosity, and assumed to be zero in the Stokes' hypothesis $\frac{1}{3}(\tau_{xx} + \tau_{yy} + \tau_{zz}) = 0$. The second viscosity coefficient then can be written as

$$\lambda = -\frac{2}{3}\mu(T). \tag{2.8}$$

Therefore, the stress tensor $\tau_{i,j}$ becomes

$$\tau_{i,j} = \mu(T)\left(\frac{\partial u_i}{\partial x_j} + \frac{\partial u_j}{\partial x_i}\right) - \frac{2}{3}\delta_{i,j}\mu(T)\frac{\partial u_k}{\partial x_k} \tag{2.9}$$

where $\delta_{i,j}$ is the Kronecker delta, which is defined as δ_{ij} if $i = j$ and $\delta_{i,j} = 0$ if $i \neq j$. The dynamic viscosity $\mu(T)$ is given by Sutherland's law Sutherland, 1893 for air,

$$\frac{\mu(T)}{\mu_\infty} = \left(\frac{T}{T_\infty}\right)^{\frac{3}{2}}\left(\frac{1 + 110.4/T_\infty}{(T + 110.4)/T_\infty}\right). \tag{2.10}$$

We also assume that the heat-flux vector is proportional to the gradient of the temperature. The heat-flux vector q is obtained by Fourier's law,

$$q_j = -k\frac{\partial T}{\partial x_j} \tag{2.11}$$

where k is the thermal conductivity. Here, the thermal conductivity, the heat capacity at the constant pressure, the sound speed, and the ideal gas law are

$$k = \frac{\mu(T)c_p}{\mathrm{Pr}}, c_p = \frac{\gamma \mathrm{R}}{\gamma - 1}, a = \sqrt{\gamma \mathrm{R} T}, T = \frac{p}{\rho \mathrm{R}} \tag{2.12}$$

where R is gas constant, and thus, the heat flux is

$$q_j = -\frac{\mu(T)C_p}{\mathrm{Pr}}\frac{\partial T}{\partial x_j} = -\frac{\mu(T)}{\mathrm{Pr}}\frac{\gamma \mathcal{R}}{\gamma - 1}\frac{\partial T}{\partial x_j} = -\frac{\mu(T)}{\mathrm{Pr}}\frac{1}{\gamma - 1}\frac{\partial a^2}{\partial x_j} \tag{2.13}$$

where Pr is Prandtl number that indicates the ratio of the viscous diffusion and temperature diffusion. The value set as Pr = 0.72, the same as air.

Non-Dimensionalization of Navier–Stokes Equations

Navier–Stokes equations are non-dimensionalized by introducing the freestream quantities ρ_∞, a_∞, and μ_∞) and the reference length L_R

$$x_i = \frac{x_i^*}{L_R^*}, t = \frac{t^*}{L_R^*/a_\infty^*}, \rho = \frac{\rho^*}{\rho_\infty^*}, u_i = \frac{u_i^*}{a_\infty^*}, e = \frac{e^*}{\rho_\infty^* {a_\infty^*}^2}, \tag{2.14}$$

$$p = \frac{p^*}{\rho_\infty^* {a_\infty^*}^2} = \frac{p^*}{\gamma p_\infty^*}, \mu = \frac{\mu^*}{\mu_\infty^*}, \tau_{ij} = \frac{\tau_{ij}^*}{\mu_\infty^* a_\infty^* / L_\mathrm{R}^*}, q_i = \frac{q^*}{\mu_\infty^* {a_\infty^*}^2 / L_R^*}, \tag{2.15}$$

where the asterisk denotes dimensional quantities. The non-dimensional Navier–Stokes equations in the Cartesian coordinate system can be obtained by substituting these non-dimensional physical properties into eq. (2.1).

$$\frac{\partial Q}{\partial t} + \frac{\partial E}{\partial x} + \frac{\partial F}{\partial y} + \frac{\partial G}{\partial z} = \frac{1}{Re}\left(\frac{\partial E_\mathrm{v}}{\partial x} + \frac{\partial F_\mathrm{v}}{\partial y} + \frac{\partial G_\mathrm{v}}{\partial z}\right) \tag{2.16}$$

where *Re* is the Reynolds number. which can be interpreted as the ratio of inertial and viscous forces, the definition follows:

$$Re = \frac{\rho^*_\infty a^*_\infty L^*_\mathrm{R}}{\mu^*_\infty}, Re = \frac{1}{M_\infty}\frac{\rho^*_\infty a^*_\infty L^*_\mathrm{R}}{\mu^*_\infty}, M_\infty = \frac{u^*_\infty}{a^*_\infty} \tag{2.17}$$

Navier–Stokes Equations in Carvilinear Coordinate System

In the present study, the governing equations were solved on the body-fitted grid. Therefore, the Navier–Stokes equations in the curvilinear coordinate system were solved. The governing equations of eq. 2.1 are transformed from those in the Cartesian coordinate system to the general curvilinear coordinate system. Each coordinate system is related as follows:

$$\begin{cases} x = x\left(\xi, \eta, \zeta, \tau\right) \\ y = y\left(\xi, \eta, \zeta, \tau\right) \\ z = z\left(\xi, \eta, \zeta, \tau\right) \\ t = \tau \end{cases} \Longleftrightarrow \begin{cases} \xi = \xi(x, y, z, t) \\ \eta = \eta(x, y, z, t) \\ \zeta = \zeta(x, y, z, t) \\ \tau = t \end{cases} \tag{2.18}$$

The differential form of the Cartesian coordinate system (x, y, z, t) is

$$\begin{bmatrix} \mathrm{d}x \\ \mathrm{d}y \\ \mathrm{d}z \\ \mathrm{d}t \end{bmatrix} = \begin{bmatrix} x_\xi & x_\eta & x_\zeta & x_\tau \\ y_\xi & y_\eta & y_\zeta & y_\tau \\ z_\xi & z_\eta & z_\zeta & z_\tau \\ 0 & 0 & 0 & 1 \end{bmatrix} \begin{bmatrix} \mathrm{d}\xi \\ \mathrm{d}\eta \\ \mathrm{d}\zeta \\ \mathrm{d}\tau \end{bmatrix} \tag{2.19}$$

where $t_\xi = t_\eta = t_\zeta$ and t_τ. Similarly, the differential from of the curvilinear coordinate system (ξ, η, ζ, τ) is

$$\begin{bmatrix} \mathrm{d}\xi \\ \mathrm{d}\eta \\ \mathrm{d}\zeta \\ \mathrm{d}t \end{bmatrix} = \begin{bmatrix} \xi_x & \xi_y & \xi_z & \xi_t \\ \eta_x & \eta_y & \eta_z & \eta_t \\ \zeta_x & \zeta_y & \zeta_z & \zeta_t \\ 0 & 0 & 0 & 1 \end{bmatrix} \begin{bmatrix} \mathrm{d}x \\ \mathrm{d}y \\ \mathrm{d}z \\ \mathrm{d}t \end{bmatrix} \tag{2.20}$$

where $\tau_x = \tau_y = \tau_z = 0$ and $\tau_t = 1$. Consequently, the relations between the Cartesian coordinate system and the curvilinear coordinate system can be derived from eqs. 2.19 and 2.20. From this relationship, we obtain the metrics $\xi_x, \xi_y, \xi_z, \cdots$ with the derivatives $x_\xi, x_\eta, x_\zeta, \cdots$ as follows.

$$\begin{aligned}
\begin{bmatrix} \xi_x & \xi_y & \xi_z & \xi_t \\ \eta_x & \eta_y & \eta_z & \eta_t \\ \zeta_x & \zeta_y & \zeta_z & \zeta_t \\ 0 & 0 & 0 & 1 \end{bmatrix} &= \begin{bmatrix} x_\xi & x_\eta & x_\zeta & x_\tau \\ y_\xi & y_\eta & y_\zeta & y_\tau \\ z_\xi & z_\eta & z_\zeta & y_\tau \\ 0 & 0 & 0 & 1 \end{bmatrix}^{-1} \\
&= J \begin{bmatrix} y_\eta z_\zeta - y_\zeta z_\eta & z_\eta x_\zeta - z_\zeta x_\eta & x_\eta y_\zeta - x_\zeta y_\eta & -x_\tau \left(y_\eta z_\zeta - y_\zeta z_\eta\right) - y_\tau \left(z_\eta x_\zeta - z_\zeta x_\eta\right) - z_\tau \left(x_\eta y_\zeta - x_\zeta y_\eta\right) \\ y_\zeta z_\xi - y_\xi z_\zeta & z_\zeta x_\xi - z_\xi x_\zeta & x_\zeta y_\xi - x_\xi y_\zeta & -x_\tau \left(y_\zeta z_\xi - y_\xi z_\zeta\right) - y_\tau \left(z_\zeta x_\xi - z_\xi x_\zeta\right) - z_\tau \left(x_\zeta y_\xi - x_\xi y_\zeta\right) \\ y_\xi z_\eta - y_\eta z_\xi & z_\xi x_\eta - z_\eta x_\xi & x_\xi y_\eta - x_\eta y_\xi & -x_\tau \left(y_\xi z_\eta - y_\eta z_\xi\right) - y_\tau \left(z_\xi x_\eta - z_\eta x_\xi\right) - z_\tau \left(x_\xi y_\eta - x_\eta y_\xi\right) \\ 0 & 0 & 0 & 1 \end{bmatrix}
\end{aligned} \tag{2.21}$$

where J is the transformation Jacobian from the Cartesian coordinate system (x, y, z, t) to the curvilinear coordinate system (ξ, η, ζ, τ):

$$\begin{aligned}
J \equiv \frac{\partial(\xi, \eta, \zeta)}{\partial(x, y, z)} = \left(\frac{\partial(x, y, z)}{\partial(\xi, \eta, \zeta)}\right)^{-1} &= \frac{1}{\det \begin{pmatrix} x_\xi & x_\eta & x_\zeta \\ y_\xi & y_\eta & y_\zeta \\ z_\xi & z_\eta & z_\zeta \end{pmatrix}} \\
&= \frac{1}{x_\xi y_\eta z_\zeta + x_\eta y_\zeta z_\xi + x_\zeta y_\xi z_\eta - x_\xi y_\zeta z_\eta - x_\eta y_\xi z_\zeta - x_\zeta y_\eta z_\xi}
\end{aligned} \tag{2.22}$$

To be summarized, the coordinate transformation metrics are obtained as follows:

$$\begin{aligned}
&\xi_x = J\left(y_\eta z_\zeta - y_\zeta z_\eta\right), \quad \xi_y = J\left(z_\eta x_\zeta - z_\zeta x_\eta\right), \quad \xi_z = J\left(x_\eta y_\zeta - x_\zeta y_\eta\right),\\
&\eta_x = J\left(y_\zeta z_\xi - y_\xi z_\zeta\right), \quad \eta_y = J\left(z_\zeta x_\xi - z_\xi x_\zeta\right), \quad \eta_z = J\left(x_\zeta y_\xi - x_\xi y_\zeta\right),\\
&\zeta_x = J\left(y_\xi z_\eta - y_\eta z_\xi\right), \quad \zeta_y = J\left(z_\xi x_\eta - z_\eta x_\xi\right), \quad \zeta_z = J\left(x_\xi y_\eta - x_\eta y_\xi\right).
\end{aligned} \tag{2.23}$$

Since the computational grids do not deform, the Jacobian is constant with time in the present study. Equation 2.23 are the conventional forms of metrics, so-called "nonconservative metrics". The expressions of eq. 2.23 are analytically true, but the use of the high-order finite-difference scheme on their discretization generally causes a numerical error due to violation of the geometric conservation law, which is called freestream preservation error.

The transformation of each terms of the governing equations is based on the following Chain rule:

$$\begin{aligned}
\frac{\partial}{\partial x} &= \xi_x \frac{\partial}{\partial \xi} + \eta_x \frac{\partial}{\partial \eta} + \zeta_x \frac{\partial}{\partial \zeta}\\
\frac{\partial}{\partial y} &= \xi_y \frac{\partial}{\partial \xi} + \eta_y \frac{\partial}{\partial \eta} + \zeta_y \frac{\partial}{\partial \zeta}\\
\frac{\partial}{\partial z} &= \xi_z \frac{\partial}{\partial \xi} + \eta_z \frac{\partial}{\partial \eta} + \zeta_z \frac{\partial}{\partial \zeta}\\
\frac{\partial}{\partial t} &= \xi_t \frac{\partial}{\partial \xi} + \eta_t \frac{\partial}{\partial \eta} + \zeta_t \frac{\partial}{\partial \zeta} + \frac{\partial}{\partial \tau}
\end{aligned} \tag{2.24}$$

The non-dimensionalized three-dimensional compressible Navier–Stokes equations in the curvilinear coordinate system can be written as follows:

$$\frac{\partial \hat{Q}}{\partial t} + \frac{\partial \hat{E}}{\partial x} + \frac{\partial \hat{F}}{\partial y} + \frac{\partial \hat{G}}{\partial z} = \frac{1}{Re}\left(\frac{\partial \hat{E}_\mathrm{v}}{\partial x} + \frac{\partial \hat{F}_\mathrm{v}}{\partial y} + \frac{\partial \hat{G}_\mathrm{v}}{\partial z}\right) \tag{2.25}$$

where

$$\hat{Q} = \frac{1}{J}\begin{bmatrix} \rho \\ \rho u \\ \rho v \\ \rho w \\ e \end{bmatrix}, \quad \hat{E} = \frac{1}{J}\begin{bmatrix} \rho U \\ \rho u U + \xi_x p \\ \rho v U + \xi_y p \\ \rho w U + \xi_z p \\ (e+p)U - \xi_t p \end{bmatrix}, \quad \hat{F} = \frac{1}{J}\begin{bmatrix} \rho V \\ \rho u V + \eta_x p \\ \rho v V + \eta_y p \\ \rho w V + \eta_z p \\ (e+p)V - \eta_t p \end{bmatrix}$$

$$\hat{G} = \frac{1}{J}\begin{bmatrix} \rho W \\ \rho u W + \zeta_x p \\ \rho v W + \zeta_y p \\ \rho w W + \zeta_z p \\ (e+p)W - \zeta_t p \end{bmatrix}, \quad \hat{E}_v = \frac{1}{J}\begin{bmatrix} 0 \\ \xi_x \tau_{xx} + \xi_y \tau_{xy} + \xi_z \tau_{xz} \\ \xi_x \tau_{yx} + \xi_y \tau_{yy} + \xi_z \tau_{yz} \\ \xi_x y_{zx} + \xi_y \gamma_{zy} + \xi_z \tau_{zz} \\ \xi_x \beta_x + \xi_y \beta_y + \xi_z \beta_z \end{bmatrix}, \tag{2.26}$$

$$\hat{F}_v = \frac{1}{J}\begin{bmatrix} 0 \\ \eta_x \tau_{xx} + \eta_y \tau_{xy} + \eta_z \tau_{xz} \\ \eta_x \tau_{yx} + \eta_y \tau_{yy} + \eta_z \tau_{yz} \\ \eta_x \tau_{zx} + \eta_y \tau_{zy} + \eta_z \tau_{zz} \\ \eta_x \beta_x + \eta_y \beta_y + \eta_z \beta_z \end{bmatrix}, \hat{G}_v = \frac{1}{J}\begin{bmatrix} 0 \\ \zeta_x \tau_{xx} + \zeta_y \tau_{xy} + \zeta_z \tau_{xz} \\ \zeta_x \tau_{yx} + \zeta_y \tau_{yy} + \zeta_z \tau_{yz} \\ \zeta_x \tau_{zx} + \zeta_y \tau_{zy} + \zeta_z \tau_{zz} \\ \zeta_x \beta_x + \zeta_y \beta_y + \zeta_z \beta_z \end{bmatrix}.$$

U, V, and W are so-called contravariant velocities in the ξ, η, and ζ directions as follows:

$$\begin{aligned} U &= \xi_x u + \xi_y v + \xi_z w, \\ V &= \eta_x u + \eta_y v + \eta_z w, \\ W &= \zeta_x u + \zeta_y v + \zeta_z w. \end{aligned} \tag{2.27}$$

2.1.2 Computational Methods

Simulations were performed by DNS of the Navier–Stokes equations on a body-fitted coordinate (BFC). The Navier–Stokes equation was non-dimensionalized by the freestream density, the sound speed, and the diameter of the sphere. The convection term was evaluated by the sixth-order adaptive central and upwind weighted essentially non-oscillatory scheme (WENOCU6-FP) proposed by Nonomura et al., 2015, and the viscous term was evaluated by the sixth-order central difference method. The time integration was conducted by the third-order total variation-diminishing Runge–Kutta method proposed by Gottlieb and Shu, 1998. In the present study, the central difference in WENOCU6-FP was replaced by one of the splitting types proposed by Pirozzoli, 2011 for more stable calculation. In particular, the WENO numerical flux F_{weno} for the convective term can be rewritten as the following expression:

$$F_{\text{weno}} = F_{\text{central-div}} + F_{\text{weno-dissipation}} \tag{2.28}$$

where $F_{\text{central-div}}$ and $F_{\text{weno-dissipation}}$ are the numerical fluxes corresponding to the sixth-order central difference and the sixth-order dissipation term for the sixth-order WENOCU method, respectively. Even though F_{central} is usually written in the divergence form, here it is replaced by the splitting form $F_{\text{central-split}}$ of Pirozzoli, 2011.

2.1.3 Computational Grids

Computational Grid for Uniform Flow Cases

A computational grid around the sphere was generated as a body-fitted grid. The coordinate system and generated grid are shown in figures 2.1, 2.2 and 2.3, respectively.

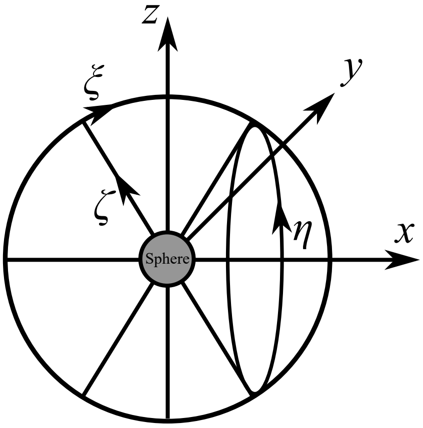

FIGURE 2.1: Coordinate system.

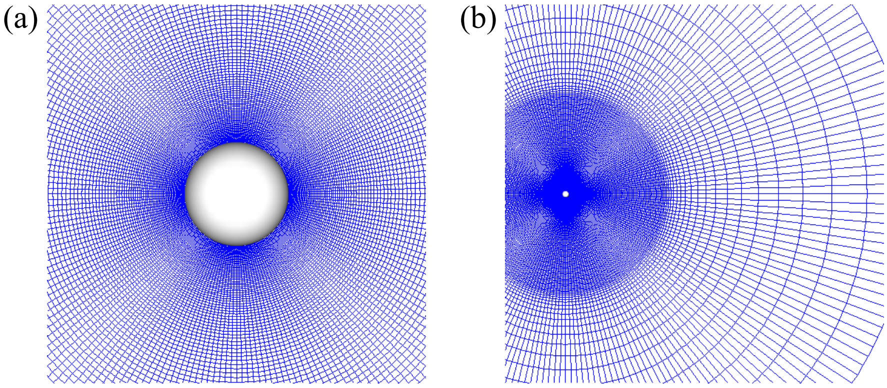

FIGURE 2.2: Base grid. (a) Close-up view; (b) far view.

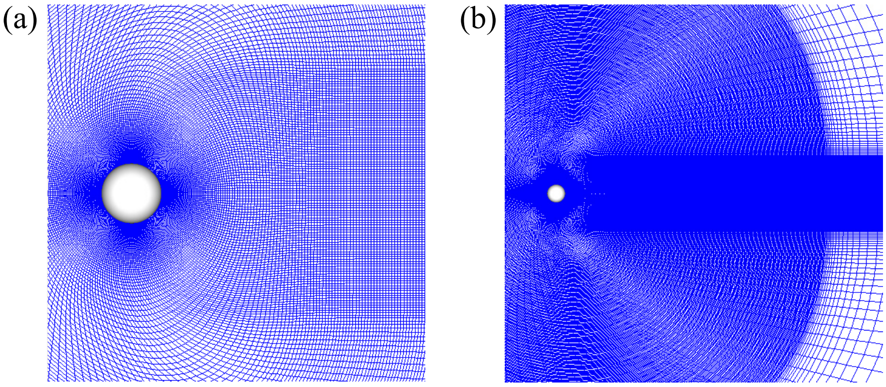

FIGURE 2.3: Wake-fine grid. (a) Close-up view; (b) far view.

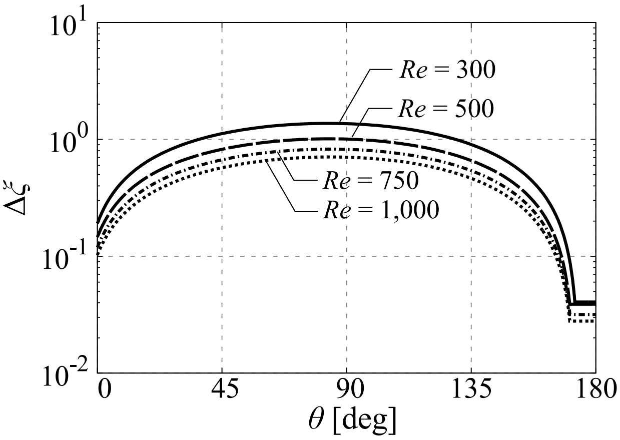

FIGURE 2.4: Distribution of the grid width of the wake-fine gird.

In the uniform flow cases, the two kings of types of computational grids, which are a base grid and wake-fine grid, were used. In the case of the wake-fine grid, the resolution of the computational grid was retained in the downstream of the sphere in the diameter of $4d$. The region of $0.5d \le x \le 15d$ and $\sqrt{(y^2 + z^2)} \le 4d$ is the high-resolution region to capture the wake structures. The grid size in the ζ direction $\Delta\zeta$ was spread by 1.03 times from the minimum grid size, and the grid size became constant when the grid width reached $\Delta\zeta_{\mathrm{max}} = 0.05d$ in the region in $\zeta \le 15d$ for the case of $Re \le 300$. It is noted that the computational grid for $Re = 300$ was used for the case of $Re \le 300$. The minimum grid width in ζ direction for the case of $Re > 300$ is determined as follows:

$$\Delta\zeta_{\mathrm{max}} = \Delta\zeta_{\mathrm{max\_ref}} \frac{\sqrt{Re_{\mathrm{ref}}}}{\sqrt{Re}}. \tag{2.29}$$

The minimum grid size in the ζ direction was calculated using the following formula adopted by Johnson and Patel, 1999:

$$\Delta\zeta_{\min} = \frac{1.13}{\sqrt{Re} \times 10.0}. \tag{2.30}$$

	Re	ξ direction	η direction	ζ direction	Total
Base grid	≤ 300	107	48	177	909,072
Wake-fine grid	≤ 300	127	62	358	2,818,892
	500	165	82	444	6,007,320
	750	201	98	529	10,420,242
	1,000	231	110	601	15,271,410

TABLE 2.1: Number of grid point (computational grids for uniform cases).

From $15d$ outward, the grid size is increased by 1.2 times toward the outer boundary as a buffer region to prevent pressure wave reflection. Note that the diameter of the analysis region was $100d$ so that the distance between the surface of the sphere and the outer boundary was much larger (the) than that in previous incompressible studies. The minimum grid size for the ξ and η direction was also determined as same as eq. 2.29. Table 2.1 shows the summary of the number of grid points for each Re condition.

Computational Grid for Linear Shear Flow Case

In the linear shear flow cases, an overset grid consists of the non-uniform Cartesian grid (zone 1) and the O-type body-fitted grid (zone 2), because there is no numerical scheme that can be satisfied the freestream preservation on the linear shear flow with a curvilinear grid. Figure 2.5 shows the computational grid for the linear shear flow. The domain size of zone 1 shown in red in figure 2.5 was $(-30d \leq x \leq 50d, -30d \leq y \leq 30d, -30d \leq z \leq 30d)$ and the number of grid point of zone 1 was $x \times y \times z \times = 212 \times 207 \times 207$. The grid width in each direction of $|x| = |y| = |z| \leq 3d$ was fixed in $\Delta x = \Delta y = \Delta z = 0.05d$ and increases by 1.1 times at $|x| = |y| = |z| > 3d$. The domain size of zone 2 was $0.5d \leq \xi \leq 2.5d$ and the grid width in ζ

direction was spread by 1.03 times from the minimum grid width (eq. 2.30) and is limited at $\Delta\zeta = 0.05d$. The total number of grid point of zone 2 was $\xi \times \eta \times \zeta \times = 127 \times 118 \times 81$. It is noted that the computational grid for $Re = 300$ was used for all simulations.

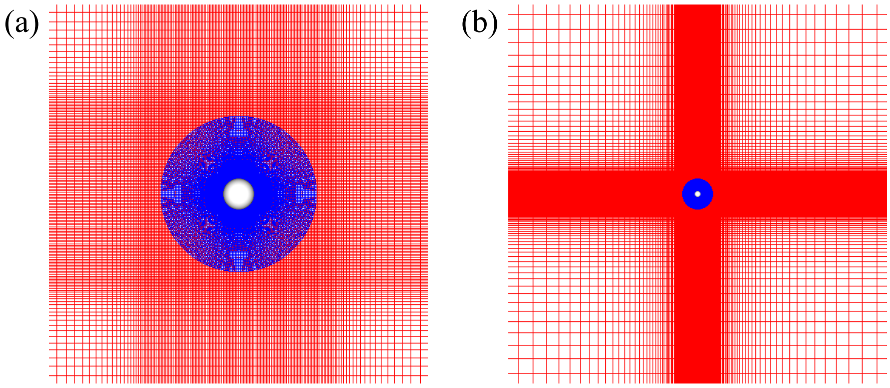

FIGURE 2.5: Computational grid for linear shear flow cases. (a) Close-up view; (b) far view.

FIGURE 2.6: Ballistic range and shock tube installed in the Institute of Fluid Science.

2.2 Experimental Equipment

The experimental studies were conducted at the Institute of Fluid Science, Tohoku University. The free-flight experiment and the shock-sphere interaction experiment were carried out using the ballistic range (left hand side of figure 2.6) and shock tube (center of figure 2.6), respectively.

2.2.1 Ballistic Range

A ballistic range was used to conduct free-flight experiments. Figure 2.7 is a schematic diagram of the ballistic range used in the present study in the single-stage light gas gun mode. Three types of launchers, a single-stage light gas gun, a powder gun, and a two-stage gas gun, can be used. The velocity ranges for each launchers are 100–700 m/s, 400–2,400 m/s, and 2,000–7,000 m/s, respectively. The single-stage light gas gun was used in the present study. In this case, the test model is accelerated by the high-pressure gas discharged from a high-pressure driver gas chamber through a launch tube approximately 6 m long.

2.2.2 Shock Tube

A shock tube was used to conduct shock-sphere interaction experiments. Figure 2.8 is the schematic diagram of the shock tube used in the present study. This shock tube is a non-diaphragm type shock tube with a total length of approximately 22 m long. Between the high-pressure chamber and low-pressure channel is separated by a piston which is supported by the high-pressure gas-charged in the sub-high-pressure chamber. Between the sub-high-pressure chamber and its leak section is separated by the intermediate-pressure chamber formed by two membranes. The intermediate-pressure chamber is implausibly pressurized, and membranes are broken at the execution, and the piston is then pushed and the high-pressure gas goes into the low-pressure channels. Pressure waves are formed behind the piston and the planar-shock wave is formed during propagation in the long distance. In the present study, the flow of high-pressure gas into the intermediate-pressure chamber was controlled by a solenoid valve, and there is the high-pressure source with a regulator in the upstream of the solenoid valve. The solenoid valve is opened by TTL signals.

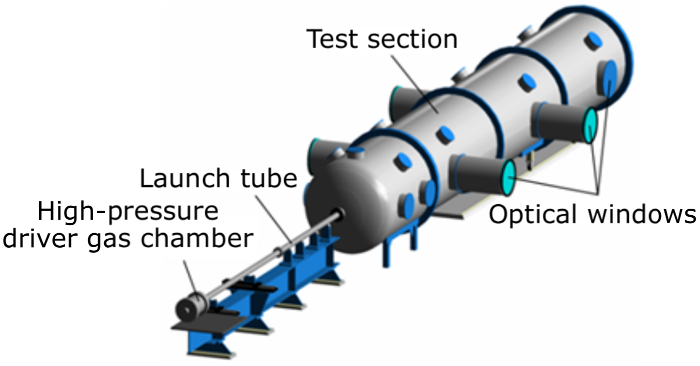

FIGURE 2.7: Overview of the ballistic range at the Institute of Fluid Science.

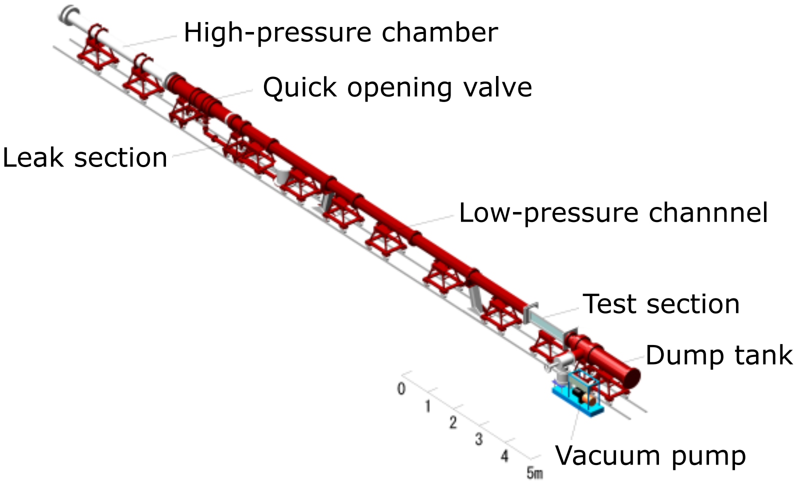

FIGURE 2.8: Overview of the shock tube at the Institute of Fluid Science.

Chapter 3

Flow over a Stationary Adiabatic Sphere

List of Symbols

C_D	Drag coefficient
C_{D_P}	Pressure drag coefficient
C_{D_v}	Viscous drag coefficient
C_f	Friction coefficient
C_L	Lift coefficient
C_P	Pressure coefficient
ΔC_D	Difference from the incompressible standard drag curve
L_r	Separation length
L_s	Shock standoff distance
M	Mach number
Q	Q-criterion
Re	Reynolds number
St	Strouhal number
a	Sound speed
d	Diameter of the sphere
f	frequency
t	Time
$\boldsymbol{u}$	Velocity vectors
u, v, w	Velocity in x, y, and z directions
u_ξ	Velocity in $\xi direction$
x, y, z	Cartesian coordinates
δ	Boundary layer thickness
δ_D	Boundary layer thickness
μ	Dynamic viscosity coefficient
θ	Angle from x-axis
θ_s	Separation point
ρ	Density
ξ, η, ζ	Curvilinear coordinates

Subscripts

r.m.s.	Root-mean-square
∞	Freestream

3.1 Introduction

Studies of flow over generic bodies such as a flat plate, cylinder, or sphere, have contributed to a better understanding of fluid mechanics and the modeling of complex phenomena. Particularly, a sphere is the simplest three-dimensional body, but flow over a sphere is complicated and varies depending on flow conditions.

The behaviour of flow past a sphere also varies with a Reynolds number ($Re = \rho_\infty u_\infty / \mu_\infty$) based on the freestream density ρ_∞, the velocity u_∞, the viscosity coefficient μ_∞, and the diameter of the sphere d. This has been examined by various researchers experimentally and numerically under incompressible flows. Taneda, 1956 experimentally examined the wake of a sting-mounted sphere at $5 \leq Re \leq 300$. He determined that the critical Re of the formation of an axisymmetric vortex ring behind a sphere is $Re \approx 24$. Also, he observed a very long period oscillation of the axisymmetric vortex ring when Re reached 130. Magarvey and Bishop, 1961 experimentally examined wake structures of a falling liquid droplet in liquid at $0 \leq Re \leq 2,500$. They observed asymmetry in the recirculation region at approximately $Re > 210$. Nakamura, 1976 also observed an asymmetry in a steady recirculation region at $Re > 190$. Taneda, 1978 experimentally examined the wake behind a sphere at Re ranging from $O(10^4)$ to $O(10^6)$ using the surface-oil flow, smoke, and tuft-grid methods. He observed wave motion in the wake at $O(10^4) \leq Re \leq 3.8 \times 10^5$ and noted that it forms a pair of streamwise vortices at $3.8 \times 10^5 \leq Re \leq 10^6$. Sakamoto and Haniu, 1990 experimentally investigated vortex shedding from a sphere in a uniform flow at $300 \leq Re \leq 4.0 \times O(10^4)$. They examined the wake of a sphere by hot-wire and flow visualization experiments. They showed that the wake vortices change from laminar to turbulent when Re reached ≈ 800. In addition, they found that the higher- and lower-frequency modes of the Strouhal number ($St = fd/u_\infty$) of the vortex shedding frequency f coexist at $800 \leq Re \leq 1.5 \times 10^4$. Johnson and Patel, 1999 experimentally and numerically examined $20 \leq Re \leq 300$. They numerically identified the critical Re for a steady axisymmetric flow ($Re \leq 210$), steady nonaxisymmetric flow ($210 \leq Re \leq 270$), and unsteady (periodic) flow ($Re > 270$) by DNS of the Navier–Stokes equations. Further more, numerical studies at higher-Re conditions of flow over a sphere were studied by Tomboulides and Orszag, 2000 and Rodriguez et al., 2011 for $25 \leq Re \leq 1,000$ and $Re = 3,700$, respectively.

For compressible low-*Re* flow, drag coefficients of a sphere have been investigated by several researchers. Data for the sphere drag coefficient in the compressible low-*Re* flow have been used for the construction of particle drag models (Carlson and Hoglund, 1964; Crowe, 1967; Henderson, 1976; Loth, 2008; Parmar, Haselbacher, and Balachandar, 2010). Such drag models can be used in the simulation of compressible multiphase flows, for example. However, Saito, Marumoto, and Takayama, 2003 pointed out that the result of the numerical simulation of the compressible particle-laden flow using the particle drag model is changed depending on the drag model. In the aerospace field, compressible multiphase flows appear in exhaust jets of rocket engines and other combustion flows. Recently, particle-resolved simulations of compressible viscous particle-laden flow using the immersed boundary method (IBM) were conducted by (Mizuno et al., 2015; Schneiders et al., 2016; Das et al., 2017). However, because flow properties around a sphere have not been understood sufficiently, the examination of the flow physics of a compressible low-*Re* flow over a single isolated sphere will be helpful for modeling and understanding the compressible multiphase flow and extending the knowledge of fluid mechanics.

May, 1957 obtained the drag coefficient of a sphere at $1.5 < M < 3.0$ and $350 < Re < 3,000$ by free-flight experiments using a ballistic range. Sphere drag coefficients were obtained from the position-time data under supersonic low-*Re* conditions using a low-pressure test section and a small sphere. Sreekanth, 1961 measured the drag coefficient of a sting-supported sphere at $M = 2$ and Knudsen numbers of 0.1 to 0.8 in a low-density wind tunnel. The influence of support interference on the measured drag force was also reported. Bailey and Hiatt, 1971; Bailey and Hiatt, 1972; Bailey, 1974; Bailey and Starr, 1976 also carried out free-flight experiments using a ballistic range at $0.1 \leq M \leq 6$ and $O(10^{-2}) \leq Re \leq O(10^{7})$, and estimated the sphere rag coefficient for a wide range of Re and M. Crowe et al., 1968 calculated the drag coefficients of micron-size particles in subsonic free-flight experiments by measuring the deceleration of the flight speed with a Faraday cage. In addition, Zarin and Nicholls, 1971 conducted wind tunnel experiments with a sphere at $0.1 \leq M \leq 0.57$ and $40 \leq Re \leq 5,000$. They used a one-component magnetic balance and suspension system to subtract the support interference. However, because these studies only focused on the drag coefficient, the number of studies on the flowfield at compressible low-*Re* flows remains few.

Numerical examinations of the compressible low-Re in the continuum regime have also been conducted. Meliga, Sipp, and Chomaz, 2010 studied linear dynamics of global eigenmodes in compressible axisymmetric wake flows of the sphere at $0 \leq M \leq 0.7$ and $270 \leq Re \leq 285$. They determine the boundary separating the stable and unstable domains in the M and Re coordinates, and showed that an increase in M yields a destabilization of the flow past the sphere. They clarified that the destabilization effect due to compressibility is caused by a significant increase of the backflow velocity of recirculation region. Recently, the flow past a sphere under compressible low-Re flow has numerically been studied through the fully three-dimensional simulation by us (since 2016), Riahi et al., 2018, and Sansica et al., 2018. Riahi et al., 2018 computed the compressible flow-Re flow over a sphere at $0.3 \leq M \leq 2.0$ and $50 \leq Re \leq 600$ by the IBM flow solver. They found that the wake structure for $M = 0.95$ is unsteady (alternating hairpin wake) at $Re = 600$ and the wake for $M = 2.0$ is steady at $Re \leq 600$. Sansica et al., 2018 carried out the global stability analysis (GSA) at $0.1 \leq M \leq 1.2$ and $200 \leq Re \leq 370$. They examined the effects of Re and M on the unsteadiness of the flowfield and drew a stability map based on the bifurcation boundaries for various Re and M. These studies showed that the flow behind a sphere is considerably stabilized when M increases, and unsteady flow patterns have not been observed at supersonic flow in the numerically investigated Re ranges.

In this chapter, the fundamental properties of flow past an isolated stationary adiabatic sphere at $50 \leq Re \leq 1,000$ and $0.3 \leq M \leq 3.0$ is investigated by DNS of the three-dimensional compressible Navier–Stokes equations. Flow regime maps for various Re and M values are drawn. Also, characteristic parameters of flow geometries, such as the length of the recirculation region, the position of the separation point, and the shock standoff distance and aerodynamic force coefficients, are examined.

3.2 Computational Setup

3.2.1 Flow Conditions

In this chapter, uniform flows over a stationary adiabatic sphere were computed. A Reynolds number was set to be between 50 and 1,000 and M was set to be between 0.3 and 2.0. Summary of the flow conditions are given in table 3.1.

					M				
		0.3	0.7	0.8	0.95	1.05	1.2	1.5	2.0
	50	A		A			A		A
	100	A		A			A		A
	150	A		A			A		A
	200	A		A			A		A
Re	250	C		C	B	B	A		A
	300	C	A	C	C	C	C	C	C
	500	B		B	B	B	B		B
	750	B		B	B	B	B		B
	1,000	B		B	B	B	B	B	B

TABLE 3.1: Flow conditions for an stationary adiabatic sphere.

Flow conditions for an stationary adiabatic sphere. A: computed on the base gird; B: computed on the wake-fine grid; C: computed on the base and wake-fine grids.

Also, the resolution of the computational grid was retained in the downstream region $4d$ in diameter. Result of the grid convergence study is shown in appendix A.2.1.

3.2.2 Boundary Conditions

The boundary at the sphere surface was no-slip and adiabatic conditions. At the surface of the sphere, the velocity was fixed to zero, the density was extrapolated from the one point inside the boundary, the pressure was calculated from the momentum normal to the surface. The periodic boundary condition with the six overlapped grid points was imposed at the boundaries in the ξ and η directions. The inflow and outflow boundary conditions were imposed at the outer boundary where the flow goes inside and outside at one point inside the boundary, respectively. All flow variables were fixed to their freestream values at the subsonic and supersonic inflow boundaries. All the variables were extrapolated from one point inside of the boundary at the supersonic outflow boundaries. The density and the velocities were similarly extrapolated and the pressure was fixed to its freestream values in the subsonic outflow condition. On the singular point of the x-axis, all the variables were set to be an average of the nearest surrounding nodes.

3.3 Results and Discussion

3.3.1 Far-Field Properties

Figure 3.1 illustrates M and Re effects on the wake structure visualized by the isosurface of the second invariant of velocity gradient tensor (Q-criterion). The thresholds of Q-criterion was 5.0×10^{-4} which is normalized value by the freestream velocity. Several kinds of wake structures appear at $M \leq 2.0$ and $Re \leq 1,000$, and the wake structures become complex and simple as Re and M increase, respectively. Streamwise steady vortices are generated at the downstream of sphere at $Re = 250$ and $M = 0.3$. At $Re = 300$ and 500, hairpin vortices are generated in the recirculation region and the wake becomes unsteady flow. When Re further increases to 750 and 1,000, the wake vortices form a helical structure with a high mode and a low mode. The size of the recirculation region at $M = 0.8$ becomes large compared to that at $M = 0.3$, and the pressure coefficient distribution changes. The Re evolution of the flow patterns is similar to $M = 0.3$ in figure 3.1, but the wake structure at $M = 0.8$ seems to be more complicated compared to that at $M = 0.3$. Thus, the critical Re for each flow pattern might be different between $M = 0.3$ and 0.8. However, the details cannot be discussed due to the lack of DNS data in the Re direction. The compressibility effect on the wake vortices becomes obvious for $M \geq 0.95$. The pressure coefficient distribution is drastically changed and a recompression wave can be observed around the end of the recirculation region at $M = 0.95$. In this case, there is only a steady recirculation region, and no unsteady wake vortices are formed downstream of the sphere up to $Re = 300$. At $Re = 500$, streamwise vortices can be observed, similar to those at $Re = 250$ and $M = 0.3$, and the wake becomes helical at $Re \geq 750$, as at $M = 0.3$ and 0.8, but its structure is more complex than that under subsonic conditions. A detached shock wave is formed upstream of the sphere at $M \geq 1.05$, and those waves including expansion and recompression waves become stronger as M increases. The flow behind the sphere remains steady flow up to $Re = 500$, and hairpin structures appear at $M = 1.05$ and $Re \geq 750$. Stabilization effects of the wake by compressibility become strong as M increases, and the wake is steady at $M \geq 1.5$ and $Re \leq 1,000$.

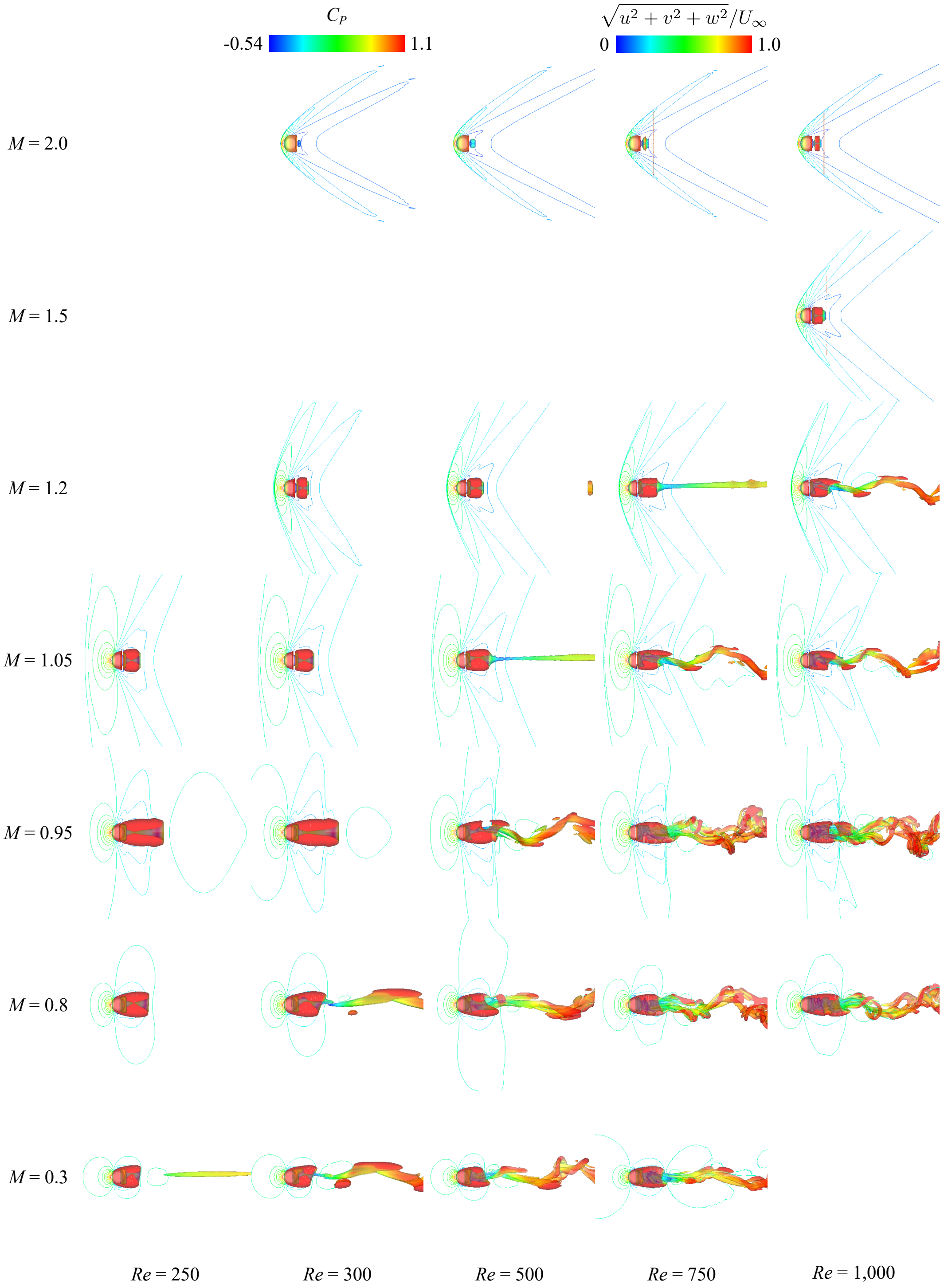

FIGURE 3.1: Instantaneous wake structures. The structures are identified by the isosurface of the normalized second invariant value of the velocity gradient tensor, which is normalized with respect to the freestream velocity ($Q/u_\infty^2 = 5.0 \times 10^{-4}$).

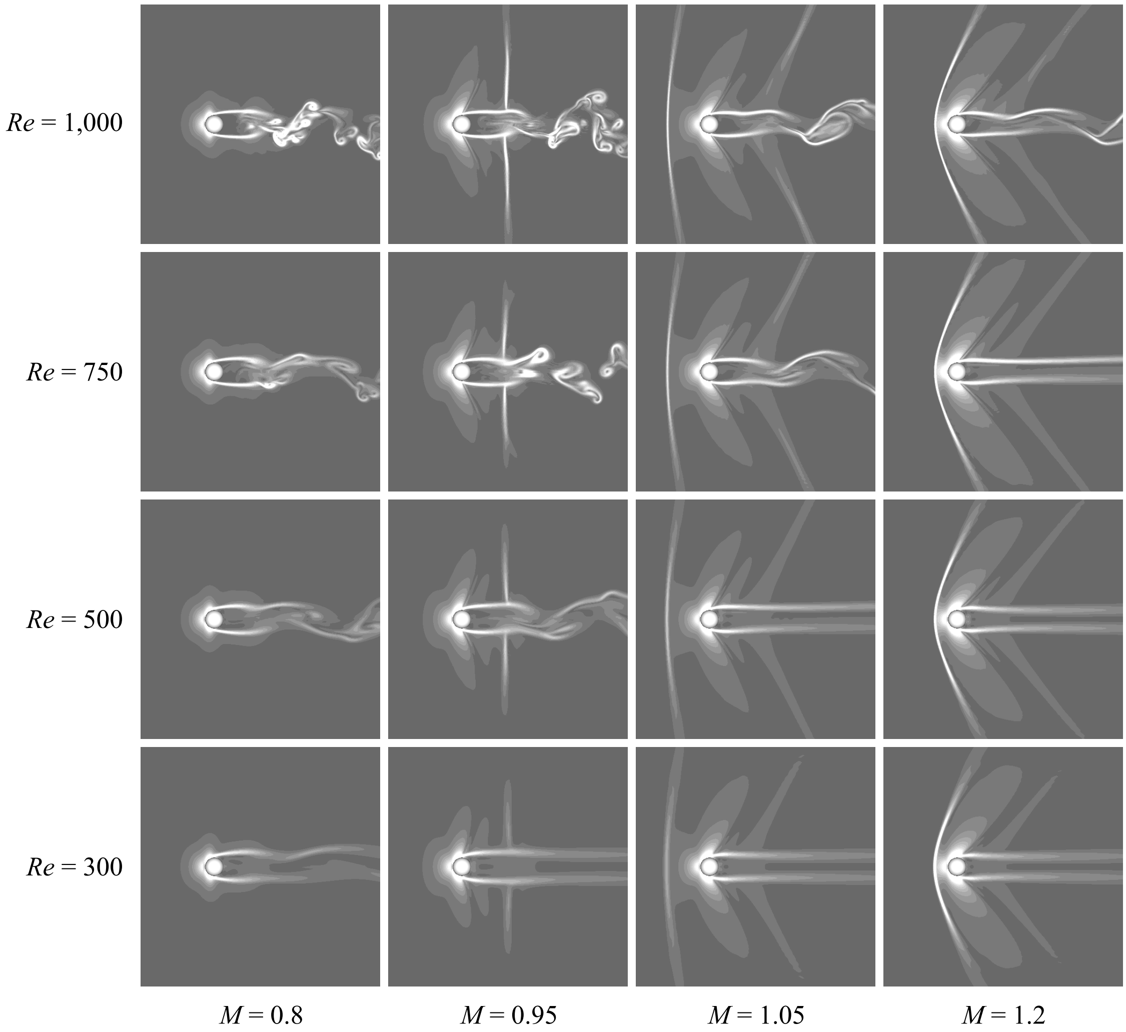

FIGURE 3.2: Distribution of absolute values of density gradient.

Figure 3.2 shows schlieren-like images for $300 \leq Re \leq 1,000$ at around the transonic condition. At $M = 0.8$, there is a small white region, the λ-shock, around $\theta = 90$ deg, and it becomes clearer as Re increases. The flow structure behind the sphere becomes different from the incompressible flow because the λ-shock changes the position of the separation point. Hence, it seems that the wake structure at $M = 0.8$ is more complicated compared to that at $M = 0.3$, as shown in figure 3.2. The λ-shock becomes clearer and a wake shock wave is formed downstream of the sphere at $M = 0.95$. Also, those shock waves become clearer as Re increases because the viscous dissipation decreases. For $Re \geq 500$, the wake becomes unsteady and wake vortices appear to be generated around the wake shock wave. This trend is similar to that under the higher-Re conditions with similar M values. It will be discussed in chapter 6. In that case, *Re* is 1.9×10^5, which created a completely different flow regime, but a large-scale oscillation of the wake is generated around the wake shock wave. A detached shock wave is formed upstream of the sphere, and a recompression wave is formed around the root of the wake shock wave at $M \geq 1.05$. The oscillation of the wake generated around the recompression wave is observed also at $8.1 \times 10^3 \leq Re \leq 1.0 \times 10^5$ with a similar M.

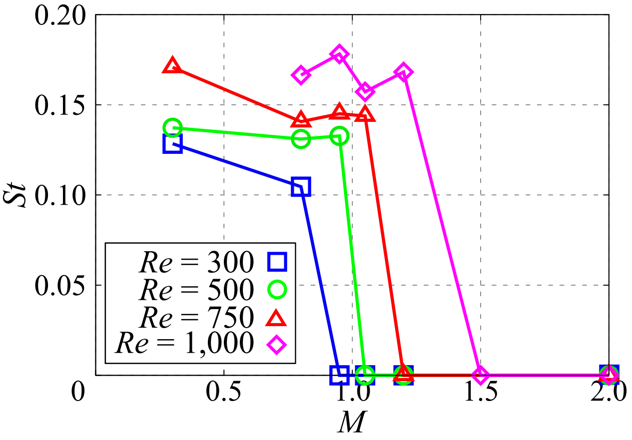

FIGURE 3.3: Effect of M on the St of vortex shedding.

Figure 3.3 shows the influence of M on the St of vortex shedding. The St of vortex shedding for $Re = 300$ and $Re > 300$ were computed by the time variation of the lift coefficient and the velocity fluctuation at the maximum TKE point in the downstream, respectively. Overall, St of vortex shedding increases as Re increases, and the critical M, at which St of vortex shedding becomes zero, move to the higher-M side as Re increases. The St of vortex shedding at $Re = 300$ decreases as M increases under the subsonic conditions and rapidly approaches zero around $M = 0.95$ because there is no vortex shedding at $Re = 300$ and $M \geq 0.95$. The trend of the St of vortex shedding at $Re = 500$ is similar to that at $Re = 300$, but the St of vortex shedding does not decrease up to $M = 0.95$ and sharply approaches zero at around $M = 1.0$. The St of vortex shedding decreases at $0.3 \leq M \leq 0.8$ and there are no M effects on the St of vortex shedding at $0.8 \leq M \leq 1.05$. The decrease in the St of vortex shedding at $0.3 \leq M \leq 0.8$ corresponds to the change in the wake structure. As shown in figure 3.1, the wake structure at $M = 0.8$ and 0.95 for $Re = 750$ is more complicated (resembling a higher-*Re* condition) compared to that at $M = 0.3$ or at incompressible flow, because the weak shock wave formed near the separation point and the flow separation is promoted by the effect of the weak shock wave. This results in the unsteadiness of the recirculation region and complicated vortex structure. However, the flowfield is strongly stabilized under the supersonic regime as the same as the lower-Re cases, and then the St of vortex shedding becomes zero at $M \leq 1.2$. Under the sufficiently high-Re conditions, for example, $Re \geq O(10^5)$, the λ-shock wave is formed and the flow separation is induced at approximately $\theta = 90$ deg. However, under lower-Re conditions, for example, $Re < O(10^3)$, the boundary layer becomes thicker and attenuates the λ-shock wave on the surface of the sphere; thus, the effect of the λ-shock wave becomes weak.

3.3.2 Flow Regime

According to studies of incompressible flow at the low-Re conditions by Taneda, 1956; Magarvey and Bishop, 1961; Sakamoto and Haniu, 1990; Johnson and Patel, 1999, the flow structure at $Re \leq 1,000$ can be classified into six regimes. At $Re < 24$, the flow is attached-laminar flow over the entire surface (fully attached flow). Laminar separation occurs and a steady axisymmetric vortex ring forms behind the sphere at $24 < Re \leq 210$ (steady-axisymmetric flow). At $211 \leq Re \leq 275$, the flowfield is still steady, but axisymmetrical breakup occurs and the vortex ring assumes an asymmetric shape (steady planar-symmetric flow). The flow over an isolated sphere becomes unsteady and hairpin vortex shedding begins at $Re \geq 275$. The hairpin vortex is periodically generated in the recirculation region at $275 \leq Re \leq 420$. In this Re range, the vortex shedding is highly organized (hairpin wake). The hairpin vortices are periodically generated up to $Re \leq 800$, but the direction of the heads of the hairpin vortices roll in an azimuthal direction at $420 \leq Re \leq 800$ (hairpin wake with azimuthal oscillation). At $Re \geq 800$, the wake vortices become complicated and strongly random. The wake consists of low-mode and high-mode structures and large-scale vortex structure forms and rolls in the azimuthal direction (helical wake).

Figure 3.4 shows the map of the flow regime in the Re–M plane under compressible conditions. Riahi et al., 2018 and Sansica et al., 2018 are shown for comparison with those of the present study. Riahi et al., 2018 used three-dimensional DNS with IBM, and Sansica et al., 2018 used fully three-dimensional GSA. In this plot, the six different flow regimes described above are indicated as follows: fully-attached flow (FA), steady-axisymmetric flow (SA), steady planar-symmetric flow (SP), hairpin wake (HaW), hairpin wake with azimuthal oscillation (HaWAO), and helical wake (HeW). However, in the study of Riahi et al., 2018, fully attached flow and hairpin wake with azimuthal oscillation did not appear. It seems that those flow regimes are included in steady-axisymmetric flow and unsteady periodic flow (HaW in this thesis) in their articles, respectively. Figure 3.4 illustrates that the flow regime under the low subsonic flow up to $M = 0.3$ is similar to that of incompressible flows. The region of steady-axisymmetric flow, steady planar-symmetric flow, and hairpin wake are slightly shifted to the higher-Re side under high subsonic flows. This means that the steady regime expands to the higher-Re side. Under the transonic and supersonic conditions, the relationship between flow regime and Re is drastically changed, and the flowfield is significantly stabilized. Particularly, even non-axisymmetric flow does not appear for $Re \leq 1,000$ at $M \geq 1.5$.

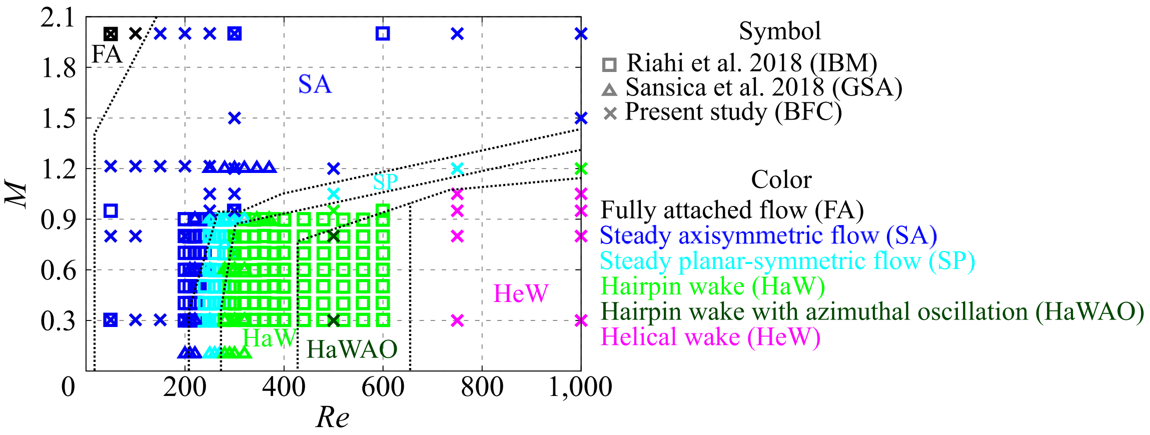

FIGURE 3.4: Distribution of flow regimes.

3.3.3 Turbulent Kinetic Energy

Figure 3.5 shows the distribution of the turbulent kinetic energy (TKE) in the wake. Here, the TKE in figure 3.5 was normalized by the freestream kinetic energy as follows:

$$\overline{\mathbf{u}'} = \sqrt{\left|\mathbf{u}^2 - \overline{\mathbf{u}}^2\right|} \tag{3.1}$$

$$\mathrm{TKE} = \frac{1}{2}\frac{\overline{u'}^2 + \overline{v'}^2 + \overline{w'}^2}{u_\infty} \tag{3.2}$$

where u', v', and w' is fluctuation components of velocity. Also, the TKE was calculated in the high-resolution region ($0.5d \leq x \leq 15d$ and $\sqrt{y^2 + z^2} \leq 4d$), and we determined the volume average for every $\Delta x = 0.2d$. Figure 3.5(a) illustrates that the TKE increases approximately up to $x = 2.5d$ because the end of the recirculation region in the unsteady case exists at around $x = 2.0d$. The TKE gradually decreases as the distance from the sphere increases. Also, the TKE increases as M increases up to $M \leq 0.95$ and is less than 10^{-4} at $M > 0.95$ because the wake becomes a steady flow. At $Re = 1,000$ (figure 3.5(b)), the trend of spatial distributions of the TKE is similar to that at $Re = 500$ and its value is higher than that at $Re = 500$. Figure 3.5(b) illustrates that the TKE increases and decreases as M increases at $M \leq 0.95$ and $M \geq 1.05$, respectively. Therefore, it was confirmed that the TKE downstream of the sphere under the higher-M conditions is larger than that under the lower-M conditions with the same flow regime. In contrast, the TKE decreases as M increases at $M \geq 1.05$ and $Re = 1,000$ due to a change in the flow regime from helical wake to hairpin wake, and the TKE becomes less than 10^{-4} at $M > 1.2$ because of the steady wake. Hence, the compressibility effect not only leads to the stabilization of the flowfield but also leads to the unsteadiness of the wake under an unsteady flow regime. In particle-laden flow, the wake vortices generated by particles have a impact not only on the turbulent structure of the continuum phase but also on the distribution of the particles themselves (Kajishima and Takiguchi, 2002). Therefore, it is suggested that the relative M between particles and the gas phase might be effective for forming particle clusters.

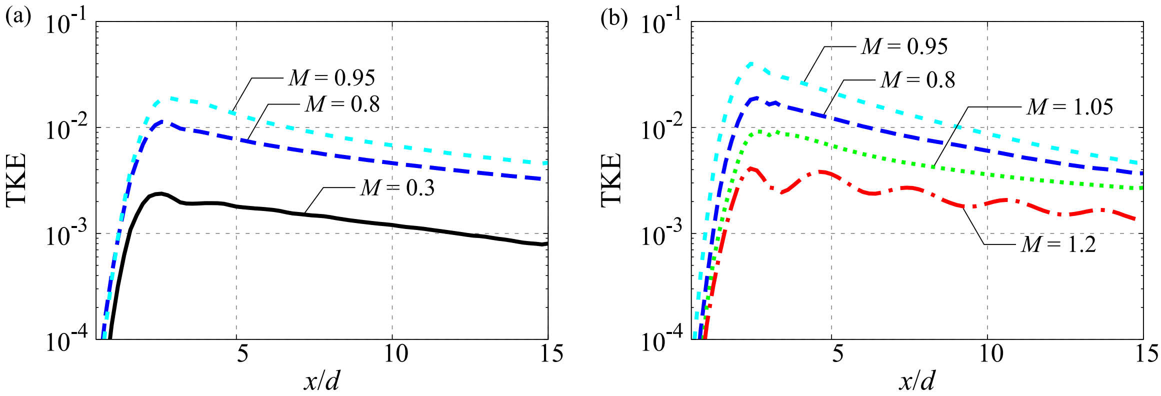

FIGURE 3.5: Normalized TKE distribution in the wake region: (a) $Re = 500$; (b) $Re = 1,000$.

3.3.4 Near-Field Structure

Separation Point and Recirculation Region

Figure 3.6 shows the schematic diagram of the definition of the position of the separation point and the separation length. In the present study, the position of the separation point was defined as the angle from the upstream stagnation point, and the separation length was defined as the distance between the downstream stagnation point and the end of the recirculation region.

Figure 3.7 shows the M and Re effects on the position of the separation point. Figure 3.7(a) illustrates the effect of M, which moves the position of the separation point upstream as M increases up to $M = 0.8$ because the flow separation is enhanced due to the λ-shock formed at around $\theta = 90$ deg. In contrast, the position of the separation point moves downstream as M increases at $M > 0.8$ due to the expansion wave. The flow direction behind the expansion wave changes to the direction toward the recirculation region, which reduces the flow separation, and its effect becomes strong under the higher-M conditions. Figure 3.7(b) depicts the Re effect, which moves the position of the separation point upstream as Re increases for all M values investigated in the present study. Also, the Re effect on the separation point is similar in each M, and thus there is no clear influence of Re on the M effect on the separation point position.

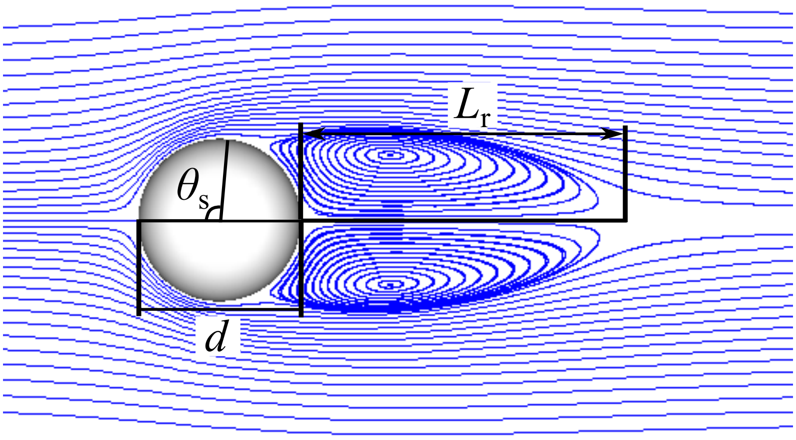

FIGURE 3.6: Schematic diagram of the flow geometry.

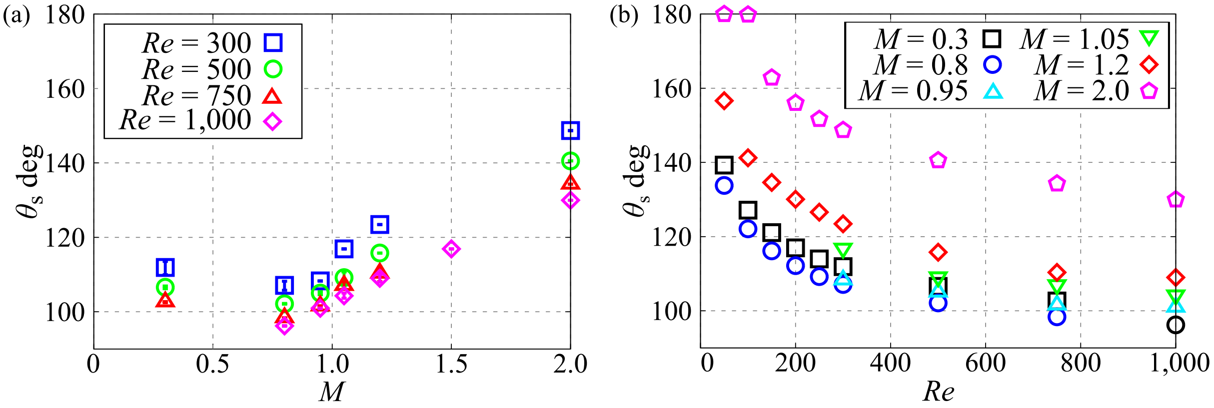

FIGURE 3.7: Dependence of separation point position on M and Re: (a) M dependence; (b) Re dependence.

Figure 3.8 shows the effects of M and Re on the separation length. Figure 3.8(a) shows the influence of M and illustrates that the separation length increases and decreases as M increases under subsonic and supersonic conditions, respectively, creating an inflection point in the M evolution. The behaviour of the separation length is linked with the separation point position. However, the increment of the separation length rapidly increases at around the transonic regime, except at $Re = 1,000$. The inflection point moves towards the higher-M side as Re increases because the separation length increases to its maximum value at around the critical M, which is the point at which the flow regime transitions from steady to unsteady. Also, the maximum value of the separation length decreases as Re increases. Figure 3.8(b) depicts the Re effect on the separation length and the M effect on the separation length. The separation length increases as Re increases at $Re \leq 1,000$ and $M = 0.3$. However, at $M = 0.8$, the separation length increases and decreases as Re increases for $Re \leq 300$ and $Re \geq 300$, respectively. Also, a similar inflection point of the separation length exists at $Re = 750$ and $M = 1.2$, again because the inflection point appears when the flow transitions from steady to unsteady. Therefore, it is considered that the inflection point for $M = 2.0$ will appear at $Re \geq 1,000$.

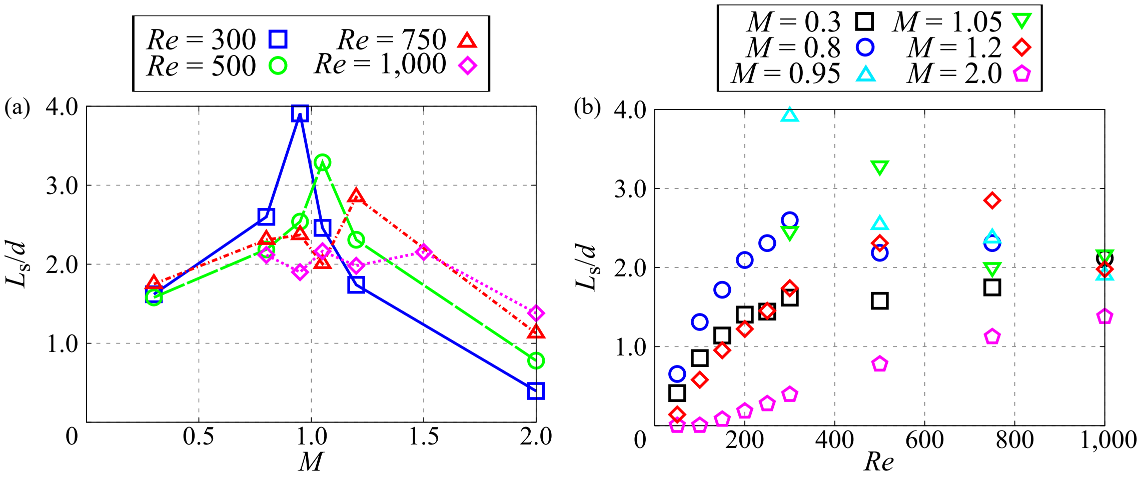

FIGURE 3.8: Dependence of length of the recirculation region on M and Re: (a) M dependence; (b) Re dependence.

Shock Standoff Distance

Figure 3.9(a) shows the relationship between M and shock standoff distance L_s. The study by Sugimoto (1944) (see Hida, 1953) and Heberle, Wood, and Gooderum, 1950 produced experimental results. The dotted line represents the value predicted by the empirical expression proposed by Ambrosio and Wortman, 1962. This empirical model was constructed using the experimental data of a cone-sphere model. The position of the detached shock wave was identified by the local streamwise velocity u_{local} and the local sound speed a_{local} on the x-axis as follows:

$$\begin{aligned} u_{\mathrm{local}} - a_{\mathrm{local}} &> 0 \quad \text{outside}, \\ u_{\mathrm{local}} - a_{\mathrm{local}} &= 0 \quad \text{shockwave}, \\ u_{\mathrm{local}} - a_{\mathrm{local}} &< 0 \quad \text{inside}. \end{aligned} \tag{3.3}$$

Figure 3.9(a) illustrates that the present computation at $Re = 300$ agree with the previous experimental results and empirical expression. Figure 3.9(b) illustrates the relationship between Re and shock standoff distance L_s. The empirical expression by Ambrosio and Wortman, 1962 does not include Re, because the experiment was conducted under sufficiently high-Re conditions. However, the DNS results show the Re dependence. The shock standoff distance increases as Re decreases at $Re \leq 300$ due to an increase in the displacement thickness. The difference between the empirical expression and DNS results becomes small as Re increases. However, the Re dependence is still observed at $Re > 300$ and the shock standoff distance further decreases as Re increases. At $M = 1.2$, the shock standoff distance converges to the value of the empirical expression at around $Re = 1{,}000$. At $M = 2.0$, conversely, there is a larger difference compared to that at $M = 1.2$ even when $Re = 1{,}000$. It seems that the influence of the displacement thickness becomes more effective due to the smaller shock standoff distance.

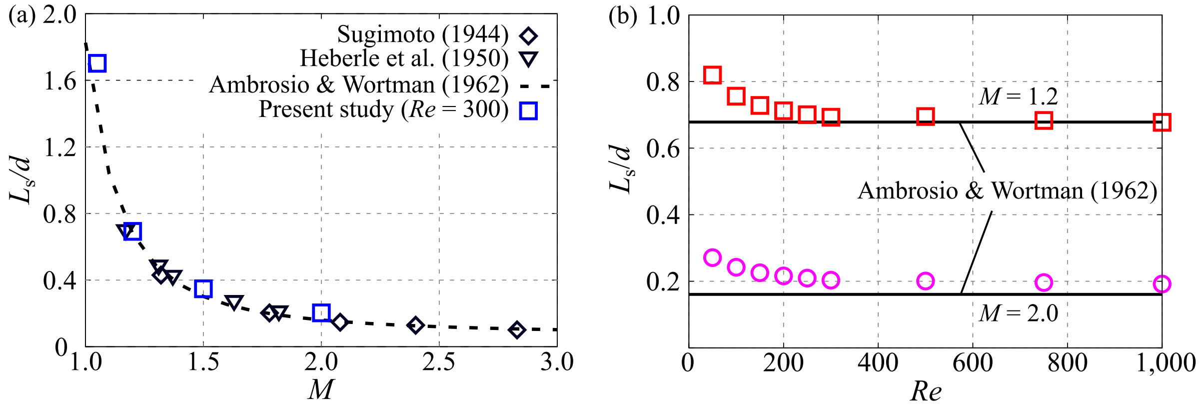

FIGURE 3.9: Shock standoff distance: (a) effect of M; (b) effect of Re.

Figure 3.10 depicts the relationship between the displacement thickness and the change in the shock stand-off distance. Here, the change in the shock stand-off distance was calculated to be the difference between that of the results at low-Re condition L_s and that predicted value by the empirical model by Ambrosio and Wortman, 1962 for a limit of inviscid flow $L_{\mathrm{s\_ref}}$. The displacement thickness δ_D was calculated as follows:

$$\delta_\mathrm{D} = \int_0^\delta \left(1 - \frac{u_{\xi\mathrm{local}}}{u_{\xi\mathrm{edge}}}\right) \mathrm{d}\zeta \tag{3.4}$$

Here, $u_{\xi\mathrm{local}}$ and $u_{\xi\mathrm{edge}}$ denote the local velocity in ξ direction and the velocity in the ξ direction at the boundary layer edge, respectively. Figure 3.11 depicts the distribution of the tangential velocity at around the upstream side stagnation point. The velocity profiles of u_ξ in ζ direction are shown in figure 3.11. The displacement thickness at around the stagnation point was estimated by eq. 3.4 and the velocity distribution (see B.1. Specifically, the boundary layer edge was assumed to be the local maximum point of the velocity in the ξ direction at $M = 1.2$. However, the edge of the boundary layer at $M = 2.0$ was identified by the change in the velocity gradient because of the influence of the detached shock wave. Figure 3.10 illustrates that the shock stand-off distance increases as the displacement thickness increases because the displacement thickness decrease by decreasing *Re*. Consequently, the shock stand-off distance increases because of the increase in the effective size of the sphere. Since the boundary layer is thicker at low-*Re*, the shock stand-off distance is more significantly influenced than that at high-*Re*. Also, 3.12 shows the relationship between the normalized displacement thickness and change in the shock stand-off distance. The first and second axes are normalized by the shock stand-off distance predicted by Ambrosio and Wortman, 1962. This figure indicates that the change ratio in the shock stand-off distance seems to be in the clear relationship with the ratio of the displacement thickness to the shock stand-off distance, though the limited data.

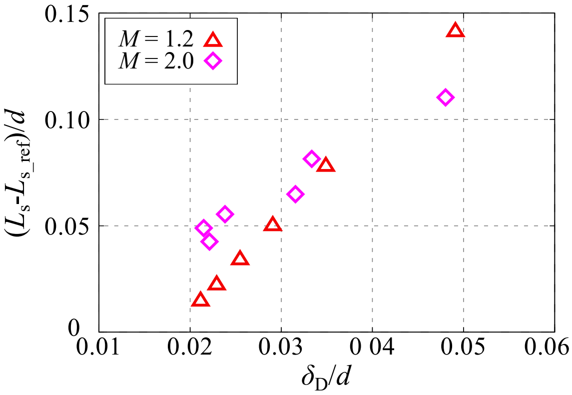

FIGURE 3.10: Relation of the displacement thickness and the change quantity of the shock stand-off distance around the stagnation point.

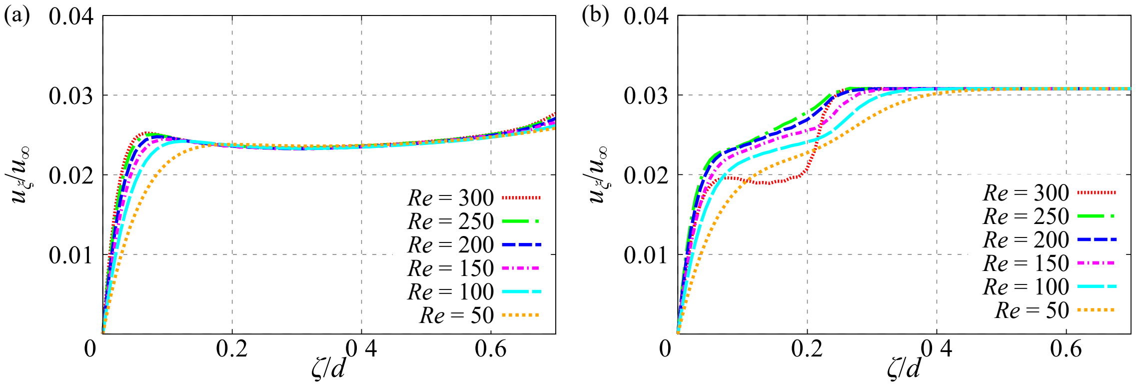

FIGURE 3.11: Distribution of the normalized ξ-direction velocity at $\theta = 1.74$ deg from the stagnation point: (a) $M = 1.2$ and (b) $M = 2.0$.

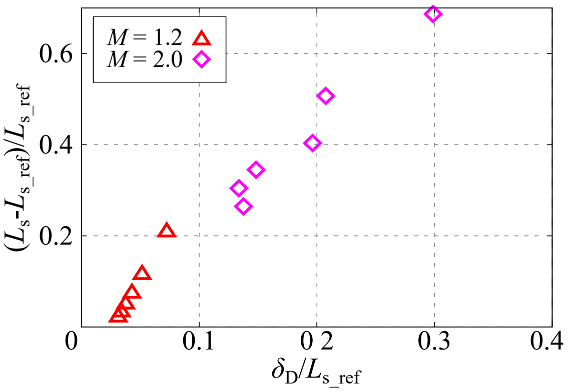

FIGURE 3.12: Relationship between the normalized change quantity of shock stand-off distance and normalized displacement thickness.

Pressure Coefficient Distribution

Figures 3.13 and 3.14 show the distribution of pressure and friction coefficients, respectively, at Re = 300 and 1,000 for various M. The pressure and friction coefficients were calculated in the time-averaged field and were averaged around the x-axis. Figure 3.13(a) illustrates that the pressure coefficient increases as M increases. Discontinuity due to the shock wave is not observed. The minimum value of C_P exists at around θ = 90 deg, and its position moves downstream by increasing M increases. Also, the minimum value of C_P decreases and increases as M increases in the subsonic and supersonic flows, respectively. The minimum value of C_P at M = 2.0 is almost the same as C_P at the downstream stagnation point. The trend of the M effect on the C_P distribution under the subsonic conditions is similar to that of a cylinder at Re = 20 and 40 for $M \leq 0.5$, as reported by Canuto and Taira, 2015. Also, at $M \leq 0.8$, the position where the C_P value is minimized moves downstream as M increases, even though the position of the separation point moves upstream. The influence of M on the C_P distribution at $Re = 1,000$ is similar to that at Re = 300, but the influence of M on the C_P minimum becomes more clear as shown in figure 3.13(b).

Figure 3.14 shows the distribution of C_f at Re = 300 and 1,000 for various M. The value of C_f at Re = 300 is maximized at around θ = 70 deg as shown in figure 3.14(a), and the peak position moves downstream by increasing M. Also, the peak value of C_f increases and decreases as M increases in the subsonic and supersonic flows, respectively. The maximum value of C_f under the higher-M conditions of the upstream side is smaller than that of the lower-M cases, particularly under supersonic conditions, due to the detached shock. The dynamic viscosity coefficient at the subsonic flows also increases because of aerodynamic heating, but the effect of the deceleration of the flow by the detached shock wave is more effective. In contrast, C_f under the higher-M condition is larger at the downstream region where C_f becomes maximum because the position of the separation point moves downstream as M increases at $M \geq 0.8$. Figure 3.14(b) illustrates that a similar trend can be observed at $Re = 1,000$.

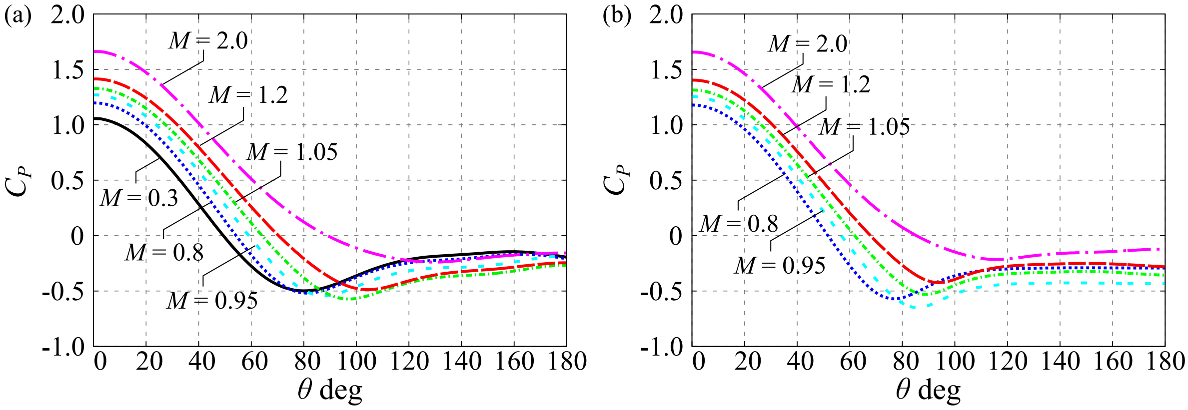

FIGURE 3.13: Pressure coefficient distribution on the sphere surface: (a) $Re = 300$; (b) $Re = 1,000$.

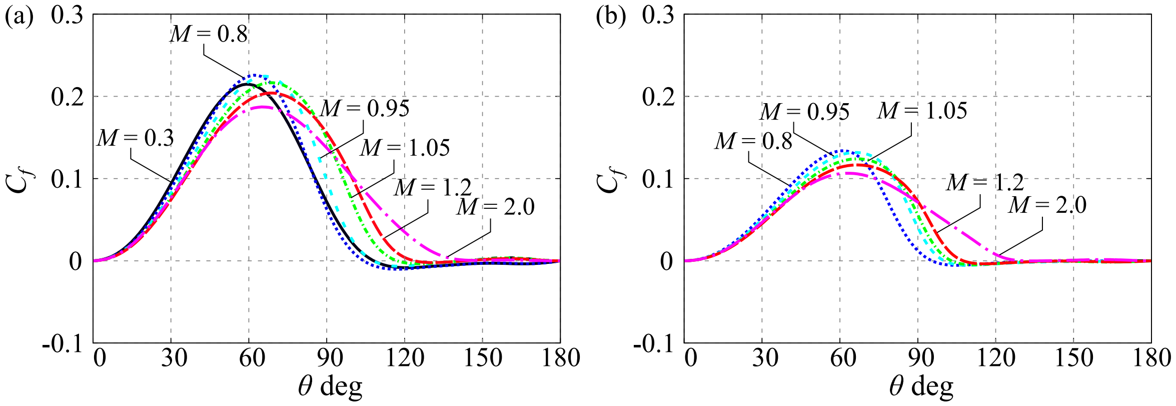

FIGURE 3.14: Friction coefficient distribution on the sphere surface: (a) $Re = 300$; (b) $Re = 1,000$.

3.3.5 Drag Coefficient

Figure 3.15 shows the M effect in the drag coefficients at $Re = 100, 300, 750$, and 1,000. The total drag coefficient C_D increases as M increases, and its increment under the transonic conditions is greater than that under the subsonic and supersonic conditions due to the increased wave drag. The increment of the drag coefficient becomes almost zero under the supersonic conditions, and is independent of M at around $M > 1.5$. This trend is well known as Oswatitsch's Mach number independence principle. The increment of the total drag coefficient by the effect of M is almost equivalent to the increase of the pressure component C_{D_P}, as shown in figure 3.15(b). The M effect on the pressure drag coefficient can be predicted by the Prandtl–Glauert transformation shown by the dotted lines up to the high-subsonic conditions. In addition, the increment of the pressure component at $M > 0.9$ is mainly according to the increment of the wave drag. However, the influence of M on the viscous component C_{D_v} is smaller than that of the pressure component. The viscous component slightly decreases as M increases under the subsonic conditions because the separation point moves upstream as M increases. Under the transonic conditions, the separation point moves downstream, and the velocity gradient on the sphere surface increases, particularly behind the attached shock wave. Thus, the viscous component increases as M increases. In contrast, the viscous component is almost constant under the supersonic conditions, despite the separation becoming delayed as M increases, because of the decrease in the velocity gradient on the sphere surface due to the deceleration of the flow at the detached shock wave. In this case, the fluid viscosity increases due to increasing temperature, but the decrease in the velocity gradient is more effective, as shown in figure 3.14.

Figure 3.16 depicts the relationship between Re and C_D at $0.3 \le M \le 2.0$, and the present results are compared to the drag curves predicted by the Loth, 2008 model and the experimental drag data acquired by Sreekanth, 1961; Goin and Lawrence, 1968; Zarin and Nicholls, 1971; Bailey and Starr, 1976. Figure 3.16 illustrates that C_D increases as Re decreases for each M. The drag coefficients predicted by the drag model, observed in experiments, and present DNS show good agreement at $M = 0.3$. At $M = 0.8$, the present result agrees well with some experimental data at $Re > 600$, but the drag coefficient by the Loth model is slightly lower than that from the experiments and DNS. The difference between the experiment, model, and DNS becomes large as M increases under the transonic conditions at $0.95 \le M \le 1.2$, particularly in the low-Re regime. However, the difference between the experimental and DNS data also becomes large at further high-M conditions in the lower-Re regime. At $M = 2.0$, the drag model and experimental data show good agreement, but DNS overestimates the drag coefficient compared with the drag model and experimental data, particularly in the low-*Re* regime. The overestimation by DNS is due to the influence of the no-slip boundary condition, and thus the difference between DNS and other data becomes small as *Re* increases because the rarefaction effect weakens. However, the Knudsen number at $M = 2.0$ is less than 0.001 at $Re > 250$ so that the rarefaction effect is sufficiently small in that region, but there is the difference between the predicted value of the drag model and the experimental and DNS data.

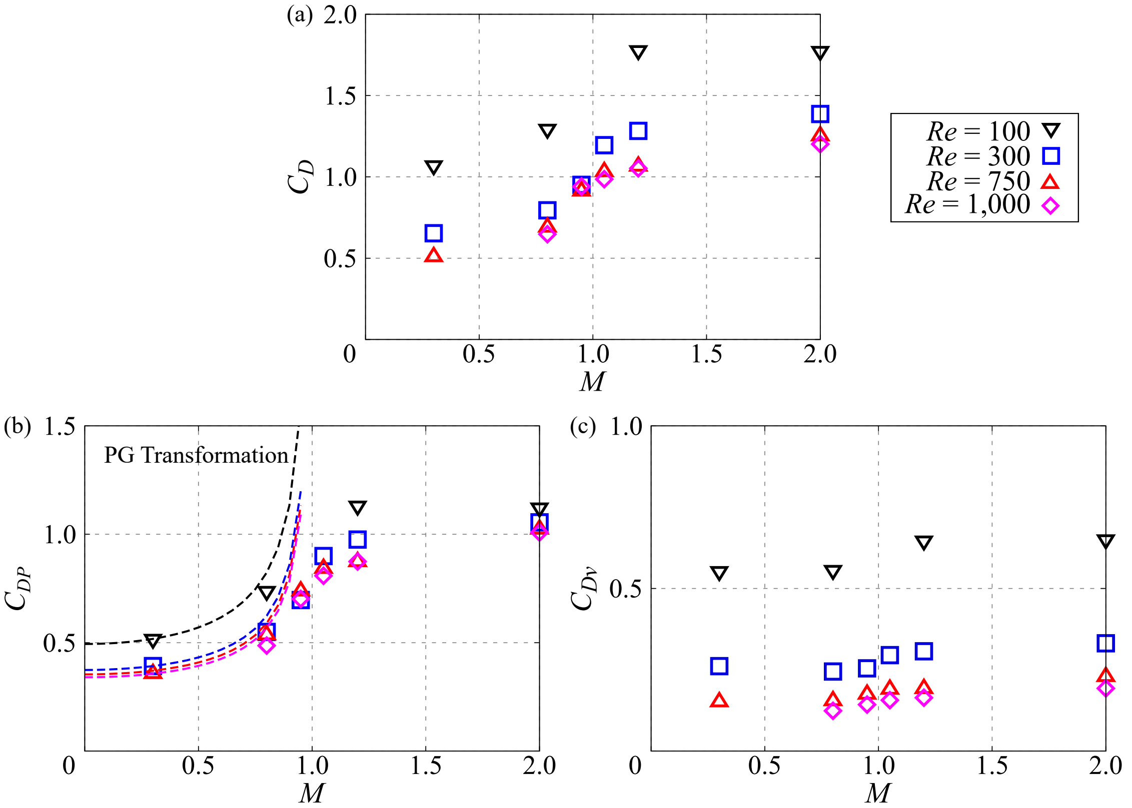

FIGURE 3.15: Effect of M on C_D: (a) total drag coefficient; (b) pressure drag coefficient; (c) viscous drag coefficient.

Loth, 2008 introduced the "Nexus" point ($C_D \approx 1.63$ at $Re = 45$ for all M and Kn) to connect the two equations which for the compression-dominated regime ($Re > 45$) and rarefaction-dominated regime ($Re < 45$). However, the "Nexus" point does not base on the numerical or experimental data, and it was clarified that the drag coefficient at $Re = 45$ is not constant at around $C_D \approx 1.63$. The recent study using by the direct simulation Monte Carlo of the Boltzmann equation and DNS of the Navier–Stokes equations clarified that the drag coefficients at $Re = 45$ in the subsonic and supersonic flows are $C_D \approx 1.63$, but it is larger than that of the subsonic and supersonic conditions at the transonic condition. In the continuum regime, the drag coefficient under the supersonic conditions is larger than that under the subsonic conditions, but the increment of the drag coefficient caused by the M effect decreases at a rarefied regime due to rarefaction effects. Thus the drag coefficient under the supersonic conditions of $Re = 45$ is the same level as that of the subsonic conditions. On the other hand, the rarefaction effect is still weak at transonic conditions of $Re = 45$, so that the drag coefficient around the transonic condition at $Re = 45$ is larger than that under the subsonic and supersonic conditions. The detailed discussions will be published as a journal paper, which is now preparing. Other compressible drag models are compared with DNS data in figure A.4 at appendix A.1.

Figure 3.17 shows the increment of the total drag coefficient with an increasing M. In the present study, ΔC_D was defined as follows:

$$\Delta C_D = C_D(Re, M) - C_D(Re, 0) \tag{3.5}$$

where $C_D(Re, M)$ indicates the drag coefficient predicted by the present DNS or previous experiments and $C_D(Re, 0)$ indicates the drag coefficient under incompressible flow, which was predicted by the drag model proposed by Clift and Gauvin, 1971. Figure 3.17(a) illustrates that ΔC_D increases as M increases at $M \geq 0.3$. In addition, ΔC_D appears to be only a function of M, and Re has no clear influence on ΔC_D. The increment of ΔC_D under the transonic conditions is particularly larger than that under the subsonic and supersonic conditions. The increment of ΔC_D under the subsonic conditions is a compressibility effect, which can be explained by the Prandtl–Glauert transformation, and the pressure drag increase due to a decrease of the attached region, as illustrated in figure 3.15(b) and figure 3.7(a). The increment of the wave drag is almost constant at $M > 1.5$ and moderate Re; hence, the increment of ΔC_D becomes small under the higher-M conditions but also under the low-Re conditions. At $M = 0.3$, ΔC_D is negative because C_D at $M = 0.3$ is slightly smaller than that under the incompressible flow, due to the position of the separation point existing upstream compared with that under incompressible flow. In addition, the position of the separation point under the lower-Re conditions exists downstream compared with that under the higher-Re conditions, and thus the decrements of ΔC_D are larger under the lower-Re conditions.

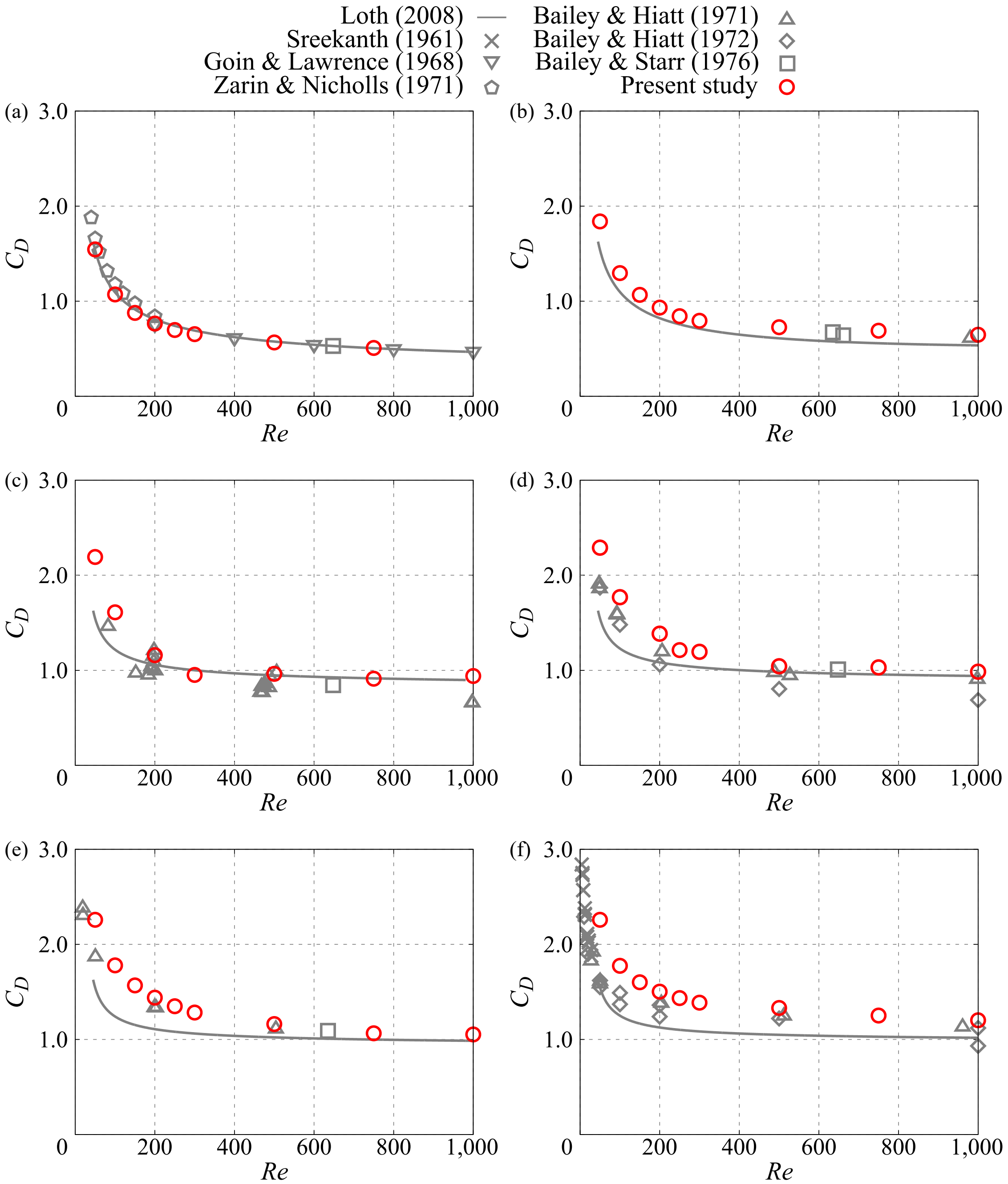

FIGURE 3.16: Relationship between Re and C_D: (a) $M \approx 0.3$, (b) $M \approx 0.8$, (c) $M \approx 0.95$, (d) $M \approx 1.05$, (e) $M \approx 1.2$, (f) $M \approx 2.0$.

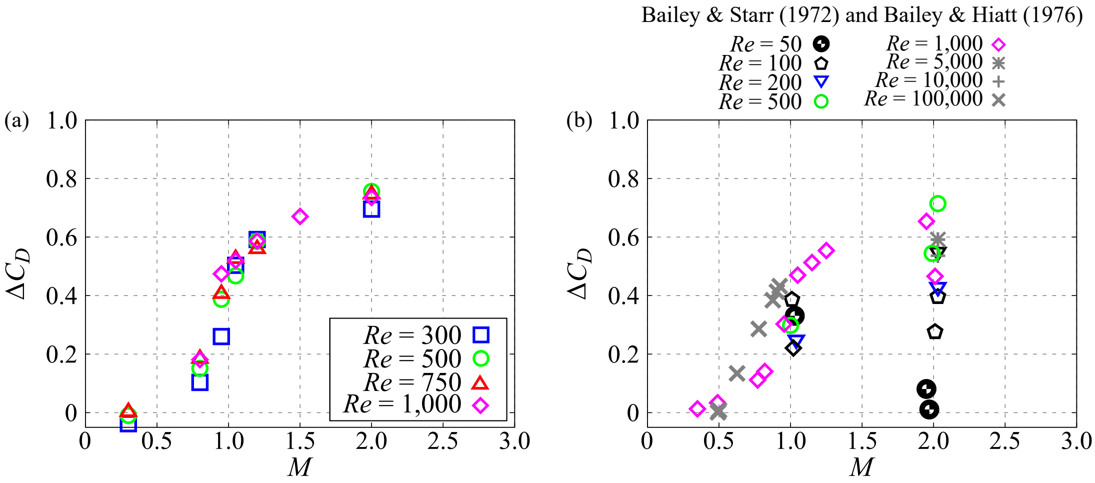

FIGURE 3.17: Increment of C_D by M effects: (a) present study, (b) published experimental results.

Figure 3.17(b) shows ΔC_D as calculated using published experimental data. In this case, ΔC_D is approximately characterized by M at $M < 1.5$, but the Re dependence appears at $M = 2.0$. At $M = 2.0$, ΔC_D for the lower-Re conditions, particularly at $Re \leq 200$, decreases as Re decreases, because the Knudsen number based on the freestream and the sphere diameter is greater than 0.01 at $Re \leq 200$ and $M = 2.0$. Hence, the slip effect on the wall caused by the rarefaction effect gradually strengthens as Re decreases.

3.3.6 Characterization of Drag Coefficient and Flow Regime by Position of Separation Point

Figure 3.18 shows the relationship between the position of the separation point and the drag coefficient. Figures 3.18(a)–(c) illustrate that the total, pressure, and viscous drag coefficients become small when the position of the separation point moves upstream at $Re \leq 1,000$. Also, the $\theta_s - C_D$ curve for each M value has a similar shape. The position of the $\theta_s - C_D$ curve for each M condition and the gradient of curve depends on M. However, a different trend can be seen in the pressure component, as shown in figure 3.18(b). For the pressure component, the shape of the $\theta_s - C_{D_P}$ curve is different the under subsonic, transonic, and supersonic conditions. Under the subsonic conditions, the θ_s–C_{D_P} curve has nonlinearity. In contrast, nonlinearly in the $\theta_s - C_{D_P}$ curve under the supersonic conditions is relatively weak. In addition, the trend of the

θ_s–C_{D_P} curves for the transonic conditions are different from the trend under the subsonic and supersonic conditions. In particular, the gradient of the θ_s–C_{D_P} curve at $M = 0.95$ is negative. Therefore, the behaviours of the pressure field and the flow geometry is different from those under the subsonic and supersonic conditions due to the formation of shock waves. Regarding M, C_{D_P} increases as M increases, but the position of the separation point is approximately the same up to $M = 1.05$. The increment of C_{D_P} with increasing M in this regime is caused by the compressibility effects, which can be explained by the Prandtl–Glauert transformation and the wave drag. At $M \geq 1.05$, in contrast, the increment of C_{D_P} with increasing M is smaller and the position of the separation point moves downstream as M increases. Regarding C_{D_v}, as shown in figure 3.18(c), the trend of the θ_s–C_{D_v} curves is similar at each M, and M does not have a large impact on C_{D_v}, despite the position of the separation point moving downstream as M increases, particularly under the supersonic conditions. This trend is caused mainly by the detached shock wave. Under the supersonic low-*Re* flow, the flow separation is reduced and the position of the separation point moves downstream as M increases. Moreover, the flow is decelerated at the detached shock wave, and thus the normalized velocity gradient on the surface of the sphere normalized by the freestream velocity is lower than that in the subsonic cases. Because of this reducing the lower wall shear stress, C_{D_v} does not increase when M increases.

Under the incompressible flows at $Re \leq 1,000$, the position of the separation point moves from downstream to upstream as Re increases, and the flow pattern transitions from fully attached flow to helical wake through steady-axisymmetric, steady planar-symmetric, and hairpin wake regimes. In other words, the flow pattern appears to depend on the position of the separation point. Figure 3.19 characterizes the flow regime according to the position of the separation point. This figure illustrates that the flow regime can be characterized by the position of the separation point for every M investigated in the present study. For all values of M, the flow pattern transitions to an unstable wake as the position of the separation point moves upstream; hence, the relationship between the flow regime and the position of the separation point under the compressible flow is similar to that under the incompressible flow. However, the effect of M on the flow regime still remains, even when characterized using the position of the separation point. For example, the separation point at $M = 0.3$ and 0.8 shifts upstream, and the separation point for each flow pattern also shifts upstream with increasing M. This indicates that the flow pattern change with increasing M is not merely a change in the separation point position. As M increases, a certain flow pattern appears when the position of the separation point exists relatively upstream up to $M = 0.95$. This means that the flow becomes stable despite the separation point existing relatively upstream (resembling a higher-Re condition) compared to the position under the lower-M conditions. However, the situation under the supersonic conditions is different from that under the subsonic and transonic conditions because the separation angle is different due to the expansion wave even if the separation point exists in the same location. For the same separation point with different M values, Re of the flow in the supersonic case is higher than that in the subsonic cases, and thus the wake in of the supersonic case appears to be less stability compared to subsonic flows.

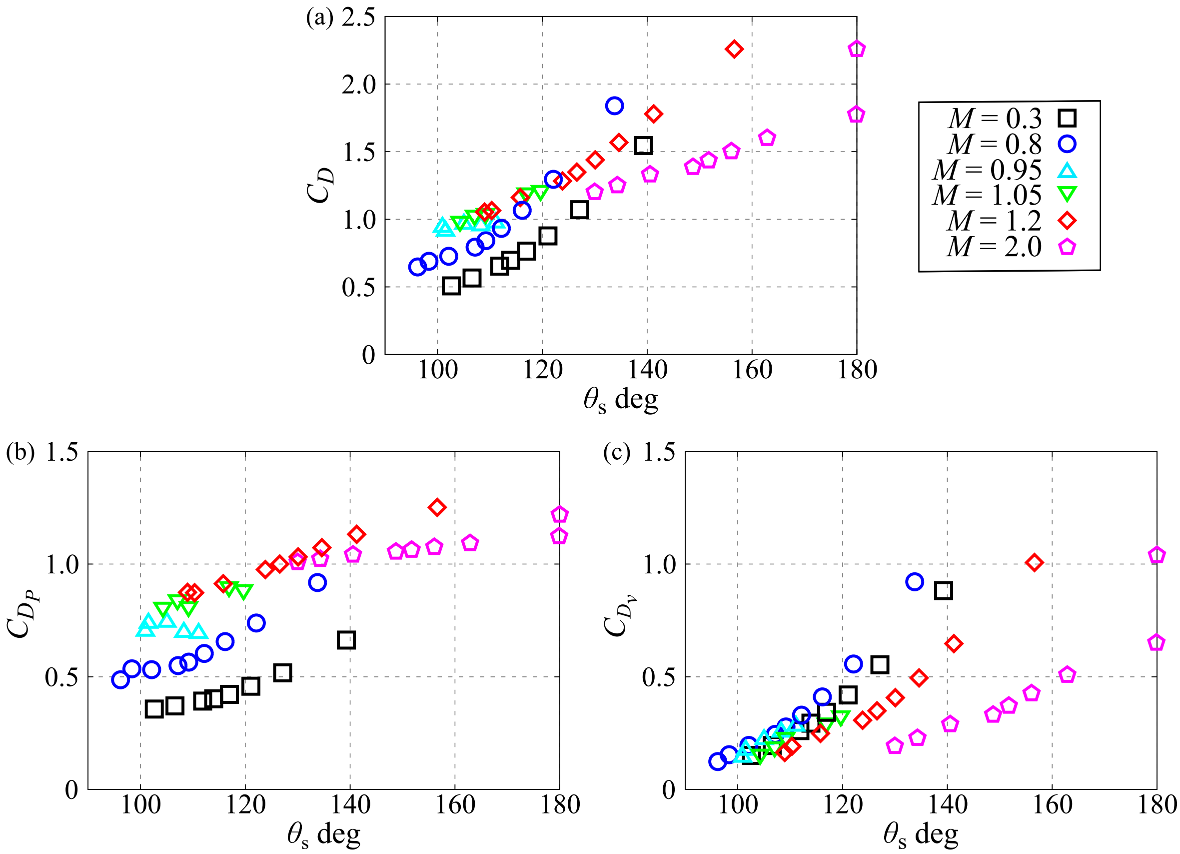

FIGURE 3.18: Characterization of the drag coefficients by the position of the separation point: (a) total drag; (b) pressure component; (c) viscous component.

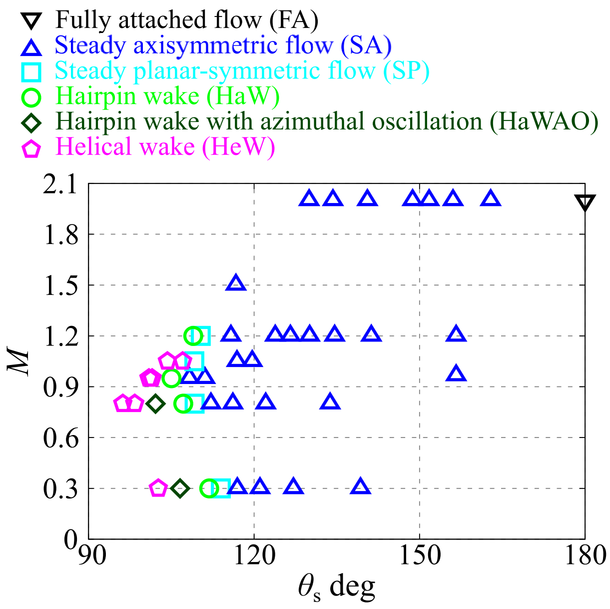

FIGURE 3.19: Characterization of the flow regime by the position of the separation point.

3.4 Conclusions

In chapter 3, the compressible low-*Re* flow over a stationary adiabatic sphere was investigated by DNS of the three-dimensional compressible Navier–Stokes equations using a body-fitted grid with high-order schemes. The flow conditions were $50 \leq Re \leq 1,000$ and $0.3 \leq M \leq 2.0$. It was clarified that the effect of M and Re on the far-field flow properties and the near-field flow properties.

The computational results showed that the wake is significantly stabilized as M increases. In the case of $M = 1.2$, for example, steady axisymmetric, steady-planar symmetric, and hairpin wakes were observed at $Re = 500$, 750, and 1,000, respectively. These flow regimes appear at $24 \leq Re \leq 210$, $211 \leq Re \leq 275$ and $275 \leq Re \leq 420$, respectively, in the incompressible flow. Thus, the critical Re for compressible cases is shifted into the higher-Re side that at the incompressible cases. The difference in the wake behavior between the low-speed and high-speed flows that wake instability under transonic and supersonic conditions appears near the wake shock. This characteristic is the same as that under higher-Re conditions of $Re \leq O(10^4)$ in a similar M range (see chapter 6).

The position of the separation point moves upstream and downstream as M increases under subsonic and greater-than-transonic conditions, respectively. Also, the separation point moves upstream as Re increases, and the magnitude of the change is almost the same for each M; hence, the interaction of M and Re effects do not change the position of the separation point. In contrast, the effects of M and Re interact to change in the length of the recirculation region, which is a steep peak at around the transonic condition. The peak value of the length of the recirculation region decreases as Re increases, and the point at which the length of the recirculation region increases to its maximum value is shifted to higher M values as Re increases. The recirculation length becomes the maximum value at around the critical M which the flow regime becomes steady flow due to the compressibility effect.

The drag coefficient increases as M increases and it increases mainly under transonic conditions due to the compressibility effect described by the Prandtl–Glauert transformation and the wave drag. The Reynolds number also affects the drag coefficient, but the increment of the drag coefficient due to compressibility effects can be characterized by only M in the continuum regime despite the low-Re conditions. Since few data are available for the drag coefficient under compressible low-Re conditions, particularly under transonic conditions, it seems that the accuracy of the previous drag model for transonic conditions was relatively low compared to that for subsonic and supersonic conditions.

Finally, the drag coefficient and the distribution of the flow regime were discussed based on the position of the separation point. The drag coefficient can be characterized by the position of the separation point for each M. This result suggests that the effect of Re on the drag coefficient can be characterized by the position of the separation point regardless of the compressibility effect. However, although the influence of M is not characterized completely, characterization using the position of the separation point works well compared to characterization using Re and M.

Chapter 4

Effect of Sphere Temperature

List of Symbols

A = Area
C_D = Drag coefficient
C_{D_P} = Pressure drag coefficient
C_{D_v} = Viscous drag coefficient
C_L = Lift coefficient
C_P = Pressure coefficient
C_Y, C_Z = Aerodynamic force coefficients in y and z directions
Kn = Knudsen number
L_r = Length of recirculation region
L_s = Shock standoff distance
M = Mach number
Nu = Nusselt number
Q = Q-criterion, amount of heat
Re = Reynolds number
St = Strouhal number
T = Temperature
TR = Temperature ratio between freestream and sphere surface
a = Sound speed
d = Diameter of the sphere
h = heat transfer coefficient
k = Thermal conductivity
t = Time
u, v, w = Velocity in x, y, and z directions
μ = Dynamic viscosity coefficient
ν = kinematic viscosity coefficient
θ_s = Separation point
ρ = Density
ξ, η, ζ = Curvilinear coordinates

Subscripts

local = Local values

r.m.s. = Root-mean-square

surf = Surface of sphere

∞ = Freestream

4.1 Introduction

The temperature difference in the fluid and particle has a large impact on the flow over a sphere. In the compressible multiphase flows, it is considered that there is a temperature difference in the particle and the fluids when the particles across the shock wave, for example. Under the incompressibe flow, Mansoorzadeh et al., 1998 numerically investigated the flow over a heated/cooled sphere by solving the three-dimensional incompressible Boussinesq equations in the primitive variable form by a Galerkin finite element method. They showed that the drag coefficient is significantly influenced by the heat of the sphere. Kurose et al., 2012 investigated the characteristics of the flow over a heated/cooled sphere at $50 \leq Re \leq 400$ under the incompressible conditions, examining the effect on the flow properties of the temperature ratio between the sphere to that of the freestream. They clarified that the drag coefficients of the heated and cooled spheres are larger and smaller than that of the adiabatic sphere, respectively. Also, the Nusselt number of the heated and cooled spheres are smaller and larger than that of the predicted values by the widely used empirical models. The flow structure such as the the separation point, the length of the recirculation region, and St of vortex shedding also strongly influenced by the temperature difference in the sphere and ambient fluid.

For compressible cases, Salimipour and Anbarsooz, 2019 investigated the surface temperature effect on the flow over a rotating cylinder for $Re = 200$ and $0.1 \leq M \leq 0.4$. They revealed that the lift coefficient of the rotating cylinder decreases as surface temperature increases. Also, the vortex shedding pattern and the mean Nusselt number are influenced by the surface temperature as reported in the previous incompressible studies. The Nusselt number at $M = 0.3$ significantly increases as a rotation rate increases, but at $M = 0.2$, the increment of the Nusselt number is quite smaller than that of $M = 0.3$. Therefore, there are significant compressibility effects on the influence of the surface temperature despite low-subsonic flows.

The heat transfer between objects and ambient fluids is one of the most important issue so that several researchers proposed the Nusselt number model of spherical objects (Ranz and Marshall, 1952; Sauer, 1951; Fox, Rackett, and Nicholls, 1978). Sauer, 1951 suggested the Nusselt number model for the sphere by extending the theoretical formula for the heat transfer oft flat plates, and Ranz and Marshall, 1952 and Fox, Rackett, and Nicholls, 1978 proposed Nusselt number models based on the estimated amount of heat transfer through experiments on the evaporation of liquid droplets and the shock wave ignition of magnesium powders, respectively.

The drag and Nusselt number model for the sphere is essential for the simulation of multiphase flow by point-particle approach. In addition, the surface temperature effects on the presence or absence of the wake vortices might have a large impact on the energy dissipation of the flowfield of multiphase flows because there is the turbulent modulation caused by the interaction of the turbulence and generated vortices by particles. However, there are few studies that investigated the influence of the temperature difference between the sphere surface and freestream, particularly there is no numerical examination under the compressible regime. Hence, an examination of the flow properties such as the drag coefficient, the Nusselt number, and the flow structure is essential to improve the the compressible multiphase flow model. In this chapter, we investigate the influence of the temperature difference in the sphere and freestream on the flow characteristics under compressible low-Re flow and the applicability of previous drag models by performing the DNS of flow over a stationary isothermal sphere.

4.2 Computational Setup

4.2.1 Flow Conditions

In the present chapter, uniform flows over a stationary isothermal sphere was computed for $100 \leq Re \leq 300$, $0.3 \leq M \leq 2.0$, and $0.5 \leq TR \leq 2.0$. Here, TR is defined as follows:

$$TR = \frac{T_{\mathrm{surf}}}{T_{\infty}}, \tag{4.1}$$

where T_{surf} and T_{∞} is the temperature of the sphere and the temperature of the freestream, respectively. The summary of the flow conditions is given in table 4.1. The present study is focusing on the particles in a high-speed multiphase flow, and thus the relative M of the flow over a particle is considered to be less than 2.0 except for those particles passing through the quite strong shock waves.

		M			
		0.3	0.8	1.2	2.0
	100	A	A	A	A
	150	A	A	A	A
Re	200	A	A	A	A
	250	B	B	A	A
	300	B	B	A	

TABLE 4.1: Flow conditions for a stationary isothermal sphere. A: TR = 0.5, 0.9, 1.1, 1.5, and 2.0 computed by the base gird; B: TR = 0.5, 0.9, 1.1, 1.5, and 2.0 computed by the base gird and TR = 0.5, 1.0, and 2.0 computed by the wake-fine grid.

Also, the resolution of the computational grid was retained in the downstream of the sphere for the diameter of $4d$. Computational grid that used in chapter 3 for $Re = 300$ was used. Result of the grid convergence study is shown in appendix A.2.2.

4.2.2 Boundary Conditions

The boundary at the sphere surface was no-slip and isothermal conditions. At the surface of the sphere, the velocity was fixed to zero, the density was fixed to the value computed from the pressure and the temperature at the surface of the sphere, the pressure was calculated from the momentum normal to the surface. The periodic boundary condition with the six overlapped grid points was imposed at the boundaries in the ξ and η directions. All the variables on the singular point on the x-axis were set to be an average of the nearest surrounding nodes. The inflow and outflow boundary conditions were imposed at the outer boundary where the flow goes inside and outside at one point inside the boundary, respectively. At the inflow boundaries, all flow variables were fixed to their freestream values. All the variables were extrapolated from one point inside of the boundary at the supersonic outflow boundaries. The velocities and the density were similarly extrapolated and the pressure was fixed to its freestream values in the subsonic outflow boundaries.

4.3 Results and Discussion

4.3.1 Flow Regime

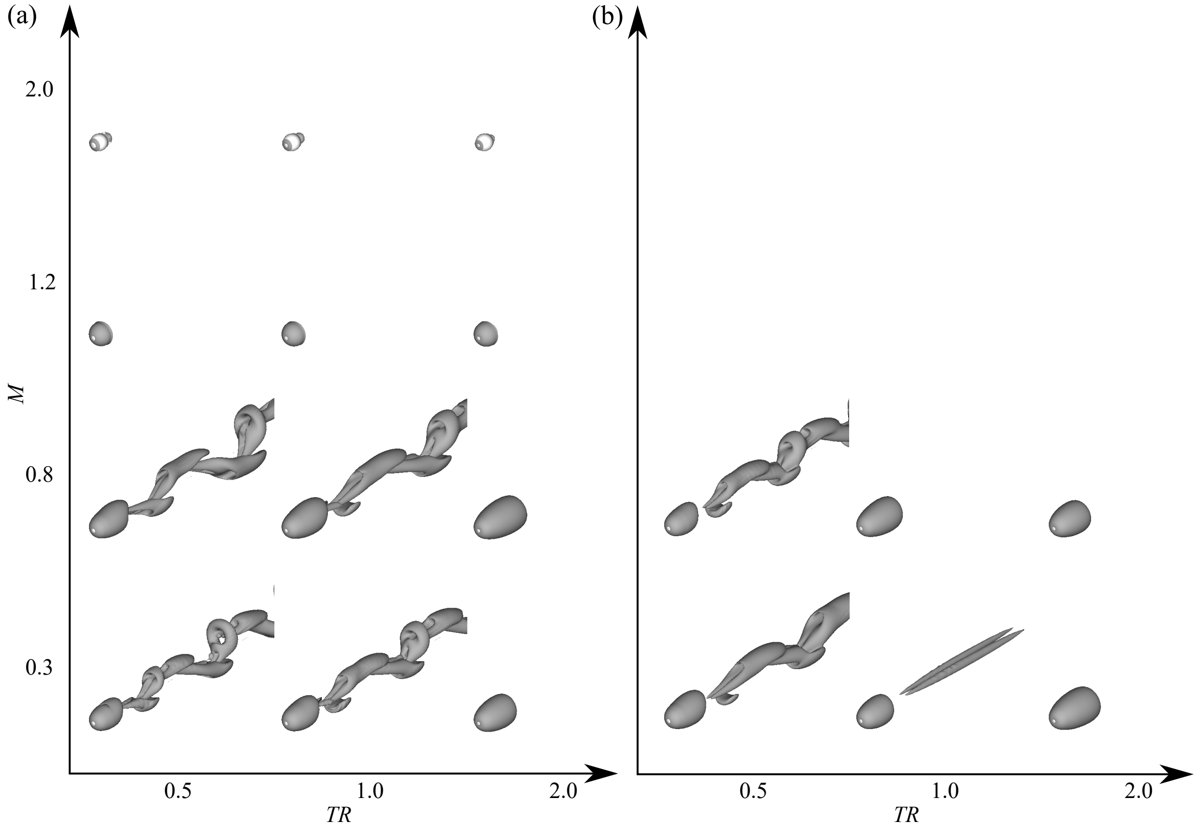

FIGURE 4.1: Instantaneous wake structures. The structures are identified by the isosurface of the normalized second invariant value of the velocity gradient tensor, which is normalized with respect to the freestream velocity ($Q/u_\infty^2 = 5.0 \times 10^{-4}$). (a) Re = 250; (b) Re = 300.

Figure 4.1 depict the wake structure visualized by the isosurface of the Q-criterion. The threshold is normalized with respect to the freestream velocity. At $Re = 300$, hairpin vortices are generated by the sphere at $M = 0.3$ and 0.8 of $TR = 1.0$. At $Re = 250$, on the other hand, the hairpin vortices disappear and the wake structure transitions to a double-threaded structure at $M = 0.3$ and $TR = 1.0$. The wake vortices disappear at $Re = 250$ and $M = 0.8$ and further low-Re flows. This trend is similar to that of incompressible flows up to $Re = 300$. In the case of a cooled sphere ($TR = 0.5$) at $Re = 250$, the wake has hairpin structures. Conversely, in the case of a heated sphere ($TR = 2.0$), no hairpin structures are observed. In other words, the wake structures of the cooled and heated spheres are similar to the wake structure in high- and low-Re conditions, respectively. Therefore, the wake structure becomes similar to that of high-Re flows as TR decreases and becomes similar to that of low-Re flows as TR increases. Under supersonic conditions, on the other hand, the wake structure does not change even if Re or TR changes in the investigated conditions.

The type of flow pattern was categorised based on the normalized TKE normalized by the freestream kinetic energy and the deviation of the separation point. Here, u', v' and w' are the fluctuation components of the fluid velocity. Under the conditions in which the calculations were conducted in the this study, the flow regimes can be classified into three types: a fully attached flow (black symbols), a steady axisymmetric flow (blue symbols), a steady planar-symmetric flow (light blue symbols), and a hairpin wake (green symbols). The type of the flow pattern for each TR and for adiabatic conditions is shown in figure 4.3. The classification criteria are given in table 4.2. Here, the hairpin wake is the case in which the maximum normalized TKE in the wake is greater than 0.5% and periodic variation of the lift forces can be observed. The steady planar-symmetric flow is the case in which bias of the separation point can be observed and the maximum normalized TKE in the wake is less than 0.5%. The steady axisymmetric flow is the case in which no deviation in the separation point is observed and the maximum normalized TKE in the wake is less than 0.5%. The fully attached flow is the case in which no separation is observed. In this study, the TKE was averaged up to the section of $x \leq 2.5d$ from the surface of the sphere on the downstream side of the x-axis. Under adiabatic and incompressible flow conditions, the flow regime is the steady axisymmetric flow at $50 \leq Re \leq 210$. The type of flow pattern becomes steady planar-symmetric flow at $Re < 280$. As Re further increases, the flow pattern becomes hairpin wake at $Re \gtrapprox 280$. The results at $M = 0.3$ agree with those of a previous incompressible study (Johnson and Patel, 1999). It should be noted that Johnson and Patel, 1999; Magarvey and Bishop, 1961 reported the steady planar-symmetric flow by numerical and experimental studies at incompressible flows. Those studies showed clearly that the steady planar-symmetric flow is a solution of the Navier–Stokes equations of the flow over a sphere. A similar solution was obtained in our DNS at $M = 0.3$ and 0.8 of $TR = 1.0$ for $Re = 250$. The trigger for the asymmetry that appears at $Re = 250$ is a tiny disturbance. In numerical studies, Johnson and Patel, 1999 pointed out that the trigger for non-axial symmetry is possibly a round-off error in the computation.

In low-*Re* or supersonic cases, the TKE is almost zero because no hairpin vortices are generated. Figure 4.2 shows the distribution of the TKE in the downstream of the sphere at $M = 0.3$ and 0.8 for $Re = 300$. The TKE is calculated as pointwise values on the x-axis in the downstream of the sphere. In addition, the TKE is normalized relative to the freestream kinetic energy. Figure 4.2 illustrates that the peak in the TKE in the vicinity of the sphere decreases as TR increases. This is due to the increase in viscous dissipation with the increase in the molecular viscosity. In addition, the TKE in the wake is changed by the properties of the hairpin vortices. In unsteady cases, hairpin vortices are generated periodically in the recirculation region. Under subsonic conditions, the recirculation region becomes large as M increases. For the same TR in subsonic flows, therefore, it is consider that the hairpin vortices at $M = 0.8$ are larger than these for $M = 0.3$. Hence, the maximum value of the TKE at $M = 0.8$ is greater than that at $M = 0.3$ for each TR, and the peak position of the TKE depends on M.

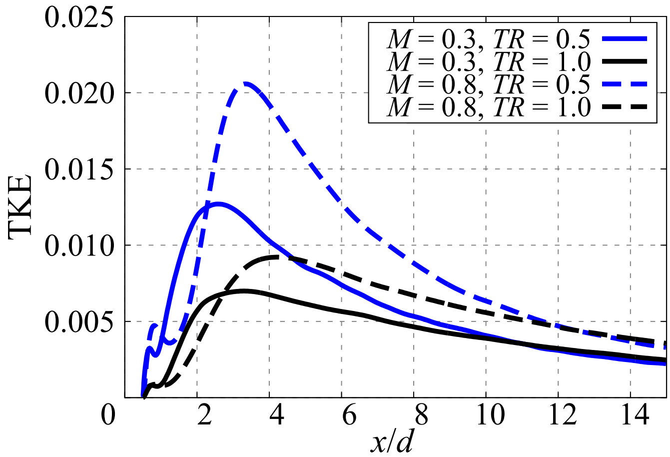

FIGURE 4.2: Distribution of TKE in the wake for unsteady cases ($Re = 300$).

Effects of TR appear on the type of flow pattern. Under high-TR conditions, the flowfield becomes stable. Conversely, under low-TR conditions, the flowfield becomes unstable. As shown in figure 4.3(e), there are no hairpin wake at $TR = 2.0$. In addition, the steady axisymmetric flow can be observed up to $Re = 250$ at $M = 0.3$, and the flow regime at $Re = 300$ is the steady planar-symmetric flow. However, the steady axisymmetric flow appears up to $Re = 150$. In addition, at $Re = 250$, the flow becomes the unsteady periodic flow. Therefore, the flow regimes under high- and low-TR conditions are similar to those of lower- and higher-*Re* flows with the adiabatic sphere. This trend can also be seen at $M = 0.8$. It is thought that this trend is caused by changes in the power balance of the inertial and viscous forces due to changes in the density and the viscosity coefficient (i.e., a change in the kinematic viscosity coefficient) in the boundary layer. However, the type of flow pattern under the supersonic conditions investigated in this study is the steady axisymmetric flow. Accordingly, we cannot discuss the effect of temperature on the type of flow pattern under supersonic conditions. However, the manner in which the temperature affects the flow pattern is considered to be similar to that for subsonic flows because the effect of TR is mainly in the change of the kinematic viscosity coefficient in boundary layer. The characterization of the effect of the temperature on the flow properties is discussed in section 4.3.4.

Flow regime	Flow properties
Steady axisymmetric flow	Maximum normalized TKE in the wake < 0.5% Axisymmetric separation point
Steady planar-symmetric flow	Maximum normalized TKE in the wake < 0.5% Planar-symmetric separation point
Hairpin wake	Maximum normalized TKE in the wake > 0.5% Periodic vibration of the fluid force

TABLE 4.2: Classification criteria of flow regime.

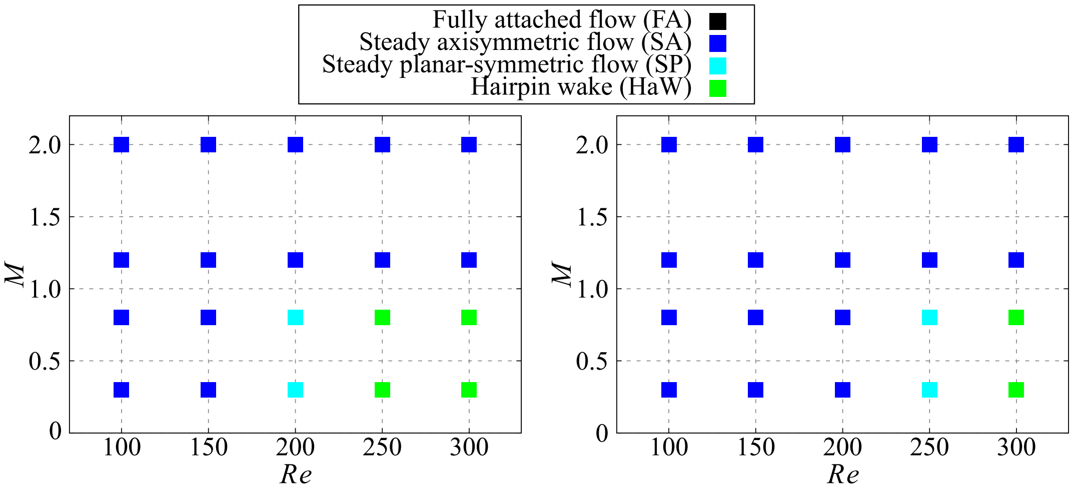

(a) $TR = 0.5$ (b) $TR = 0.9$

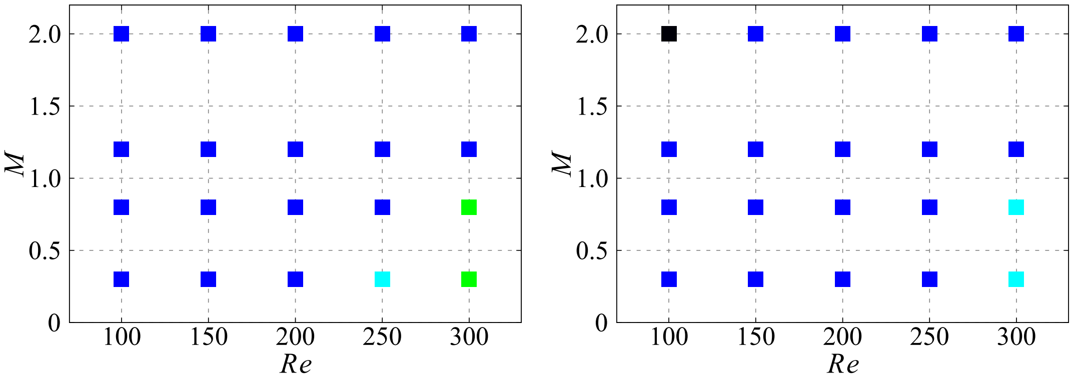

(c) $TR = 1.1$ (d) $TR = 1.5$

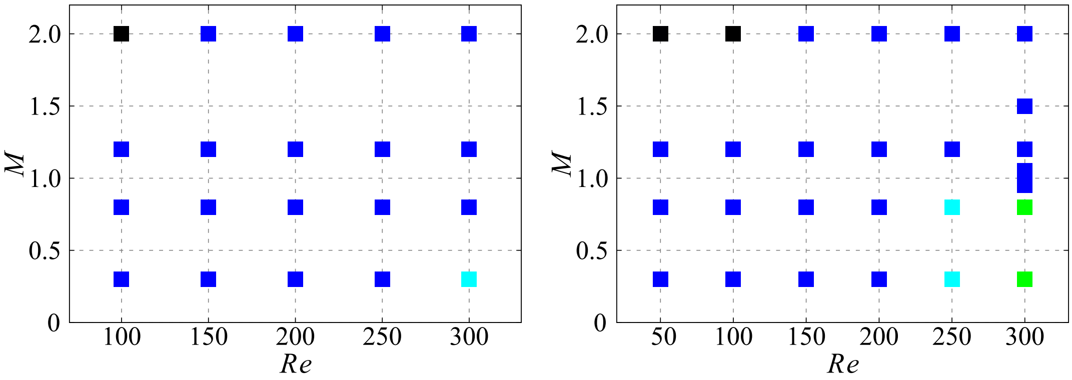

(e) $TR = 2.0$ (f) Adiabatic

FIGURE 4.3: Flow regime for each set of thermal boundary conditions.

4.3.2 Near-Field Structure

Pressure Coefficient Distribution

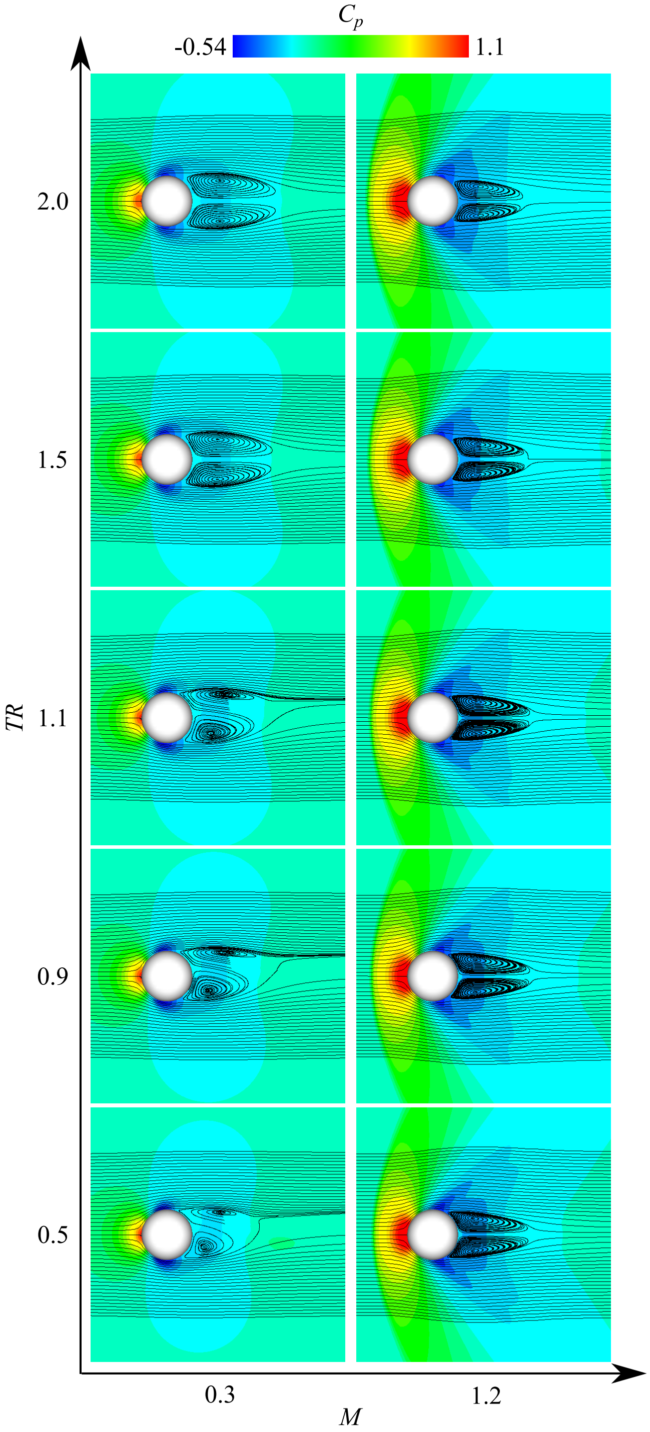

FIGURE 4.4: Pressure coefficient distribution and streamlines at $Re = 250$ in time-averaged field ($x - z$ plane).

Figure 4.4 shows the pressure coefficient distribution and the streamlines at $Re = 250$ of $M = 0.3$ and 1.2. These snapshots were taken from the time-averaged field. The calculations were carried out for durations longer than 10 vortex-shedding periods in the unsteady cases, from which the time-averaged fields were obtained. Figure 4.4 illustrates that TR affects the flow structure in the near-field of the sphere. The shape of the recirculation region at $M = 0.3$ is non-axisymmetric for $TR = 0.5$, 0.9, and 1.1. As the temperature of the sphere increases, the recirculation region becomes axisymmetric at $TR = 1.5$ and 2.0. In the case of $M = 1.2$, conversely, the symmetric shape of the recirculation region hardly changes.

Separation Point and Recirculation Region

Figures 4.5 and 4.6 show the separation point and the length of the recirculation region for $Re = 100$ and 200, respectively. The values in these figures were acquired in the time-averaged field. However, in the case of the hairpin wake and the planar-symmetric flows, the separation point and the recirculation region vary around the x-axis so that the error bars in these figures indicate the maximum and minimum values of each quantity. The flowfield for $Re < 200$ is axisymmetric at $0.3 \leq M \leq 2.0$ and $0.5 \leq TR \leq 2.0$. The separation point is identified based on the sign of the velocity gradient in the temporally and azimuthally averaged flowfield. Figure 4.5 illustrates that the separation point moves upstream and downstream sides as TR decreases and increases, respectively. In addition, it moves toward upstream and downstream sides as Re increases and decreases for adiabatic cases up to $Re = 300$ as discussed in chapter 3. For the separation point, therefore, the effect of the increasing TR is similar to that of decreasing Re. It is thought that this behavior results from the change in the kinematic viscosity coefficient in the vicinity of the sphere. Under high-TR conditions, for example, the kinematic viscosity coefficient in the vicinity of the sphere becomes lower than that in the adiabatic cases. This implies that the viscous force becomes more influential than it is in the adiabatic cases. Under low-TR conditions, conversely, the kinematic viscosity coefficient in the vicinity of the sphere becomes lower than that in adiabatic cases, and the inertial force becomes more influential than it is in the adiabatic cases. The characterization of the effect of the temperature on the flow properties is discussed in section 4.3.4.

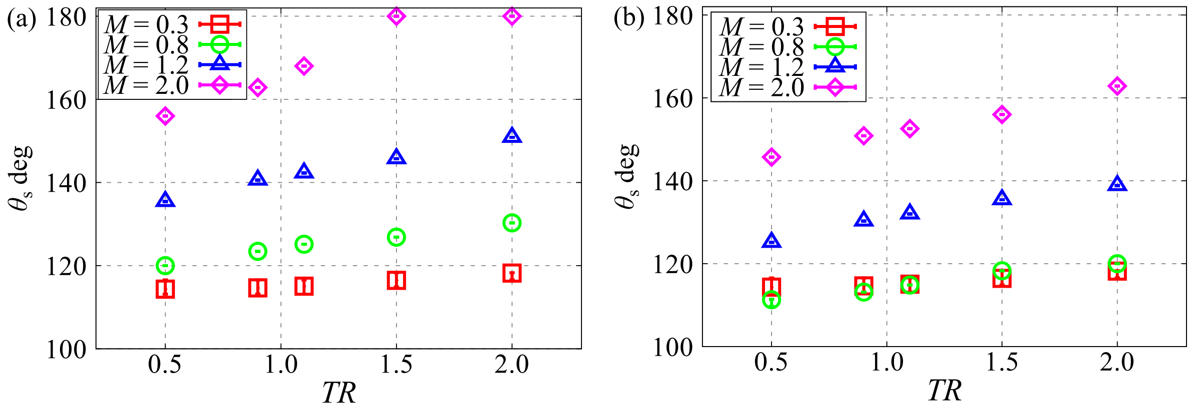

FIGURE 4.5: Effect of TR on the position of the separation point. (a) $Re = 100$; (b) $Re = 200$

Figure 4.6 illustrates that the recirculation region shortens as TR increases at $Re = 100$ under supersonic conditions. Under subsonic conditions, conversely, the length of the recirculation region hardly changes even if TR changes. At $Re = 200$, however, it stretches and shortens as TR increases under subsonic and supersonic conditions, respectively, even though the separation point moves toward the downstream side. In the case of a free jet, the potential core of a cooled jet is longer than that of a hot jet because the momentum of the cooled jet is larger than that of the hot jet (Lau, 1981). This difference in momentum is due primarily to the different densities of the fluid. However, the length of the recirculation region at $Re = 200$ under subsonic conditions increases as TR increases, even though the density of the fluid in the recirculation region decreases. This trend is the opposite trend to that for a free jet. Kurose et al., 2012 reported a similar trend with the present study under incompressible conditions. According to their paper, the recirculation region for the heated and cooled spheres at $Re = 100$ is longer and shorter than that in the adiabatic case, respectively. Conversely, at $Re = 50$ for both the heated and cooled cases, the recirculation region is shorter than that in the adiabatic case. In addition, the recirculation region for the heated sphere at $Re = 50$ is shorter than that in the cooled case as shown in table 4.3. In other words, the effect of temperature on the length of the recirculation region differs for $Re = 50$ and 100. In the case of supersonic conditions, the aerodynamic heating and the Prandtl–Meyer expansion influences the near wake of the sphere. Hence, the effect of TR on the length of the recirculation region in the compressible flows is more complex than it is in incompressible flows.

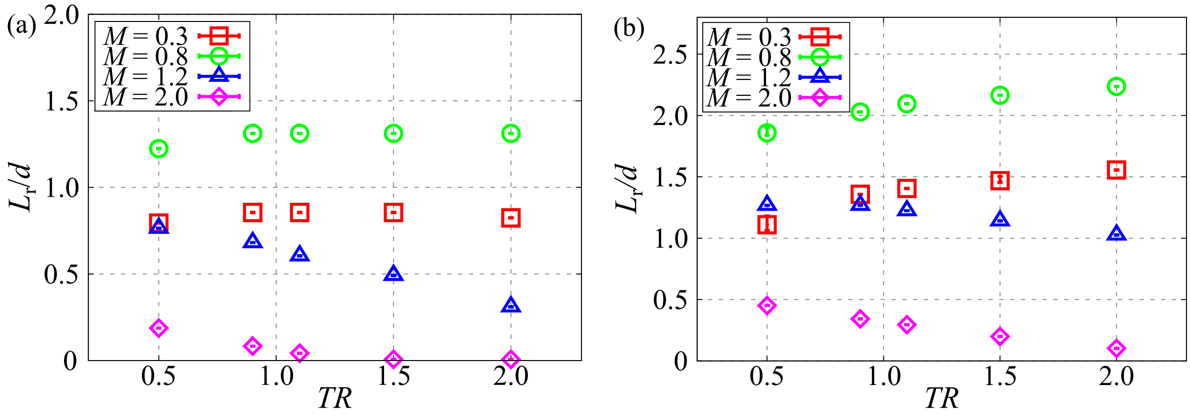

FIGURE 4.6: Effect of TR on the length of the recirculation region. (a) $Re = 100$; (b) $Re = 200$.

Flow condition			Length of recirculation region (compared with adiabatic case)
Incompressible flow ((Kurose et al., 2012))	$Re = 50$	Heated	Larger
		Cooled	Smaller
	$Re = 100$	Heated	Larger
		Cooled	Smaller
Compressible flow (Present study)	$M \leq 1.2$	Heated	Hardly changed
	$Re = 100$	Cooled	Hardly changed
	$M \geq 1.2$	Heated	Smaller
	$Re = 100$	Cooled	Larger
	$M \leq 1.2$	Heated	Larger
	$Re = 200$	Cooled	Smaller
	$M \geq 1.2$	Heated	Smaller
	$Re = 200$	Cooled	Larger

TABLE 4.3: Behavior of the length of the recirculation region compared with adiabatic cases.

Shock Standoff Distance

Figure 4.7 shows the absolute value of the density gradient in the time-averaged field. The position of the detached shock wave is influenced not only by M but also by Re and TR. Figure 4.8 shows the TR dependence of the shock standoff distance; the shock standoff distance increases as TR increases. In adiabatic cases under low-Re conditions, the shock standoff distance increases as Re decreases because of the change in the displacement thickness as discussed in chapter 3. Hence, the effect of TR on the shock standoff distance is the influence of the change in the displacement thickness due to the change in the kinematic viscosity coefficient in the boundary layer.

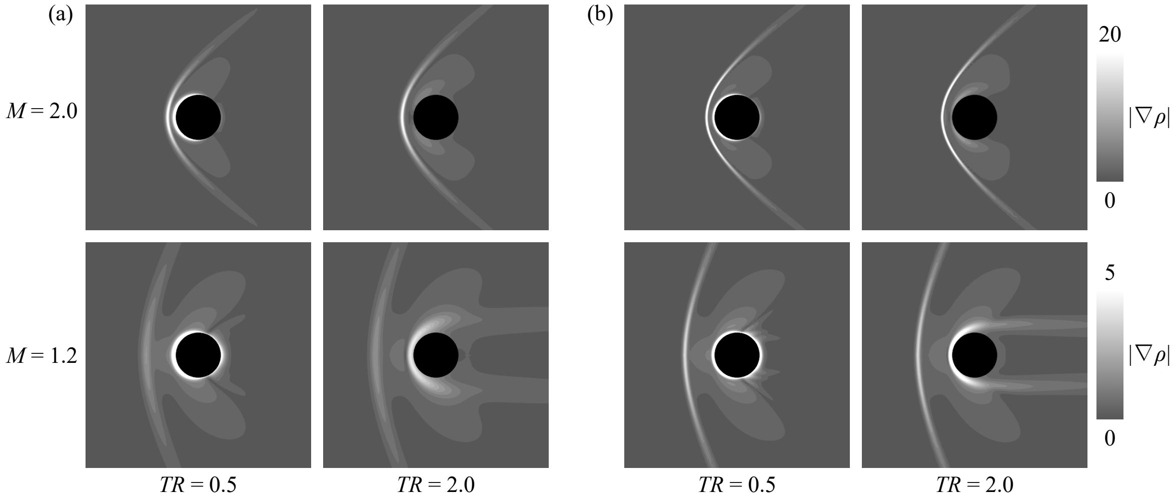

FIGURE 4.7: Schlieren-like images of time-averaged fields ($x-z$ plane). (a) Re = 100; (b) Re = 300.

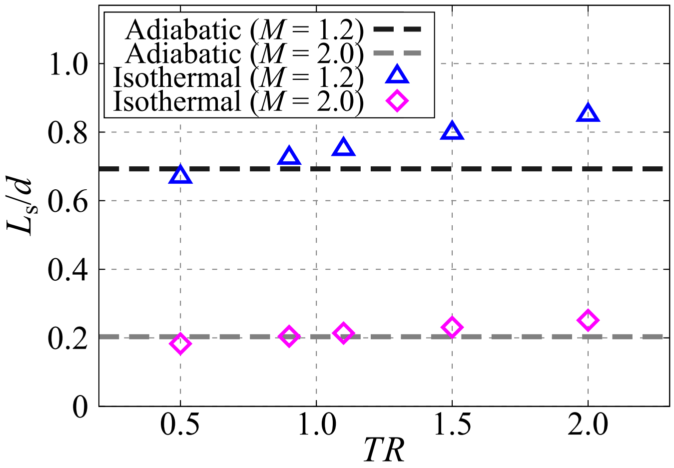

FIGURE 4.8: Effect of TR on the shock standoff distance (Re = 100).

4.3.3 Aerodynamic Force Coefficient

Time Variation of Lift Coefficient

Figure 4.9 shows the time variation of the lift coefficient, which in this study is defined as the square root of the sum of the squares of the hydrodynamic force coefficient in y and z directions: $\sqrt{{C_Y}^2 + {C_Z}^2}$. Because of the periodically released hairpin vortices, the lift coefficient oscillates in the case of the hairpin wake. Also, in the case of $Re = 300$, $M = 0.8$, and $TR = 0.5$ (blue line in figure 4.2(d)), a low-frequency mode appears in the time variation of the lift coefficient. This low-frequency mode is caused by the azimuthal rotation of the head of the hairpin vortices. Makita, 2007 reported such a helical mode appearing in incompressible flows at $Re = 2,000$. However, in the case of $Re = 300$, $M = 0.8$, and $TR = 0.5$, the rotation frequency of that azimuthal direction is considerably lower than that observed in the previous incompressible study. We presume that this was due to compressibility or temperature effects, but it was difficult to identify the actual cause in this study because of a lack of DNS data.

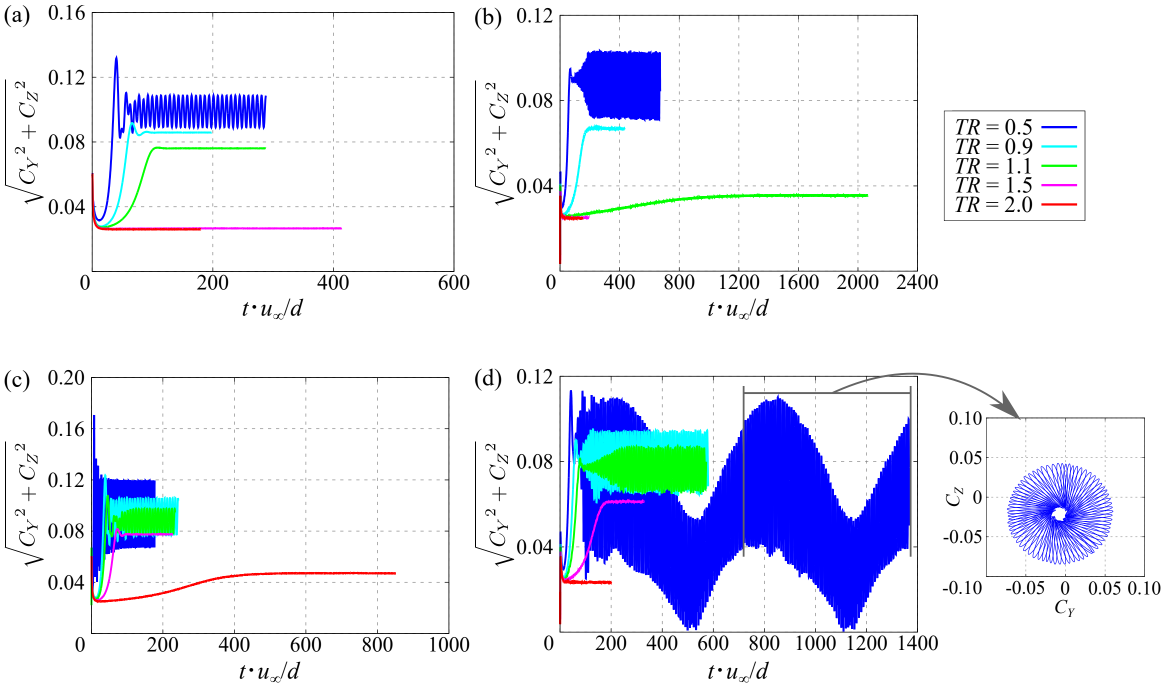

FIGURE 4.9: Time history of lift coefficient. (a) $Re = 250$ and $M = 0.3$; (b) $Re = 250$ and $M = 0.8$; (c) $Re = 300$ and $M = 0.3$; (d) $Re = 300$ and $M = 0.8$.

Figure 4.10 show the $C_{L\text{r.m.s.}}$ and St of the vortex shedding for subsonic flows at $Re = 300$, respectively. The figure indicates that the lift coefficient of the subsonic flow oscillates at low smaller TR. However, $C_{L\mathrm{r.m.s.}}$ and St of the vortex shedding decrease as TR increases. In several cases, hairpin vortices are generated from the sphere, and in these cases, the TKE is larger than it is in steady cases. The presence or absence of the wake vortex discussed in the previous section affects the dissipation of energy in the flow field. Therefore, it is valuable to investigate the modulation caused by the wake vortices generated by the particles.

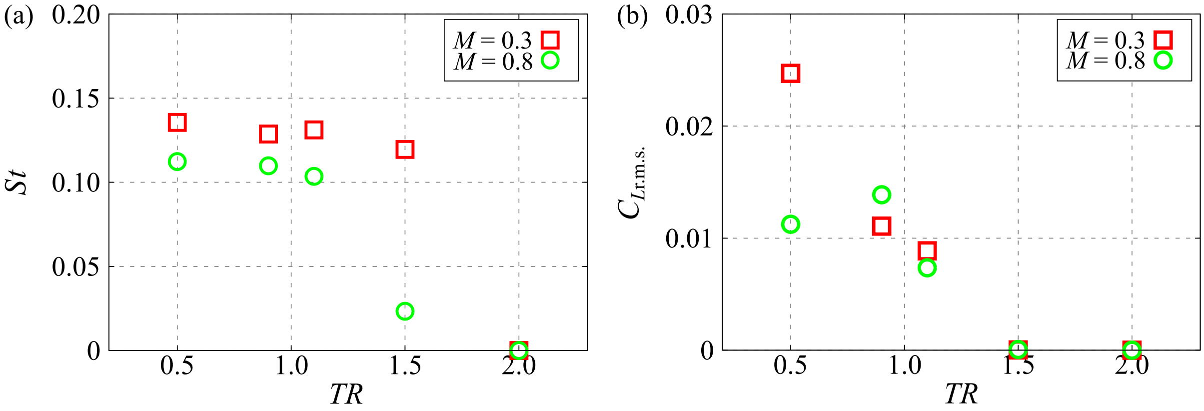

FIGURE 4.10: Effect of TR on the time variation of the lift coefficient at $Re = 300$. (a) St; (b) $C_{L\mathrm{r.m.s.}}$.

Drag Coefficient

Figure 4.11 shows the total, pressure, and viscous drag coefficients at $Re = 300$, respectively. The drag coefficient increases as TR increases, and this trend is also exhibited by the pressure and viscous drag coefficients. However, the pressure drag coefficient does not increase much in supersonic flows because the separation point is on the quite downstream side compared to subsonic cases under the same Re. Conversely, as TR is changed at $M = 0.3$ and 2.0 from 0.9 to 0.5, the viscous drag coefficient increases. Figures 4.12 and 4.13 show the mean-normalized-velocity gradient and the mean-viscosity coefficient on the entire surface of the sphere, respectively. Here, the velocity gradient in figure 4.12 was calculated as a derivative x component in the ζ direction which contributes to the viscous drag coefficient. Figure 4.12 indicates that the velocity gradient decreases as TR increases. Also, the viscosity coefficient increases as TR increases, as shown in figure 4.13. The effect of the change in the viscosity coefficient is more influential than is the change in the velocity gradient at $M = 0.8$ and 1.2;

however, for $M = 0.3$ and 2.0, the effect of the change in the velocity gradient is more influential than is the change in the viscosity coefficient. Therefore, the trends in TR dependence on the viscous drag coefficient are opposite in these cases at TR less than unity.

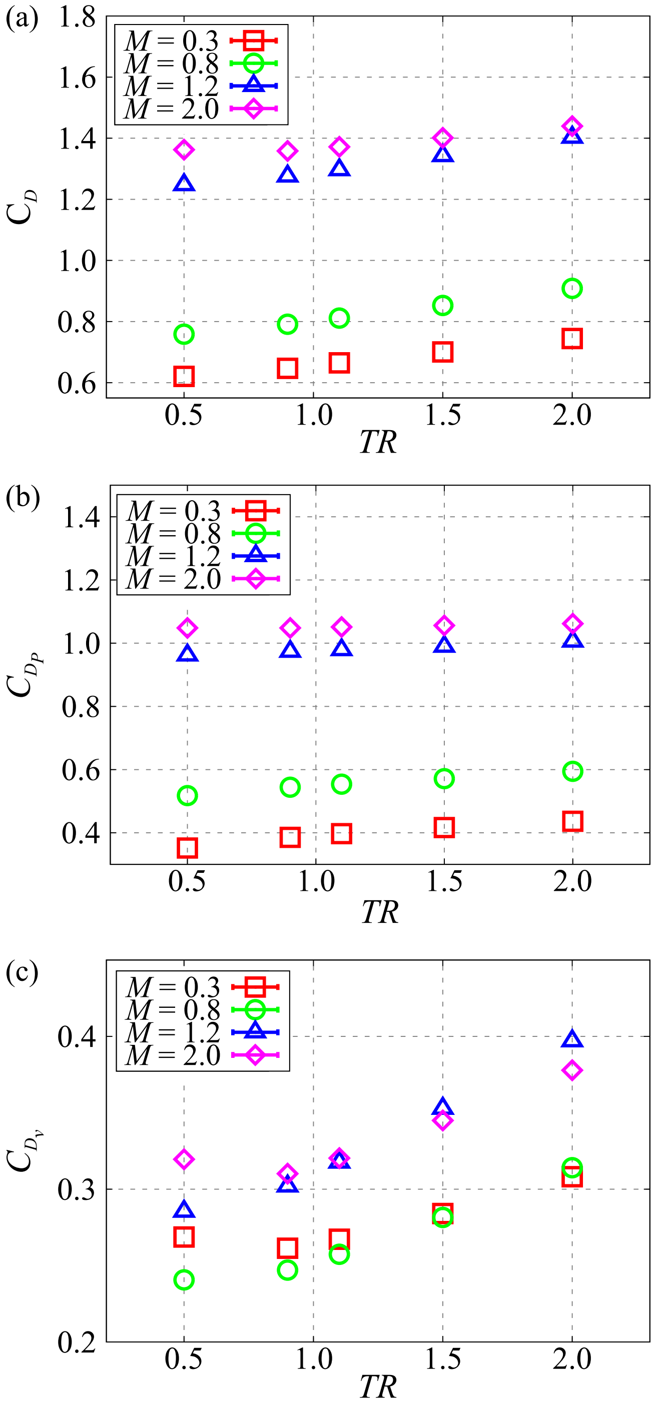

FIGURE 4.11: Effect of TR on the time variation of the lift coefficient at $Re = 300$. (a) Total; (b) pressure component; (c) viscous component.

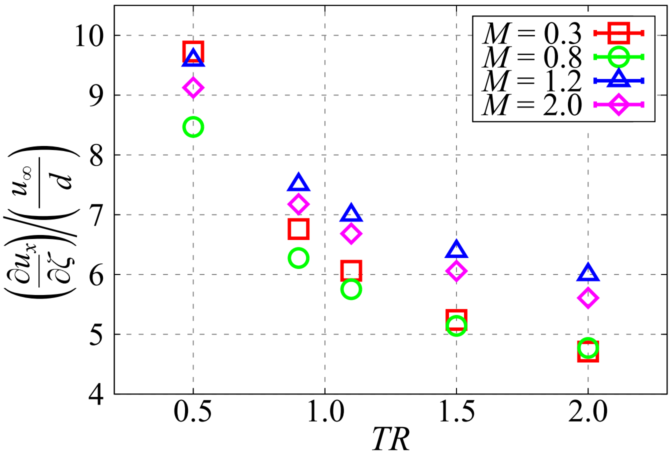

FIGURE 4.12: Mean value of the x component of the normalized velocity gradient on the sphere surface (Re = 300).

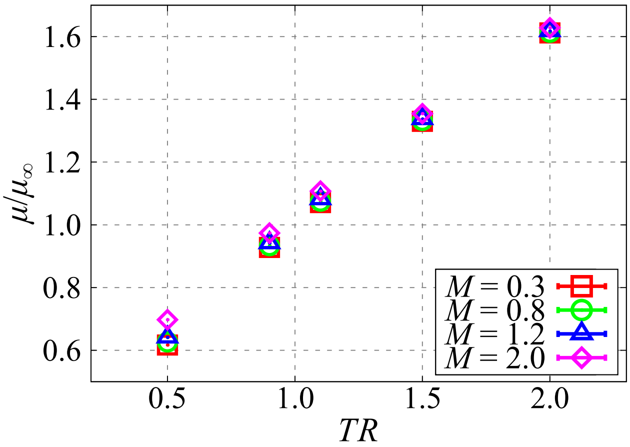

FIGURE 4.13: Mean value of the viscosity coefficient on the sphere surface (Re = 300).

In the present study, the drag coefficient calculated by DNS is compared to the predicted values by three previous drag models proposed by Crowe, 1967; Henderson, 1976; Hermsen, 1979. These relations are valid under the conditions investigated in the present study and include TR in the models. It should be noted that the drag model by Loth, 2008, which is one of the newest models, is not compared herein because the model includes TR in only the formula for the rarefaction-dominated regime. That is because the term including TR is derived from the formula of the free-molecular limit (see Schaaf and Chambre, 2017). Figure 4.14 shows comparisons of the predicted values of the previous relations and the present results. The drag coefficient is influenced by TR; however, the predicted values by the drag model hardly change, except in the Henderson, 1976 model at supersonic flows. These behaviors are likely due to the way in which the previous models were constructed. Under high-M and low-Re conditions, measurement tests of the aerodynamic forces (e.g., wind tunnel tests) are difficult. Therefore, the drag models were constructed by combining the experimental data obtained under limited conditions, theoretical formulas, and empirical corrections. Because the effect considered in each term is clear, we focus on the drag mode of Henderson, 1976 to investigate the characteristics in the following.

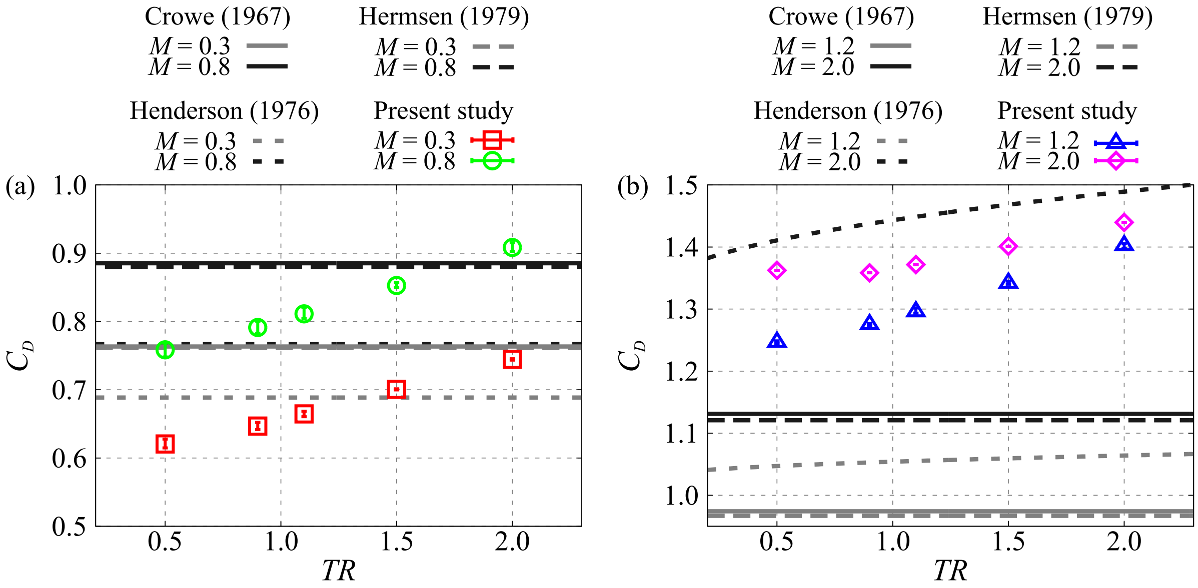

FIGURE 4.14: Comparison with previous drag models at Re = 300. (a) Subsonic condition; (b) supersonic condition.

Figure 4.15 shows the TR dependence of the drag coefficient as predicted by the drag model of Henderson, 1976 at subsonic flows. Figure 4.15 illustrates that the effect of TR on the drag coefficient of $M = 0.3$ and 0.8 clearly appears at Re less than 2.0 and 5.0, respectively. This means that TR effect appears in the Henderson model at slip or more rarefied regime (i.e., $0.1 \geq Kn$). In the Henderson model, TR is included in the first term (see Henderson, 1976), which is simplified to the formula of free-molecular regime ($Kn \geq 1$) that was proposed by Epstein, 1924; Langevin, 1905 at $Re = 0$. In other words, the Henderson model does not have a background for the effect of TR on the drag coefficient in the continuum regime ($Kn \leq 0.01$). This property is the same in the other models. Consequently, a correction to the drag model is necessary for the prediction of the drag coefficient of heated/cooled particles in the continuum regime.

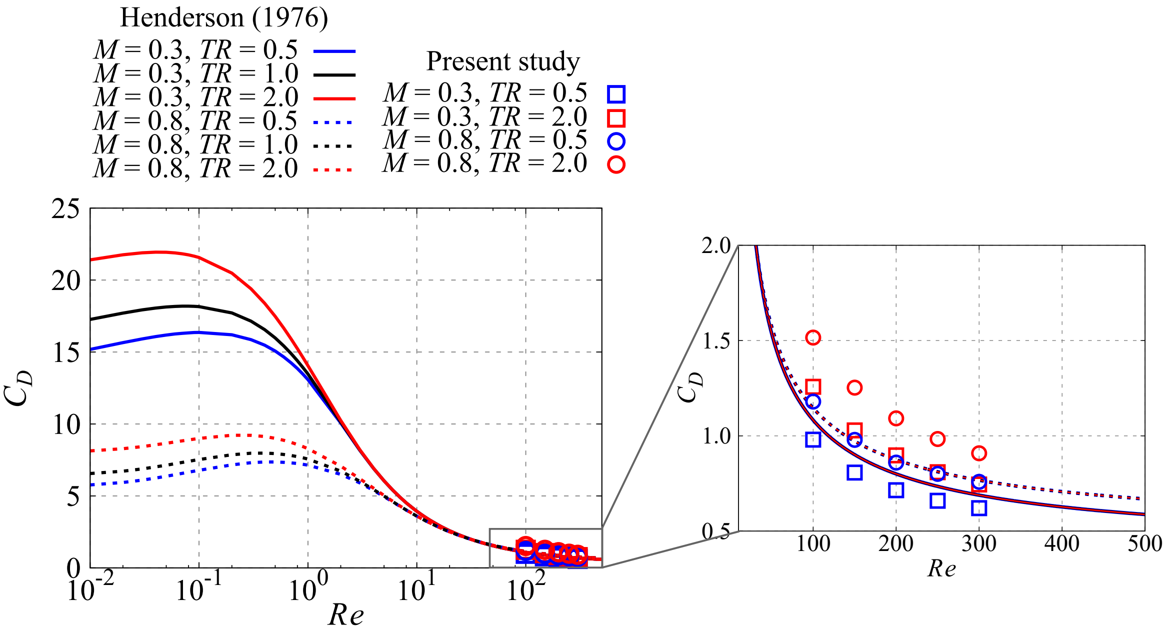

Figure 4.15: Effect of TR and Re on the drag coefficient of Henderson model (subsonic formula).

4.3.4 Characterization of Temperature Effect

Nusselt Number

The Nusselt number Nu is defined as the ratio of convective to conductive heat transfer at the boundary in the fluid:

$$Nu = \frac{hd}{k} \tag{4.2}$$

Here, h, d, and k indicate the heat transfer coefficient, the diameter of the sphere, and the thermal conductivity, respectively. The heat transfer coefficient is as follows based on Newton's law of cooling:

$$h = \frac{Q}{A(T_{\text{surf}} - T_{\infty})} \tag{4.3}$$

where A, Q, T_{surf}, and T_∞ represent the heat transfer surface area, the amount of heat transferred, and the surface and freestream temperatures, respectively. The amount of heat transferred is calculated by integrating the heat flux at each cell. In eq. 4.3, when the temperature difference is small, Nu is strongly affected by a change in the amount of heat transferred. This effect becomes large for aerodynamic heating due to detached shock wave.

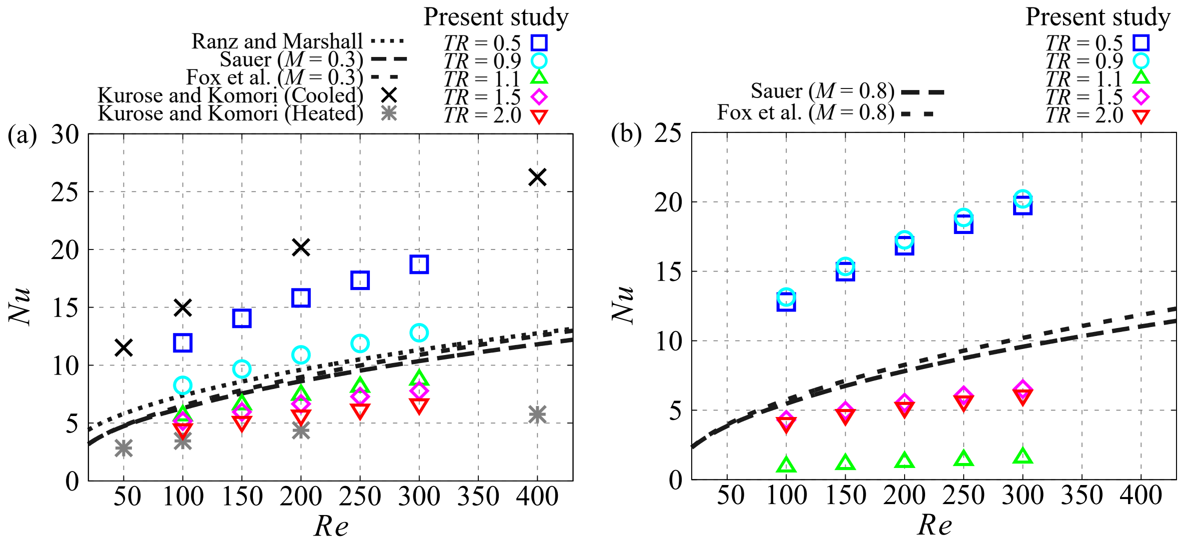

FIGURE 4.16: Comparison with the previous Nusselt number models. (a) $M = 0.3$; (b) $M = 0.8$.

Figure 4.16 show the variations in Nu for $M = 0.3$ and 0.8, respectively. Several Nusselt number models for a sphere have been proposed by Ranz and Marshall, 1952; Sauer, 1951; Fox, Rackett, and Nicholls, 1978; however, few have been proposed that are a function of only the Prandtl number, M, and Re. In figure 4.17(a), the predicted values by the models show good agreement with DNS result $TR \approx 1.0$ for $M = 0.3$; however, the difference increases as TR increases. This reflects the influence of the variation of the kinematic viscosity coefficient in the vicinity of the sphere. For the case of large temperature differences, the state of the fluid around the sphere differs from that of the freestream. Therefore, the differences between the predicted values of the models and the DNS results become large when the temperature difference is large. At low-TR, Nu of the present DNS is larger than that of the predicted values of the previous models. Conversely, under high-TR conditions, Nu of the present DNS is less than that of the predicted values of the previous models. The values of Nu under high- and low-TR conditions are similar to the predicted values of the previous models under lower- and higher-Re conditions.

It is considered that the amounts of forced-convection heat transfer and the heat conduction are due to changes in the kinematic viscosity coefficient. This trend was reported previously by Kurose et al., 2012 for incompressible flows. Furthermore, the aerodynamic heating has an apparent effect on Nu.

Figure 4.17 show the TR dependence of Nu at $Re = 300$. Here, Re in the Fox, Rackett, and Nicholls, 1978 model for supersonic flows should be based on the diameter of the sphere and the shock-behind conditions along the stagnation streamline. In the present study, the Re behind the detached shock was estimated as that of the normal shock, and the shock-behind conditions were calculated using the Rankine–Hugoniot relations. Figure 4.19 illustrates that Nu is changed significantly when TR close to 1.0 at $M = 0.8$ due to the aerodynamic heating. For the heat transfer coefficient calculated using eq. 4.3, the effect of the aerodynamic heating on Nu is large at TR close to 1.0 in high-speed flows because heat due to aerodynamic heating is not considered in eq. 4.3. Also, Nu is negative for $TR = 1.1$ under supersonic conditions. In that case, the heat transfer direction determined by the temperature of the freestream and the surface of the sphere is into the fluid. However, the direction of the heat transfer determined by the temperatures in the vicinity of the sphere and the surface of the sphere is into the sphere. Therefore, Nu becomes negative as the heat transfer coefficient becomes negative, and thus it is necessary to consider TR when estimating Nu because of the aerodynamic heating. Traditional multiphase flow models assume that the fluid is heated by the difference in kinetic energy between the particles and the fluid and that the particles are then heated via the heat transfer. In such models, the heating of the fluid is considered to be the average in each cell. Consequently, the estimated temperature increase is smaller than that estimated from a microscopic perspective. Therefore, it is considered that the heat transfer is larger than that predicted by the previous multiphase flow models. Such an effect was not considered in the previous multiphase flow models, but it was confirmed to be important in this study. Hence, it is necessary to consider the aerodynamic heating in sub-grid-scale models used to analyze supersonic multiphase flows.

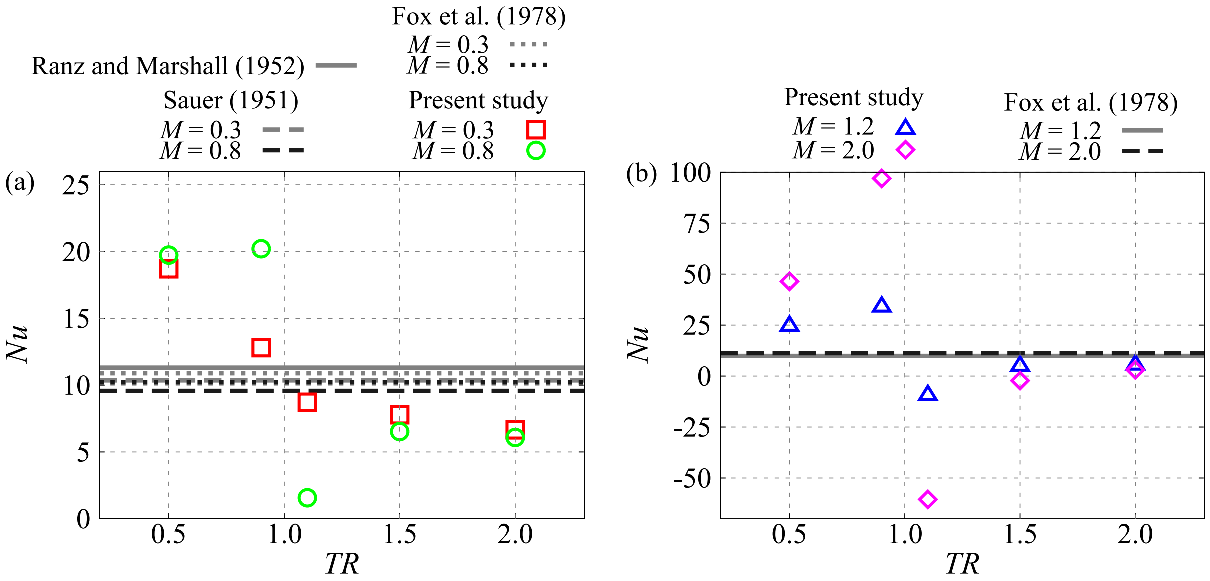

FIGURE 4.17: Effect of TR on Nu at $Re = 300$. (a) Subsonic conditions; (b) supersonic conditions.

Summary of Temperature Effect on Boundary Layer Properties

In the previous sections, we discussed the effect of the temperature on the flow properties, and it is clear that TR affects the flow properties. For the ultimate goal of our study, it is necessary to characterize the effects of TR. Firstly, we postulate that the temperature of the sphere mainly affects the kinematic viscosity coefficient in the vicinity of the sphere because it is a function of temperature. Secondly, the flow properties can be characterized by Re based on the sphere diameter and the freestream quantities for incompressible flows.

Figure 4.18 shows the local Reynolds number Re_{local} based on the local kinematic viscosity coefficient, the freestream velocity, and the diameter of the sphere as a function of the distance from the surface of the sphere. Figure 4.18 illustrates that Re_{local} which is calculated using the local density ρ_{local} and the local viscosity coefficient μ_{local} around the sphere. Here, Re_{local} was averaged around the sphere at the point equidistance from the surface of the sphere in the time-averaged field. Herein, the velocity and length scales are chosen as the freestream velocity and the diameter of the sphere, respectively, because the heat of the sphere does not have a large impact on the characteristic velocity and length scales of the flow over the sphere. The velocity distribution in the boundary layer is influenced by TR, but this seems to be caused mainly by the change in the kinematic viscosity coefficient. Since the kinematic viscosity coefficient decreases, Re_{local} increases as TR decreases.

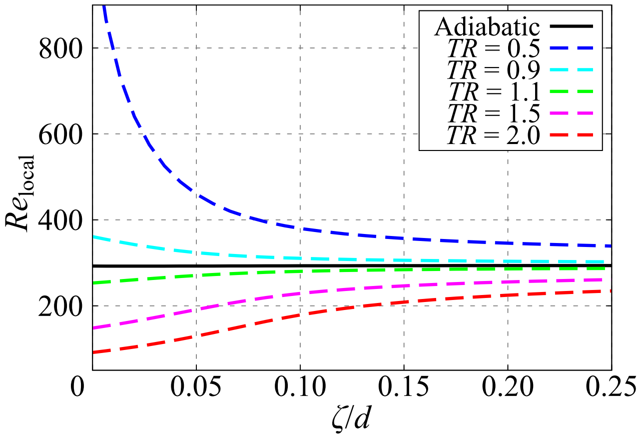

FIGURE 4.18: Profile of averaged Re_{local} in the vicinity of the sphere at $Re = 300$ and $M = 0.3$.

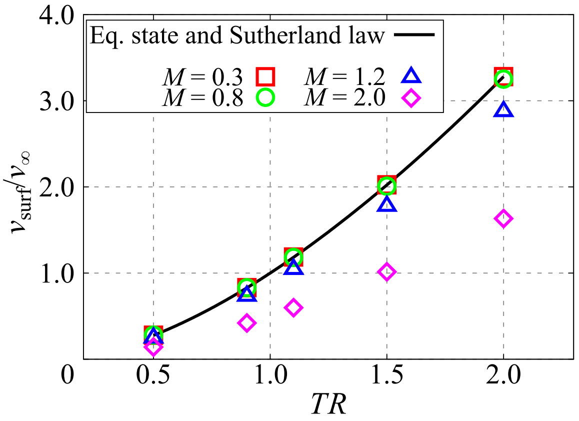

FIGURE 4.19: Effect of TR on the averaged kinematic viscosity coefficient at the sphere surface for $Re = 300$.

However, the kinematic viscosity coefficient around the sphere is influenced not only by TR but also by M as shown in figure 4.19. It is due to the change in the density at the vicinity of the sphere by compressibility effects (figure 4.20). Therefore, the effect of TR cannot be characterized as the function of TR alone. The effect of the temperature appears in the boundary layer, and the separation point is considered to be particularly influenced. Accordingly, we discuss the effective characterization of the various data under isothermal and adiabatic conditions based on the position of the separation point, which is strongly affected by the state of the boundary layer. If this characterization works well for each M condition, the results would imply that the effect of TR could be described by the fluid properties in the vicinity of the sphere. In addition, such a discussion can examine the effect of TR on the flow properties and its Re and M dependencies. In the following section, the data under the adiabatic condition are those of chapter 3.

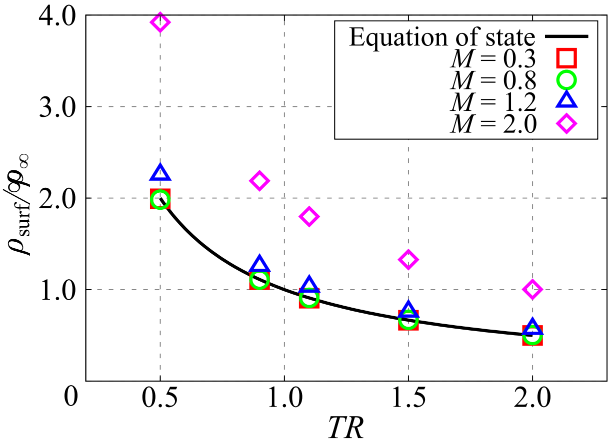

FIGURE 4.20: Effect of TR on the averaged density at the sphere surface for $Re = 300$.

Separating Compressibility and Temperature Effects through an Examination of the Separation Point

In adiabatic cases, the flow properties can be characterized by Re or Re and M in incompressible or compressible flows. However, as discussed in the previous sections, the flow properties are influenced by the temperature of the sphere because of the change in the kinematic viscosity coefficient of the fluid in the vicinity of the sphere due to the temperature difference between the freestream and the surface of the sphere. For example, figure 4.21 shows the relationship between Re and the drag coefficient for adiabatic and isothermal cases. As discussed in chapter 3, the drag coefficient in the compressible flow can be characterized by Re in each M. However, there is also TR dependence in the isothermal conditions, and thus the drag coefficient cannot be characterized by only Re even though the same M. It is considered that the position of the separation point appears to be most sensitive to the influence of the temperature of the sphere surface. Thus, the relationship between the position of the separation point and various flow properties will be discussed in this section.

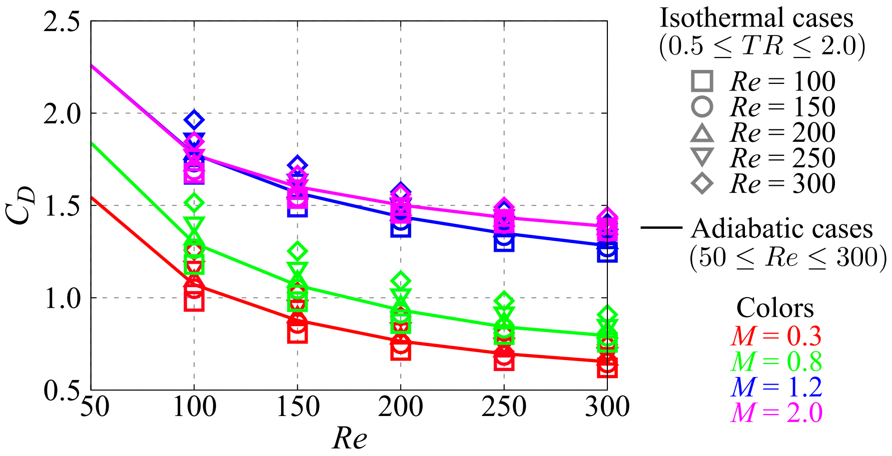

FIGURE 4.21: Relationship between the separation point and the drag coefficient of the isothermal and adiabatic cases.

Figure 4.22 shows the relationship between the separation point and the drag coefficient. In figure 4.22(a), a very clear trend can be seen between the separation point and the drag coefficient under the adiabatic condition in each M condition. This illustrates that the Re dependence of the drag coefficient in each M is linked primarily to the change in the separation point. Conversely, in figure 4.22(b), the M dependence of the drag coefficient is more complex than is the Re dependence. If M changes, several flow properties also change, such as the strength of the shock waves, the separation point, and the size of the recirculation region. The trend of the M effect on the flow properties differently under subsonic and supersonic conditions. In addition, the interaction among these parameters is complicated, particularly in the transonic region. Therefore, the M dependence of the drag coefficient cannot be characterized by the separation point alone. Figure 4.22(c) shows a comparison of the drag coefficient in the adiabatic and isothermal cases. In this figure, the effect of TR on the relationship between the separation point and the drag coefficient is clear under subsonic conditions. However, the TR dependence of the drag coefficient becomes complex as M increases. This effect is due to the aerodynamic heating, but the effect of TR can approximately be characterized by the separation point for each M. In this comparison, the drag coefficient under isothermal conditions agrees with that under adiabatic conditions. In other words, the effect of the temperature difference on the drag coefficient can be characterized by the position of the separation point. It is considered that several flow properties including the drag coefficient can be characterized by the separation point because the position of the separation point reflects the state of the boundary layer.

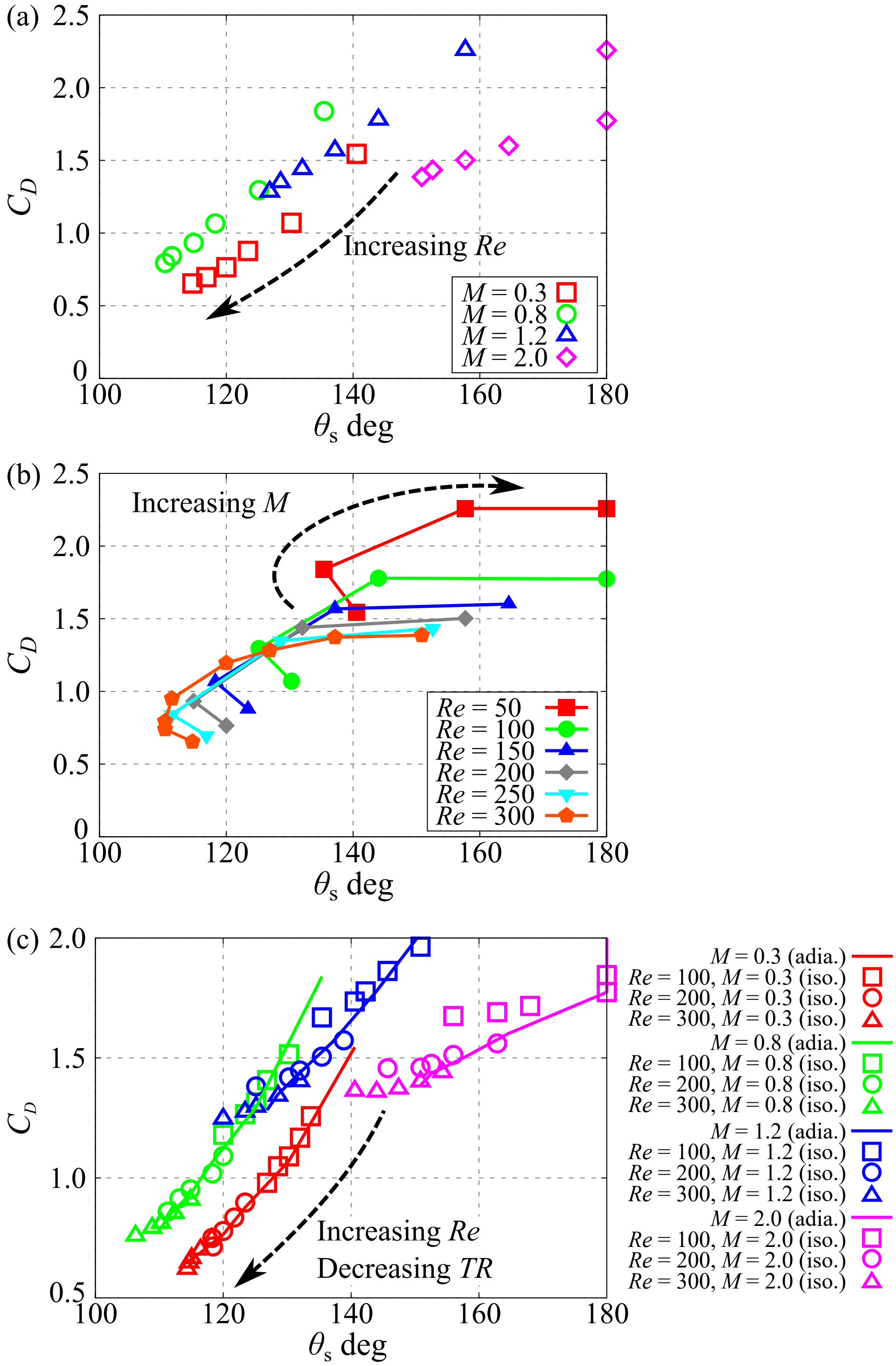

FIGURE 4.22: Relationship between the separation point and drag coefficients. (a) Effect of *Re* (adiabatic case: $50 \leq Re \leq 300$); (b) effect of *M* (adiabatic case: $0.3 \leq M \leq 2.0$); (c) comparison of the adiabatic and isothermal cases.

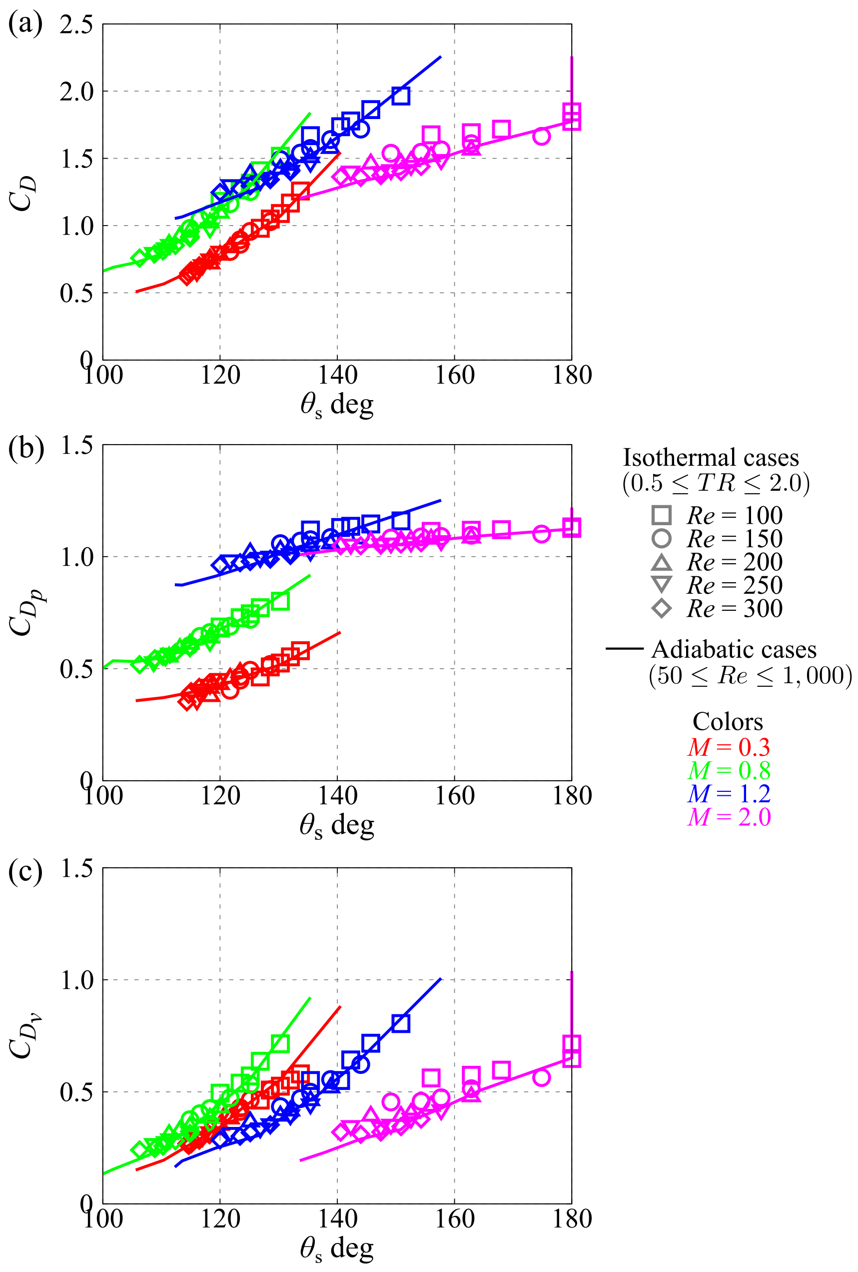

FIGURE 4.23: Relationship between the separation point and (a) total, (b) pressure, and (c) viscous drag coefficients of the isothermal and adiabatic cases.

The clear trend can be seen in the drag coefficient even though plotted separately by component as shown in figure 4.23. This result implies that the position of the separation point reflects the temperature effects on the drag coefficients, including physical meaning. The pressure drag coefficient in this *Re* range at each *M* is dominated by the position of the separation point because it depends on the backpressure related to the size of the recirculation region (see 3 in detail). Figure 4.23 illustrates that the effect of the temperature on the pressure drag coefficient for the isothermal case is the effect of the change in the position of the separation point same as the adiabatic case. In addition, the viscous drag coefficient is determined by the area of the attached flow region and the dynamic viscosity coefficient, and area of the attached flow region is the function of the dynamic viscosity coefficient in this *Re* range. Hence, the viscous drag coefficient in the adiabatic case can be characterized by the position of the separation point. Simultaneously, the change in the viscous drag coefficient due to the temperature effect is driven by the same mechanism with the adiabatic case, and the dynamic viscosity coefficient in the isothermal case depends on the surface temperature of the sphere. Hence, the characterization by the position of the separation point is capable of the evaluation of the temperature effect on the viscous drag coefficient.

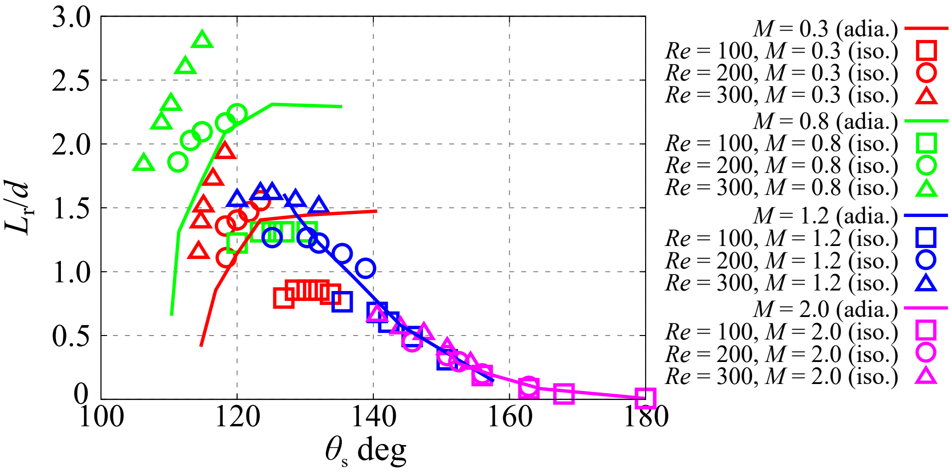

FIGURE 4.24: Relationship between the separation point and the length of recirculation region.

Figures 4.24–4.26 show the relationships between the separation point and the other flow properties, namely the length of the recirculation region, the shock standoff distance, and the type of flow pattern. The lines show the results of the adiabatic cases, while the symbols show the results of the isothermal cases. Figure 4.24 shows the relationship between the separation point and the length of the recirculation region. The TR dependence differs between subsonic and supersonic conditions in the length of the recirculation region. In supersonic flows, the difference between the isothermal and adiabatic cases is not large; however, the difference becomes large as the separation point moves toward the upstream side. Under subsonic conditions, on the other hand, the TR dependence of the length of the recirculation region does not agree with the characterization using the separation point. For the length of the recirculation region, there is the effect of the mixture of the fluids between the freestream and the vicinity of the sphere, and its effect seems to become large at the subsonic regime.

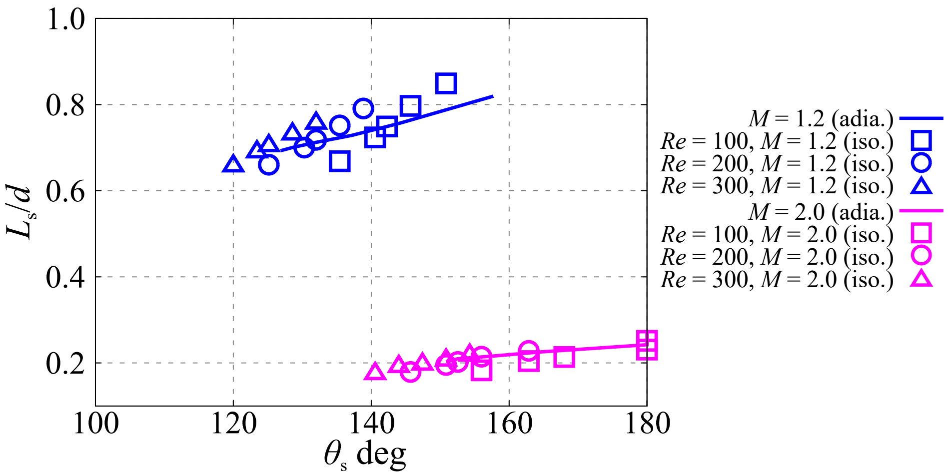

FIGURE 4.25: Relationship between the separation point and the shock standoff distance.

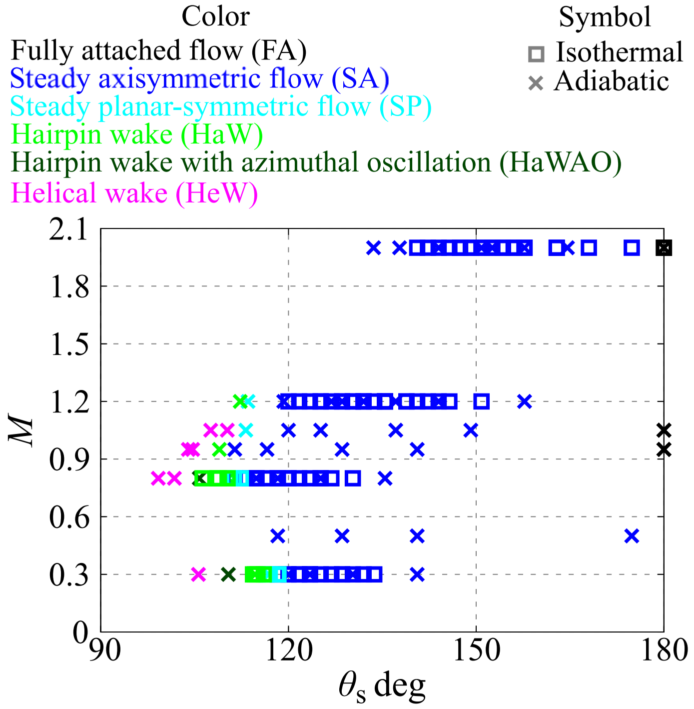

FIGURE 4.26: Distribution of flow regime characterized by M and the position of the separation point.

Figure 4.25 shows the shock standoff distance, which can be characterized by the separation point. Under low-Re conditions, the shock standoff distance is influenced by Re due to the change in the displacement thickness as discussed in chapter 3. Therefore, the TR dependence of the shock standoff distance can be characterized by the position of the separation point, which is associated with the state of the boundary layer.

Figure 4.26 shows the distribution of the type of flow pattern. In subsonic cases, the TR dependence of the type of flow pattern corresponds to the separation point. Also, it can be seen that the type of flow pattern is influenced not only by the separation point but also by M. However, in supersonic conditions, we cannot discuss the applicability of using the separation point to characterize the TR dependence of the type of flow pattern because of a lack of DNS data.

4.3.5 Conclusions

In chapter 4, the compressible low-Re flow over a stationary isothermal sphere was investigated by DNS of the three-dimensional compressible Navier–Stokes equations using a body-fitted grid with high-order schemes. The flow conditions were $100 \leq Re \leq 300$, $0.3 \leq M \leq 2.0$, and $0.5 \leq TR \leq 2.0$. It was clarified that the effect of the temperature difference between the freestream and particles on the flow properties, and the effects of M and Re on the characteristics of the heat transfer between the sphere and fluids.

In the subsonic regime, the unsteady wake of the sphere becomes steady under high-TR conditions, and the separation point moves downstream as TR increases. Conversely, the flowfield becomes unsteady by decreasing TR in a part of the flow conditions which is steady flow in adiabatic condition, and the separation point moves upstream as TR decreases. These trends are caused by a change in the power balance of the inertial and viscous forces that is due to a change in the kinematic viscosity coefficient in the vicinity of the sphere. The length of the recirculation region at the steady flow conditions, the influence of TR is different between the subsonic and supersonic conditions. The length of the recirculation region decreases and increases as TR increases and decreases, respectively. In addition, the detached shock wave moves upstream as the temperature of the sphere increases. It implies that the increase of the displacement thickness at the upstream stagnation point as showed in chapter 3.

The drag coefficient increases as TR increases, an effect that was not considered in previous drag models despite those models include the terms of TR. The included terms for TR in the previous drag model are based on the terms for the rarefied regime, and thus the effect of TR does not consider in the continuum regime. Hence, it is required that the construction of the terms to consider the effects of TR on the drag coefficient at the continuum regime. Also, there are large differences in the predicted Nusselt number by the previous Nusselt number model and obtained by the present computation, particularly at high-M flows or with large temperature differences. It seems that the decrease in the accuracy of the previous Nusselt number model is due to the change in the flow characteristics caused by the change in the kinematic viscosity coefficient in the vicinity of the sphere and the aerodynamic heating due to the detached shock wave. The conversion from the momentum energy to thermal energy, which is calculated using the drag and Nusselt number models, is very important in supersonic multiphase flow analyses that use the multiphase flow model. Therefore, further investigations and the construction of a new relation or correction to the previous relations are necessary to construct a highly accurate model for supersonic multiphase flows.

The temperature difference between the surface of the sphere and the freestream changes the flow properties, and the influences are due to the change in the kinematic viscosity in the vicinity of the sphere. In addition, the compressibility effects also have a large impact on the kinematic viscosity coefficient so that there is the interaction between the effects of TR and M. However, the effects of TR on the drag coefficient, the length of the recirculation region, the shock standoff distance, and the flow pattern can be characterized by the position of the separation point. It is because the change in the kinematic viscosity in the boundary layer has a significant effect on the flow separation, and the separation point reflects the local Re in the boundary layer.

Chapter 5

Effect of Sphere Rotation and Background Shear

List of Symbols

C_D = Drag coefficient
C_{D_P} = Pressure drag coefficient
C_{D_v} = Viscous drag coefficient
C_L = Lift coefficient
C_{MY} = Moment coefficient around y-axis
C_P = Pressure coefficient
Kn = Knudsen number
M = Mach number
Q = Q-criterion
Re = Reynolds number
St = Strouhal number
U_{theta} = Velocity along the equator of sphere
d = Diameter of the sphere
r = Radius of sphere
u, v, w = Velocity in x, y, and z directions
u_{b} = Flow velocity of uniform component
u_{s} = Flow velocity of shear component
x, y, z = Cartesian coordinates
α = Normalized shear rate
ϕ = Angle from y-axis of upstream
μ = Dynamic viscosity coefficient
Ω = Angular velocity
Ω = Normalized angular velocity
θ = Angle from x-axis of upstream
θ_{s} = Separation point
ρ = Density
ξ, η, ζ = Curvilinear coordinates
Subscripts

incomp. = Incompressible flow

r.m.s. = Root-mean-square

surf = Surface of sphere

∞ = Freestream

5.1 Introduction

A lift force acting on particles plays a major role on the particle motion following drag force, in the particle-laden flow, and thus the prediction of the lift force is important for modeling of the particle behavior in the particle-laden flow. The lift force can be divided into a rotation-induced lift and shear-induced lift. The rotation-induced lift is the lift force due to the rotation of particles, and the shear-induced lift is the lift force due to a velocity gradient of background flows.

Rotation-Induced Lift Rubinow and Keller, 1961 derived the lift coefficient, C_L, of a transversely rotating sphere in the Stokes regime at a low rotation rate ($Re = \rho u_\infty/\mu_\infty \leq 0.1$ and $\Omega^* = \Omega d/2u_\infty \leq 0.1$). Here, Re and Ω^* are the Reynolds number and the rotation rate based on the diameter of the sphere d, the freestream velocity u_∞, the freestream density ρ_∞, the freestream viscosity coefficient μ_∞, and the angular velocity Ω. Their results showed that the lift coefficient is expressed as $C_L = 2\Omega^*$ in the Stokes regime. Also, Rubinow and Keller, 1961 found that the drag coefficient in the Stokes regime under the low-Ω^* condition is not a function of Ω^*, and its value is equal to a stationary sphere Stokes drag. In the range $Re > 1$, an empirical C_L model for a rotating sphere at $Re \leq 120$ is derived by force measurement experiments in the uniform flow by Tri, Oesterle, and Deneu, 1990; Tanaka, Yamagata, and Tsuji, 1990.

Numerical simulations have also been used for the investigation of the flow properties of transversely rotating spheres. Kurose and Komori, 1999 examined the drag and lift coefficients of a rotating sphere at $1 \leq Re \leq 500$ and $0 \leq \Omega^* \leq 0.25$ using DNS (they also examined the effects of a linear shear by DNS and experiments). They provided the aerodynamic forces, flow structures, and variation frequency of the lift coefficient. Their result shows that the lift coefficient at $Re = 1$ is only half of that theoretically determined by Rubinow and Keller, 1961. The lift coefficient at $Re > 1$ provided by Niazmand and Renksizbulut, 2003 is also only half of the theoretical value by Rubinow and Keller, 1961. Moreover, You, Qi, and Xu, 2003 examined this problem at $0.5 \leq Re \leq 68.4$ and $0 \leq \Omega^* \leq 5$. In contrast to Kurose and Komori, 1999; Niazmand and Renksizbulut, 2003, the lift coefficient obtained by You, Qi, and Xu, 2003 at $Re < 1$ shows good agreement with the theoretical value obtained by Rubinow and Keller, 1961, and the lift coefficient decreases as Re increases for $Re > 100$. Giacobello, Ooi, and Balachandar, 2009 and Poon et al., 2014 comprehensively provided the flow properties over a wide range of Re and Ω^*: $100 \leq Re \leq 300$ and $0 \leq \Omega^* \leq 1.0$ and $500 \leq Re \leq 1,000$ and $0 \leq \Omega^* \leq 1.2$, respectively. Their results show that the unsteady vortex shedding is suppressed at medium Ω^* at $Re = 300$, and Kelvin–Helmholtz type instability of the shear layer appears at high-Ω^*. Also, at high-Re, the vortex structures become more complex compared with those up to $Re = 300$. Dobson, Ooi, and Poon, 2014 provided the flow properties at further high-Ω^* conditions at $1.25 \leq \Omega^*$ and $100 \leq Re \leq 300$.

On the other hand, there are few cases on the study of the Robins–Magnus lift force in compressible flows. Teymourtash and Salimipour, 2017 examined the flow around a rotating cylinder under the subsonic conditions. Their results show that the compressibility effects appear in the lift coefficient and the flow structure behind the cylinder. Volkov, 2011 studied the three-dimensional transitional flow of a rarefied monotonic gas over a spinning sphere using the direct simulation Monte Carlo (DSMC) at $0.03 \leq M \leq 2$ and $0.01 \leq Kn \leq 20$. They found that the direction and magnitude of the transverse Magnus effect in rarefied flow depends upon Kn and M. Also, the torque is a function of M and Ω^*. However, the flow properties of a transversely rotating sphere in compressible and low-Re continuum flow have not been studied even though the Robins–Magnus lift force has a large impact on the particle-laden flow. Therefore, the examination of the Robins—Magnus lift force in the compressible flow is necessary for modeling the compressible particle-laden flow such as the exhaust gas of the rocket engine.

Shear-Induced Lift Interest in the motion of small particles in the flow that has velocity gradient has been stimulated, particularly in the Poiseuille flow (Poiseuille, 1836). In the case of blood, for example, blood corpuscles in the capillaries tend to keep away from the vessel wall. Although Goldsmith and Mason, 1962 has pointed out that the deformation of non-rigid particles will produce a lift force, and Bretherton, 1962 has shown that rigid particles of an extreme shape may produce a lift force. In addition, Segré and Silberberg, 1962 has demonstrated that the neutrally buoyant sphere of various sizes in the Poiseuille flow through a tube slowly migrate laterally to a position distant 0.6 tube radius from the axis. Their result demonstrated the existence of a lateral force on a rigid spherical particle in the shear flow.

Saffman, 1965 firstly derived the shear-induced lift force in the Stokes regime based on the Ossen-type approximation. It should be noted that the fact that using Ossen-type approximation implies the importance of the inertia force on the shear-induced lift. Dandy and Dwyer, 1990 conducted DNS of the linear shear flow over a sphere at $0.1 \leq Re \leq 100$. The results indicate that the coefficient of the shear-induced lift is approximately constant at a fixed shear rate over a wide range of intermediate Re, and the drag coefficient is also approximately constant when normalized by the sphere drag in uniform flow. The equation by Saffman, 1965 including an assumption, the shear velocity is large. McLaughlin, 1991 extend the theoretical expression by Saffman, 1965 and he proposed a more general expression, which valid in conditions of small shear velocities. By summarizing these studies, Mei, 1992 proposed a lift model for a stationary isolated sphere in a linear shear flow at $Re \leq 100$. Based on the knowledge provided by these studies, the direction of the lift force due to linear shear flow acting on a stationary isolated sphere is from the low-speed side to the high-speed side. Kurose and Komori, 1999 investigated the linear shear flow over a sphere by numerical simulation of the three-dimensional incompressible Navier–Stokes equations at $0.5 \leq Re \leq 500$ and $0 \leq \alpha^* \leq 0.4$. Here, $\alpha^* = r/u_\mathrm{b} \cdot \mathrm{d}u/\mathrm{d}z$ indicates the nondimensional shear rate normalized by the radius of the sphere r and the velocity of the base flow u_b. They investigated a linear shear flow over a sphere and they clarified that the direction of the lift force due to shear flow becomes opposite, which means from high-speed side to low-speed side, at $Re \approx 60$. This fact has also been confirmed by the experiment conducted by them. The result of DNS illustrated that the reverse of the shear-induced lift is caused by the asymmetry of the recirculation region form in the downstream of the sphere. In chapter 3, we discussed the effect of M on the recirculation region of the sphere in the uniform flow, and the recirculation region is significantly stabilized by increasing M, particularly at the supersonic condition. Combining with the result at the incompressible study by Kurose and Komori, 1999, therefore, it is considered that the strength and the direction of the shear-induced lift appear to be strongly influenced by M.

In the present chapter, the uniform flow over a transversely rotating sphere and the linear shear flow over a stationary sphere are independently investigated by DNS of the three-dimensional compressible Navier–Stokes equations. In the rotating case, an isolated rigid sphere transversely rotates up to $\Omega^* = 1.0$ under conditions at $100 \leq Re \leq 300$ and $0.2 \leq M \leq 2.0$, and an stationary isolated rigid sphere is placed in the linear shear flow of $100 \leq Re \leq 300$, $0.3 \leq M \leq 1.5$, and $\alpha = 0.1$. The effect of M upon the flowfield and aerodynamic force coefficients are investigated by comparing it with the previous incompressible studies.

5.2 Computational Setup

5.2.1 Flow Conditions for Rotating Case

Flow conditions that simulated in the study for the rotating case are shown in table 5.1. In this study, the freestream Re based on the quantities at far-field and the diameter of the sphere was set between 100 and 300, the freestream M was set to be between 0.2 and 2.0 and Ω^* defined by the ratio of the freestream velocity and the surface velocity above the equator was set to be between 0 and 1.0. Also, the resolution of the computational grid was retained in the downstream region of the sphere for the diameter of $4d$. Result of the grid convergence study is shown in appendix A.2.3.

5.2.2 Flow Conditions for Linear Shear Flow Case

Flow conditions that simulated in the study for the liner-shear case are shown in table 5.2. In this study, the freestream Re based on the quantities at the far-field and the diameter of the sphere was set to be 50, 100, and 300, the freestream M was set to be between 0.3 and 1.5, and the normalized shear rate α^* which is normalized by the freestream velocity and the radius of the sphere was set to be 0.1.

			M			
		0.2	0.3	0.8	1.2	2.0
Ω^*	0.0	$Re = 300$	$Re = 250$ $Re = 300$	$Re = 250$ $Re = 300$	$Re = 300$	$Re = 300$
	0.2	$Re = 300$	$Re = 250$ $Re = 300$	$Re = 250$ $Re = 300$		
	0.3	$Re = 300$	$Re = 100$ $Re = 200$ $Re = 250$ $Re = 300$	$Re = 100$ $Re = 200$ $Re = 250$ $Re = 300$	$Re = 100$ $Re = 200$ $Re = 250$ $Re = 300$	$Re = 100$ $Re = 200$ $Re = 250$ $Re = 300$
	0.6	$Re = 300$	$Re = 100$ $Re = 200$ $Re = 250$ $Re = 300$	$Re = 100$ $Re = 200$ $Re = 250$ $Re = 300$	$Re = 100$ $Re = 200$ $Re = 250$ $Re = 300$	$Re = 100$ $Re = 200$ $Re = 250$ $Re = 300$
	0.8	$Re = 300$	$Re = 250$ $Re = 300$	$Re = 250$ $Re = 300$		
	1.0	$Re = 300$	$Re = 100$ $Re = 200$ $Re = 250$ $Re = 300$	$Re = 100$ $Re = 200$ $Re = 250$ $Re = 300$	$Re = 100$ $Re = 200$ $Re = 250$ $Re = 300$	$Re = 100$ $Re = 200$ $Re = 250$ $Re = 300$
	2.0, 3.0				$Re = 300$	$Re = 300$

TABLE 5.1: Flow conditions for rotating case.

	$M = 0.3$	$M = 0.8$	$M = 0.95$	$M = 1.05$	$M = 1.2$	$M = 1.5$
$Re = 50$	$\alpha^* = 0.1$	$\alpha^* = 0.1$	$\alpha^* = 0.1$	$\alpha^* = 0.1$	$\alpha^* = 0.1$	$\alpha^* = 0.1$
$Re = 100$	$\alpha^* = 0.1$	$\alpha^* = 0.1$	$\alpha^* = 0.1$	$\alpha^* = 0.1$	$\alpha^* = 0.1$	$\alpha^* = 0.1$
$Re = 300$	$\alpha^* = 0.1$	$\alpha^* = 0.1$	$\alpha^* = 0.1$	$\alpha^* = 0.1$	$\alpha^* = 0.1$	$\alpha^* = 0.1$

TABLE 5.2: Flow conditions for linear shear flow case.

5.2.3 Boundary Conditions for Rotating Case

The boundary condition at the surface of the sphere is adiabatic; also, the velocity on the surface is given as follows to simulate a rotating sphere:

$$u_{\mathrm{surf}} = \Omega^* u_\infty \frac{2z}{d}, v_{\mathrm{surf}} = 0, w_{\mathrm{surf}} = -\Omega^* u_\infty \frac{2x}{d}, \tag{5.1}$$

where u_{surf}, v_{surf} and w_{surf} are the x, y and z components of surface velocity, respectively, and x and z are the position vectors of the x and z components. In this study, the axis of rotation was y direction. Also, the position and velocity coordinates in the polar coordinate along the equator of the sphere is defined in $x - z$ plane at $y = 0$, as shown in figure 5.1. Here, θ and U_θ denote the angle from the x-axis of upstream and the velocity along the equator of the sphere, respectively. The density at the surface was calculated at the extrapolated value from the one point inside the boundary, the pressure was calculated from the momentum normal to the surface. At the boundaries in the ξ and η directions, the periodic boundary condition on the six overlapped grid points was imposed. The inflow and outflow boundary conditions were imposed at the outer boundary where the flow goes inside and outside at one point inside the boundary, respectively. All flow variables were fixed to their freestream values at the inflow boundaries. All the variables were extrapolated from one point inside of the boundary at the supersonic outflow boundaries. The density and the velocities were similarly extrapolated and the pressure was fixed to its freestream values in the subsonic outflow condition. All the variables on the singular point on the x-axis were set to be an average of the nearest surrounding nodes.

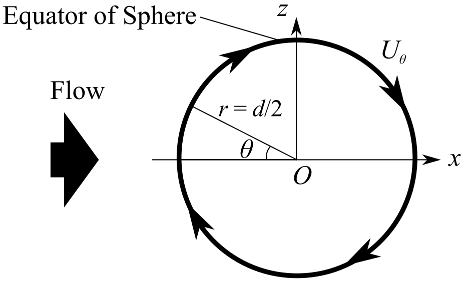

FIGURE 5.1: Velocity and position coordinates along the equator of the sphere.

5.2.4 Boundary Conditions for Linear Shear Flow Case

To enforce the linear shear flowfield in the mainstream, numerical approaches of the sponge layer proposed by Mani, 2012; Freund, 1997 were employed for the boundary conditions of the zone 1. The density, the velocity, and the pressure were gradually enforced into the mainstream values from the 10 points inside of the outer boundaries. Here, the velocity in the streamwise direction was calculated as follows, and the velocity in the streamwise distribution is linear shear flow as shown in figure 5.2.

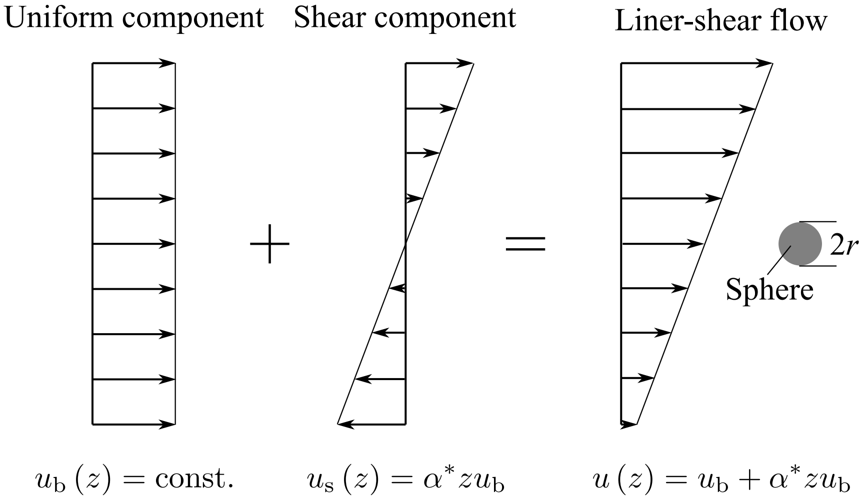

FIGURE 5.2: Velocity distribution of the linear shear flow.

$$u(z) = u_\mathrm{b} + \alpha^* z u_\mathrm{b} \tag{5.2}$$

where

$$\alpha^* = \frac{r}{u_\mathrm{b}} \frac{\mathrm{d}u}{\mathrm{d}z} \tag{5.3}$$

In zone 2, the boundary on the sphere surface was no-slip and adiabatic conditions. At the surface of the sphere, the velocity was fixed to zero, the density was extrapolated from the one point inside the boundary, the pressure was calculated from the momentum normal to the surface. At the boundaries in the ξ and η directions, the periodic boundary condition on the six overlapped grid points was imposed. All the variables on the singular point on the x-axis were set to be an average of the nearest surrounding nodes. All the variables on the grid point at outer boundaries of the zone 2 were determinant by the interpolation from the zone 1.

5.3 Results and Discussion for Rotating Case

5.3.1 Far-Field Flow Properties

Under incompressible flows for $Re \leq 300$, wake structures are classified into four types Giacobello, Ooi, and Balachandar, 2009, namely the steady wake, the steady double-threaded wake, the hairpin wake and the one-sided Ω-shaped wake. The flow patterns are changed along with Re and Ω^*. For the low-Re and low-Ω^* conditions, the flow pattern is the steady wake (e.g., $Re = 100$ and $\Omega^* = 0$). As Re or Ω^* increases, the flow pattern transitions to the steady double-threaded wake (e.g., $Re = 100$ and $\Omega^* = 0.3$). In this flow pattern, the two streamwise vortices are generated around the rotation axis of the sphere. For $Re \geq 250$, the hairpin wake appears. In this flow pattern, the hairpin vortices are periodically generated from the recirculation region behind the sphere (e.g., $Re = 250$ and $\Omega^* = 0.3$ and $Re = 300$ and $\Omega^* = 0.3$). As Ω^* further increases, the vortex shedding is reduced, and the flow pattern transitions back to the steady double-threaded wake (e.g., $Re = 300$ and $\Omega^* = 0.6$). For $Re = 300$ and $\Omega^* = 0.8$ and 1.0, the flow pattern transitions to the one-sided Ω-shaped wake. In this flow pattern, the Ω-shaped vortices are generated at the downstream of the sphere. Figures 5.3–5.6 visualize the wake structures according to the isosurface of the second invariant value of a velocity gradient tensor (Q-criterion). Here, the Q-criterion is calculated by the definition in the incompressible flows in order to visualize except shock waves region, and it is normalized by the freestream velocity. The Q-criterion threshold was set at $Q/u_{\infty^2} = 5.0 \times 1.0^{-4}$. For these figures, the wake structure is influenced not only by Re and Ω^*, but also by M. Also, a map of flow pattern type is shown in figure 5.7.

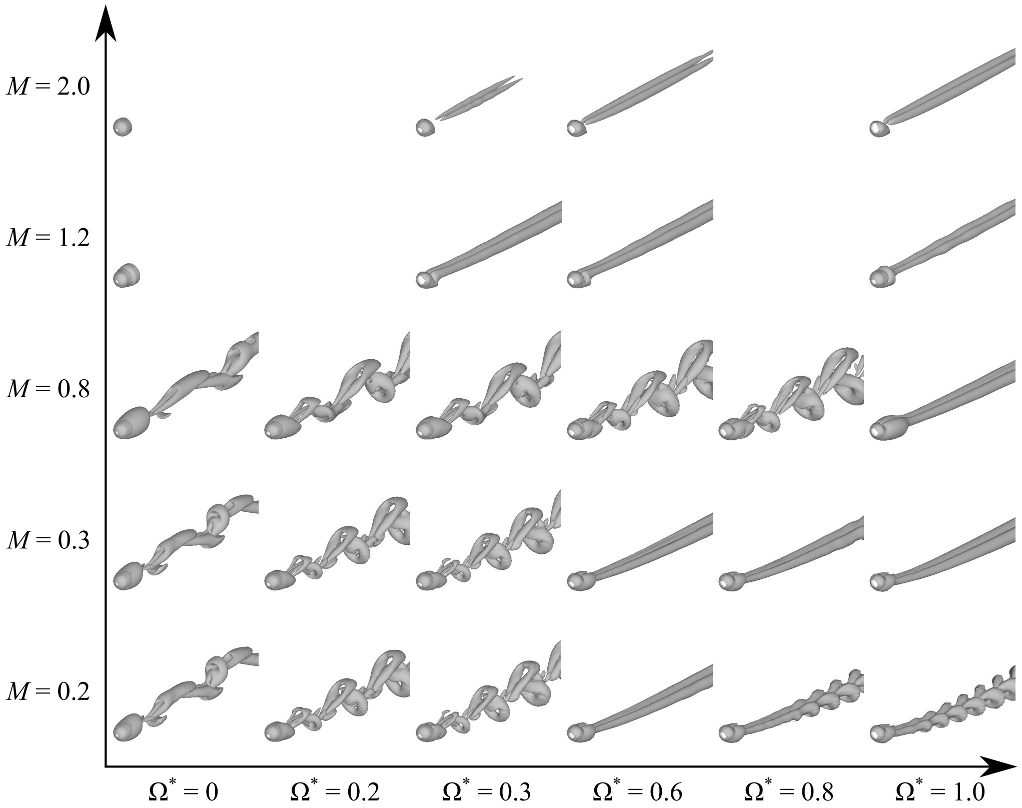

FIGURE 5.3: Isosurfaces of the second invariant value of a velocity gradient tensor ($Q/u_\infty^2 = 5.0 \times 1.0^{-4}$) at $Re = 300$.

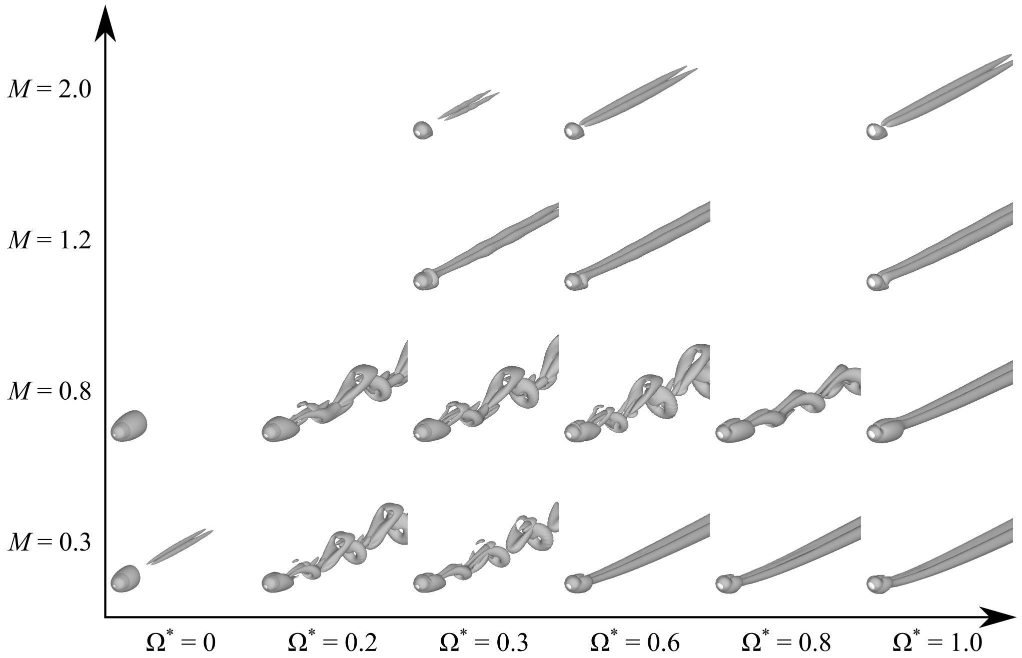

FIGURE 5.4: Isosurfaces of the second invariant value of a velocity gradient tensor ($Q/u_\infty^2 = 5.0 \times 1.0^{-4}$) at $Re = 250$.

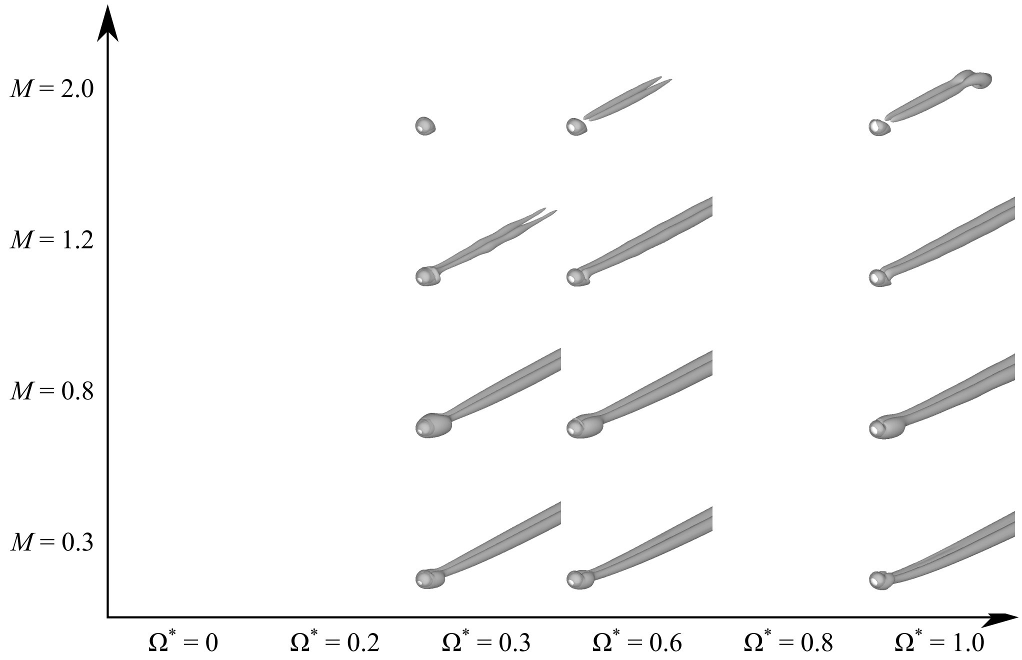

FIGURE 5.5: Isosurfaces of the second invariant value of a velocity gradient tensor ($Q/u_\infty^2 = 5.0 \times 1.0^{-4}$) at $Re = 200$.

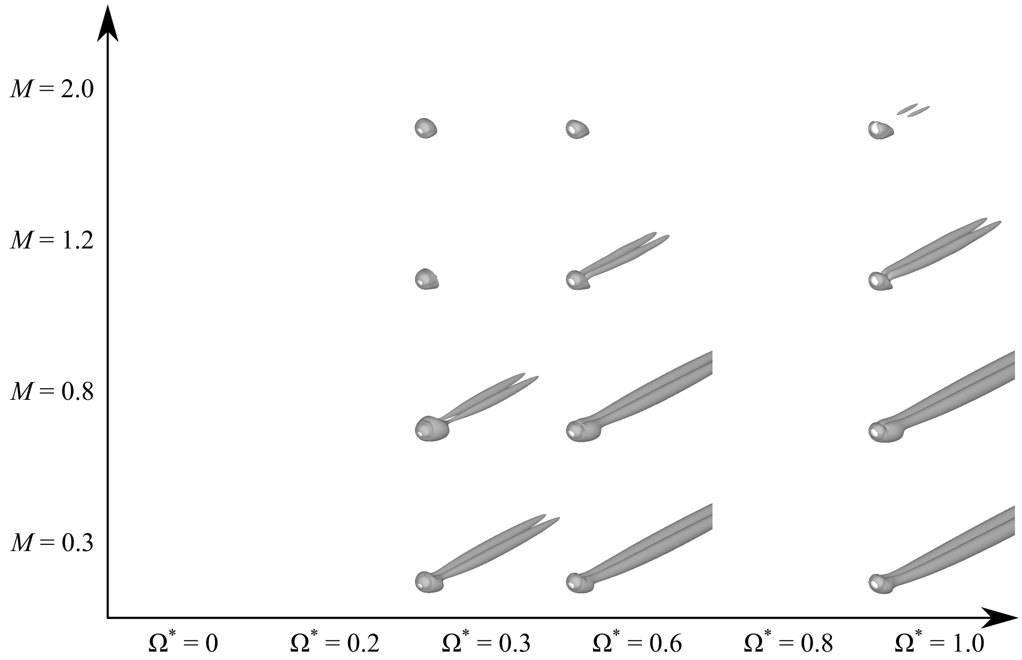

FIGURE 5.6: Isosurfaces of the second invariant value of a velocity gradient tensor ($Q/u_\infty^2 = 5.0 \times 1.0^{-4}$) at $Re = 100$.

At $Re = 300$ and $M = 0.2$, the types of flow pattern shows a trend similar to that for incompressible flows. In the case of the one-sided Ω-shaped wake, the Ω-shaped vortices form at downstream of the sphere, and their generation position approaches the sphere as Ω^* increases. The flow pattern clearly transitions from the low-mode to high-mode in the order of the steady flow, the steady double-threaded wake, the hairpin wake, the steady double-threaded wake and the one-sided Ω-shaped wake as Re and Ω^* increase for each M. For $Re = 300$ and $M = 0.3$, the type of flow pattern is similar to that of the incompressible flow for $\Omega^* \leq 0.6$. However, the flow pattern does not transition to the one-sided Ω-shaped wake for $\Omega^* \leq 0.8$. This is thought to be caused by the compressibility effect due to rotation. For the high-Ω^* cases, the fluid velocity at the retreating side ($y < 0$) and the relative velocity between the freestream and the surface of the sphere at the advancing side ($y > 0$) is larger than in stationary cases. Hence, the compressibility effect appears in rotating cases, even in low-M flows. Also, for $Re = 300$ and $M = 0.8$, the hairpin wake appears for $\Omega^* \leq 0.8$, and transitions to the steady double-threaded wake for $\Omega = 1.0$. From this result, we believe that the transition of the wake structure to the high mode is suppressed by the compressibility effects. This trend has already been reported on the study of the flow past a rotating cylinder under compressible low-Re flows ($40 \leq Re \leq 200$, $0.05 \leq M \leq 0.4$ and $0 \leq \Omega^* \leq 12$) by Teymourtash and Salimipour, 2017.

For $Re = 300$ and $M = 1.2$ and 2.0 in all cases calculated in this study, only the steady wake or steady double-threaded wake appears. In other words, no periodic vortex shedding occurs under the supersonic conditions despite $Re = 300$. It seems that the flow pattern mode is significantly lower than that in the incompressible or subsonic cases due to the strong compressibility effects as discussed in chapter 3. Also, the mode of the flow pattern for $M = 2.0$ is lower than that of $M = 1.2$ for the same Re. This trend is similar in the case for $Re \leq 250$ as shown in figures 5.3-5.7.

Figure 5.8 shows the distribution of volume-averaged turbulent kinetic energy (TKE) normalized by the freestream kinetic energy in the wake. The TKE is calculated in the high-resolution region ($0.5 \leq x \leq 15$ and $\sqrt{y^2 + z^2} \leq 4.0$) by following formula:

$$\overline{\mathbf{u}'} = \sqrt{\left|\mathbf{u}^2 - \overline{\mathbf{u}}^2\right|} \tag{5.4}$$

$$\mathrm{TKE} = \frac{1}{2}\frac{\overline{u'}^2 + \overline{v'}^2 + \overline{w'}^2}{u_\infty} \tag{5.5}$$

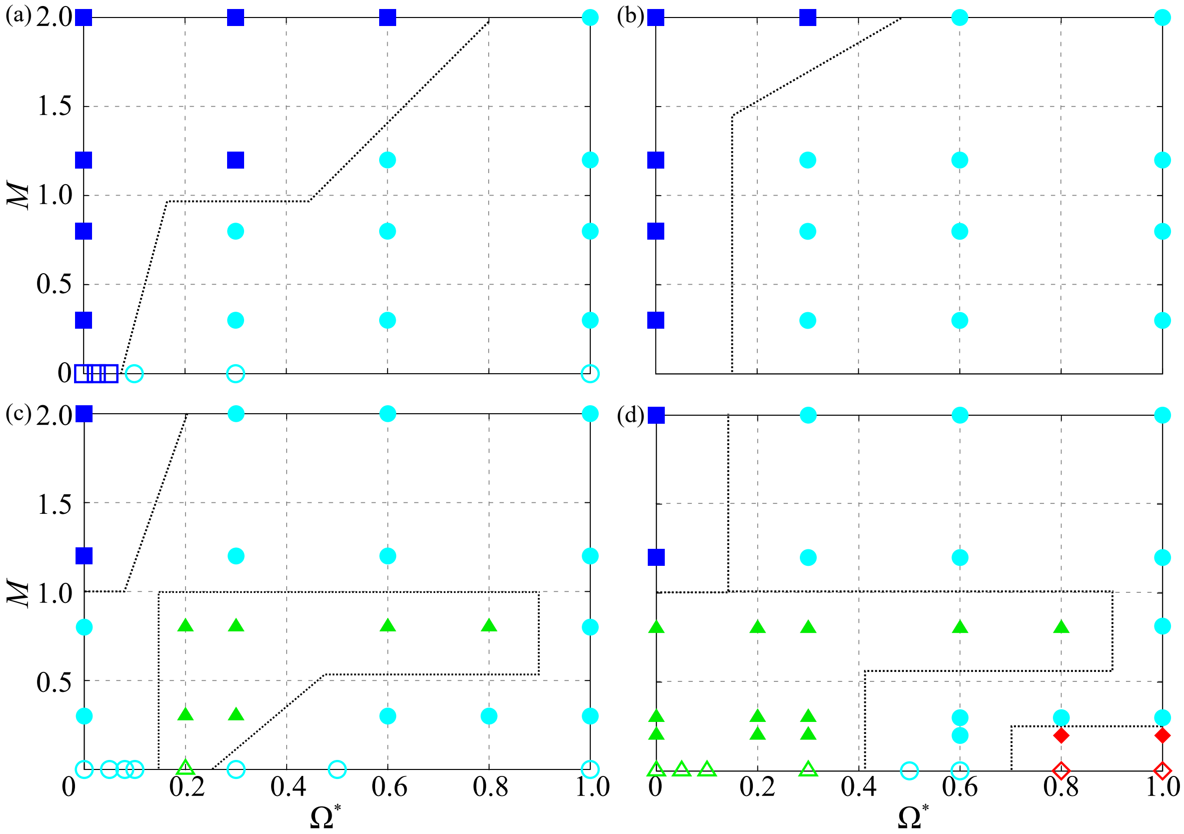

FIGURE 5.7: Map of flow regime: (a) Re = 100; (b) Re = 200; (c) Re = 250; (d) Re = 300. Giacobello, Ooi, and Balachandar, 2009 (open symbol); present study (closed symbol). Steady-axisymmetric wake (square); steady double-threaded wake (circle); hairpin wake (triangle); one-sided Ω-shaped wake (diamond).

It is also volume-averaged for every $\Delta x = 0.05d$. Figure 5.8 illustrates that the TKE is large in cases that have an unsteady wake. Furthermore, the TKE peak is significantly large in the case of an unsteady wake with rotating cases, even though the wake structure is similar to that of the stationary cases (the hairpin wake). On the other hand, the TKE for the rotating case asymptotically becomes the stationary case in the far-field ($x \approx 15d$). Moreover, the TKE for an Ω-shaped wake (e.g., $M = 0.2$ and $\Omega^* = 1.0$) is relatively small compared with the hairpin wake, even though the wake is unsteady and the peak-TKE position occurs farther from the sphere than the hairpin wake. This is due to the difference between the vortex generation processes of the wake in each case. In the case of the hairpin wake, such vortices are generated in the vicinity of the sphere such as the boundary layer and recirculation region. Therefore, the TKE peak occurs in the near-field of the sphere. For an Ω-shaped wake, conversely, the vortices are generated due to the instability of the shear layer. Hence, the TKE peak occurs relatively far downstream compared with the hairpin wake. Furthermore, the TKE peak moves upstream as $\Omega^* = 1.0$ increases. In terms of M, for rotating cases of $M = 0.8$, the peak of TKE is larger than $M = 0.2$ and 0.3. It seems that this is due to the effect of the disturbance caused by the attached shock wave formed at the retreating side, as will be discussed in the next section.

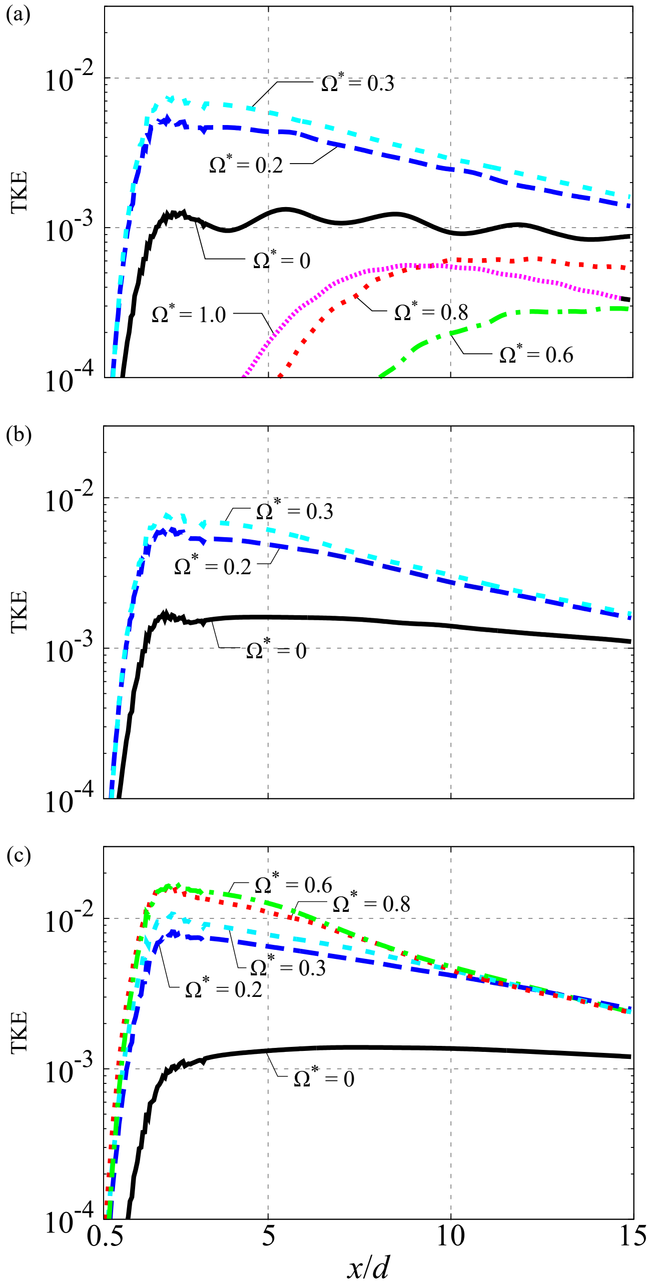

FIGURE 5.8: Normalized TKE distribution behind the sphere at $Re = 300$: (a) $M = 0.2$; (b) $M = 0.3$; (c) $M = 0.8$.

5.3.2 Near-Field Flow Properties

Figure 5.9 shows the pressure coefficient distributions and streamlines in the time-averaged fields obtained over duration longer than 10 vortex-shedding periods in unsteady cases. In stationary cases, the recirculation region in the subsonic and supersonic flows is asymmetric and symmetric, respectively, in the $x - z$ plane. This asymmetry in the time-averaged field is caused by the vortex shedding and the steady nonaxisymmetric recirculation region. On the other hand, the symmetric recirculation region appears in the supersonic flows because no vortex shedding occurs. Also, the size of the recirculation region expands (shrink) as M increases under subsonic (supersonic) flows. This trend has already been reported in chapter 3. For example, the stationary sphere at $Re = 300$, the recirculation region expands as M increase for $M \leq 0.95$. On the other hand, it shrinks as M increases for $M \geq 1.05$.

In the case of rotating cases under the subsonic conditions, an attached shock wave is formed on the retreating side, and its strength increases along with M. As a result, the recirculation region expands as M increases. By the effect of rotation, the flow structure behind the sphere becomes asymmetric under all conditions calculated in the present study. For $M = 0.3$, the recirculation region disappears for $\Omega^* \geq 0.3$. At $M = 0.8$, however, this region is retained for $\Omega^* \leq 0.6$. This difference is caused by the separation encouragement due to the disturbance induced by the attached shock wave formed on the retreating side. This effect also appears at $M = 1.2$ and $\Omega^* = 0.3$. For the supersonic cases, however, the recirculation region disappears at $M = 1.2$ and $\Omega^* \geq 0.6$ and $M = 2.0$ and $\Omega^* \geq 0.3$, even though the attached shock wave is formed, because the recirculation region in the supersonic flows at the same Re is smaller than that in the subsonic cases due to the influence of the expansion wave behind the sphere. It seems that the occurrence of the attached shock has a large impact on the change in the flow properties. Owing to the effect of the attached shock, the flow induced by the rotation effect is decelerated by the shock, and particularly effects on the recirculation region. It means that the effect of the rotation is attenuated by the attached shock. For this effect, the transition of the type of flow pattern due to rotation is suppressed by increasing M as discussed in section 5.3.1. In addition, it will be discussed in section 5.3.3, the increment of drag and lift coefficients by rotation becomes small as M increases.

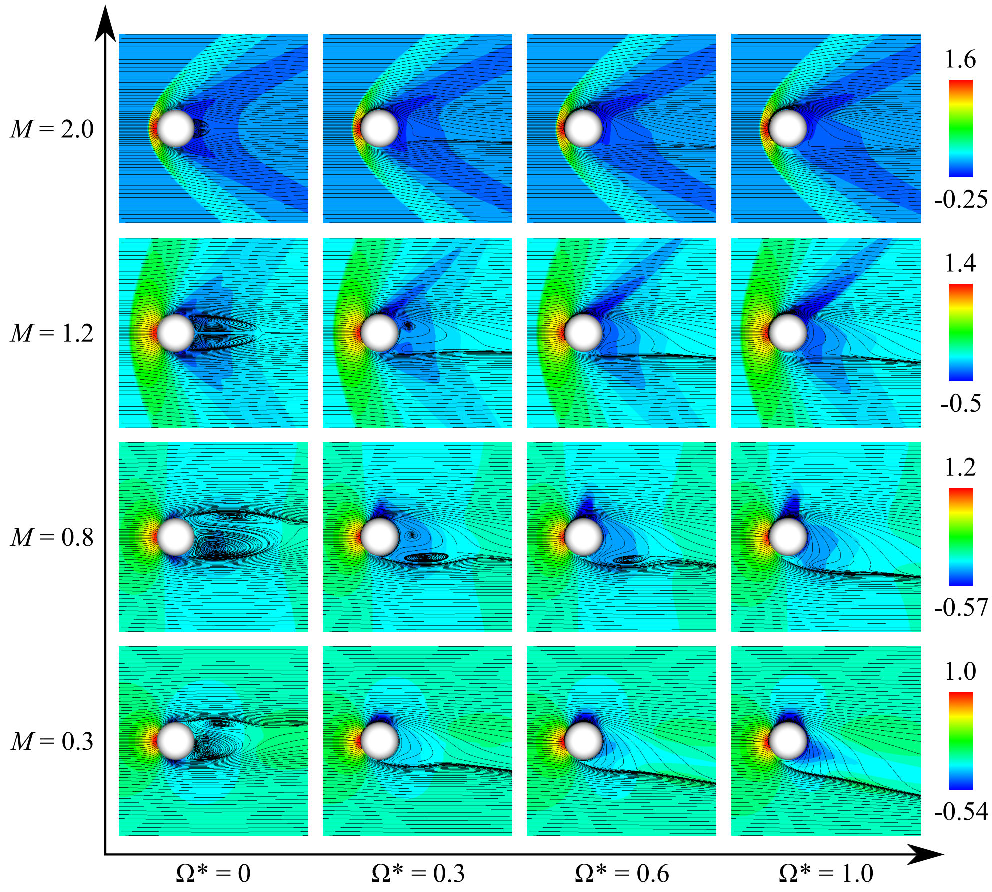

FIGURE 5.9: Pressure coefficient distributions and streamlines of the time-averaged field at $Re = 300$ ($x - z$ plane).

Figure 5.10 shows snapshots of the divergences of velocity vectors, u, in the time-averaged field. These snapshots are normalized by the freestream velocity and the diameter of the sphere. For this figure, the configuration of the attached shock waves is significantly influenced by Ω^* for each M. For stationary cases, the attached shock wave appears symmetric under supersonic conditions. For rotating cases, the strength of the attached shock wave formed at the retreating (advancing) side becomes strong (weak) as Ω^* increases. Also, the angle of the attached shock wave formed at the retreating side becomes similar to that under high-M conditions as Ω^* increases. This is due to acceleration and deceleration of fluid on the retreating and advancing sides, respectively. Also, for $M = 0.8$, a normal shock wave is formed at the retreating side and its strength increases along with Ω^*.

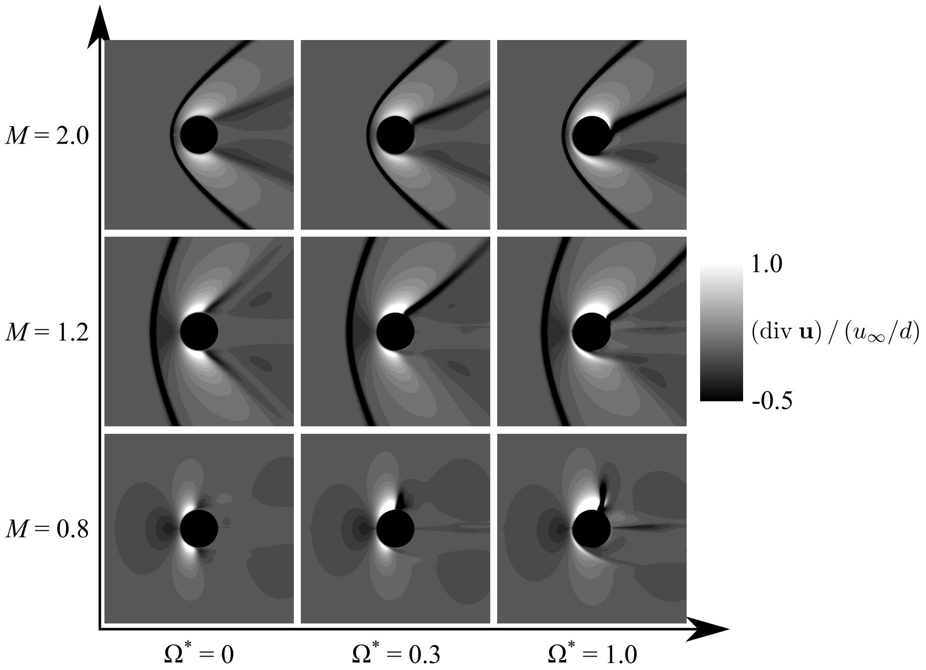

FIGURE 5.10: Schlieren-like images on a time-averaged field at $Re = 300$ ($x - z$ plane).

5.3.3 Aerodynamic Force Coefficient

Lift Coefficient—Rotation-Induced Lift

Figure 5.11 shows the relationship between Ω^* and C_L. In the case of the rotating sphere in incompressible flows, it is well known that the lift force is mainly generated by the pressure difference between the retreating and advancing sides caused by the velocity difference. In the figure, the results of the incompressible flows by Kurose and Komori, 1999; Niazmand and Renksizbulut, 2003; Giacobello, Ooi, and Balachandar, 2009; Dobson, Ooi, and Poon, 2014 are shown in gray symbols. Figure 5.11 illustrates that C_L increases as Ω^* increases, and the C_L dependence for $M = 0.3$ agree with the result of the incompressible flows. However, the increment of C_L due to rotation decreases as M increases. This trend is similar even though $Re < 300$, but the increment of C_L becomes larger at the low-Re conditions. Those M and Re effects on C_L are similar to the result of the rotating cylinder under the compressible flow reported by Teymourtash and Salimipour, 2017. In addition, according to the results at the incompressible and $1.0 < \Omega^* \leq 3.0$ by Dobson, Ooi, and Poon, 2014, C_L due to rotation saturates at approximately $\Omega^* = 1.0$ and $C_L = 0.6$. However, in the case of the supersonic conditions, C_L continuously increases for $1.0 < \Omega^* \leq 3.0$. It is considered that the upper bound of C_L due to rotation and the critical Ω^* which the increment of C_L becomes saturates are influenced by M due to the pressure rise and deceleration of fluid by the detached shock wave.

The normalized lift coefficient $C_L/C_{L,\text{incomp.}}$ is shown in figure 5.12, where C_L is monotonically decreases as M increases. The Ω^* dependence on $C_L/C_{L,\text{incomp.}}$ is changed at around $M = 0.8$. Under rotating high-subsonic conditions, $M \geq 0.8$ and $\Omega^* \geq 0.2$, the normal shock wave is formed on the retreating side because the flow velocity surpasses the sonic speed in a limited region. Hence, the lift force caused by the rotation becomes smaller than in the incompressible cases because of the decrease of the velocity difference (pressure difference) between the retreating and advancing sides.

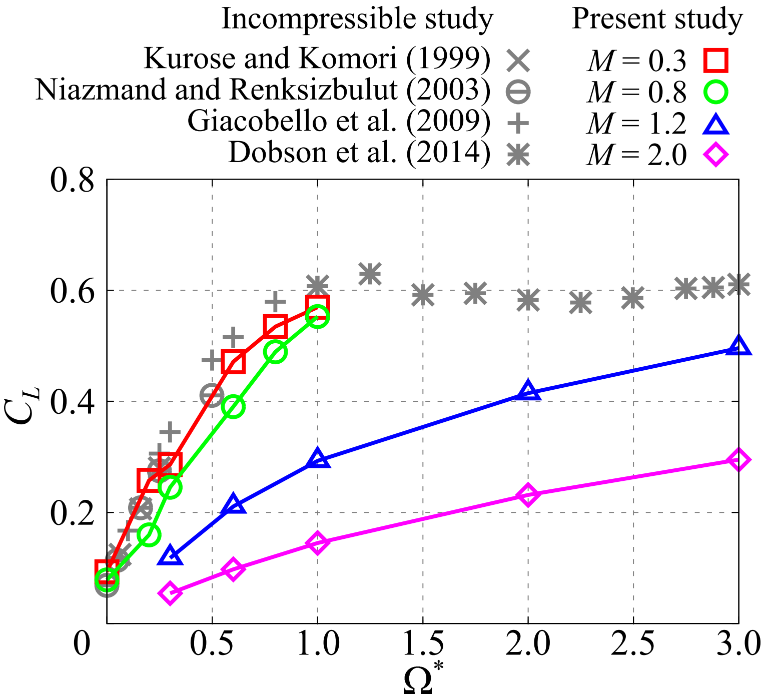

FIGURE 5.11: Time-averaged C_L at $Re = 300$ as a function of Ω^*.

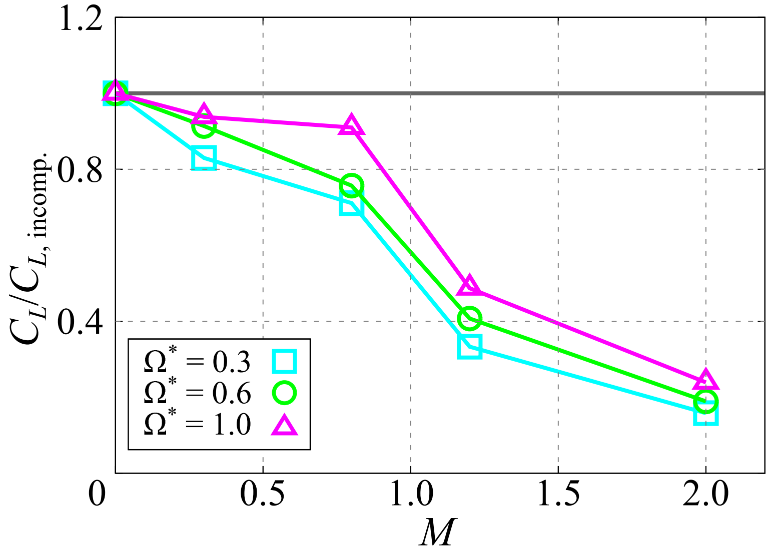

FIGURE 5.12: Effect of M on the increment of C_L at $Re = 300$.

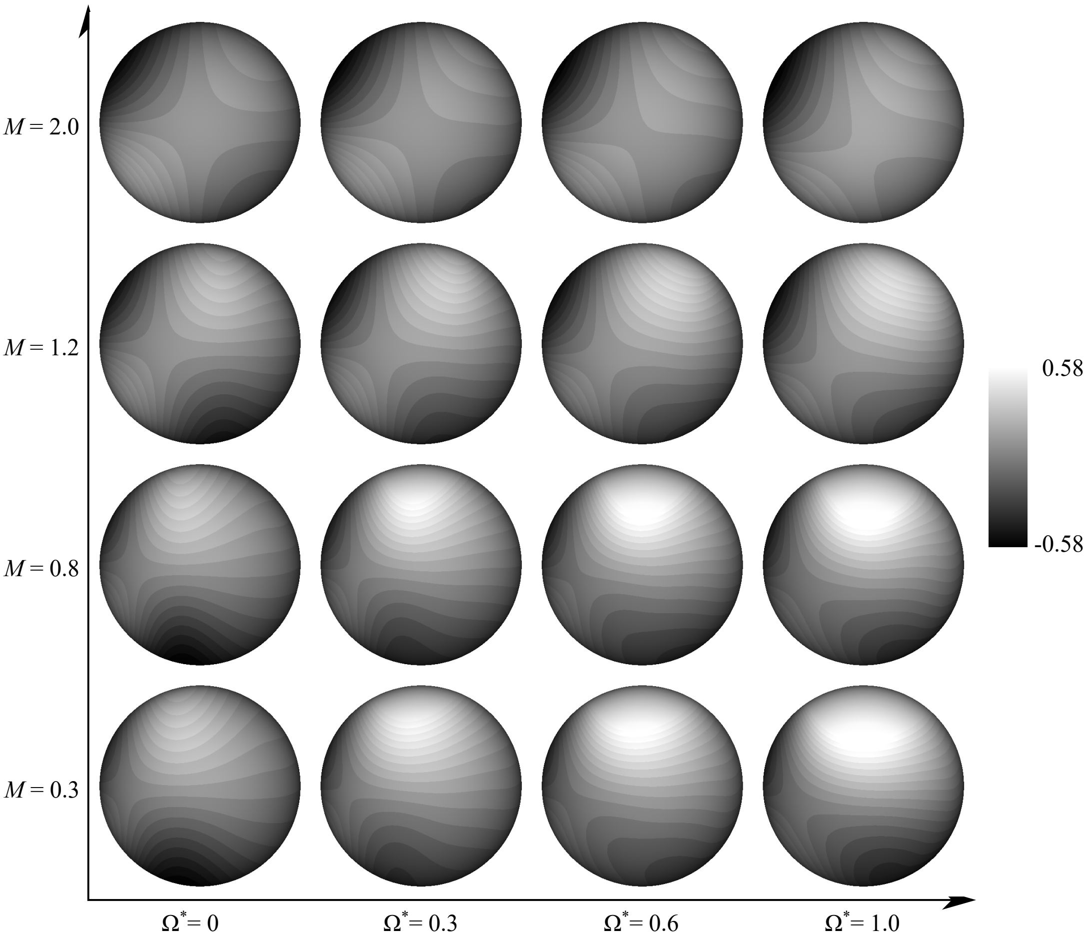

FIGURE 5.13: Distribution of the aerodynamic stress coefficient in the lift direction in the time-averaged field at $Re = 300$ (view from $-y$).

Figure 5.13 shows the aerodynamic stress distribution in the lift direction in the time-averaged field. For $M = 0.3$, the lift force is generated over a wide area of the retreating side, and its area shrinks and the position moves downstream side as M increases. On the other hand, the distribution of the aerodynamic stress in the lift force direction hardly changes with rotation at $M = 2.0$. The lift force by rotation is mainly due to the pressure component. To quantify and analyze the lift force distribution, the pressure coefficient distributions on the surface of the sphere above the equator for $\Omega^* = 0$ and 1.0 in each M is shown in figure 5.14. For this figure, the pressure coefficient distribution is drastically changed by rotation, and its variation along the equator becomes small as M increases. In the case of $M = 0.3$, a peak of the negative pressure at around $\theta/\pi = 0.25$ becomes large as Ω^* increases. On the other hand, the negative pressure region at around $\theta/\pi = 0.75$ moves toward $\theta/\pi = 0.6$ as Ω^* increases. Also, a stagnation point moves slightly toward the advancing side and the pressure coefficient at around $0.75 \leq \theta/\pi \leq 1.0$ increases as Ω^* increases. Thus, the lift coefficient increases due to rotation. For $M = 0.8$ and 1.2, the negative pressure region at around $\theta/\pi = 0.3$ moves downstream side and sharply recovers compared with the case of $M = 0.3$ due to the influence of the attached shock wave. Also, the negative pressure becomes small as M increases. In addition, there is no large impact of rotation on the pressure coefficient distribution at $M = 2.0$. This results in a decrease in the increment of the lift coefficient caused by the rotation under the high-M conditions.

Kajishima, 2004 numerically showed that the particle cluster is formed by the influence of the wake vortices generated by particles, and the lift force due to particle rotation suppresses the formation of particle clusters. The particle rotation is caused by the relative velocity difference inside and outside of the particle cluster at the edge of the cluster. However, for the present results, the lift force caused by the particle rotation is suppressed by the compressibility effect than that of the incompressible flows. In the compressible multiphase flow, therefore, the particle cluster breakdown due to the particle rotation seems to be suppressed by the compressibility effects. On the other hand, the wake vortices released from the particle are reduced as M increases, so that the formation of the particle cluster is also suppressed by the compressibility effects. Hence, the effect of the compressibility on the lift force due to the particle rotation and wake vortices generated by the particles are opposite regarding the formation of the particle cluster. The particle distribution is possibly influenced by the relative M of the particles and fluid, but flow simulation using particle-resolved DNS is necessary to discuss the compressibility effect on the behavior of the particle clusters.

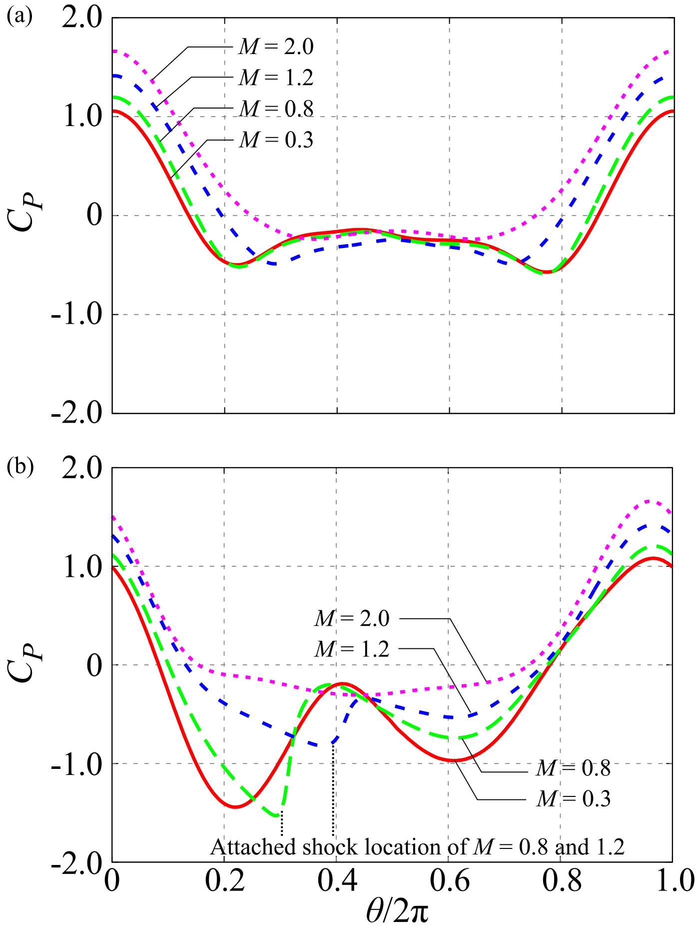

FIGURE 5.14: Pressure coefficient distribution at the surface of the sphere above the equator at Re = 300: (a) $\Omega^* = 0$; (b) $\Omega^* = 1.0$.

Figures 5.15 show the Strouhal number St and the root-mean-square (RMS) amplitude of the lift coefficient $C_{L\mathrm{RMS}}$ at $Re = 300$, respectively. The results under the compressible flows are compared with the results under the incompressible flows by Kurose and Komori, 1999; Niazmand and Renksizbulut, 2003; Giacobello, Ooi, and Balachandar, 2009. For figure 5.15(a), St in the incompressible flows and $M \leq 0.3$ increases with Ω^* for $\Omega^* \leq 0.3$. As Ω^* further increases, St becomes temporary zero because the flow becomes steady double-threaded wake (i.e., steady wake). For $\Omega^* \geq 0.8$, the flow pattern becomes the one-sided Ω-shaped wake in the incompressible flow and $M = 0.2$. In this flow pattern, the vortex shedding occurs more frequently than in the case of the hairpin wake, and St is from double to 4 times that for the hairpin wake. On the other hand, a different trend can be seen in the compressible flows. In the case of $M = 0.3$ and $\Omega^* = 0.6$, St becomes zero, as in incompressible flows. However, it remains zero even though $\Omega^* = 0.8$ and 1.0. Also, for $M = 0.8$, St is not zero at $\Omega^* = 0.6$ and 0.8. These different trends are caused by the differences in the flow pattern due to compressibility effects. For figure 5.15(b), the RMS-amplitude of C_L for $M = 0.3$ has a peak at $\Omega^* = 0.2$ similar to the incompressible flow.

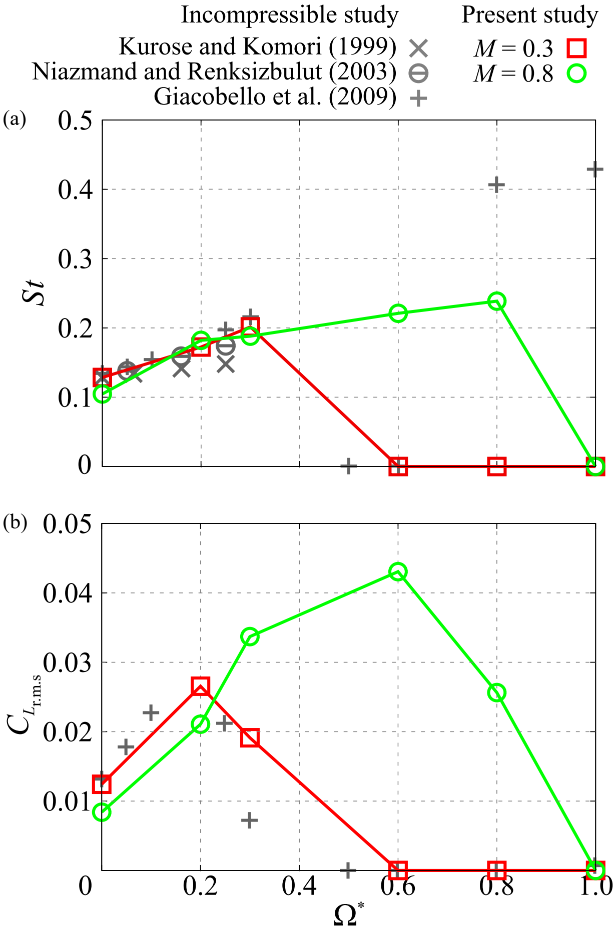

FIGURE 5.15: Comparison of a time variation of lift coefficients with the incompressible results at $Re = 300$: (a) Strouhal number; (b) RMS amplitude.

On the other hand, for $M = 0.8$, the peak RMS amplitude of C_L appears at $\Omega^* = 0.6$ and its value is approximately 1.5 times larger than that of the incompressible cases.

Figure 5.16 compares St and $C_{L\mathrm{RMS}}$ calculated at $Re = 250$ and 300 and $M = 0.3$ and 0.8. This figure indicates that St is almost the same for each M except $\Omega^* = 0$. In other words, for the same flow pattern, Re is not effective upon the St of the vortex shedding. Conversely, $C_{L\mathrm{RMS}}$

becomes small as *Re* decreases. Thus, the frequency of vortex shedding is barely not affected by *Re*, but strength of the oscillation of the wake weakens as *Re* decreases.

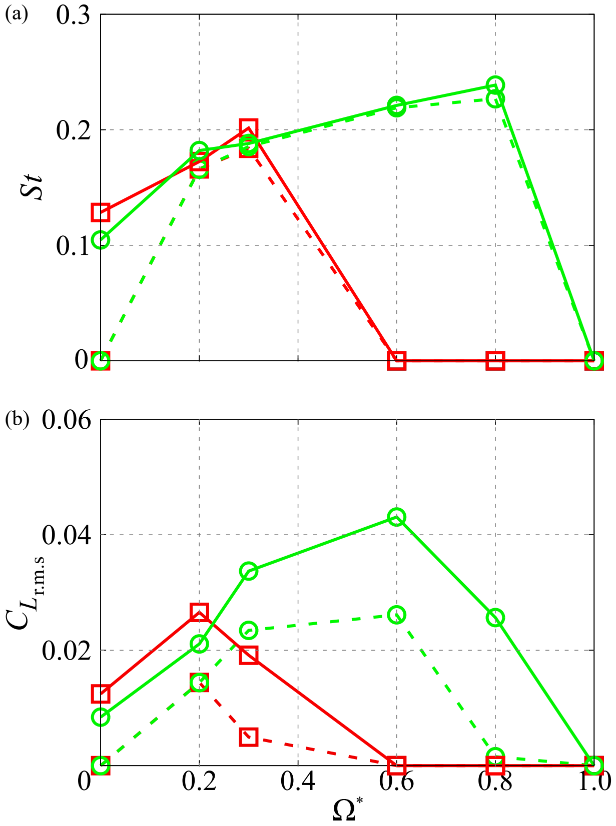

FIGURE 5.16: Effect of *Re* on the time variation of lift coefficients with (a) Strouhal number and (b) RMS amplitude: square symbols ($M = 0.3$); circles symbols ($M = 0.8$); dotted lines ($Re = 250$); solid lines ($Re = 300$).

Drag Coefficient

Figure 5.17 shows the relationship between Ω^* and the drag coefficient C_D at $Re = 300$. Figure 5.17 illustrates that the trend of C_D at $M = 0.3$ is very similar to the previous incompressible studies. The total drag coefficient basically increases as Ω^* increases. Also, this increment of C_D with Ω^* becomes small as M increases. This trend is similar to the result of the rotating cylinder under the compressible flows by Teymourtash and Salimipour, 2017. Also, at $M = 0.8$, increment of the drag coefficient starts to level off at $0.8 \leq \Omega^* \leq 1.0$. It seems that the increment of the drag coefficient is attenuated when the shock becomes strong enough by Ω^* increases. Hence, the occurrence of the attached shock has a large impact on C_D.

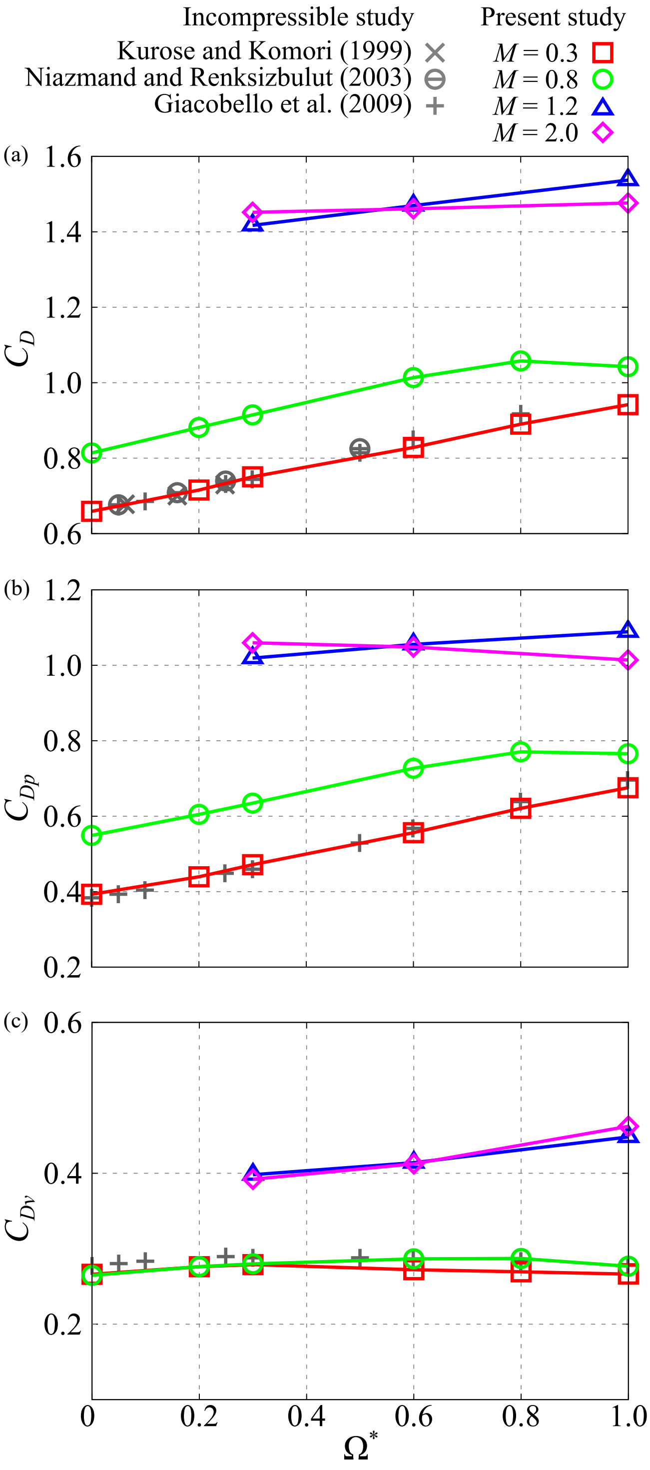

FIGURE 5.17: Time-averaged C_D with respect to Ω^* at $Re = 300$: (a) total; (b) pressure component; (c) viscous component.

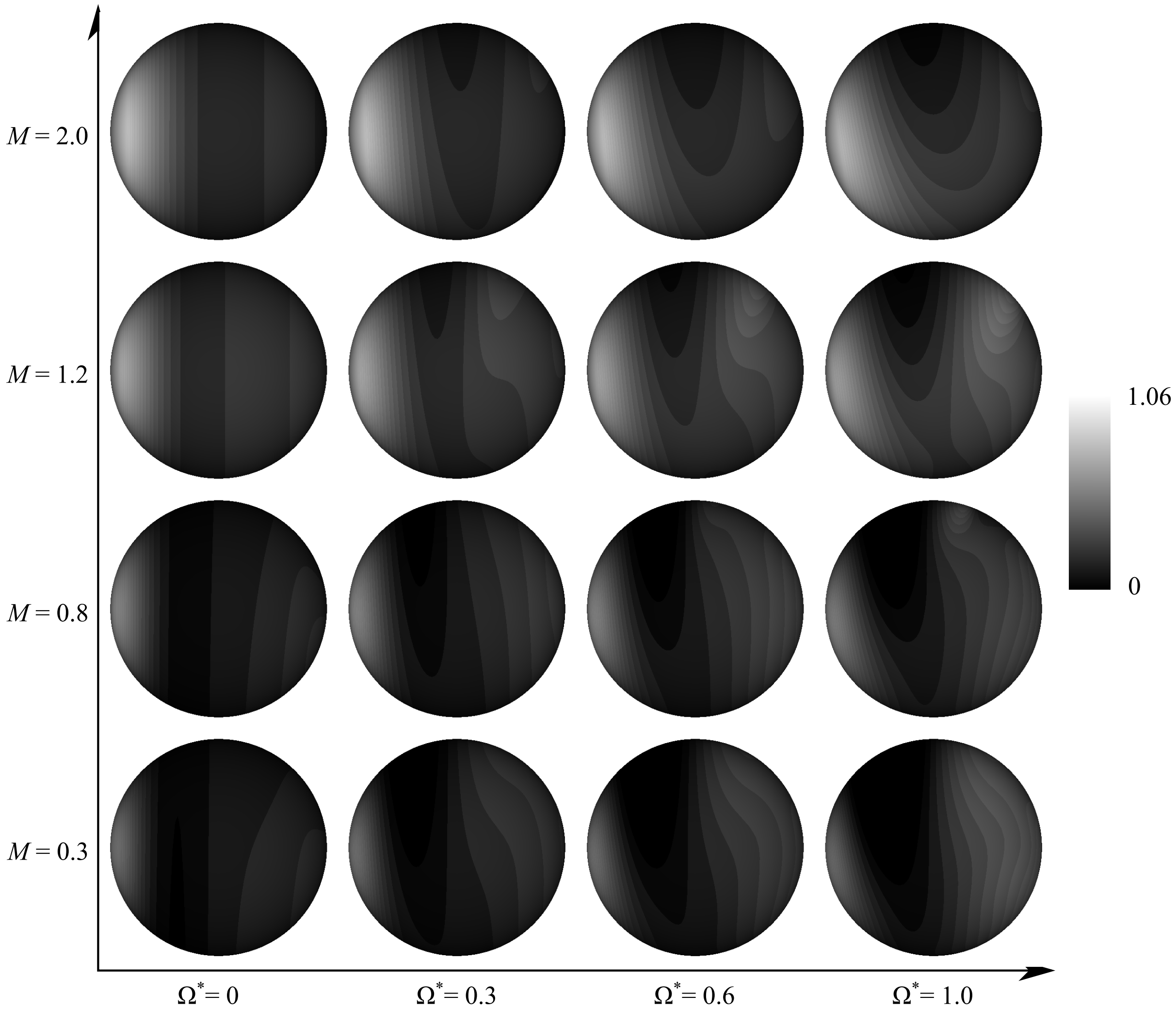

FIGURE 5.18: Distribution of the aerodynamic stress coefficient in the drag direction at the time-averaged field at $Re = 300$ (view from $-y$).

Figure 5.17(b) illustrates that the pressure drag coefficient C_{D_P} increases as Ω^* increases except at $M = 2.0$. A low-pressure region behind the sphere expands and the pressure further decreases at the high-Ω^* conditions because of the formation of the streamwise vortices. Due to this behavior, the pressure drag coefficient becomes large at the high-Ω^* conditions. On the other hand, the pressure around the stagnation point on the upstream side decreases and its position moves toward the advancing side due to the stream generated by the rotation of the sphere. This behavior contributes to a decrease in the pressure drag. Under the subsonic flow, C_{D_P} increases along with Ω^*. Conversely, under the supersonic conditions, the stream generated by rotation is more effective than in the subsonic cases because the main freestream around the sphere is decelerated by the detached shock wave. Therefore, the stream generated by the rotation of the sphere becomes relatively effective at the high-M conditions. In particular, at $M = 2.0$, C_{D_P} becomes small as Ω^* increases because the phenomenon on the upstream side is more effective than that on the downstream side. Additionally, the decrements of the pressure drag caused by the stream generated by rotation increases at low-Re conditions because the velocity boundary layer thickness is thicker.

Figure 5.18 shows the aerodynamic stress distribution in the drag direction at the time-averaged field. The drag force generated on downstream side increases as Ω^* increases, and its increment decreases as M increases. On the other hand, the drag force generated on the upstream side decreases as Ω^* increases, and its increment increases as M increases. These trends reflect the pressure coefficient distribution shown in figure 5.14. For supersonic flows, the freestream is decelerated at the detached shock wave. Hence, the effective rotation rate considered in the fluid velocity behind the detached shock wave and the rotation speed of the sphere is faster than that of the shock-free cases. The flow in the drag direction is strongly reduced due to the stream generated by the rotation of the sphere under supersonic flows. Also, the drag coefficient increases as Ω^* increases due to the movement of the negative pressure region at around $\theta/\pi = 0.7$. These trends are similar, even if M increases, but the effect of Ω^* upon the pressure coefficient distribution is weaker under the high-M conditions. Also, the pressure coefficient distribution itself drastically changes as M increases. In addition, the decrease (increase) of the pressure coefficient at the region on at around $0 \leq \theta/\pi \leq 0.25$ ($0.5 \leq \theta/\pi \leq 0.75$) caused by rotation increases (decreases) as M increases. For this behavior, the increase of the drag coefficient due to rotation becomes small under the high-M conditions.

The viscous drag coefficient C_{D_v} is hardly changed by rotation for subsonic cases. In the supersonic cases, on the other hand, C_{D_v} increases as Ω^* increases because the friction stress increases on the advancing side due to the change in the velocity gradient and the viscosity coefficient at the surface of the sphere. The viscous drag coefficient increases as Ω^* increases in supersonic flows. Figure 5.19 shows the distribution of the velocity gradient in θ-direction velocity U_θ for the r direction on the surface of the sphere above the equator. The velocity gradient was normalized by the freestream velocity and the diameter of the sphere. This figure illustrates the velocity gradient decreases as Ω^* increases in the most areas of the retreating and advancing sides. This trend is similar between the subsonic and supersonic flows, but under the supersonic condition, change in the distribution of the velocity gradient due to rotation is influenced by the shock waves. For example, the sign of the velocity gradient changes sharply at around $\theta/\pi = 0.25$ by the attached shock wave for $M = 0.8$ and 1.2. Also, the shock wave moves downstream side as M increases. For $M = 0.3$, the velocity gradient on the most of the retreating side is positive, so the friction stress on the retreating side acts to promote rotation. For $M \geq 0.8$, conversely, the region with a negative velocity gradient on the retreating side is expanded by the effect of the attached shock waves. Moreover, for $M \geq 1.2$, the peak velocity gradient on the retreating side becomes small as M increases. This trend is caused by the influence of the detached shock wave which decelerates the flow around the sphere. This results in the relative velocity between the surface of the sphere and the freestream become small as M increases.

The viscosity coefficient distribution on the surface of the sphere above the equator is shown in figure 5.20. Because of the influence of rotation, the viscosity coefficient decreases (increases) at the retreating (advancing) side. Also, the velocity gradient at the surface of the sphere on the retreating (advancing) side becomes small (large), due to the influence of rotation. Hence, the viscous drag and moment coefficients around rotational axis are larger than that in the stationary cases for the high-M and high-Ω^* conditions. The viscosity coefficient mainly increases around the upstream stagnation point due to compression, and behind the attached shock wave and the advancing side in the downstream side due to rotation. The effects of the shock waves become strong as M increases. The large aerodynamic heating occurs on the advancing side because the relative velocity on the advancing side between the fluid and surface is larger than that on the retreating side. Thus, the viscosity coefficient on the advancing side increases remarkably under the high-M condition of rotating cases.

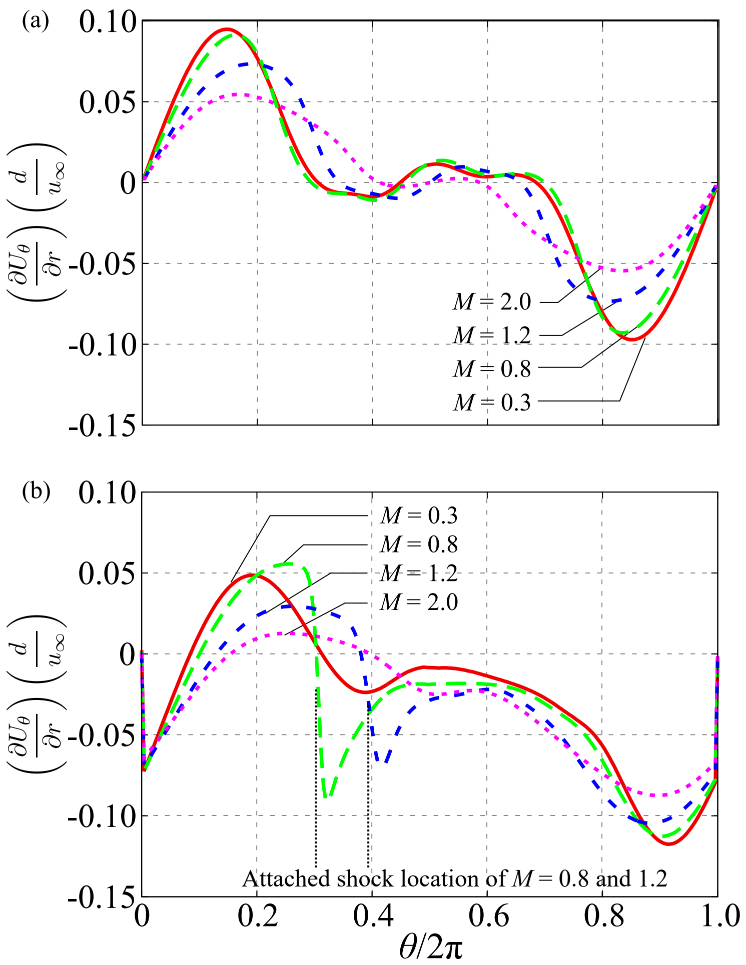

FIGURE 5.19: Normalized velocity gradient distribution at the surface of the sphere above the equator at $Re = 300$: (a) $\Omega^* = 0$; (b) $\Omega^* = 1.0$.

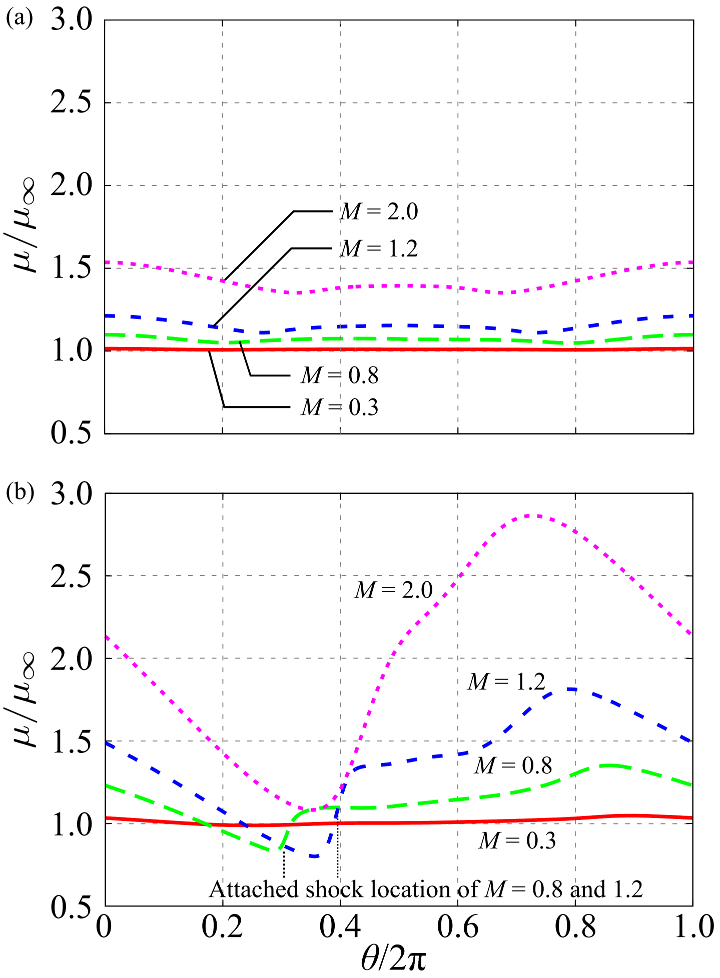

FIGURE 5.20: Normalized viscosity coefficient distribution at the surface of the sphere above the equator at $Re = 300$: (a) $\Omega^* = 0$; (b) $\Omega^* = 1.0$.

Moment Coefficient around Rotation Axis

Figure 5.21 shows the moment coefficient around the rotation axis: compressibility effects appear in the moment coefficient. In rotating cases, the moment coefficient is a negative value, meaning that moment opposes the rotation of the sphere and its strength increases along with Ω^*. Also, the increment of the moment coefficient by rotation becomes large as M increases, and this effect increases along with decreases Re.

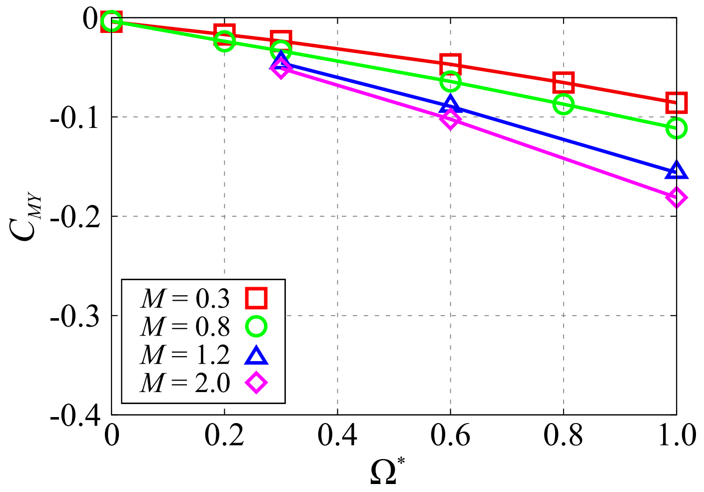

FIGURE 5.21: Effect of M on the moment coefficients around the rotation axis at Re = 300.

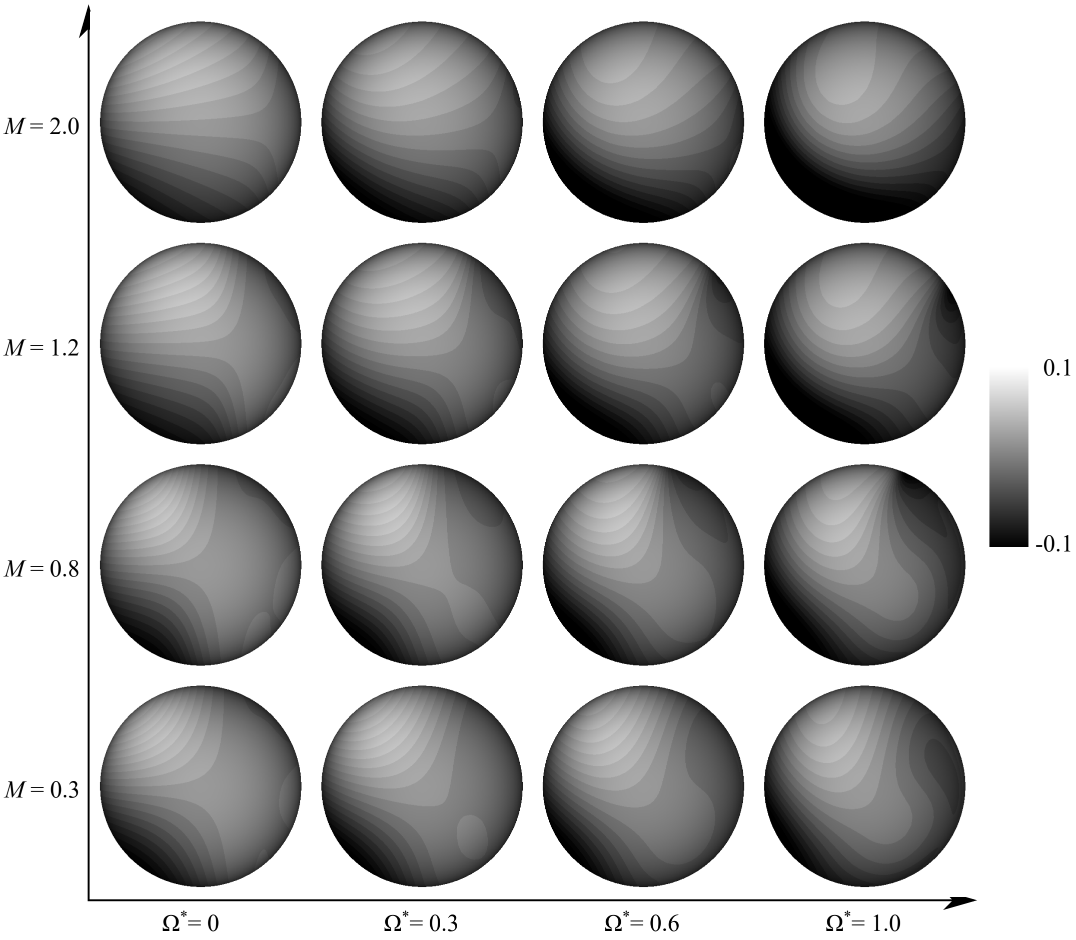

FIGURE 5.22: Distribution of the local moment coefficient in y-direction at the time-averaged field at Re = 300 (view from $-y$).

Figure 5.22 shows the distribution of the aerodynamic stress coefficient which contributes to the moment (local moment coefficient). This coefficient is calculated as the product of aerodynamic stress tangential to the surface for the ξ direction and the moment arm and is normalized by the diameter of the sphere and the dynamic pressure based on the freestream quantities. In stationary cases, the local moment coefficient around the y-axis is symmetry on the retreating and advancing sides. However, as Ω^* increases, the distribution of the local moment coefficient becomes asymmetric distributions. Thus, the relative fluid velocity between the vicinity of the sphere and the surface of the sphere on the retreating (advancing) side becomes small (large) as Ω^* increases. Also, the difference between the absolute value of the local moment coefficient on the retreating and advancing sides becomes large as M increases because of the deceleration of the fluid velocity at the detached shock wave, and the relative velocity between the surface and fluid in the vicinity is smaller than that under the subsonic conditions. As a result, the local moment coefficient on the retreating side in the supersonic conditions is smaller than that of at subsonic flows for the same Ω^*. Conversely, on the advancing side, the local moment coefficient for high-M flows is larger than that of the low-M flows due to the increase of the viscosity coefficient, as shown in figure 5.20. Also, the negative local moment coefficient appears on the retreating side for $M = 0.8$ and 1.2 under the influence of the attached shock wave. By forming this shock wave on the retreating side, the fluid in the vicinity of the sphere is decelerated. Therefore, the friction stress on the surface behind the attached shock wave increases due to the increase of the velocity gradient and the viscosity coefficient, and its effect becomes large as M and Ω^* increase. Thus, the attached shock wave formed on the retreating side has a braking effect on the particle rotation. From the above results, the particle rotation in the compressible particle-laden flow is easy to stop compared with that in the incompressible case.

	C_L	C_D	C_{M_Y}	St
When Ω increases	increases	increases	increases	increases (except steady cases)

(a) Effect of Ω on each parameter.

	ΔC_L	ΔC_D	ΔC_{M_Y}	ΔSt
When M increases	decreases	decreases	increases	not effective

(b) Effect of M on increment of each parameter due to rotation.

TABLE 5.3: Summary of the effect of Ω^* and M on each parameter.

The summary of the Ω^* effect on C_L, C_D, C_{M_Y} and St and the M effect on the increment of C_L, C_D, C_{M_Y} and St due to rotation are shown in table 5.3. The Ω^* effect on each parameter is the same between the incompressible and compressible flows. The increment of C_L and C_D becomes small as M increases. On the other hand, the increment of C_{M_Y} becomes small as M increases. Also, the increment of St is not influenced by M.

5.4 Results and Discussion for Linear Shear Flow Case

5.4.1 Near-Field Properties

Velocity Distribution

Figure 5.23 and 5.24 shows the distribution of the streamwise velocity, which is normalized by the velocity of the uniform component, at $Re = 50$ and 300, respectively. The asymmetry of the flowfield due to the velocity gradient can be observed even in $Re = 50$. The flowfield of the uniform flow over a sphere at $Re = 50$ is steady-axisymmetric flow as discussed in chapter 3. The recirculation region of the linear shear Flow at $Re = 50$ of $M = 0.3$ is almost the symmetric shape so that the effect of the shear on the velocity distribution is weak. However, the asymmetry of the flowfield becomes strong as M increases. The detached shock wave and expansion wave are formed on only the high-speed side at the transonic regime. In addition, the symmetry breakdown of the recirculation region occurs and the asymmetry becomes strong as M increases. The end of the recirculation region is formed on the low-speed side in those cases. The asymmetry of the recirculation region is related to the expansion wave formed on the high-speed side. Such flow that the expansion wave is formed, the flow direction is changed into the direction tangential to the surface due to the influence of the expansion wave as discussed in chapter 3. In the case of the linear shear flow, such kind of the effect appears only on the high-speed side at the transonic regime, and thus the asymmetry of the recirculation region appears, despite the Re range of the axisymmetric flow in the uniform case. As M further increases, the shock waves are formed on both of the high-speed and low-speed sides, but the asymmetry of the recirculation region becomes further strong. The asymmetry of the recirculation region remains even though the whole of the flow over a sphere becomes supersonic conditions, because of the difference in the local M on the high-speed and low-speed sides. It notes that the present result includes not only the effect increase in M but also the effect increase in the absolute value of the shear velocity.

At $Re = 300$, on the other hand, the recirculation region is skewed due to the velocity gradient even though $M = 0.3$. Kurose and Komori, 1999 reported that the negative shear-induced lift is generated in this Re range of the incompressible flow. The reverse of the shear-induced lift is caused by this kind of skewed recirculation region. The flowfield at $M = 0.3$ seems to be similar to the incompressible flow, but it cannot confirm because the previous incompressible studies have not provided the visualization of the flowfield. It notes that the compressibility effect seems to appear particularly in the high-speed side even though $M = 0.3$ due to shear velocity. Under subsonic conditions, the end of the recirculation region exists in the high-speed side and the length of the recirculation region increases as M increases. The detached shock and expansion waves are formed only on the high-speed side due to the difference in the local M between the low-speed and high-speed sides. The shape of the recirculation region is basically the same up to $M = 0.95$. The detached shock wave and the expansion wave becomes more strong at $M \geq 1.05$, and the shear layer between the recirculation region and freestream at the high-speed side is bend due to the expansion wave formed in the high-speed side, but the end of the recirculation region still exist in the high-speed side so that flow pattern in the downstream is similar to incompressible one. However, the end of the recirculation region exists in the low-speed side so that flow pattern in the downstream is drastically changed. This change is due to the strong expansion wave formed on the high-speed side. Although the detached shock wave and the expansion wave are formed in also the low-speed side, the strength of those waves in the high-speed side is significantly strong, and thus the flow pattern of the recirculation region is drastically changed. Based on the incompressible study, the direction of the shear-induced lift might be changed at $M = 1.5$. The M effect on the shear-induced lift will be discussed in section 5.27.

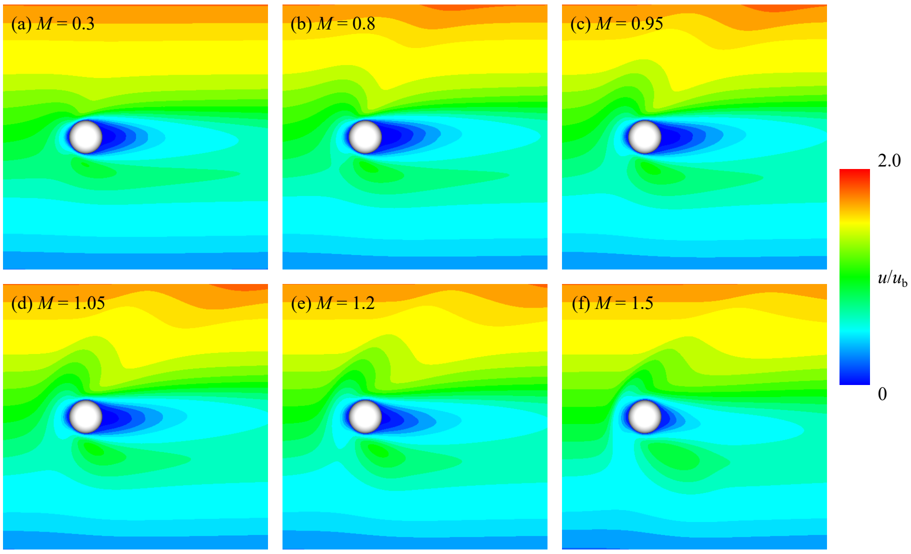

FIGURE 5.23: Streamwise velocity distribution in $x - z$ plane ($Re = 50$).

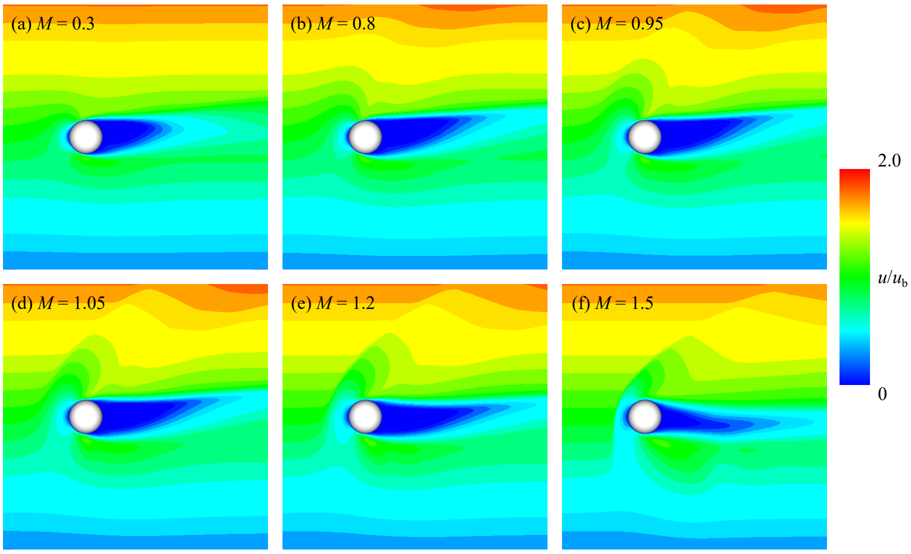

FIGURE 5.24: Streamwise velocity distribution in $x - z$ plane ($Re = 300$).

Position of the Separation Point

Distributions of the position of the separation point were investigated. The coordinate system for the discussion of the distribution of the separation point is shown in figure 5.25. The position of the separation point in the streamwise direction θ_s is defined as the angle from the upstream stagnation point, the range of $theta_s$ is $0 \leq \theta_s \leq \pi$. The upstream and downstream sides are $\theta_s < \pi/2$ and $\theta_s > \pi/2$, respectively. The position in the transverse direction was defined as the angle from the $x - y$ plane, the range of ϕ is $\pi/2 \leq \phi \leq \pi/2$. The high-speed and low-speed sides are $\phi < 0$ and $\phi > 0$, respectively.

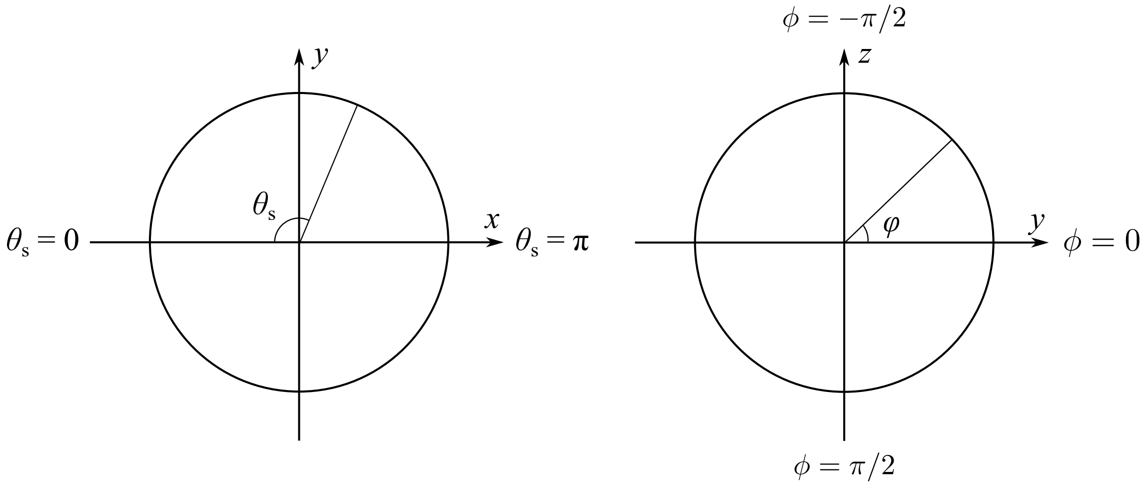

FIGURE 5.25: Coordinate system for the position of the separation point. The range of θ_s and ϕ are $0 \leq \theta_s \leq \pi$ and $\pi/2 \leq \phi \leq \pi/2$, respectively.

Figure 5.26 shows the distribution of the separation point. Circular symbols represent the separation point of the uniform flow cases discussed in section 3 (averaged around x-axis), lines represents the distribution of the separation point of the shear cases.

The position of the separation point has an asymmetry distribution due to the velocity gradient in the mainstream, and the trend in the distribution of the separation point is different in each M range. Also, the separation point moves upstream and downstream at approximately $M < 0.95$ and $M > 0.95$, respectively, as M increases (see in details in section 3). At $M = 0.3$, the separation point in the high-speed side exists in the upstream side compared with the low-speed side because the separation point moves upstream as M increases at subsonic conditions. At $M = 0.8$, on the other hand, the difference in the position of the separation point is smaller than

$M = 0.3$. The separation point in the high-speed and low-speed sides exist slightly downstream compared with the center of the sphere. The inflection point of the M effect on the separation point at $M \approx 0.95$ so that the position of the separation position the high-speed and low-speed sides exist relatively downstream and upstream compared with that of the center of the sphere because of higher- and lower-M of the critical M regarding the separation point, respectively. The separation point in the high-speed side moves downstream because of the expansion wave formed in the high-speed side. The position of the separation point on the high-speed side exist in downstream compared with the low-speed side at $M \geq 0.95$ so that the inflection point of the trend on the separation point at $Re = 300$ and $\alpha^* = 0.1$ is $M \approx 0.8$. The separation point in the high-speed side moves downstream because the separation is delayed due to the stream, which bends toward the x-axis.

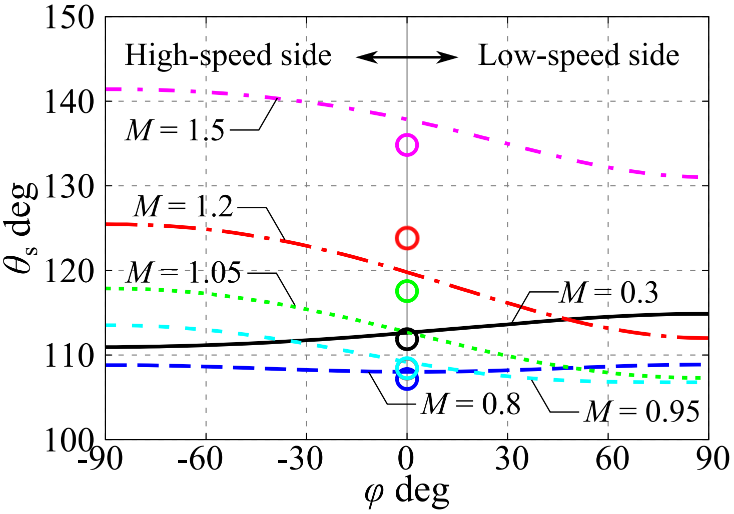

FIGURE 5.26: Distribution of separation point (Re = 300).

5.4.2 Aerodynamic Force Coefficient

Lift Coefficient—Shear-Induced Lift

Figure 5.27 shows the Re evolution of the shear-induced lift at each M. The compressible cases are compared with the results at the incompressible flow by Kurose and Komori, 1999. The shear-induced lift for the incompressible case is negative at a higher-Re side and decreases as Re decreases. The shear-induced lift is asymptotic to zero at around $Re = 10$ and becomes positive at further lower-Re conditions. The trend of the shear-induced lift at $M = 0.3$ is almost the same as the incompressible case. At $M = 0.8$, however, Re dependence on the shear-induced lift is quite small and the shear-induced lift decreases as Re decreases, and the Re effect on the shear-induced lift becomes opposite at $M \geq 0.8$ compared with $M \leq 0.3$.

Figure 5.28 shows the M effect on the coefficient of shear-induced lift. The symbols at $M = 0$ indicates the result of the incompressible study (Kurose and Komori, 1999). At $Re = 300$, the negative shear-induced lift at $M = 0.3$ is larger than that of the incompressible flow due to the M effect. Owing to the shear component in the mainstream, the M effect appears even though $M = 0.3$. The negative shear-induced lift increases as M increases up to $M \approx 1$, and it decreases as M increases at $M > 1$ so that there is the inflection point in the M effect. At lower-Re conditions, the negative shear-induced lift at the subsonic condition is smaller than that of higher-Re conditions because the negative lift at the incompressible flow decreases as Re decreases at $Re \lessapprox 50$. At transonic and supersonic conditions, conversely, the negative lift at lower-Re conditions is larger than that of higher-Re conditions. As a result, there is a cross point of the M–C_L curve at around $M = 0.8$. The mechanism of the change in the shear-induced lift will be discussed below based on the surface stress coefficient in the lift direction.

Figure 5.29 shows the surface stress distribution in the lift direction. The region where positive/negative $C_{f_L} + C_{P_L}$ generates the positive/negative lift. The lift force are zero if the stress distribution in the lateral direction is symmetry, but the flowfield is the asymmetry in the present case so that the lift force is generated. At $M = 0.3$, the positive and negative lift forces are mainly generated at the top and bottom sides of the sphere due to the negative pressure around there. In addition, there is a velocity difference in the top and bottom sides of the sphere due to the shear component and the asymmetry of the flow field so that there is a difference in the absolute value of the generated lift forces on the high-speed and low-speed sides. As a result, the total lift force becomes non-zero value. The shear-induced lift at $Re = 300$ is the negative value for the incompressible flow due to the asymmetry of the recirculation region (Kurose and Komori, 1999). As M increases, the negative lift force is generated on the sphere surface in the upstream of the upper side. The negative lift in there increases as M increases. Also, the generated lift force at the top and bottom sides of the sphere decreases as M increases. In addition, the positive lift becomes large in the upstream of the lower side of the sphere. The trend can be seen in figure 5.29.

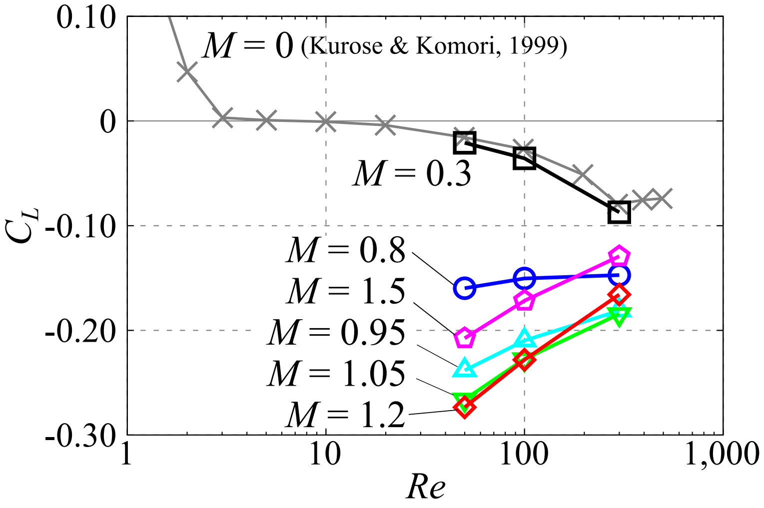

FIGURE 5.27: Effect of Re on the shear-induced lift coefficient.

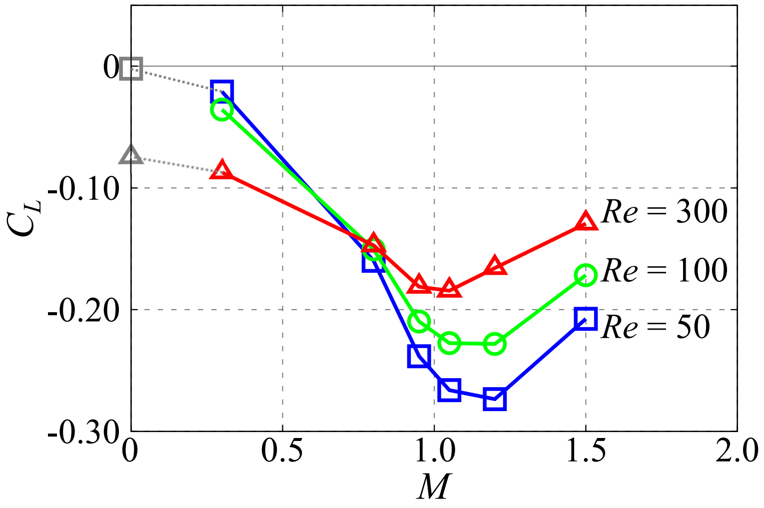

FIGURE 5.28: Effect of M on the shear-induced lift coefficient.

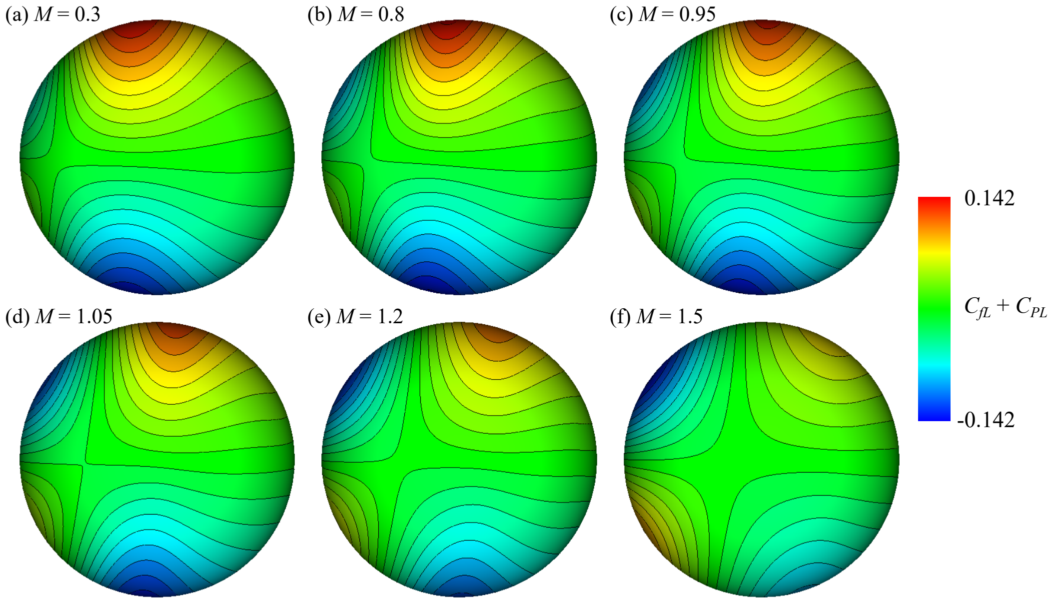

FIGURE 5.29: Distribution of the surface stress coefficient in the lift direction.

Figure 5.30 shows the distribution of the surface stress coefficient of the lift direction in the streamwise direction. The surface stress is separately averaged around x-axis in the upper and lower sides. The variable θ indicates the angle from the upstream stagnation point around y-axis. Here, $\theta = 0, 360$ and $\theta = 180$ correspond to the upstream and downstream stagnation points, respectively. Figure 5.30 illustrates that the surface stress in the lift direction decreases and increases as M increases at upstream and downstream sides, respectively. In the upper upstream side, the negative lift is generated due to compression and it increases as the M increases. At the top side, conversely, the positive lift is generated due to the low pressure caused by accelerated fluids and it decreases as M increases at $M > 0.8$. The effects of M in the stress coefficient in the lift direction are different in the upper upstream side and topside. In the case of the top side, the M effect on the pressure coefficient works to decrease and increase at subsonic and supersonic conditions, respectively. The pressure in the top side at $M \leq 0.8$ decreases due to the compressibility effect described by the Prandtl–Glauert transformation. At $M > 0.8$, conversely, the pressure increases due to the pressure rise at shock waves and strong compression in the upstream side. This trend is antisymmetric on the lower side, but local M in the lower side is lower than that of the upper side so that stress coefficient distribution in the lift direction is non-axisymmetric. Also, on the downstream side, the effect of M is quite weak because of the separated flows.

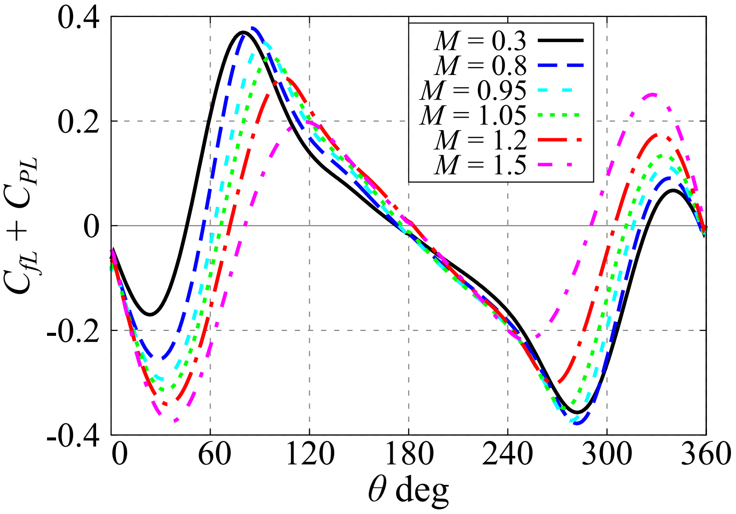

FIGURE 5.30: Distribution of the surface stress coefficient in the lift direction (averaged round x-axis for upper and lower sides).

Figure 5.31 shows the distribution of the stress coefficient in the lift direction averaged around x-axis. In the upstream side, the negative lift is generated due to the difference in the local M. At subsonic conditions, the negative lift in the upper upstream side increases but the positive lift in the lower side does not increase, because the local M in the lower side is lower than the upper side and the effect M is quite small. The increment of the negative lift in the upstream side saturates around transonic conditions, and the negative lift decreases as M increases at supersonic conditions. At high-subsonic and transonic conditions, the increment of the surface stress due to the M effect appears both upper and lower sides of the sphere so that the increment of the negative lift saturates due to the increment of the positive lift in the lower side. At supersonic conditions, the negative lift in the upstream decreases as M increases because the increment of the stress coefficient saturates in the supersonic conditions. The increment of the negative lift in the upper sides becomes small due to the conditions of the higher-M supersonic flow, but the increment of the positive lift is still large in the lower side due to the lower local M. At $\theta' = 90$ deg, the generated lift is almost zero but the small positive lift is generated due to the larger velocity in the upper side. The stress coefficient in the lift direction at $M \leq 1.05$ becomes negative again in the downstream. At supersonic conditions, conversely, the positive lift appears in the downstream area corresponding to the recirculation region. Hence, the reverse of the lift direction due to M effects occurs in the limited region corresponding to the recirculation region, but the M effect in the negative lift generated in the upstream is dominant. Hence, there is no reverse of the integrated value of the shear-induced lift caused by M effect, despite the drastic change in the flow pattern of the recirculation region.

The negative lift in the compressible flow is due to the compression in the upstream of the high-speed side so that the negative lift in the compressible flow seems to become strong in the following conditions: (1) higher-M conditions, (2) higher-shear rate conditions, and (3) lower-Re conditions. The surface stress at the upstream side becomes strong as M increases, and compression in the high-speed side becomes stronger than that of the low-speed side. The higher shear rate leads to the stronger compression in the upstream of the high-speed side. The pressure coefficient due to compression increases as Re decreases because of the larger viscosity. Therefore, it is clear that the conditions listed above appear to lead the larger negative lift in the continuum regime.

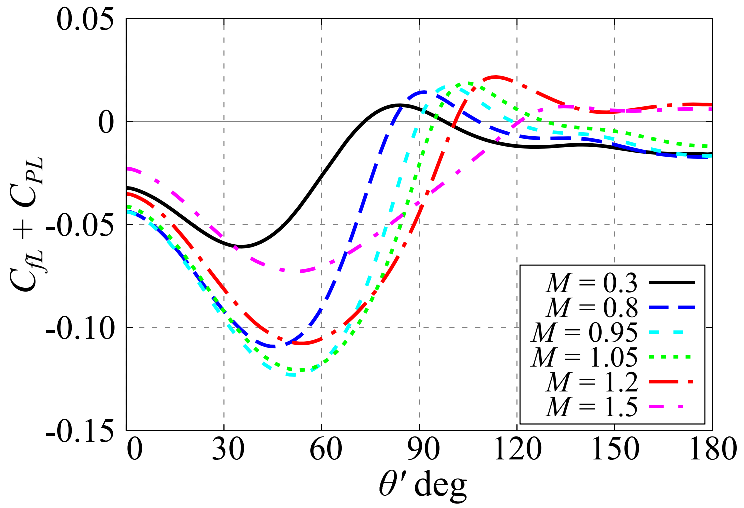

FIGURE 5.31: Distribution of the surface stress coefficient in the lift direction (averaged round x-axis).

Drag Coefficient

Figure 5.32 shows the effect of M on C_D. The diamond, squired, and circular symbols represent the results of Re = 50, 100, and 300, respectively. The red symbols represent the shear flow cases, the gray symbols represent the uniform flow cases described in chapter 3. Figure 5.32(a) illustrates that the total drag coefficient monotonically increases as M increases for both uniform and shear cases. However, there is the difference in the transonic region. The total drag coefficient rapidly increases for uniform cases. In the shear cases, conversely, the increment of C_D due to an increase of M is almost constant for all M range investigated in the present study. In other words, the gradient of M–C_D curve for the shear flow case is smaller than that of the uniform flow case. This trend is similar in the pressure component C_{D_P}, and the pressure component is dominant in the M evolution of C_D.

The increment of C_{D_P} by the M effects is due to the compressibility effects which are described by the Prandtl–Glauert transformation in the subsonic flow, and also the wave drag in the transonic and supersonic flows (see chapter 3). In particular, the drag coefficient rapidly increases in the transonic flow because of the wave drag. The difference in the increment of C_D at the transonic regime can be described by the local M. In uniform flow cases, the distribution of the local M normal to the streamwise direction is uniform so that the flow over the sphere changes simultaneously, and the increment of C_D clearly different between each flow regime. In the shear flow cases, on the other hand, the local M is different in the direction normal to the freestream, and thus the detached shock does not appear in the low-speed side at the transonic regime as discussed in 5.4.1. The drag coefficient for the shear flow case in the subsonic flow is higher than that of the uniform flow case because of the wave drag due to the partially formed shock waves in the high-speed side. Conversely, C_D for shear flow case in the high-transonic or low-supersonic flows are lower than that of the uniform flow cases. The effect of M on the increment of C_D is reduced as M increases in the supersonic regime (Oswatitsch's Mach number independence principle). Thus, the increment of C_D at the high-speed side is reduced at this flow regime. In addition, the drag force in the low-speed side is smaller than uniform flow cases so the total drag of the shear flow case in the high-transonic and low-supersonic flows is smaller than that of the uniform flow cases.

Figure 5.32(c) shows the viscous drag coefficient C_{D_v}. Effects of the shear flow on the M effect in C_{D_v} is similar to that of the effect on C_{D_P}. The increment of the viscous drag coefficient for uniform flow cases is due to the movement of the position of the separation point, and the position of the separation point rapidly moves downstream at the transonic flows so that C_{D_v} at the transonic regime rapidly increases as M increases. In the shear flow case, however, the local M is different in the high-speed and low-speed sides, and thus the movement of the position of the separation point gradually occurs from the high-speed side to the low-speed side. Hence, C_{D_v} gradually increases as M increases in the shear flow case.

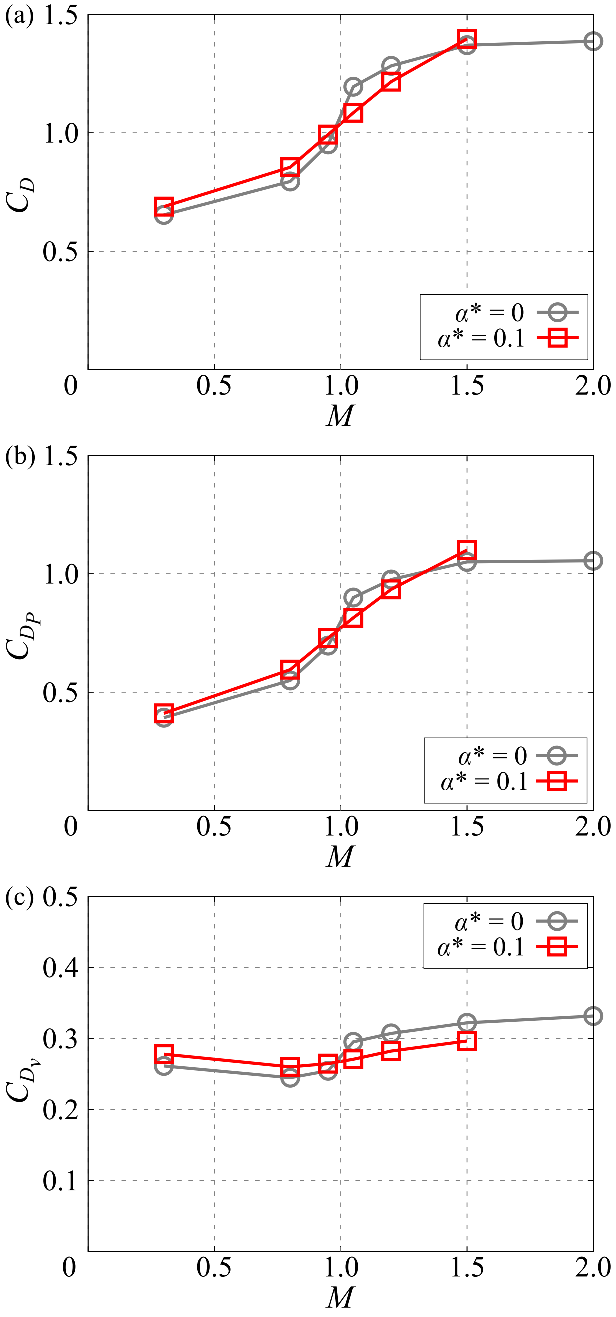

FIGURE 5.32: Effect of M on the drag coefficients: (a) total drag; (b) pressure component: (c) viscous component.

Moment Coefficient

Figure 5.33 shows the effect of M on the pitching moment coefficient (around y-axis). The pitching moment is generated due to the velocity difference in the high-speed and low-speed sides. It notes that the present computation does not consider the equation of motion so that the sphere is completely fixed. Figure 5.33 illustrates that the small pitching moment is generated, and it variates because of the effects of Re and M. At $M = 0.3$, the moment coefficient is positive at $Re = 50$ because the wall shear stress on the high-speed side is larger than that on the low-speed side. However, the moment coefficient decreases and becomes negative as Re increases. This trend in the moment coefficient is due to the change in the separation point. At lower-Re conditions, the flow over a sphere is close to the fully attached flows, and thus the wall shear stress on the high-speed side surpasses that of the low-speed side. Conversely, at higher-Re conditions, the separated area on the high-speed side is larger than that on the low-speed side because of the skewed recirculation region (see figure 5.26). The moment coefficient at the transonic and supersonic flows is negative and positive values, respectively, regardless of M. The negative value at the transonic regime is due to the shock waves formed only on the high-speed side. Because of the shock waves, the fluid on the high-speed side is decelerated and the wall shear stress in the low-speed side surpasses that of the high-speed side. As a result, the negative moment is generated. At the supersonic conditions, the strength of the shock waves is stronger than that on the low-speed side, but the attached flow region and the dynamic viscosity coefficient on the high-speed side are wider and larger than that of the low-speed side. As a result, the moment coefficient takes positive values.

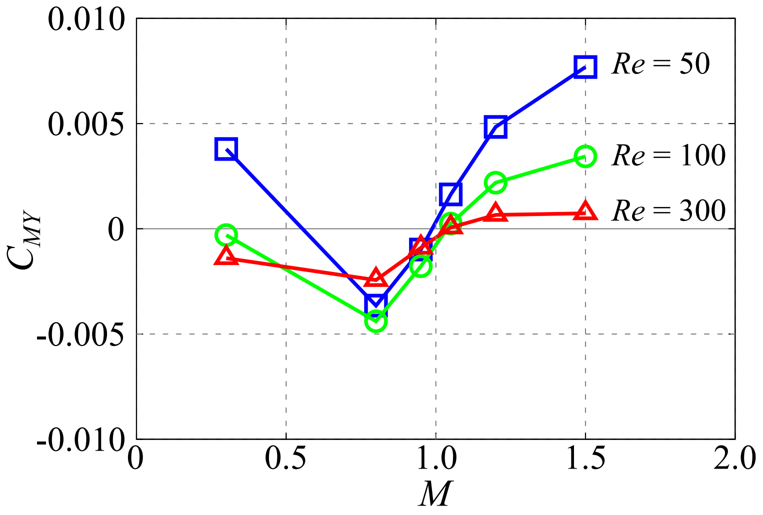

FIGURE 5.33: Effect of M on moment coefficient (around y-axis).

5.5 Conclusions

In chapter 5, the compressible low-Re flow over a rotating adiabatic sphere and the linear shear flow over a stationary adiabatic sphere were investigated by DNS of the three-dimensional compressible Navier–Stokes equations using a body-fitted grid with high-order schemes.

In the simulation of flow past a rotating sphere, the flow condition was $100 \le Re \le 300$, $0.2 \le M \le 2.0$, and $0 \le \Omega^* \le 1.0$. It was clarified that the vortex structure behind the sphere is influenced by Re, Ω^*, and M. In particular, vortex shedding is significantly reduced in supersonic flows. Also, under the subsonic and high-Ω^* conditions, the compressibility effect on the vortex structure appears strongly compared to the stationary cases. It is due to that the fluid velocity and the relative velocity between the fluid and the surface of the sphere is large in the retreating and advancing sides, respectively. The rotation-induced lift becomes large as Ω^* increases in each M. However, the increment of the lift coefficient becomes small as M increases. This is caused by the deceleration of the fluid velocity due to the attached shock waves formed on the retreating side. Also, the position of the stagnation point formed in the advancing side is influenced by M, moves downstream side as M increases. Hence, the rotation-induced lift becomes small as M increases. In addition, the moment coefficient around the rotation axis, which brakes rotation, increases along with M due to the effect of the attached shock wave on the retreating side and the increase of the viscosity coefficient around the sphere. These results mean that the effect of the particle rotation on the lift coefficient under compressible flows is smaller than that of the incompressible cases. To be summarized, at the higher-M conditions, the influence of the rotation on the wake, the lift and drag coefficients is reduced, and the rotation is easy to stop. Hence, it seems that the rotation effect is significantly reduced in supersonic conditions.

In the simulation of flow past a rotating sphere, the flow condition was $100 \leq Re \leq 300$, $0.3 \leq M \leq 2.0$, and $\alpha^* = 0.1$. The simulation results clarified that the significantly different characteristics of the shear-induced lift compared with that of the incompressible flows. In the case of the incompressible flows, the reverse of the shear-induced lift occurs at $Re \approx 50$ due to the change in the stress distribution on the sphere surface in the downstream side caused by the asymmetry of the recirculation region. Although a similar change in the flowfield was observed in the compressible regime, there is no reverse of the shear-induced lift for all M cases investigated in the present study. In the compressible case, the change in the stress distribution occurs in the dowsntream side and positive lift was generated in the downstream side despite $Re = 300$, but the larger negative lift is generated in the upstream side of the sphere at higher-M cases and it increases as M increases and becomes dominant in the shear-induced lift. The compressibility effect described by the Prandtl–Glauert transformation and the detached shock wave contribute to increase the negative lift on the sphere surface in the upstream side. These effects due to the influence of the compressibility increase the pressure coefficient in the upstream side of the sphere and the effects increases as M increases. Since the difference in the local M in the high-speed and low-speed sides, the lift force is generated in the direction from the high-speed side to the low-speed side. The negative lift becomes the maximum value at around the sonic speed because effect of the local M difference in the high-speed and low-speed sides is maximized at the transonic regime, and the M effect saturates at the supersonic conditions. The difference in the local M causes the change in the M evolution of the drag coefficient. The drag coefficient rapidly increases around the transonic regime in the uniform flow because of the wave drag and compressibility effect described by the Prandtl–Glauert transformation. However, the increment of the drag coefficient in the transonic regime is rounded in the linear shear flow because of the difference in the local M at the high-speed and low-speed sides.

The reverse in the pitching moment coefficient in the Re evolution occurs at $M = 0.3$ because of the change in the area of the attached region. The negative pitching moment is generated at higher-*Re* conditions. At the supersonic conditions, on the other hand, the pitching moment is positive regardless of *Re* because the position of the separation point in the high-speed side exists relatively downstream due to the stronger expansion wave. Also, the pitching moment at the transonic flow is negative with regardless of *Re*, despite the position of the separation point that exists relatively downstream side compared with the low-speed side. The negative pitching moment in this region seems to be caused by the detached and attached shock waves formed only on the high-speed side.

Chapter 6

Experimental Investigations at Higher-Reynolds-Number Conditions

List of Symbols

$\boldsymbol{A}$ = Data matrix

C_D = Drag coefficient

ΔC_D = Difference from drag model

D_w = Wake diameter at the end of the recirculation region

F_x = Force in the streamwise direction

M = Mach number

M_p = Particle Mach number

M_s = Shock Mach number

L_r = Length of recirculation region

L_s = Shock standoff distance

P = Pressure

Re = Reynolds number

Re_p = Particle Reynolds number

$\boldsymbol{S}$ = Singular value matrix

$\boldsymbol{U}$ = Matrix composed by left singular vectors

$\boldsymbol{V}$ = Matrix composed by right singular vectors

a = Sound speed

$\boldsymbol{a_n}$ = Data vectors

d = Diameter of sphere

f = Focal length

$\boldsymbol{s}$ = Singular value

t = Time

$\boldsymbol{u}$ = Left singular vector

u_p = Particle velocity

$\boldsymbol{v}$ = Right singular vector

x = Position in streamwise direction

μ = Focal length

θ_s = Separation point

ρ = Focal length

Subscripts

$_{\text{atm}}$ = Atmospheric quantities

6.1 Introduction

A sphere is one of the simplest three-dimensional body, but the flowfield and its properties of a sphere, such as wake structures, change in a complex manner with changing flow conditions. The flow over an isolated sphere has been studied experimentally (Taneda, 1956; Taneda, 1978; Sakamoto and Haniu, 1990; Magarvey and Bishop, 1961) and numerically (Johnson and Patel, 1999; Rodriguez et al., 2011) because it is interesting from the fluid physics point of view. In addition, knowledge of the flow over a sphere at low-Re has been utilized in multiphase flow models which are employed in numerical simulations of particle-laden flows (e.g., Schlichting and Gersten, 1960; Clift and Gauvin, 1971). For example, particle drag models based on experimental data were proposed in previous studies. In addition, the vortex structure produced by particles causes turbulent modulation and affects the particle distribution. Kajishima, 2004 showed that particle clusters are formed due to wake vortices produced by such particles in a numerical simulation of the incompressible flow regime. Hence, the effects of the wake vortices generated by particles might be important for accurate multiphase flow simulations. The studies of the flow over a sphere have contributed to the understanding of fundamental of flow dynamics and the modeling of complex problems. In chapter 3, we clarified the flow properties at $Re \leq 1,000$, but the transitional Re from steady to unsteady flows at supersonic conditions have only been found at $M = 1.2$. Studies on the compressible flow over a sphere have been investigated by free-flight experiments and wind tunnel experiments as described in chapter 3. Because of the difficulty of the experimental measurement due to the size of the test model and low atmospheric density, the drag coefficient was mainly investigated at compressible low-Re conditions and there is no visualization of the wake structure at $Re \leq O(10^4)$.

The sphere drag has also been investigated through interaction experiment between a planar-shock wave and sphere. Tanno et al., 2003; Sun et al., 2005 studied the interaction process of the planar-shock wave and sphere by the numerical simulations and the experiments using a vertical shock tube. They measured the time history of the drag force acted on the wire-suspended sphere in the vertical shock tube from the time-series data of the accelerometer. Jourdan et al., 2007 conducted the shock-particle interaction experiment with a small sphere suspended by thin wires taken from a spider web, and they estimated the sphere drag coefficient from the time-position data of the sphere. Wagner et al., 2012 reassessed the historical drag coefficient. The particle drag coefficients were measured by tracking the trajectories of 1-mm spheres in the shock-induced flow by the planar-shock at $M = 1.68, 1.93, 2.04$. However, studies on compressible low-Re flows are still much fewer than those on incompressible low-Re flows. The flow conditions of former studies by Jourdan et al., 2007 and Wagner et al., 2012 were at around $O(10^2) \leq Re \leq O(10^4)$ and $Re = O(10^4)$, respectively. However, they focused on the drag coefficient so that the flow dynamics have not been clarified at $O(10^3) \leq Re \leq O(10^4)$ in compressible flows, particularly supersonic flows.

It is important that the investigation of M and Re effects on the flow structure around a generic body such as a sphere to understanding fluid mechanics under compressible low-Re conditions. In this chapter, the flow over an isolated sphere is investigated at $O(10^3) \leq Re \leq O(10^5)$ in the subsonic to supersonic conditions. The experiments are carried out using a ballistic range and shock tube, and flow visualizations are conducted by the schlieren technique at the low-pressure conditions with small test models to archive the compressible low-Re conditions. Also, the modal decomposition is applied to extract the characteristic mode of the wake structure. In the free-flight experiments, the effects of M and Re on the flow structures, such as the recirculation region, wake structure, and so on, are investigated. In the shock-particle interaction experiments, the development of the flowfleld is observed, and the time-averaged drag coefficient is estimated.

6.2 Experimental Methods

6.2.1 Free-Flight Experiments

Optical System

The experimental setup for the free-flight experiments is shown in figure 6.1. The distance between the exit of the blast tube and optical windows used for schlieren visualization was 5.0 m. The light source was a metal-halide lamp (LS-M210, Sumita) or xenon flash lamp, and its light beam was narrowed to a point light source of 4.0 or 5.0 mm in diameter by an optical diaphragm. The diameter of the point light source was larger than that typically used in order to increase the image intensity. The light beam was parallelized by a concave mirror with a focal length of 3,000 mm, and the light beam was converged by the same concave mirror. The bottom 40% of the converged light beam was horizontally cut by a knife-edge placed at the focal point and imaged by a convex lens with a focal length of 250, 500, or 600 mm. The pixels per diameter of the sphere (ppd) in the original image was 8–28 depending on the combination of the focal length of the imaging lens and the diameter of the sphere. Also, the test duration is depending on the focal length f of the imaging lens and the free-flight M. For example, the field of view in the streamwise direction for $f = 600$ mm was 75 mm, and thus the duration for imaging was approximately 155 μs at $M = 1.4$ in that optical setup. A high-speed camera (HPV-X, Shimadzu) was used to take time-series schlieren images. The frame rate was 100,000–500,000 fps and the exposure time was 300–500 ns. The high-speed camera and the light sources were triggered by a signal from a pressure transducer (603B, Kistler) installed in front of the gas chamber. However, because the pressure change produced by a detached shock wave was small for a small sphere, a laser-cut measurement system installed at the exit of the blast tube was used for the case of $d \leq 2.0$ mm.

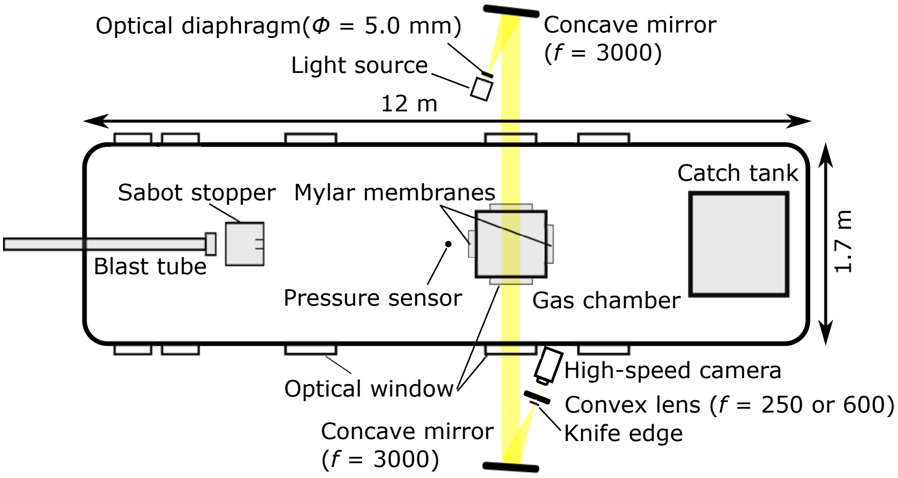

FIGURE 6.1: Schematic diagram of the optical system for free-flight experiments.

The sabot was separated from the test model by the sabot stopper, which was placed 50 cm downstream of the exit of the blast tube. Also, a gas chamber with optical windows was installed in the test section and flow visualization under low-pressure conditions was conducted inside of the gas chamber, so that the compressible low-Re condition could be achieved. The upstream and downstream apertures were sealed by Mylar membranes, which are broken during the flying test model.

The driver gas of the single-stage light gas gun was Helium gas of normal temperature and its pressure was up to 25 MPa. The dominant parameters on the launch velocity of the sabot are the pressure of the driver gas and the total mass of the sabot and projectile. In the present study, the mass of the projectile is sufficiently smaller than that of the sabot, thus, the pressure of the driver gas was determined by only the target launch velocity.

Experimental Conditions

Bearing balls 1.5–10.0 mm in diameter was used as the projectile. The surface roughness of the projectile was less than 0.04 µm. The sphere was launched with a cylindrical splitting sabot made from ultrahigh-molecular-weight polyethylene, as shown in figure 6.2. The test conditions are shown in table 6.1. In the present study, M and Re were changed by changing the free-flight speed, the pressure in the visualization section, and the diameter of the sphere. The conditions investigated in this experiment were $3.9 \times 10^3 \leq Re \leq 3.8 \times 10^5$ and $0.9 \leq M \leq 1.6$. The temperature in the visualization section was assumed to be the same as that of the test section due to the structure of the experimental equipment. However, the volume of the gas chamber was sufficiently small and there was more than 30 minutes of the temperature stabilization time due to the experimental procedure so that the temperature in the test section and the visualization section seems to be equivalent.

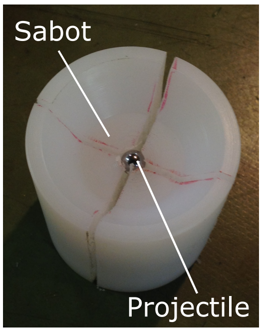

FIGURE 6.2: Projectile and sabot.

Mach number $M = u/a$	Diameter of sphere d mm	Pressure at visualization section P/P_{atm}	Reynolds number $Re = \rho u d/\mu$
0.9	9.53	1.0	186,700
0.97	9.53	1.0	201,700
1.04	10.0	1.0	222,300
1.13	1.5	0.1	3,900
1.14	9.53	0.2	52,300
1.15	1.5	0.2	7,400
1.18	2.0	0.2	10,100
1.18	2.0	0.34	18,500
1.2	2.0	0.1	5,600
1.21	2.0	1.0	56,900
1.21	9.53	1.0	251,200
1.21	2.0	0.34	18,100
1.23	10.0	1.0	325,700
1.26	2.0	0.1	5,700
1.32	2.0	0.2	12,300
1.39	3.0	1.0	102,600
1.39	9.53	0.1	35,500
1.4	3.0	0.34	31,500
1.4	3.0	1.0	89,300
1.41	1.5	0.1	4,400
1.41	9.53	0.2	58,300
1.41	9.53	0.34	106,100
1.41	9.53	0.2	73,100
1.42	1.5	0.2	9,500
1.42	3.0	0.34	28,700
1.44	2.0	1.0	68,900
1.45	2.0	0.34	24,700
1.45	3.0	0.34	30,000
1.45	9.53	0.34	100,600
1.45	9.53	0.34	103,900
1.45	9.53	1.0	311,000
1.48	2.0	0.1	8,100
1.48	2.0	0.2	15,400
1.49	10.0	0.34	101,400
1.51	9.53	0.1	31,500
1.54	6.5	0.34	65,300
1.55	6.5	0.34	72,100
1.55	10.0	1.0	360,600
1.58	10.0	1.0	381,500

Table 6.1: Flow conditions for free-flight experiments.

Image Processing

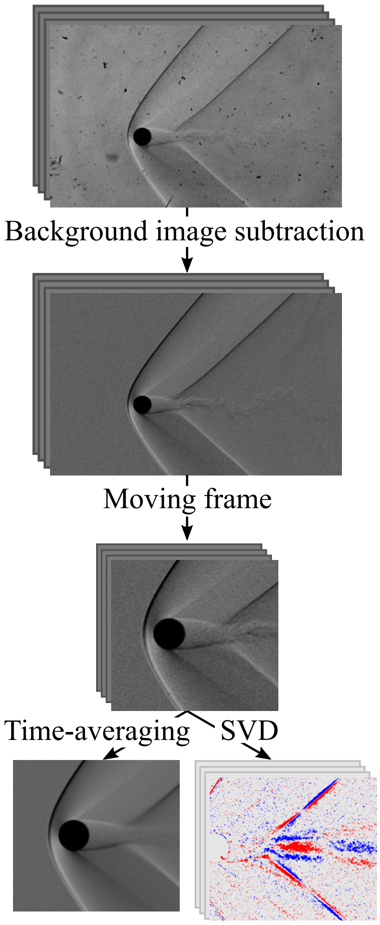

FIGURE 6.3: Image processing procedure.

The size of the sphere and the atmospheric pressure were reduced to decrease Re. In such situations, the sensitivity of schlieren visualization becomes low because the wake width and the density fluctuations of the gas decrease. Therefore, the image processing procedure shown in figure 6.3 was applied to investigate the flow structure, particularly the wake vortices. The test model crosses the visualization section during a free-flight measurement test so that the test-model fixed-visualization images were acquired using a moving frame based on image correlations. The image around a sphere excluding the bow shock and wake, which were cropped from instantaneous visualization images, was used as the template image. In addition, the background image subtraction was conducted to remove scratches on the optical window from the visualization images. The background image was the averaged image in the visualization section before the projectile arrived. The mage resolution enhancement was carried out by the bicubic method (Keys, 1981).

Time-averaging and singular-value decomposition (SVD) (Golub and Loan, 1983) were applied to investigate the effect of M and Re on the mode of the wake structure, respectively. In the time-averaged image, the effect of the M and Re on the shock standoff distance L_s, the position of the separation point θ_s, the length of the recirculation region L_r, and the wake diameter at the end of the recirculation region D_w were investigated as shown in figure 6.4. Here, the position of the separation point and the length of the recirculation region are expressed as the angle from the upstream stagnation point and the distance between the downstream stagnation point and the end of the recirculation region, respectively. The position where the separated shear layer and the expansion wave are generated on the surface of the sphere is almost the same for high-Re conditions. Therefore, in the present study, the position of the separation point was determined by the position of the expansion waves in the time-averaged schlieren image. Also, the end of the recirculation region was determined as the position with a minimum wake diameter. All the length scales were normalized based on the diameter of the sphere.

In the SVD analysis, data matrix $\boldsymbol{A}$ is decomposed to left singular vectors $\boldsymbol{U}$, the singular value matrix $\boldsymbol{S}$, and right singular vectors $\boldsymbol{V}$. In turn, these denote the time variation of each mode as follows:

$$\boldsymbol{A} = \boldsymbol{U}\boldsymbol{S}\boldsymbol{V}^\mathrm{T} \tag{6.1}$$

where for n mages,

$$\boldsymbol{A} = \begin{bmatrix}\boldsymbol{a}_1 \cdots \boldsymbol{a}_n\end{bmatrix}, \boldsymbol{U} = \begin{bmatrix}\boldsymbol{u}_1 \cdots \boldsymbol{u}_n\end{bmatrix}, \boldsymbol{S} = \begin{bmatrix} s_1 & 0 & \cdots & 0 \\ 0 & \ddots & 0 & \vdots \\ \vdots & 0 & \ddots & 0 \\ 0 & \cdots & 0 & s_n \end{bmatrix}, \boldsymbol{V} = \begin{bmatrix}\boldsymbol{v}_1 \cdots \boldsymbol{v}_n\end{bmatrix} \tag{6.2}$$

where $\boldsymbol{u}$ and $\boldsymbol{v}$ are the left and right singular vectors for each mode, which is the eigenvectors of $\boldsymbol{A}\boldsymbol{A}^\mathrm{T}$ and $\boldsymbol{A}^\mathrm{T}\boldsymbol{A}$, respectively, and s represents the singular values, which are the absolute values of the eigenvalues of matrix $\boldsymbol{A}$. These values represent the square root of the energy of each mode. In the present study, the number of frames acquired for obtaining the time-averaged field and SVD mode was more than 15 frames, which includes more than two periods of the low-frequency wake oscillation. Note that the number of frames is depending on the framerate, angle of view (focal length of imaging lens), and velocity and diameter of the sphere. The effect of data length in the time direction on the extracted SVD modes is shown in Appendix B.2.

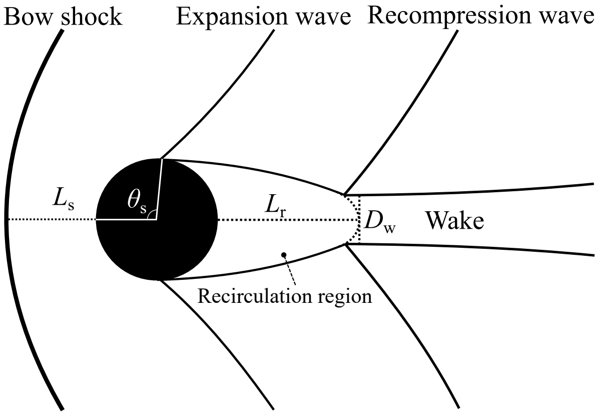

FIGURE 6.4: Schematic diagrams of flow structures.

6.2.2 Shock-Particle Interaction Experiments

Optical System

Figure 6.5 shows the optical system for the schlieren visualization of the shock-particle interaction experiments. The point light source was generated by a xenon flash lamp or metal-halide lamp (LS-M210, Sumita) with an optical diaphragm with a diameter of $\phi = 4$ mm. The light beam was collimated by a concave mirror with a focal length of $f = 3,000$ mm and converged by the same concave mirror. The bottom 40% of the light beam was horizontally cut by a knife-edge placed at the focal point of the concave mirror. A imaging lens was a convex lens with a focal length of $f = 1,000$ or 1,500. A high-speed camera (HPV-X, Shimadzu) was used for visualization experiments, and a high-speed camera (SA-X2, Photron) was used for drag estimation experiments. Table 6.2 shows the camera settings. The frame rate was set to be sufficiently high to capture the instantaneous flow structures, particularly wake structure. In the case of the drag estimation experiment, on the other hand, longer recording times with wide view angle images are required so that the different camera was used for each experiment.

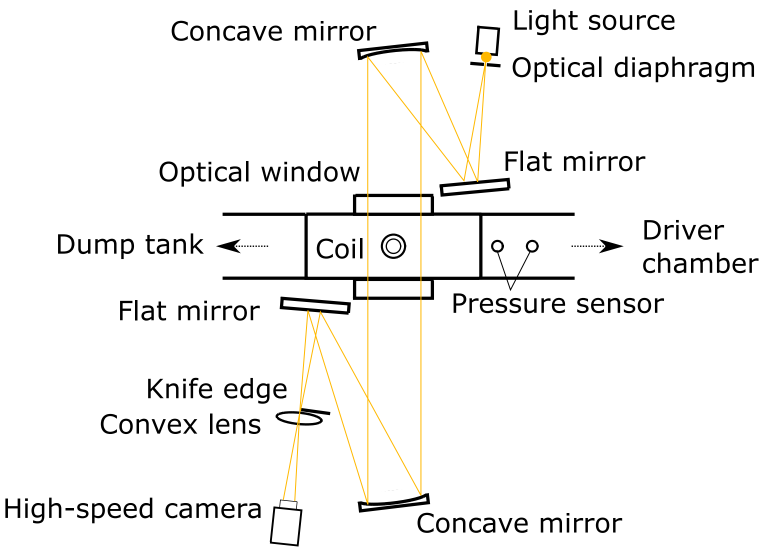

FIGURE 6.5: Schematic diagram of the optical system for shock-particle interaction experiments.

	Flow visualization	Drag estimation
Visualization method	Schlieren method	Shadow graph
Light source	Xenon flash lamp	Metal-halide lamp
Focal length of imaging lens f [mm]	1,000	1,500
Camera	HPV-X	SA-X2
Exposure time [µs]	0.4	50
frame rate [fps]	100K–1M	12K–20K
Number of pixels	400×250	1024×888 1024×512
Spatial resolution	100 µm/pixel	34.5 µm/pixel

TABLE 6.2: Settings for optical system of the shock-sphere interaction experiments.

Sphere Drop-Off System

Figure 6.6 shows the sphere drop-off system immersed in the upper wall of the shock tube. The sphere drop-off system was consists of a drop-off port, coil, and electric circuit for the coil. The sphere was held on the drop-off port by magnetic forces generated by the coil. Here, the sphere was placed in the small hollow on the drop-off port for the stability of its position. Also, the iron core of the coil and sphere was separated to minimizing the effect of the residual magnetic field and to retain airtightness. Figure 6.7 shows the flowchart of the execution sequence. The master trigger was generated by the function generator. The two TTL signals which were for the coil and for the solenoid valve of the shock tube were generated with a certain time difference. The normally-opened and normally-closed relay circuits were included in the electric circuits of the coil and normally-closed solenoid valve. The solenoid valve was for the operation of the shock tube. The electric circuit of the coil and solenoid valve were closed and opened by the trigger TTL signals generated by the function generator. In the present study, the electrical circuit for the coil was cutoff first, and then the electrical circuit for the solenoid valve was connected with a certain delay to adjust the interaction position of the shock and sphere. The imaging system was consists of a high-speed camera and light source. The light source for the flow visualization (xenon flash lamp) and a high-speed camera were triggered by the pressure rise caused by the incident shock captured by a pressure transducer (Type 603B, Kistler), and the trigger signal was generated by an scopecorder (DL750, Yokogawa). In addition, two pressure transducers were mounted on the upper wall of the shock tube in the upstream of the test section with known clearance, and thus the shock speed can be calculated.

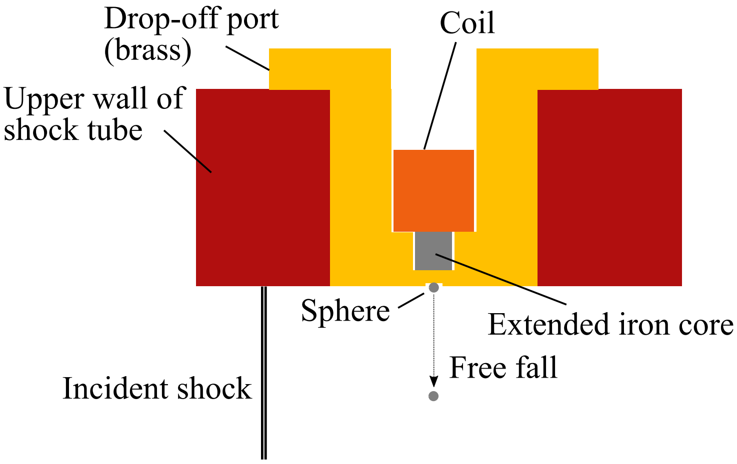

Figure 6.6: Schematic diagrams of the drop-off system of a sphere.

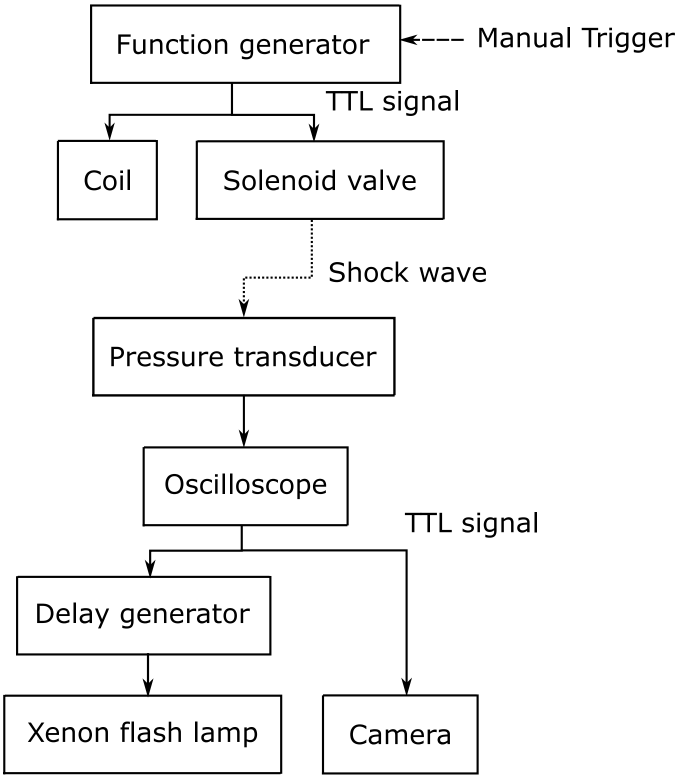

FIGURE 6.7: Flowchart of experimental sequence of shock-sphere interaction experiments.

Experimental Conditions

Experimental conditions for the flow visualization and the drag estimation are shown in tables 6.3 and 6.4, respectively. The flow visualization experiments were conducted at the subsonic, transonic, and supersonic conditions behind the incident shock. The drag estimation experiments were conducted at the subsonic condition behind the incident shock. The driver gas of the shock tube was Nitrogen and Helium for the subsonic and the transonic and supersonic conditions, respectively.

Shock Mach number M_s	1.42, 2.02, 2.64
Particle Mach number behind incident shock M_p	0.53, 0.98, 1.24
Pressure behind incident shock P/P_atm	0.72, 0.79, 0.43
Diameter of sphere d [mm]	1.0, 1.5
Particle Reynolds number behind incident shock Re_p	4,000–14,000

TABLE 6.3: Experimental conditions for flow visualization of shock-sphere interaction experiments.

Shock Mach number M_s	1.42
Particle Mach number behind incident shock M_p	0.53
Pressure behind incident shock P/P_atm	0.72
Diameter of sphere d mm	0.5, 0.7, 1.0, 1.5
Particle Reynolds number behind incident shock Re_p	3,000–9,200

TABLE 6.4: Experimental conditions for drag estimation through shock-sphere interaction experiments.

Test models are shown in figure 6.8. Spheres $0.5 \leq d \leq 1.5$ in diameter made of high-carbon chromium steel (SUJ2) and tungsten carbide were used as a test model. The surface roughness was less than 0.04 µm.

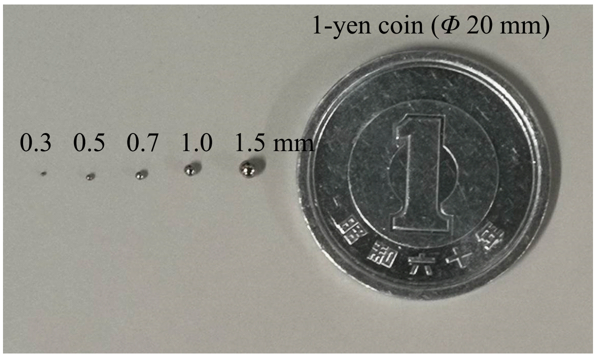

FIGURE 6.8: Test model for shock-sphere interaction experiments.

6.3 Results and Discussion of Free-Flight Experiments

6.3.1 Instantaneous Flowfield

The wake of a sphere in an incompressible flow (Sakamoto and Haniu, 1990; Johnson and Patel, 1999) is unsteady, with hairpin vortex shedding at around $Re \geq 280$, and large-scale oscillation in the wake appears at around $Re \geq 700$. High-Re condition produce the wake oscillation and hairpin vortices called the "low mode" and "high mode", respectively (Makita, 2007). The Strouhal number for the low mode is constant at approximately 0.2 and the frequency of the high mode increases as Re increases.

In the present study, conditions with high-M and low-Re conditions were realized using a small test model and a low-pressure visualization section. However, the sensitivity of schlieren visualization decreases as the atmospheric density decreases. Also, the image resolution against the flow structure decreases as the size of the test model decreases. Figure 6.9 shows the influence of the gas density at the visualization section on the instantaneous schlieren images for $M \approx 1.4$. This figure demonstrates that the density at the visualization section has a large impact on visualization. Note that the density effect includes not only a decrease in the sensitivity of schlieren visualization but also a decrease of Re. In figure 6.9(a), the bow shock, the expansion wave, the recompression wave, the recirculation region, and the wake structure are visualized. Particularly, the hairpin (high-mode) structure in the wake can be observed in the low-mode structure in the near field. Conversely, in figure 6.9(b), the high-mode structure cannot be observed, but the low-mode structure can be. In figure 6.9(c), the low-mode structure can be observed in the near field, but the wake structure is not noticeable in the schlieren image farther from the sphere. In figure 6.9(d), the wake structure cannot be seen. Moreover, the edge of the recirculation region, the bow shock, and the recompression wave also become unclear in this low-density condition.

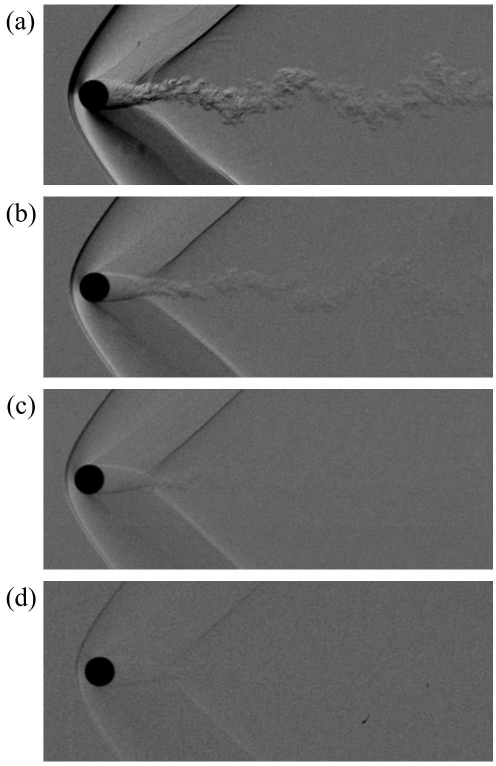

Figure 6.9: Influence of gas density in the visualization section the on instantaneous schlieren images at $M \approx 1.4$: (a) $P/P_{\mathrm{atm}} = 1.0$ ($Re = 3.1 \times 10^5$), (b) $P/P_{\mathrm{atm}} = 0.34$ ($Re = 1.0 \times 10^5$), (c) $P/P_{\mathrm{atm}} = 0.21$ ($Re = 7.3 = \times 10^4$), and (d) $P/P_{\mathrm{atm}} = 0.10$ ($Re = 3.6 \times 10^4$).

Figure 6.10 shows the influence of the image resolution in terms of ppd in instantaneous schlieren images for $M \approx 1.45$ and the pressure at the visualization section of $P/P_{\mathrm{atm}} = 0.34$. In this figure, images were produced with an imaging lens focal length of $f = 250$ mm and sphere diameters of $d = 9.53$, 6.5, and 3.0 mm. Note that figure 6.10 shows the case with the lowest resolution in this study, that is, ppd = 8. It can be seen that the small test model makes it difficult to visualize fine-scale structures due to reduced image resolution against the size of flow structures. However, the main flow structure can be visualized even at a resolution as low as ppd = 8, as shown in figure 6.10(c). Note that the effect of decreasing the size of the test model includes not only a decrease in the image resolution but also a decrease in Re.

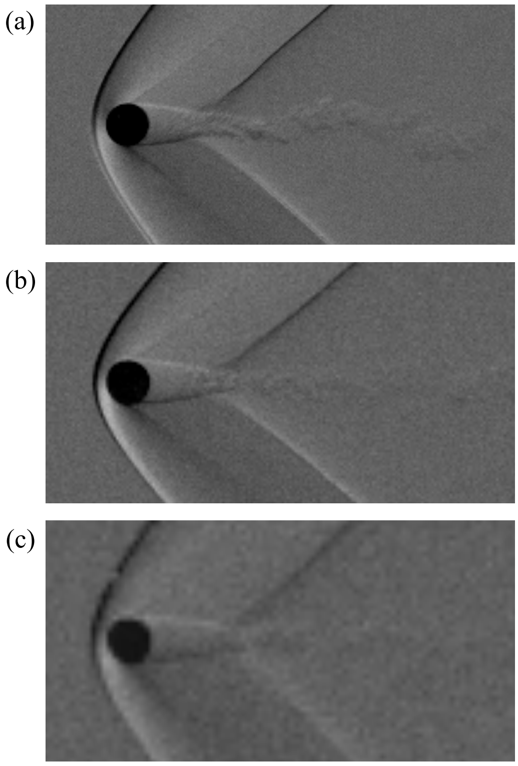

Figure 6.10: Influence of pixels per diameter (ppd) on the instantaneous schlieren images at $M \approx 1.45$ and $P/P_{\mathrm{atm}} = 0.34$: (a) ppd = 25 ($Re = 1.0 \times 10^5$), (b) ppd = 17 ($Re = 7.2 \times 10^4$), and (c) ppd = 8 ($Re = 2.9 \times 10^4$).

6.3.2 Effect of Mach and Reynolds numbers on Instantaneous Flowfield

Mode decomposition using SVD analysis was applied to the time-series visualization images to investigate the wake structure. The instantaneous flowfield and reconstructed images for $M = 0.9$ and $Re = 1.9 \times 10^5$ are shown in figure 6.11 as an example. Figure 6.11(a) is the instantaneous image, figure 6.11(b) is the reconstructed image for the first SVD mode, and figures 6.11(c)–(f) are the spatial mode for the second to fifth SVD modes. The first mode is similar to the time-averaged field, and characteristic modes of the fluctuation component are decomposed into higher SVD modes. In the present study, SVD analysis was applied to the time-series schlieren images and with the knife edge placed in a horizontal orientation, so that the low- and high-intensity regions are inverted at the horizontal centerline even though the flowfield is symmetric. Therefore, symmetric (asymmetric) flow modes in the horizontal direction are decomposed as asymmetric (symmetric) SVD modes. In figure 6.11, the oscillation of the separated shear layer and the recompression wave are extracted in the second mode. Also, the large-scale helical mode and the symmetric mode are decomposed in the third and fourth modes, respectively. The characteristic and lower modes were chosen for each case in figures 6.12 and 6.13.

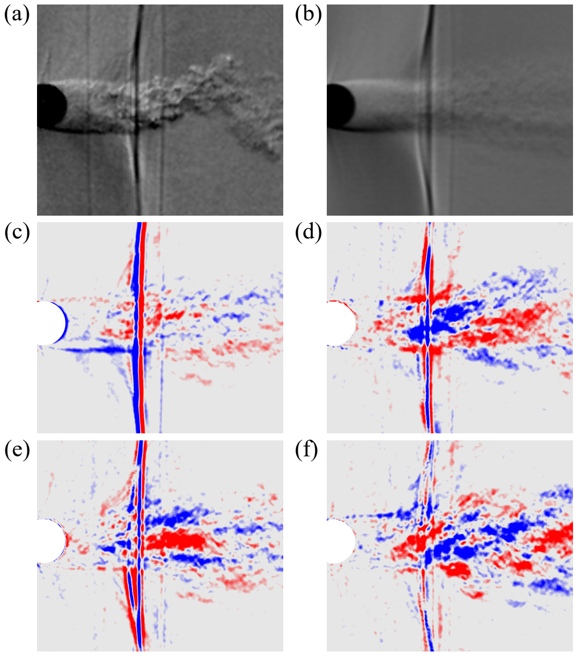

FIGURE 6.11: Example of the result of mode decomposition using SVD. (a) Instantaneous flowfield and (b)–(f) reconstructed images for $M = 0.9$, $Re = 1.9 \times 10^5$. Reconstructed images for the first mode and spatial mode for modes 2–5 are shown in (b) and (c)–(f), respectively.

The instantaneous flow structures for $M = 0.9$, 1.21 and, 1.39 are shown on the left-hand side of figure 6.12. For $M = 0.9$, weak shock waves are formed on the surface of the sphere. Also, recompression waves are formed downstream of the sphere and these shock waves are almost vertical. In addition, a change in the wake structure occurs near the recompression waves and a large-scale oscillation can be seen in the wake. As M increases, a detached shock wave is formed upstream of the sphere and the angle of the expansion and recompression waves decreases. In addition, the oscillation of the wake structure decreases as M increases. The right-hand side of figure 6.12 shows an image of the characteristic and energetic modes computed by SVD. The oscillation of the wake structure and recompression wave can be seen in the right-hand side of figure 6.12. For $M = 0.9$ and 1.39, the helical and alternating modes are extracted at the wake, and the oscillation is related to that of the recompression wave. The helical mode is extracted also at $M = 1.21$, but it seems to have an intermediate structure between helical and alternating modes and thus the helical modes ware not observed in higher-M conditions. These results show that the mode of the wake structure is significantly changed by M, and different wake structures can be identified by SVD. The change in the wake structure due to the M effect seems to be caused by the expansion wave because the direction of the flow near the recirculation region is forced by the flow directed by the effect of the expansion wave. In addition, the effect of the expansion wave becomes strong as M increases so that the wake seems to be stabilized.

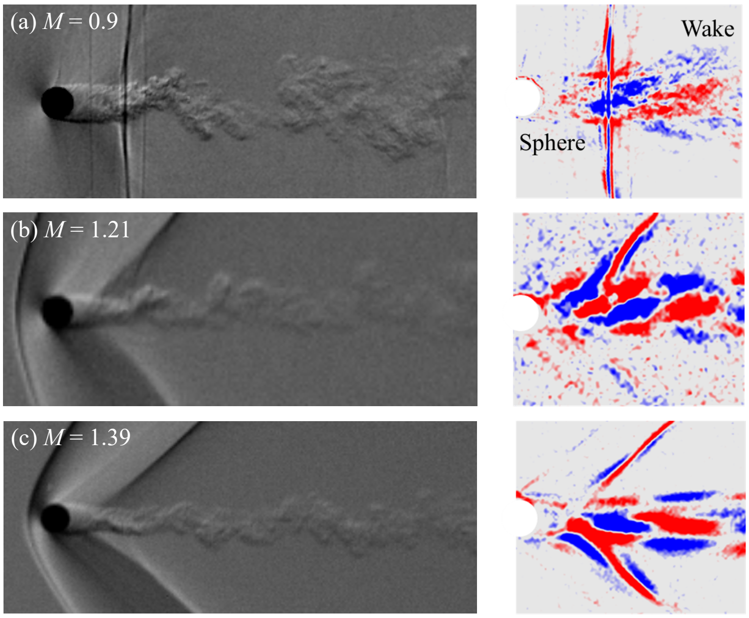

FIGURE 6.12: Influence of M on the instantaneous flowfield and the spatial mode: (a) $M = 0.9, Re = 1.9 \times 10^5$ ($P/P_{\mathrm{atm}} = 1.0$), (b) $M = 1.21, Re = 5.7 \times 10^4$ ($P/P_{\mathrm{atm}} = 1.0$), and (c) $M = 1.39, Re = 1.0 \times 10^5$ ($P/P_{\mathrm{atm}} = 1.0$).

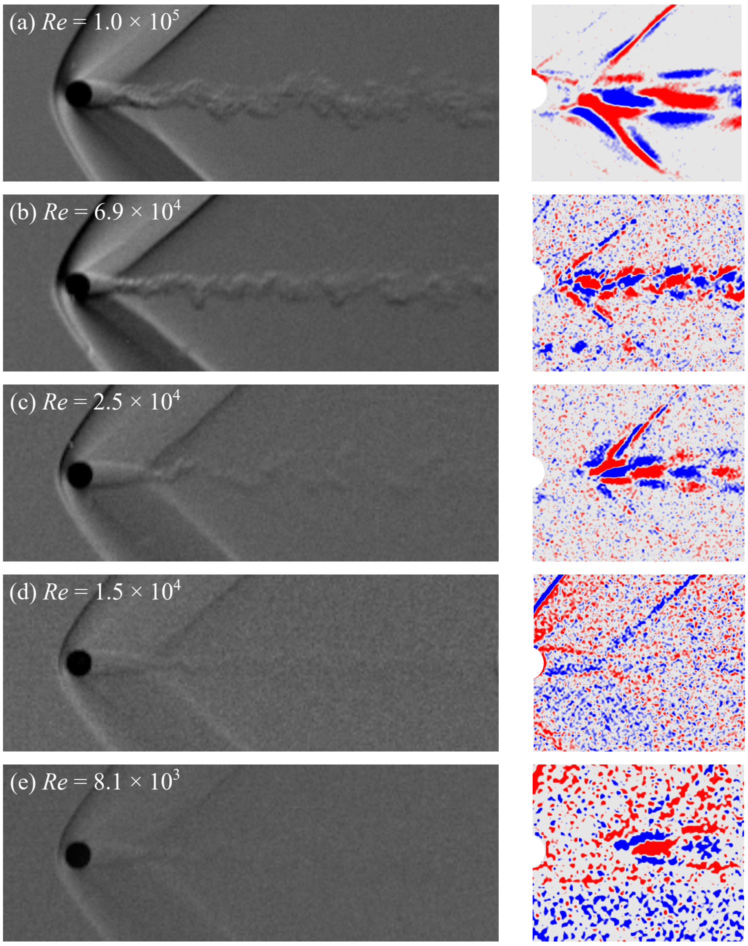

FIGURE 6.13: Influence of Re on instantaneous flowfield and spatial mode for $1.39 \leq M \leq 1.48$: (a) $Re = 1.0 \times 10^5, M = 1.39$ ($P/P_{\text{atm}} = 1.0$), (b) $Re = 6.9 \times 10^4, M = 1.44$ ($P/P_{\text{atm}} = 1.0$), (c) $Re = 2.5 \times 10^4, M = 1.45$ ($P/P_{\text{atm}} = 0.34$), (d) $Re = 1.5 \times 10^4, M = 1.48$ ($P/P_{\text{atm}} = 0.21$), and (e) $Re = 8.1 \times 10^3, M = 1.48$ ($P/P_{\text{atm}} = 0.1$).

The left-hand side of figure 6.13 shows instantaneous flowfields for the different Re at $M \approx 1.4$. The low-frequency oscillation of the wake and the hairpin structures in the large-scale structures can be seen in the case of $Re = 1.0 \times 10^5$ and $Re = 2.5 \times 10^4$. However, the low-frequency oscillation of the wake structure cannot clearly be seen in the cases of $Re = 6.9 \times 10^4$ and $Re = 1.5 \times 10^4$. In addition, the wake structure was not noticeable due to the low-density condition for $Re = 8.1 \times 10^3$. The spatial modes are shown on the right-hand side of figure 6.13, which permits us to investigate Re effect on the wake structure. By using the SVD, we can visualize the characteristic structures and the effect of Re on the mode of the wake structure. A similar structure, which is the alternating mode, can be seen in all cases except

$Re = 1.5 \times 10^4$, but the scale of the structure is different. The difference in the scale of the wake for the same M seems to be caused by the difference in the frequency of the oscillation of the low-mode structure. The scale in the structure on the extracted mode for $Re = 1.0 \times 10^5$ is large compared to other cases because the low-frequency oscillation of the wake is dominant. However, finer-scale structures can be seen in the lower modes at $Re = 6.9 \times 10^4$, because there is no low-frequency wake oscillation. Also, the scale of the wake structure for $Re = 2.5 \times 10^4$ is smaller than that for $Re = 1.0 \times 10^5$ but larger than that for $Re = 6.9 \times 10^4$. However, the characteristic mode, such as that the extracted from other cases, does not appear up to 5th mode in the case of $Re = 1.5 \times 10^4$. This means that the noticeable periodic mode does not exist when $Re = 1.5 \times 10^4$. In the case of $Re = 8.1 \times 10^3$, the reconstructed image is noisy because density fluctuation is smaller than other cases due to lower-density conditions and small diameter of the sphere. However, the alternating mode can be found even though such unclear schlieren images.

We investigated the effect of M and Re on the wake vortices at $0.3 \leq M \leq 2.0$ and $50 \leq Re \leq 1000$ in chapter 3. These studies showed that the wake for at the supersonic and transonic conditions for $Re =\leq 300$ is stable compared with that of the incompressible flow. For example, the wake structure under incompressible flows for $Re = 1,000$ is a helical wake. Under supersonic flow, in contrast, the wake structures for $M = 1.2$ and $M = 2.0$ at $Re = 1,000$ were a hairpin wake and a steady axisymmetric wake, respectively. These wake structures are similar to those of $270 \leq Re \leq 420$ and $20 \leq Re \leq 210$ under incompressible flows, respectively (Sakamoto and Haniu, 1990; Johnson and Patel, 1999). This fact suggests that the wake structure for $Re \leq O(10^4)$ in supersonic flows is similar to that of incompressible flows for lower Re. In the present study, the gas density in the visualization section was reduced to decrease Re so that the smaller-scale structure disappears from the schlieren image as the gas density (Re) decreases shown in figure 6.9. It is due to the decrease in the sensitivity of the schlieren method. However, the SVD results indicated that the smaller scale becomes dominant instead of the low-frequency wake oscillation as Re (gas density) decreases. Therefore, we considered that the change in the wake structure is due to the effect of Re.

6.3.3 Time-Averaged Flowfield

The main structure of the flowfield and its characteristic parameters were investigated with the time-averaged field. Numerical results discussed in chapter 3 indicated that the shock standoff distance, the separation point, and the length of the recirculation region are influenced not only by M but also by Re for $Re \leq 1,000$. In the present study, those three parameters were extracted from the time-averaged images and compared to the previous result in the different Re conditions.

The time-averaged field obtained in this study for $M \approx 1.45$ is shown in figure 6.14. Here, the image resolution with respect to the diameter of the sphere is different in each image: figures 6.14(a) ppd = 25, figure 6.14(b) ppd = 17, and figure 6.14(c) ppd = 8. In figure 6.14, the main flow structures are clearly visualized even in low-ppd cases. The effect of Re can be seen in the length of the recirculation region and the position of the recompression wave. The positions of the end of the recirculation region and the recompression wave moved downstream as Re decreases.

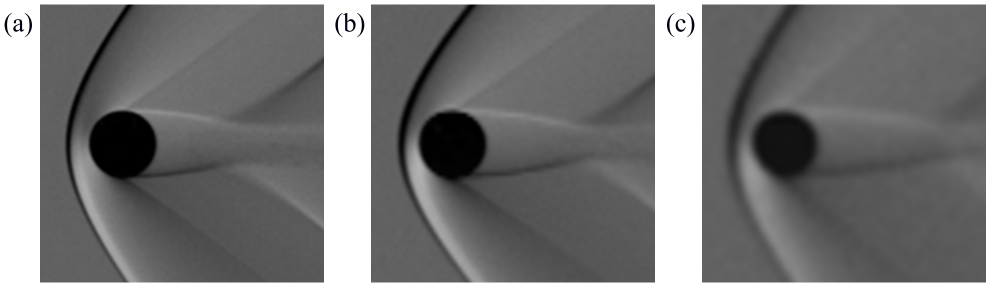

FIGURE 6.14: Time-averaged near-field structures for $M \approx 1.45 at P/P_{\text{atm}} = 0.34$: (a) $Re = 1.0 \times 10^5$ (ppd = 25), (b) $Re = 7.2 \times 10^4$ (ppd = 17), and (c) $Re = 2.9 \times 10^4$ (ppd = 8).

Figure 6.15 shows the relationship between M and the shock standoff distance. The present results are compared to the empirical formula by Ambrosio and Wortman, 1962, which is based on experimental results using a cone-sphere model. Figure 6.15 indicates that the trend of M dependence obtained by the present study shows good agreement with the empirical formula. For $Re \leq 10^3$, the shock standoff distance changes not only with M but also with Re due to the influence of the change in the boundary layer (displacement) thickness as discussed in chapter 3.

In contrast, figure 6.15 illustrates that the *Re* has no clear influence at $10^3 \leq Re \leq 10^5$ because the boundary layer is sufficiently thin under the conditions used in this study.

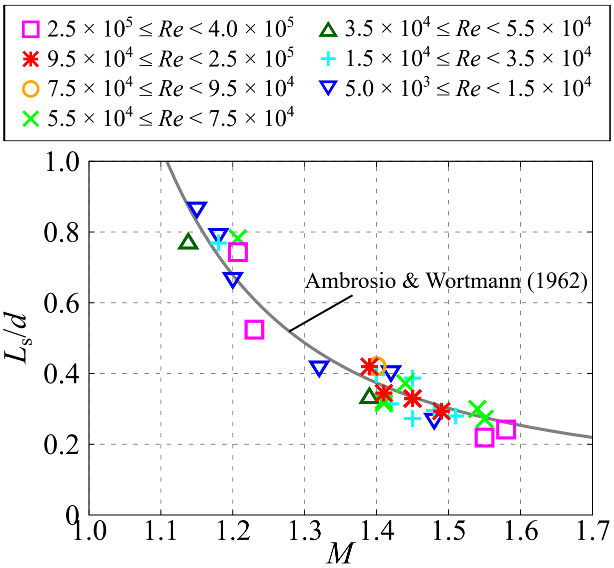

FIGURE 6.15: Effect of M on the shock standoff distance.

Figures 6.16 and 6.17 show the *Re* dependence on the position of the separation point and the length of the recirculation region. The results were compared with previous numerical studies of incompressible (Johnson and Patel, 1999; Rodriguez et al., 2011) and compressible flows (chapter 3). Figure 6.16 shows that the position of the separation point strongly depends on *Re* at $Re \leq O(10^3)$. However, the *Re* dependence becomes weak at $Re \geq O(10^3)$. The influence of M is also weak under supersonic conditions, but the difference between transonic and supersonic conditions appears because the flow separation is induced by the expansion wave, and its position is different under transonic and supersonic conditions.

Figure 6.17 illustrates that the length of the recirculation region increases as *Re* increases at $Re \leq O(10^3)$, but decreases as *Re* increases at $Re \geq O(10^3)$. Hence, an inflection point exists at around $Re = O(10^3)$, which seems to change the flow regime. Also, the inflection point and the maximum length of the recirculation region strongly dependent on M as discussed in chapter 3. It is considered that the M dependence is due to a change in the stability of the mixing layer between the recirculation region and the outer flow of the recirculation region, together with a change in the properties of the expansion wave.

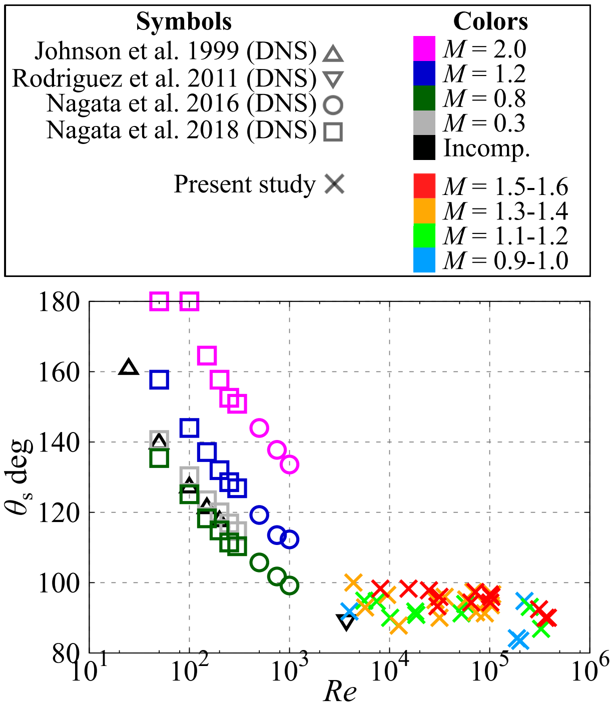

FIGURE 6.16: Effect of Re on the position of separation point.

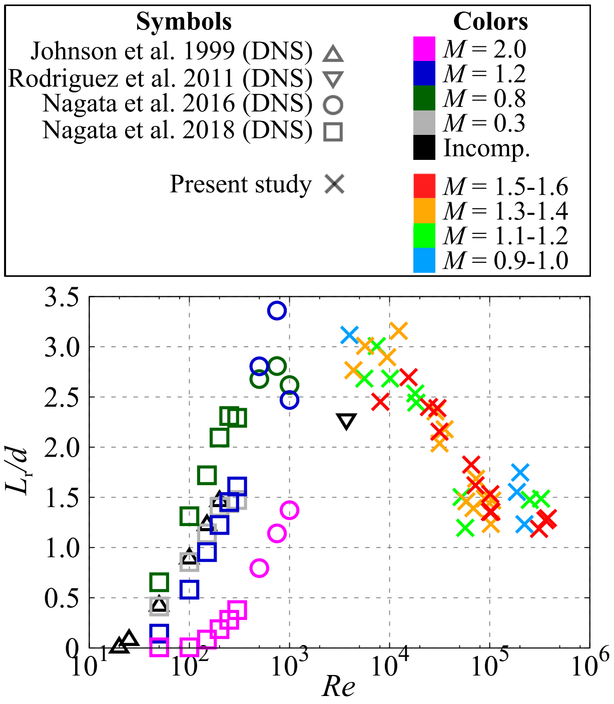

FIGURE 6.17: Effect of Re on the length of the recirculation region.

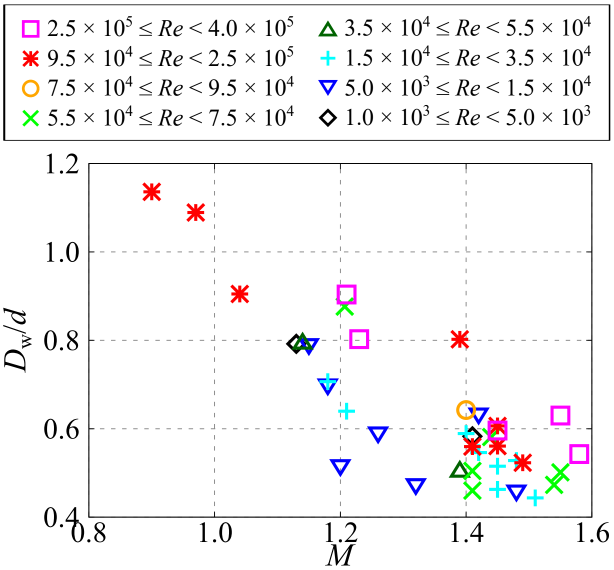

FIGURE 6.18: Effect of Re on the wake diameter at the end of the recirculation region.

Taneda, 1978 found that the wake of the sphere in incompressible flows begins wave motion for $O(10^4) \leq Re \leq 3.8 \times 10^5$. In contrast, the wake structure in compressible flows is influenced not only by Re but also by M. Particularly, the oscillation of the wake structure is suppressed under supersonic conditions. This study indicated that the diameter of the wake at the end of the recirculation region is related to the amplitude of the wake oscillation. The effect of M on the wake diameter at the end of the recirculation region D_w in the time-averaged field is shown in figure 6.18. The figure indicates that the diameter of the wake at the end of the recirculation region becomes small as M increases. The shape of the recirculation region under supersonic and lower-speed conditions are different because the behavior of the separated shear layer released from the sphere surface is different due to the presence or absence of the expansion wave formed near the separation point. For high-M conditions, the flow in the direction along the sphere surface is introduced by the expansion wave and it creates a recirculation region with a conical shape. Hence, the wake diameter at the end of the recirculation region decreases and the wake oscillation is reduced as M increases. Also, figure 6.19 illustrates that the wake diameter at the end of the recirculation region decreases as Re decreases. The same trend can be seen for the lower-Re conditions of $Re \leq 300$ in the supersonic flow as discussed in chapter 3. The shape of the recirculation region at $Re \leq 300$ is conical for steady flows in $0.3 \leq M \leq 2.0$.

Conversely, a barrel-shaped recirculation region was observed, particularly in the case of flows with large-scale wake oscillation, such as the helical wake structure shown in figure 6.12. Hence, it is considered that the wake diameter at the end of the recirculation region reflects the stability of the wake, regardless of *Re* and *M*.

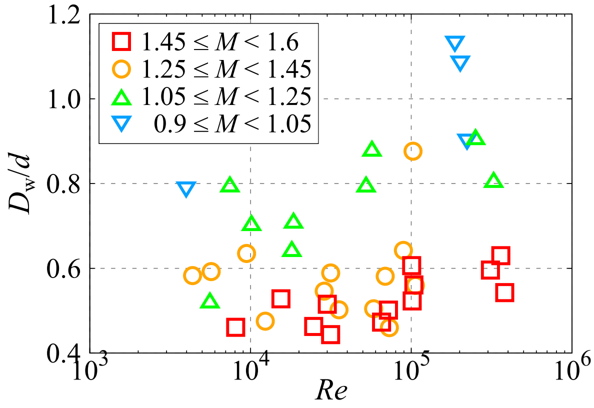

FIGURE 6.19: Effect of *Re* on the wake diameter at the end of the recirculation region.

6.4 Results and Discussion of Shock-Particle Interaction Experiments

6.4.1 Instantaneous Flowfield

Figures 6.20–6.25 show the time series schlieren images of the interaction process of the planar-shock wave and a free-falling sphere at M_s = 1.42, 2.02, and 2.64. Figures 6.20 and 6.21 show the time-series schlieren images at M_s = 1.42. The relative Mach number between the sphere and the flow behind the planar-shock wave is a transonic condition ($M_p \approx 0.53$). Until t = 10 μs, regular and Mach reflections occur on the surface of the sphere (transition angle is around 40 deg (Sun et al., 2005)). In addition, the curved Mach stem forms a ring shape and it is converged at the rear stagnation point of the sphere. The converged Mach stem also forms a ring shape wave (t = 10 μs), and those two ring shape waves propagate to the far field. Also, vortices are formed at downstream of the sphere at t = 35 μs and it grows up and released to downstream of the sphere.

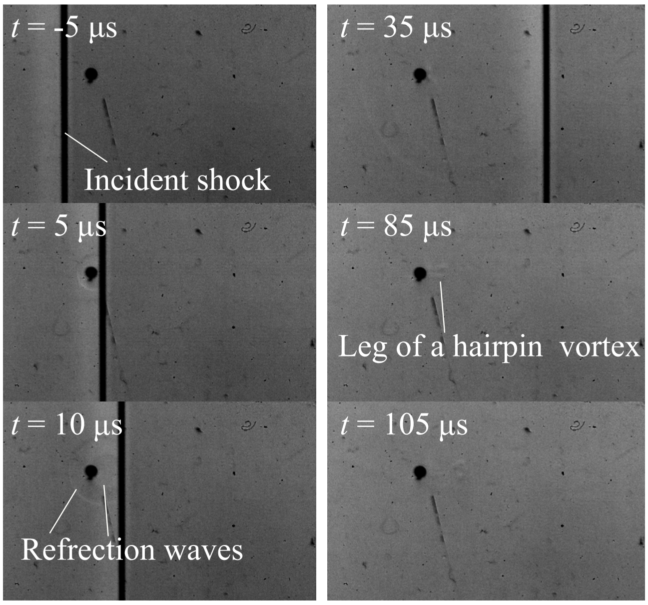

FIGURE 6.20: Time-series schlieren images of the shock-sphere interaction process at M_s = 1.42 (d = 1.5 mm).

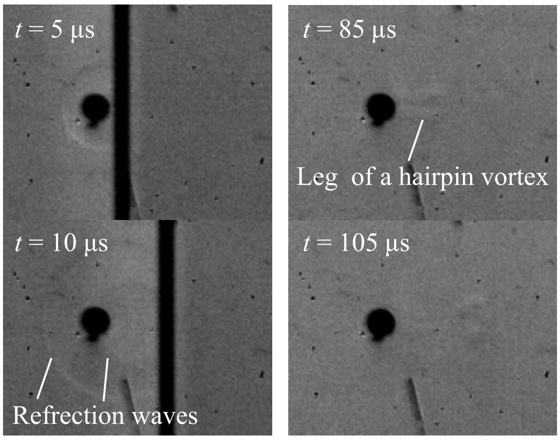

FIGURE 6.21: Close-up view of the time-series schlieren images of the shock-sphere interaction process at M_s = 1.42 (d = 1.5 mm).

Figures 6.22 and 6.23 shows the time-series schlieren images at $M_\mathrm{s} = 2.02$ ($M_\mathrm{p} \approx 0.98$). In this condition, ring shape waves are also formed, but those are fixed at upstream and downstream of the sphere as the detached and recompression waves, respectively. The wake vortices are generated and have low-frequency oscillations. As discussed befor sections, the generation point of the low-frequency oscillations are around the recompression wave. At $t = 244$, the streamwise pattern appears due to the boundary-layer formed on the optical window.

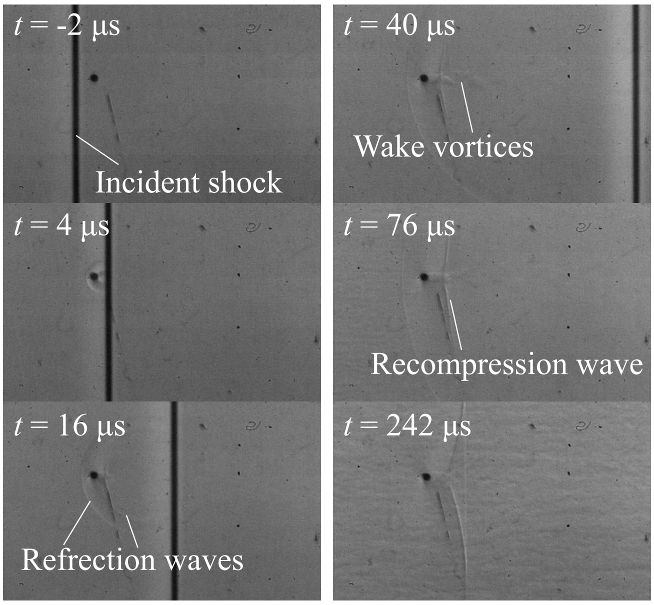

FIGURE 6.22: Time-series schlieren images of the shock-sphere interaction process at M_s = 2.02 (d = 1.0 mm).

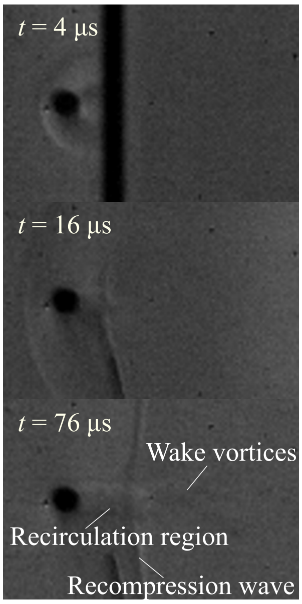

FIGURE 6.23: Close-up view of the time-series schlieren images of the shock-sphere interaction processat M_s = 2.02 (d = 1.0 mm).

Figures 6.24 and 6.25 shows the time-series schlieren images at M_s = 2.64 ($M_p \approx 1.24$). In this condition, the particle Mach number is the supersonic condition so that the bow shock is formed. Also, the wake vortices cannot be observed due to due to the lower-pressure conditions. In the case of the free-flight experiment, there is no stream, and thus only the disturbance due to the sphere exists in the test section. In the case of the shock-sphere interaction experiment, on the other hand, there is another disturbance due to the wall turbulence on the optical window even though the smaller model can be used. Therefore, the sensitivity to capture the flow structure though the shock-particle interaction experiment is lower than that through the free-flight experiments.

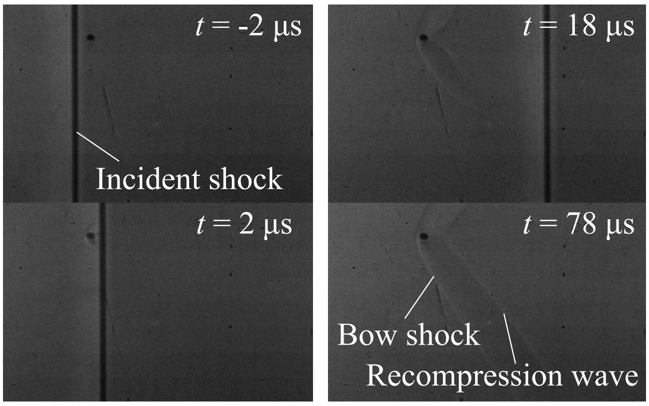

FIGURE 6.24: Time-series schlieren images of the shock-sphere interaction process at M_s = 2.64 (d = 1.0 mm).

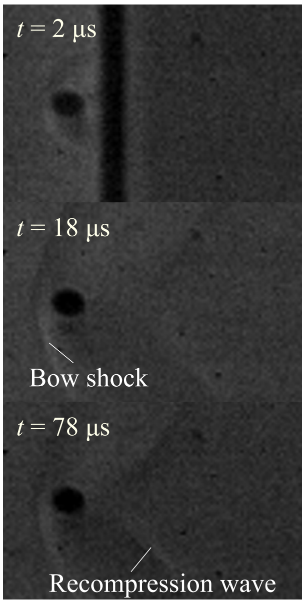

FIGURE 6.25: Close-up view of the time-series schlieren images of the shock-sphere interaction process at M_s = 2.64 (d = 1.0 mm).

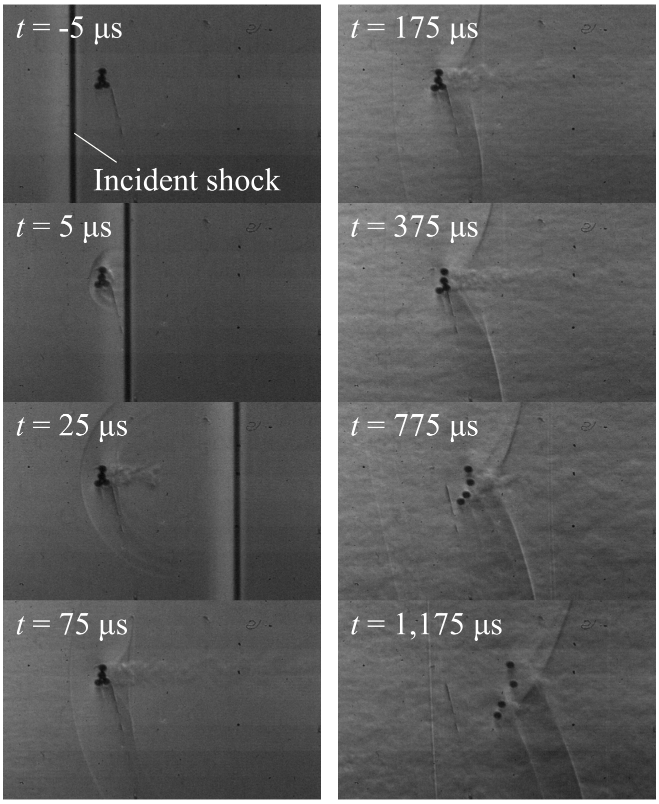

FIGURE 6.26: Time-series schlieren images of the shock-sphere cluster interaction process at M_s = 2.02 (d = 1.0 mm).

Figure 6.26 shows the interaction process of the planar-shock and clustered spheres at $M_\mathrm{s} = 2.02$ ($M_\mathrm{p} \approx 0.98$). At $t = 5$ μs, the sphere cluster interacts with a planar-shock wave, and the complex structure of the reflected waves can be seen. At t = 25–175 μs, the wake vortices generated from the sphere cluster and the recompression wave at the downstream of the sphere cluster are developed. At t = 375μs, the breakup of the sphere cluster seems to begin. The upper side and lower side spheres go toward the upper and lower sides, respectively. This movement implies that the existence of the aerodynamic interaction between the spheres. It can be considered that the strength of the interaction force in the compressible flow is larger than that at the incompressible flow because of the shock wave issues. Therefore, it appears to be valuable that the investigation of the aerodynamic interaction between the particle on the particle cluster.

6.4.2 Estimation of Drag Force

The time history of the drag force acted on the sphere was estimated from the time-position data extracted from the time-series schlieren images. The Mach number of the incident shock was set to be $M_\mathrm{s} = 1.42$, and the diameter of the sphere was varied in the ranging 0.5–1.5 mm. Therefore, Re_p and Stokes number were varied at the constant M_p of 0.53. At the steady state, the drag coefficient of the sphere is the function of Re and M, however, there is the influence of the unsteady forces such as added mass and Basset forces so that the drag coefficient in the non-steady state is different from the steady state (Jourdan et al., 2007; Wagner et al., 2012; Igra and Takayama, 1993; Suzuki et al., 2005; Parmar, Haselbacher, and Balachandar, 2010). Figures 6.27–6.29 show the time history of the position and velocity of the sphere in the streamwise direction and the streamwise forces acted on the sphere. The velocity was calculated as first derivative of the time-position data. In these figures, $t = 0$ ms and $x = 0$ mm indicate the incident time and the position at $t = 0$ ms. Figures 6.27 and 6.28 illustrate that the position and velocity of the sphere in the horizontal direction changes quadratically and linearly with respect to the time so that the movement of the sphere in the streamwise direction is the isoacceleration motion. Here, x–t diagram at $t > 4$ ms is non-linear because the duration time of the shock-induced flow based on the time-history of pressure was 4 ms for the present experiments. Figure 6.29 shows the time history of the drag force acting on the sphere computed by the time history of the acceleration of the sphere and the equation of motion. Here, the acceleration of the sphere was computed as the second derivative of the time-position data. There are the large variation in the time history of the drag force particularly for the larger spheres, because the amount of movement of the larger sphere is quite smaller than that of the smaller spheres due to difference in the mass. However, the time history of the drag illustrates that the constant drag force was acting except earlier time and at $t > 4$ ms. The previous studies reported that the quite large drag is generated at the earlier time after the shock incidence. However, the present experimental system does not provide the sensitivity and time resolution to capture the instantaneous arising of the drag sphere. Therefore, the time history of the drag force is not fully time-resolved data.

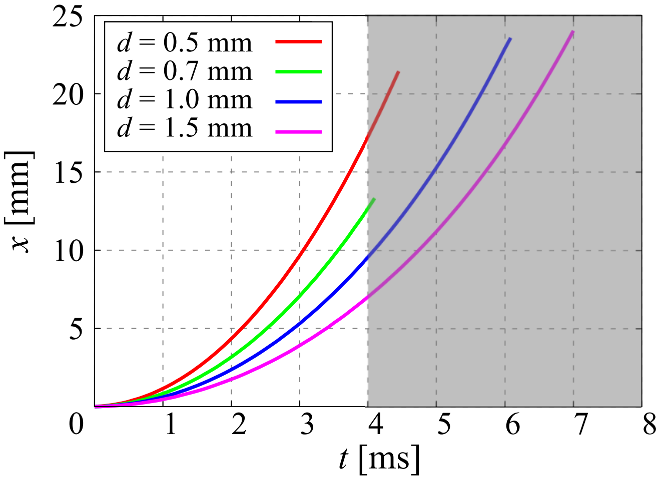

FIGURE 6.27: Time histories of the horizontal position of the sphere.

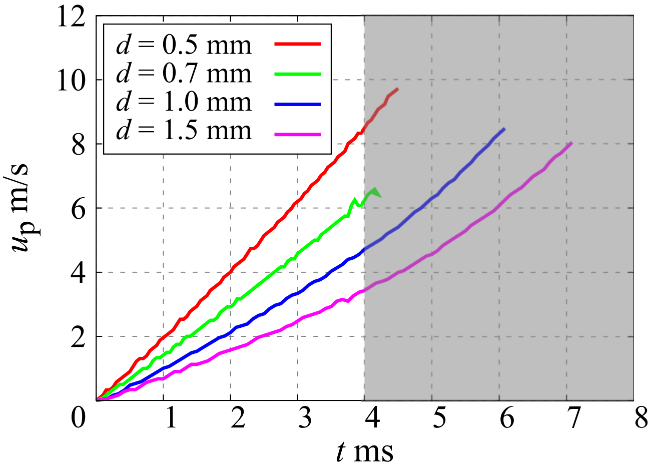

FIGURE 6.28: Time histories of the streamwise velocity of the sphere.

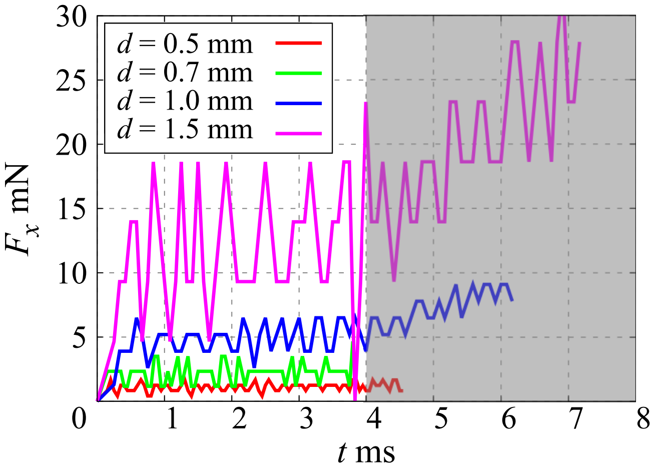

FIGURE 6.29: Time histories of the streamwise aerodynamic force.

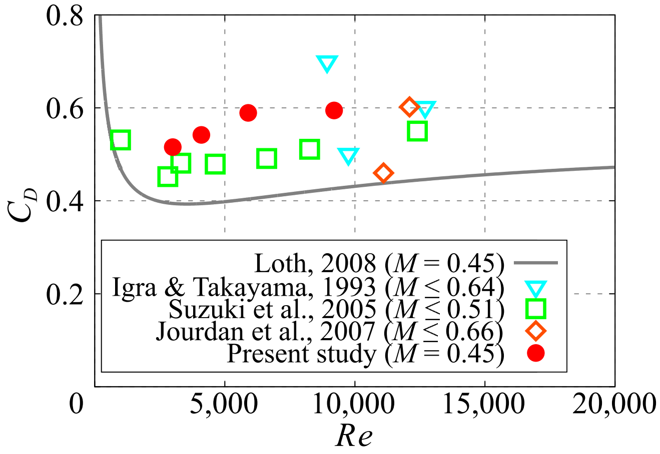

FIGURE 6.30: Comparison of the drag coefficients.

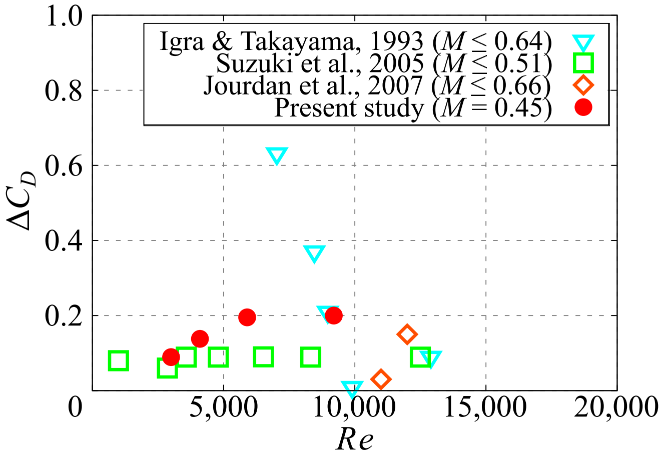

FIGURE 6.31: Difference in the measured drag coefficients and predicted drag coefficient by the drag model of Loth, 2008.

Figure 6.30 shows the relationship between *Re* and the drag coefficient and for the previous and present shock-particle interaction experiments. The line in figure 6.30 indicates the drag coefficient predicted by the drag model for steady state proposed by Loth, 2008. Also, figure 6.31 shows the difference from the Loth model. The drag force for this figure was computed from the average acceleration estimated by the time-position data between 1.0–3.0 ms with quadratic function fit. Also, the averaged-relative velocity between the shock induced flow and the sphere at 1.0–3.0 ms and the gas density behind the incident shock was used to calculate the dynamic pressure. The drag coefficient acquired by the present study is larger than the value predicted by the drag model as well as the previous experimental study. Also, the difference between the drag model and experimental data becomes large as Re increases. It seems that Re was changed by changing the diameter of the sphere so that the mass of the sphere was not constant for the different Re. This difference leads the difference in the stokes number so that influence of the unsteadiness should be investigated more carefully.

6.5 Conclusions

In chapter 6, the flow over a sphere at $O(10^3) \leq Re \leq O(10^5)$ at speeds ranging from transonic to supersonic and the flow over a sphere at $O(10^3) \leq Re \leq O(10^4)$ at speeds ranging from subsonic to supersonic were investigated by free-flight and shock-sphere interaction experiments with schlieren visualization.

The flow condition for the free-flight experiment was $0.9 \leq M \leq 1.6$ and $3.9 \times 10^3 \leq Re \leq 3.8 \times 10^5$. Visualization of the instantaneous flowfield showed that M and Re had a greater effect on the wake structure at $O(10^3) \leq Re \leq O(10^5)$. Also, SVD was applied to the time-series schlieren images in order to extract the mode of the wake structure from the noisy and unclear visualization images. The use of SVD revealed the differences in the wake structure between the transonic and supersonic conditions and allowed observation of the effect of Re. Under transonic conditions, the amplitude of the wake structure is larger than that under supersonic conditions. In addition, the mode of wake structure changes from the helical mode to the alternating mode as M increases. The visualization image and SVD mode for $M \approx 1.4$ showed that large-scale wake oscillations can be observed for $Re = 1.0 \times 10^5$, but the oscillation amplitude and size of the wake structure decreases with decreasing Re. This result suggested a change in the flow regime and the dominant frequency of the wake oscillations. In the present study, the gas density in the visualization section was reduced to decrease Re so that the smaller-scale structure disappears as the gas density (Re) decreases shown in figure 6.9 due to the decrease in the sensitivity of the schlieren method. However, the SVD results indicate that the smaller scale becomes dominant instead of the larger scale as Re (gas density) decreases. Therefore, it is considered that the change in the wake structure is the effect of Re.

The time-averaged field showed that the length of the recirculation region decreases with decreasing Re. This trend is opposite to that at $Re < O(10^3)$. In contrast, there is no the

Re dependence on the position of the separation point. Moreover, it is clarified that the wake diameter at the end of the recirculation region in the time-averaged field is influenced by Re and M. Particularly, the effect of M is strong because the recirculation region forcibly closed due to the expansion wave. Thus, this parameter seems to be important for the flow pattern of the wake.

In the shock-sphere interaction experiment, the flow visualization and drag estimation were conducted. The experimental system for the shock-sphere interaction experiment was established to investigate the flow properties of the sphere at $Re = O(10^3)$. The flow condition of the flow visualization was $0.45 \leq M \leq 1.28$ and $4.0 \times 10^3 \leq Re \leq 1.4 \times 10^4$, and the flow condition of the drag estimation was $M = 0.45$ and $3.0 \times 10^3 \leq Re \leq 9.2 \times 10^3$. This experimental system allows us to conduct the schlieren visualization of the isolated and clustered spheres and the drag measurements of the isolated sphere at $Re = O(10^3)$. At subsonic conditions, the schlieren visualization captured the propagation of the reflected waves and formation of the hairpin vortex during the shock-sphere interaction process. However, the wake structure after the shock wave passed was not captured except the initial stage of the vortex formation behind the sphere due to the small model and low-dynamic pressure so that improvement of the sensitivity of the flow visualization is required to capture the wake structure at further low-Re conditions. At the transonic condition, on the other hand, the recompression wave and wake structures were captured due to larger-dynamic pressure. However, the pattern caused by the wall turbulence formed on the optical glasses becomes strong after a certain time. Because of that influence, the observation of the wake structure becomes harder. Therefore, the separation of the wake structure and the wall turbulence by the image processing is required to get the image of the instantaneous wake structure in better quality. At the supersonic conditions, the wake structures did not captur even though higher-M, because the pressure behind the shock wave was low to decrease Re. The time history and the time-averaged drag forces acting on the sphere was estimated from the time-series shadowgraph images. The average drag coefficient at the state in the fully developed flow was compared to the result of the previous shock-particle interaction experiment and the drag model for the steady-state. The present result showed the higher drag coefficients compared with the predicted value of the previous model as well as the previous shock-particle interaction experiment.

Chapter 7

Concluding Remarks

In the present study, the characteristics of the compressible low-*Re* number flow over an isolated sphere were investigated toward the modeling of the compressible multiphase flows. The investigations were conducted by DNS of the Navier–Stokes equations, the free-flight experiment, and the shock-sphere interaction experiment. The DNS was conducted on the body-fitted grid with high-order schemes of sufficient accuracy. The free-flight and shock-sphere interaction experiments were carried out by using a ballistic range and a shock tube, respectively.

In chapter 3, the uniform flow over a stationary isolated adiabatic sphere was investigated by the direct numerical simulation of the three-dimensional compressible Navier–Stokes equations. The flow condition was $50 \leq Re \leq 1,000$ and $0.3 \leq M \leq 2.0$. The wake of the sphere is significantly stabilized as M increases, particularly at $M \geq 0.95$. Since the stabilization effect at higher-M conditions, the flow regime at high-M conditions is similar to that at the lower-*Re* conditions. However, the turbulent kinetic energy at the higher-M is higher than that at lower-M of similar flow regimes. Therefore, it is considered that the particle M affect the turbulent modulation due to the wake vortices generated by the particles in the flow. The length of the recirculation region rapidly increases around the critical M which unsteady flows become steady flows because of the compressibility effects. The drag coefficient increases as M increases mainly in the transonic condition and the increment is the almost pressure component. In addition, the increment of the drag coefficient in the continuum regime is approximately the function of M and is regardless of *Re* despite the low-*Re* condition. The relationship between the flow geometry and drag coefficient is similar in the incompressible and compressible flows, the effect of M and *Re* on such properties can approximately be characterized by the position of the separation. The drag coefficient provided by the experiment and predicted by DNS shows great agreement with the predicted value by the previous drag model at subsonic conditions. However, the difference in the drag model and the results of the present DNS and experimental studies becomes large at the transonic conditions, particularly low-*Re* conditions, because the previous drag model was constructed mainly based on the incompressible experimental data in a wide range of *Re*, the compressible experimental data in high-*Re* conditions, empirical collections, and theoretical expressions and experimental data in the rarefied regime. Consequently, it seems that the accuracy of the previous drag model becomes worsen at the compressible low-*Re* conditions.

In chapter 4, the uniform flow over a stationary isolated isothermal sphere was investigated by DNS at $100 \leq Re \leq 300$, $0.3 \leq M \leq 2.0$, and $0.5 \leq TR \leq 2.0$. The unsteady vortex shedding from the sphere is promoted and suppressed in the case of the heated and cooled spheres, respectively. In other words, the flowfield of the heated and cooled sphere is similar to that at the lower- and higher-Re of the adiabatic spheres, respectively. It is due to the change in the kinematic viscosity coefficient of the fluid in the vicinity of the sphere. A similar effect can be seen in the flow geometry, such as the position of the separation point, the length of the recirculation region, and the drag coefficient. However, the previous drag model cannot predict the effect of the surface temperature on the drag coefficient, despite they contain the term of the temperature ratio. It is due to that the terms for the temperature ratio in the previous compressible drag model are originated in the formula in the rarefied regime so that those terms do not work in the continuum regime. The effect of the surface temperature on the flow geometry and the drag coefficient can be characterized by the position of the separation point because the kinematic viscosity coefficient in the boundary layer has a significant effect on the flow separation. The Nusselt number models proposed in the previous studies showed good agreement with the present result when the temperature ratio is close to unity at subsonic conditions. However, the difference in the predicted values of the previous model and the present DNS becomes large as the temperature difference or M increases.

In chapter 5, the flow over a rotating isolated adiabatic sphere and the linear-shear flow over a stationary adiabatic sphere were investigated by DNS.

The flow condition of the case of the rotating sphere was $100 \leq Re \leq 300$, $0.3 \leq M \leq 2.0$, and $0 \leq \Omega^* \leq 1.0$. The effects of M and Re on the wake structure are similar to the stationary sphere; the pattern of the wake structure becomes similar to that at the low-Re conditions as M increases. At high-Ω^* conditions, however, the stabilization of the wake due to the compressibility effect appears even though $M = 0.3$. The lift coefficient increases as Ω^* increases under subsonic conditions, and the effect of Ω^* is similar in also supersonic conditions, however, the increment of the lift coefficient is reduced as M increases. Also, the increment of the lift coefficient for low-speed cases saturates at around $\Omega^* = 1.0$, whereas the lift coefficient at the supersonic condition continuously increases at $\Omega^* \geq 1.0$. Reducing the lift coefficient is caused by the influence of the strong compression at the detached shock wave and around the upstream side surface of the retreating side. Because of those effects, the pressure at the region where the low-pressure region is generated in the shock-free flow becomes increases at the transonic and supersonic flows. The increment of the drag coefficient also increases with increasing Ω^* and its increment decreases with increasing M. The pitching moment in the opposite direction to the rotation of the sphere at the same Ω^* is increased as M increases because of the increase in the attached region, the viscosity coefficient, and the velocity gradient on the surface behind the attached shock waves. To be summarized, at the higher-M conditions, the influence of the rotation on the wake, lift and drag coefficients is reduced, and the rotation is easy to stop. Hence, it seems that the rotation effect is significantly reduced in supersonic conditions.

The flow condition of the case of the sphere in the linear-shear flow was $50 \leq Re \leq 300$, $0.3 \leq M \leq 2.0$, and $\alpha = 1.0$. The flow structure at the low-subsonic condition appears to be similar to that of the incompressible flow. However, the expansion wave and the detached shock wave are formed only on the high-speed side at the high-subsonic and transonic conditions. This is due to the difference in the local M of the mainstream because of the shear velocity. This influence is the same in the supersonic condition, and it results in the formation of the stronger shock waves on the low-speed side. The shape of the recirculation region at the compressible condition is significantly influenced by the expansion wave. At the incompressible and subsonic flows, the recirculation region is skewed into the high-speed side at $Re > 50$. At the supersonic flow, conversely, the recirculation region is skewed into the low-speed side. Under the incompressible condition, the reverse of the lift force at $Re \approx 50$ occurs due to the asymmetry of the recirculation region. In this case, the change in the stress distribution on the downstream side caused by the change in the shape of the recirculation region is important. However, there is no reverse of the lift force despite the drastic change in the shape of the recirculation region at the supersonic conditions. In the compressible case, the change in the lift coefficient at the compressible flows is related to the pressure distribution in the upstream side of the sphere surface rather than that on the downstream side. The change in the pressure distribution in the upstream side is due to the compressibility effect which is described by the Prandtl–Glauert transformation and the detached shock wave. Because of those effects, the pressure coefficient increases as M increases so that the pressure on the high-speed side is higher than that on the low-speed side. Thus, the lift force acting from the high-speed side to the low-speed side and becomes large as M increases. However, the compressibility effect on the pressure coefficient saturates in the supersonic regime, and the difference in the pressure coefficient on the high-speed side and low-speed side becomes small as M of the mainstream increases, and thus the negative lift decreases as M increases.

In chapter 6, the flow over an isolated sphere at $Re \leq O(10^3)$ was investigated through a free-flight experiment and a shock-sphere interaction experiment.

The flow condition of the free-flight experiment was $3.7 \times 10^3 \leq Re \leq 3.8 \times 10^5$ and $0.9 \leq M \leq 1.6$. The small sphere (the minimum diameter of 1.5 mm) was launched into the low-pressurized test section by a single-stage light gas gun driven by helium gas, and the flowfield was visualized by the time-resolved schlieren measurement. The time-resolved and the time-averaged images of the near field of the sphere were obtained and compared with numerical results at $50 \leq Re \leq 1,000$. The singular value decomposition was applied to the time-series schlieren image and it enabled us to extract the characteristic mode of the wake structure despite the low-signal-to-noise ratio. The experimental results clarified the structure of shock waves, recirculation region, and wake structures at $O(10^3) \leq Re \leq O(10^5)$ under transonic and supersonic flows. The amplitude of the wake oscillation is attenuated as M increases. In addition, the width of the wake at the end of the recirculation region on the time-averaged field is reduced by increasing M. There is less effect of Re on the separation point, but the length of the recirculation region rapidly increases as Re decreases. The trend in the Re effect on the length of the recirculation region is opposite to that at $Re \leq O(10^3)$. The change in trend in the length of the recirculation region suggests the change in the pattern of the wake structure occurs at around $Re = O(10^3)$.

The flow conditions of the shock-sphere interaction experiment based on the quantities behind the shock was $1.8 \times 10^3 \leq Re \leq 1.4 \times 10^4$ and $0.4 \leq M \leq 1.3$. The sphere dropoff system synchronized with the shock tube operation was constructed and applied to the experiment. The small sphere (the minimum diameter of 0.3 mm) was held on the upper wall of the shock tube by the magnetic force and was released at the appropriate timing for the observation of the interaction with the planar-shock wave. The flowfield acquired by the schlieren technique, and the drag coefficient was estimated from the position-time data of the sphere. The present experiment achieved the visualization of the flow structure not only shock wave but also the wake structures formed behind the sphere. Also, it was shown that the constructed setup can conduct the visualization experiment of the clustered spheres-shock interaction, and its scattering process was observed. The time history of the drag force acting on the sphere and the mean drag coefficient were estimated from the time-position data of the sphere. The estimated drag coefficient was higher than that of the estimated by the drag model in steady-state. It is a similar trend with the previous experimental results.

From the above results, the fundamental characteristics of the flow over a sphere at the compressible low-*Re* condition were clarified in the wide range of flow conditions. The obtained knowledge will contribute to understanding the influence of the particles in the compressible particle-laden flow and fluid mechanics of the compressible low-*Re* flows.

Appendix A

Validation and Verification

A.1 Comparisons with Previous Incompressible Studies and Drag Models

Tables A.1–A.5 is the summary of the comparison on the flow geometry and drag coefficients reported by the incompressible study by Johnson and Patel, 1999 and the present study as verification. The computational grid was the baseline grid which is the lowest accurate grid for the present study.

	Johnson and Patel, 1999	Present result ($M = 0.3$)	Error [%]
$Re = 50$	139.5	140.57	0.77
$Re = 100$	127.0	130.29	2.59
$Re = 150$	121.1	123.43	1.92
$Re = 200$	117.4	120.00	2.21

TABLE A.1: Position of the separation points θ_s.

	Johnson and Patel, 1999	Present result ($M = 0.3$)	Error [%]
$Re = 50$	0.42	0.41	2.38
$Re = 100$	0.89	0.86	3.37
$Re = 150$	1.22	1.14	6.56
$Re = 200$	1.46	1.40	4.11

TABLE A.2: Lengths of the recirculation region L_r/d.

	Johnson and Patel, 1999	Present result ($M = 0.3$)	Error [%]
$Re = 50$	0.64	0.64	0.00
$Re = 100$	0.76	0.76	0.00
$Re = 150$	0.88	0.83	5.68
$Re = 200$	0.83	0.89	7.23

TABLE A.3: Center of the recirculation regions in x direction x_c/d.

	Johnson and Patel, 1999	Present result ($M = 0.3$)	Error [%]
$Re = 50$	0.21	0.22	4.25
$Re = 100$	0.29	0.30	1.83
$Re = 150$	0.33	0.33	0.00
$Re = 200$	0.36	0.36	0.00

TABLE A.4: Center of the recirculation regions in y direction y_c/d.

	Johnson and Patel, 1999	Present result ($M = 0.3$)	Error [%]
$Re = 50$	1.58	1.54	2.53
$Re = 100$	1.09	1.07	1.83
$Re = 150$	0.90	0.88	2.22
$Re = 200$	0.78	0.76	2.56

TABLE A.5: Verification of drag coefficient C_D.

The comparisons of the flow geometry and the drag coefficients with incompressible studies (Taneda, 1956; Pruppacher, Le Clair, and Hamielec, 1970; Johnson and Patel, 1999; Tomboulides, Orszag, and Karniadakis, 1993; Magnaudet, Rivero, and Fabre, 1995; Roos and Willmarth, 1971) shown in figure A.1, A.2, and A.3.

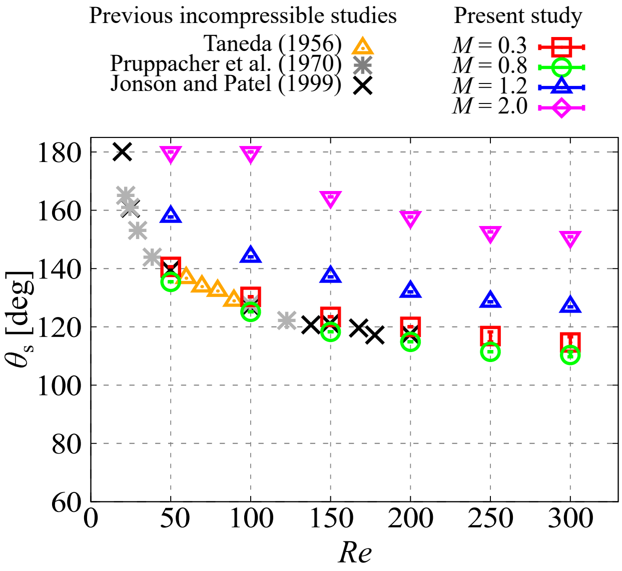

FIGURE A.1: Comparison of the position of the separation point reported by previous incompressible studies and the present study.

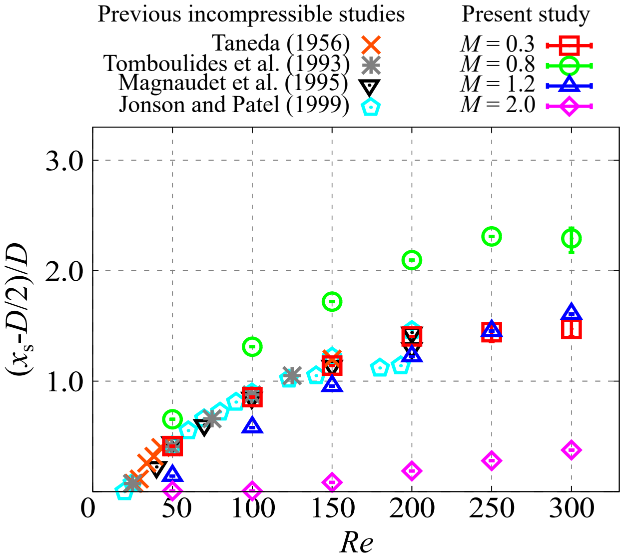

FIGURE A.2: Comparison of the length of the recirculation region reported by previous incompressible studies and the present study.

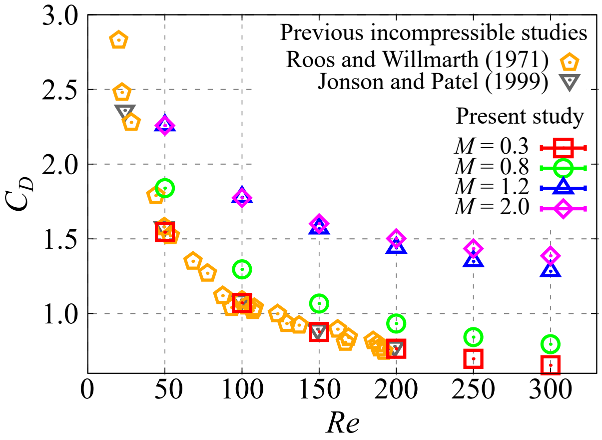

FIGURE A.3: Comparison of the drag coefficient reported by previous incompressible studies and the present study.

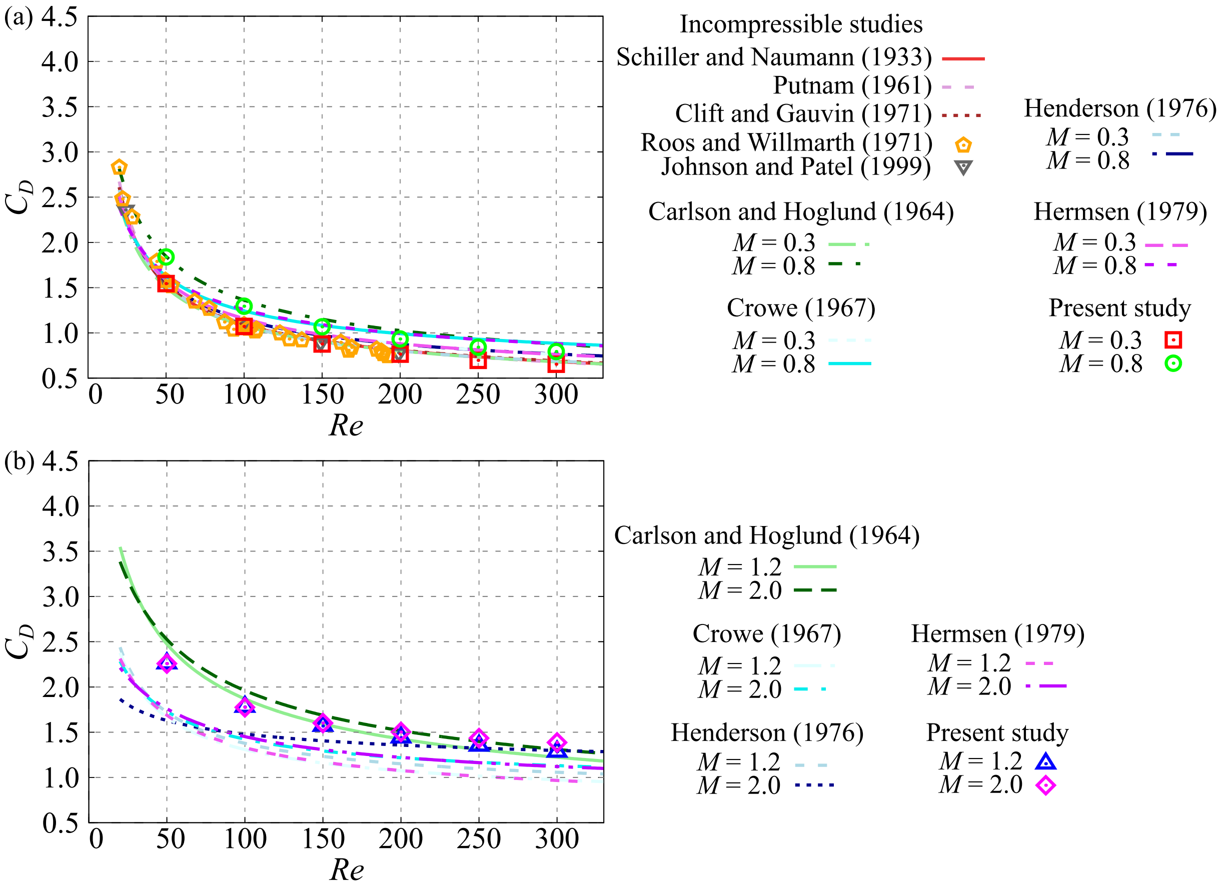

FIGURE A.4: Comparison of the drag coefficient reported by previous incompressible studies, predicted by drag models, and the present study.

The comparison of the drag coefficients with incompressible experimental data (Roos and Willmarth, 1971; Johnson and Patel, 1999), incompressible drag models (Schiller and Naumann, 1933; Putnam, 1961; Clift and Gauvin, 1971), and compressible drag models (Carlson and Hoglund, 1964; Crowe, 1967; Henderson, 1976; Hermsen, 1979) are shown in figure A.4.

A.2 Grid Convergence Studies

A.2.1 Adiabatic Case

Table A.6 illustrates the grid size dependence on the drag coefficient. The result by the baseline grid used in chapter 3 and its finer grid are compared. The grid resolution of the fine grid was 1.4 times of the base grid in each direction. The flow at $Re = 300, M = 0.3$ and $Re = 300, M = 2.0$ were conducted, and the relative error on the drag coefficients was less than 1%.

	Baseline	Fine	Error [%]
$M = 0.3$	0.6536	0.6582	0.0835
$M = 2.0$	1.3866	1.3965	1.4158

Table A.6: Verification of the grid convergence for the base grid in adiabatic cases at $Re = 300$ (drag coefficient).

Table A.7 shows the drag coefficients computed using baseline and fine grids at $300 \leq Re \leq 1,000$. The fine grid for each Re correspond to the baseline grid for the next-higher Re value; for example, the fine grid for $Re = 750$ corresponds to the baseline grid for $Re = 1,000$.

	$Re = 300$		$Re = 500$		$Re = 750$		$Re = 1,000$	
	$M = 0.3$	$M = 2.0$	$M = 0.3$	$M = 2.0$	$M = 0.3$	$M = 2.0$	$M = 0.3$	$M = 2.0$
Baseline	0.6587	1.452	0.5658	1.331	0.5078	1.251	0.6473	1.197
Fine	0.6644	1.458	0.5679	1.336	0.5085	1.254	0.6507	1.201

Table A.7: Verification of the grid convergence for the wake-fine grid in adiabatic cases (drag coefficient).

A.2.2 Isothermal Case

Table A.8 compares of the drag coefficients between the baseline and the fine grids. The resolution of the fine grid in each direction was 1.4 times that of the baseline grid same as the grid convergence study for adiabatic cases.

	$M = 0.3$		$M = 2.0$	
	$TR = 0.5$	$TR = 2.0$	$TR = 0.5$	$TR = 2.0$
Baseline	0.6206	0.7445	0.6341	0.7359
Fine	1.362	1.440	1.417	1.446
Error [%]	2.129	1.169	3.881	0.4149

Table A.8: Verification of the grid convergence for the base grid in isothermal cases at $Re = 300$ (drag coefficient).

A.2.3 Rotating Case

Table A.2.3 shows the results of the validation and verification studies. The number of grid points of finer grid in each direction was 1.4 times of the baseline gird, and the size of the computational domain of wider grid was 1.5 times of the baseline grid. As a result, the grid size and domain size independence were confirmed on the aerodynamic force coefficients.

		Baseline	Fine grid	Wide domain	WENOCU6-FP (before blowing up)
$M = 0.3$	C_L	0.56951	0.58423	0.56955	0.54950
	C_D	0.94177	0.94727	0.94179	0.88885
	C_{M_Y}	−0.085754	−0.085308	−0.085750	−0.073502
$M = 2.0$	C_L	0.14502	0.14618	0.14493	0.146156
	C_D	1.4764	1.4903	1.4764	1.4369
	C_{M_Y}	−0.18108	−0.18277	−0.18107	−0.15906

Table A.9: Comparisons of aerodynamic force coefficients at $Re = 300$ and $\Omega^* = 1.0$.

In the present study, the central difference of the WENOCU6-FP method was replaced into one of the splitting type proposed by Pirozzoli, 2011, in order to stabilize the calculation. The numerical viscosity is introduced only by the dissipation term for the sixth-order WENOCU in the replaced WENOCU6-FP. This kind of an approach is originally used by Yee, Sandham, and Djomehri, 1999. In addition, by numerical tests using the central difference scheme (Pirozzoli, 2011), it has been confirmed that this splitting-type scheme gives an accurate and stable solution over conventional central discretization. Table A.9 includes the aerodynamic force coefficients provided by the original WENOCU6-FP. Also, the time history of C_L and instantaneous C_P distribution are shown in figures A.5 and A.6, respectively. It should be note that the computation by the original WENOCU6-FP blows up as shown in figure A.5. Therefore, the aerodynamic force coefficients shown in table A.2.3 might not be accurate. However, the C_P distribution before blowing up is very similar.

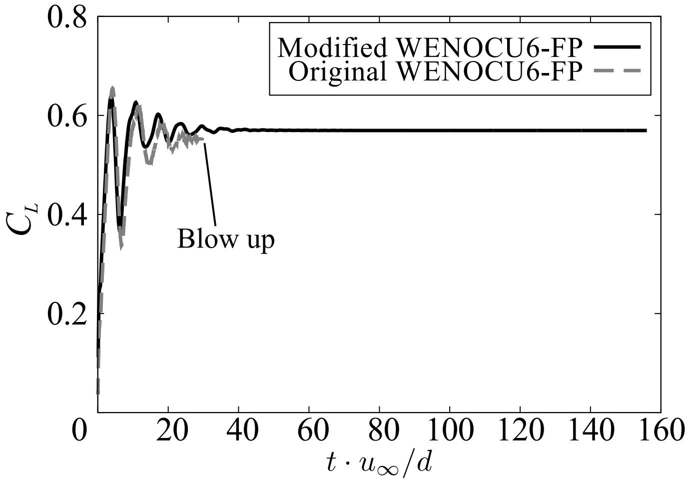

FIGURE A.5: Comparisons of C_L time history computed by modified WENOCU6-FP and original WENOCU6-FP (Re = 300, M = 0.3, and Ω^* = 1.0).

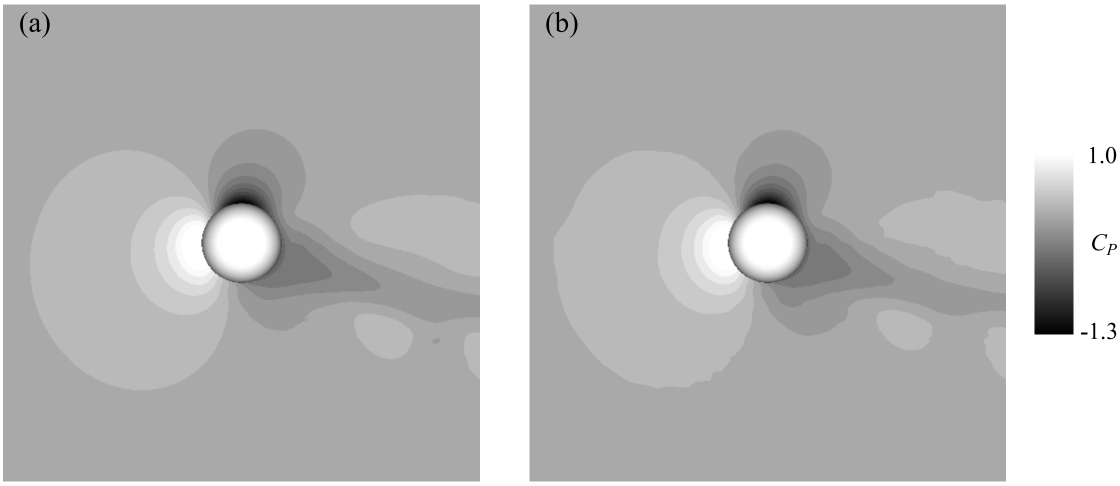

FIGURE A.6: Comparisons of C_P distribution computed by modified WENOCU6-FP and original WENOCU6-FP (before blowing up) for$Re = 300, M = 0.3$, and $\Omega^* = 1.0$.

Appendix B

Supplementary Materials

	M=1.2		M=2.0	
Re	δ	U_{edge}	δ	U_{edge}
50	0.19922	0.02382	0.13150	0.02056
100	0.12134	0.02421	0.09259	0.02138
150	0.09259	0.02453	0.08356	0.02343
200	0.08356	0.02478	0.06628	0.02255
250	0.07479	0.02505	0.05801	0.02249
300	0.06628	0.02525	0.05801	0.01923

TABLE B.1: Boundary layer thickness and velocity at the boundary layer edge.

B.1 Estimated Flow Conditions at Boundary Layer Edge

Table B.1 is the summary of the boundary layer thickness δ and the velocity in xi-direction at the boundary layer edge U_{edge}.

B.2 Effect of Data Length in Time Direction on Extracted SVD Modes

Figure B.1 shows the influence of the data length in the time direction on the extracted SVD modes for $M = 1.39$ and $Re = 1.0 \times 10^5$ ($P/P_{\text{atm}} = 1.0$). This is the same case with figures 6.12(c) and 6.13(a). This dataset includes 4 periods of low-frequency oscillation of the wake, and the number of frames for SVD analysis was 61 frames. The mode corresponding to the low-frequency oscillation of the wake can be extracted even though 25% (only one period of the low-frequency oscillation of the wake) of the original data. However, the mode corresponds to the low-frequency oscillation of the wake could not be captured from the 10% dataset of the original data. In this case, the finer structure was extracted in lower modes, because the mode of the low-frequency phenomena were not captured due to short-time data. It should be noted that the such finer modes were extracted in the higher mode for the SVD mode of the original data.

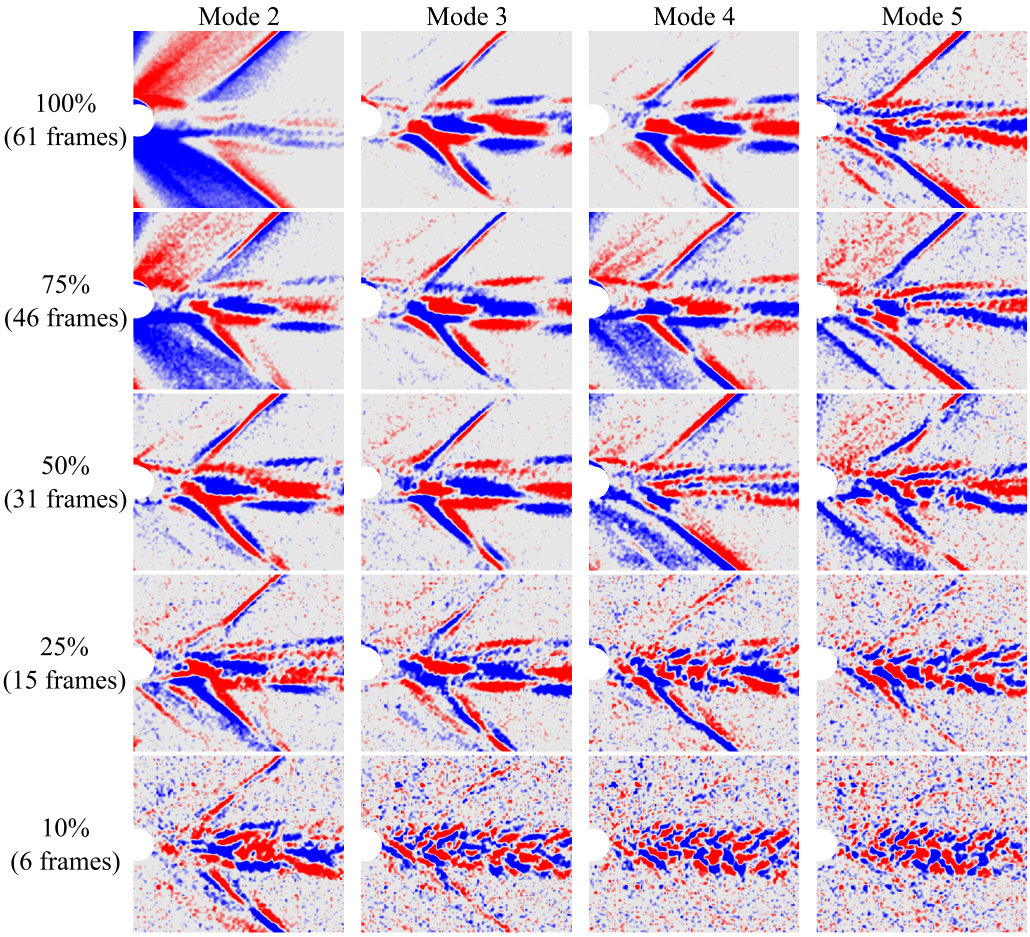

FIGURE B.1: Effect of data length in the time direction on the extracted fluctuating modes by SVD ($M = 1.39$ and $Re = 1.0 \times 10^5$).

Bibliography

Ambrosio, A. and A. Wortman (1962). *Stagnation point shock detachment distance for flow around spheres and cylinders*.

Bailey, A. B. (1974). “Sphere drag coefficient for subsonic speeds in continuum and free-molecule flows”. In: *Journal of Fluid Mechanics* 65.2, pp. 401–410.

Bailey, A. B. and J. Hiatt (1971). *Free-flight measurements of sphere drag at subsonic, transonic, supersonic, and hypersonic speeds for continuum, transition, and near-free-molecular flow conditions*. Tech. rep. AD0721208. Arnold Engineering Development Center Arnold AFS TN.

— (1972). “Sphere drag coefficients for a broad range of Mach and Reynolds numbers”. In: *AIAA Journal* 10.11, pp. 1436–1440.

Bailey, A. B. and R. F. Starr (1976). “Sphere drag at transonic speeds and high Reynolds numbers”. In: *AIAA Journal* 14.11, pp. 1631–1631.

Basset, A. B. (1888). “III. On the motion of a sphere in a viscous liquid”. In: *Philosophical Transactions of the Royal Society of London.(A.)* 179, pp. 43–63.

Behara, S. and S. Mittal (2010). “Wake transition in flow past a circular cylinder”. In: *Physics of Fluids* 22.11, p. 114104.

Boussinesq, J. (1895). “Theorie analytique de al Chaleur”. In: 2, p. 224.

Bretherton, F. P. (1962). “The motion of rigid particles in a shear flow at low Reynolds number”. In: *Journal of Fluid Mechanics* 14.2, pp. 284–304.

Buchta, D. A., G. Shallcross, and J. Capecelatro (2019). “Sound and turbulence modulation by particles in high-speed shear flows”. In: *Journal of Fluid Mechanics* 875, pp. 254–285.

Canuto, D. and K. Taira (2015). “Two-dimensional compressible viscous flow around a circular cylinder”. In: *Journal of Fluid Mechanics* 785, pp. 349–371.

Carlson, D. J. and R. F. Hoglund (1964). “Particle drag and heat transfer in rocket nozzles”. In: *AIAA Journal* 2.11, pp. 1980–1984.

Chen, F. et al. (2017). “Tracking characteristics of tracer particles for PIV measurements in supersonic flows”. In: *Chinese Journal of Aeronautics* 30.2, pp. 577–585.

Chorin, A. J. (1968). “Numerical solution of the Navier-Stokes equations”. In: *Mathematics of Computation* 22.104, pp. 745–762.

Clift, R. and W. H. Gauvin (1971). “Motion of entrained particles in gas streams”. In: *The Canadian Journal of Chemical Engineering* 49.4, pp. 439–448.

Costa, P. et al. (2015). “Collision model for fully resolved simulations of flows laden with finite-size particles”. In: *Physical Review E* 92.5, p. 053012.

Coutanceau, M. and R. Bouard (1977). “Experimental determination of the main features of the viscous flow in the wake of a circular cylinder in uniform translation. Part 1. Steady flow”. In: *Journal of Fluid Mechanics* 79.2, pp. 231–256.

Crowe, C. T. (1967). “Drag coefficient of particles in a rocket nozzle.” In: *AIAA Journal* 5.5, pp. 1021–1022.

Crowe, C. T. et al. (1968). *Measurement of particle drag coefficients in flow regimes encountered by particles in a rocket nozzle*. Tech. rep. AD850098. United Technology Center.

Crowe, C. T. et al. (2011). *Multiphase flows with droplets and particles*. CRC press.

Cundall, P. A. and O. D.L. Strack (1979). “A discrete numerical model for granular assemblies”. In: *Géotechnique* 29.1, pp. 47–65.

Dandy, D. S. and H. A. Dwyer (1990). “A sphere in shear flow at finite Reynolds number: effect of shear on particle lift, drag, and heat transfer”. In: *Journal of Fluid Mechanics* 216, pp. 381–410.

Das, P. et al. (2017). “A sharp interface Cartesian grid method for viscous simulation of shocked particle-laden flows”. In: *International Journal of Computational Fluid Dynamics* 31.6-8, pp. 269–291.

Das, P. et al. (2018). “Strategies for efficient machine learning of surrogate drag models from three-dimensional mesoscale computations of shocked particulate flows”. In: *International Journal of Multiphase Flow* 108, pp. 51–68.

Delany, N. K. and N. E. Sorensen (1953). *Low-speed drag of cylinders of various shapes*. Tech. rep. NACA-TN-3038. National Advisory Committee for Aeronautics.

Dennis, S. C. R. and G.-Z. Chang (1970). “Numerical solutions for steady flow past a circular cylinder at Reynolds numbers up to 100”. In: *Journal of Fluid Mechanics* 42.3, pp. 471–489.

Dobson, J., A. Ooi, and E. K. W. Poon (2014). “The flow structures of a transversely rotating sphere at high rotation rates”. In: *Computers & Fluids* 102, pp. 170–181.

Dyke, Milton van (1982). “An album of fluid motion”. In:

Dyment, A. and P. Gryson (1979). “Study of turbulent subcritical and supercritical flows by high-speed visualisation”. In: *AGARD Paper* 28.

Eldred, K. M. (1971). *Acoustic loads generated by the propulsion system*. NASA-SP-8072. National Aeronautics and Space Administration.

Epstein, P. S. (1924). “On the resistance experienced by spheres in their motion through gases”. In: *Physical Review* 23.6, p. 710.

Feng, Z.-G. and E. E. Michaelides (2004). “The immersed boundary-lattice Boltzmann method for solving fluid–particles interaction problems”. In: *Journal of Computational Physics* 195.2, pp. 602–628.

Fox, T. W., C. W. Rackett, and J. A. Nicholls (1978). “Shock wave ignition of magnesium powders”. In: *Proceedings of 11th International Symposium on Shock Tubes and Wave*, pp. 262–268.

Freund, J. B. (1997). “Proposed inflow/outflow boundary condition for direct computation of aerodynamic sound”. In: *AIAA Journal* 35.4, pp. 740–742.

Fukada, T., S. Takeuchi, and T. Kajishima (2016). “Interaction force and residual stress models for volume-averaged momentum equation for flow laden with particles of comparable diameter to computational grid width”. In: *International Journal of Multiphase Flow* 85, pp. 298–313.

— (2019). “Estimation of fluid forces on a spherical particle for two-way coupling simulation based on the volume averaging”. In: *International Journal of Multiphase Flow* 113, pp. 165–178.

Fukada, T. et al. (2018). “A numerical approach for particle-vortex interactions based on volume-averaged equations”. In: *International Journal of Multiphase Flow* 104, pp. 188–205.

Fukuda, K. et al. (2011). “Examination of sound suppression by water injection at lift-off of launch vehicles”. In: *17th AIAA/CEAS Aeroacoustics Conference (32nd AIAA Aeroacoustics Conference)*, p. 2814.

Gerrard, J. H. (1961). “An experimental investigation of the oscillating lift and drag of a circular cylinder shedding turbulent vortices”. In: *Journal of Fluid Mechanics* 11.2, pp. 244–256.

Ghias, R., R. Mittal, and H. Dong (2007). “A sharp interface immersed boundary method for compressible viscous flows”. In: *Journal of Computational Physics* 225.1, pp. 528–553.

Giacobello, M., A. Ooi, and S. Balachandar (2009). “Wake structure of a transversely rotating sphere at moderate Reynolds numbers”. In: *Journal of Fluid Mechanics* 621, pp. 103–130.

Goin, K. L. and W. R. Lawrence (1968). “Subsonic drag of spheres at Reynolds numbers from 200 to 10,000.” In: *AIAA Journal* 6.5, pp. 961–962.

Goldsmith, H. L. and S. G. Mason (1962). “The flow of suspensions through tubes. I. Single spheres, rods, and discs”. In: *Journal of Colloid Science* 17.5, pp. 448–476.

Golub, G. H. and C. F. van Loan (1983). *Matrix computations*. Johns Hopkins University Press.

Gottlieb, S. and C.-W. Shu (1998). “Total variation diminishing Runge-Kutta schemes”. In: *Mathematics of Computation of the American Mathematical Society* 67.221, pp. 73–85.

Gowen, F. E. and E. W. Perkins (1953). *Drag of circular cylinders for a wide range of Reynolds numbers and Mach numbers*. Tech. rep. NACA-TN-2960. National Advisory Committee for Aeronautics.

Handa, T., S. Koike, and K. Imabayashi (2017). “Estimation of the Particle Drag Coefficients for Compressible and Rarefied Flows Using PIV and MTV Data”. In: *International Symposium on Shock Waves*. Springer, pp. 1149–1154.

Heberle, J. W., G. P. Wood, and P. B. Gooderum (1950). *Data on shape and location of detached shock waves on cones and spheres*. Tech. rep. NACA Technical Note 2000. National Aeronautics and Space Administration Washington DC.

Henderson, C. B. (1976). “Drag coefficients of spheres in continuum and rarefied flows”. In: *AIAA Journal* 14.6, pp. 707–708.

Hermsen, R. W. (1979). “Review of particle drag models”. In: *JANAF Performance Standardization Subcommittee 12th Meeting Minutes*. Vol. 113.

Hida, K. (1953). “An approximate study on the detached shock wave in front of a circular cylinder and a sphere”. In: *Journal of the Physical Society of Japan* 8.6, pp. 740–745.

Hoerner, S. F. (1965). *Fluid dynamic drag*. Hoerner fluid dynamics.

Hoomans, B. P. B. et al. (1996). “Discrete particle simulation of bubble and slug formation in a two-dimensional gas-fluidised bed: a hard-sphere approach”. In: *Chemical Engineering Science* 51.1, pp. 99–118.

Hosseinzadeh-Nik, Z., S. Subramaniam, and J. D. Regele (2018). “Investigation and quantification of flow unsteadiness in shock-particle cloud interaction”. In: *International Journal of Multiphase Flow* 101, pp. 186–201.

Ignatius, J. K., S. Sathiyavageeswaran, and S. R. Chakravarthy (2014). “Hot-flow simulation of aeroacoustics and suppression by water injection during rocket liftoff”. In: *AIAA Journal* 53.1, pp. 235–245.

Igra, O. and K. Takayama (1993). “Shock tube study of the drag coefficient of a sphere in a non-stationary flow”. In: *Proceedings of the Royal Society of London. Series A: Mathematical and Physical Sciences* 442.1915, pp. 231–247.

Ishii, T. et al. (2012). “Acoustic measurement of 1: 42 scale booster and launch pad”. In: *Proceedings of Meetings on Acoustics 164ASA*. Vol. 18. 1. ASA, p. 040009.

Johnson, T. A. and V. C. Patel (1999). “Flow past a sphere up to a Reynolds number of 300”. In: *Journal of Fluid Mechanics* 378, pp. 19–70.

Jourdan, G. et al. (2007). “Drag coefficient of a sphere in a non-stationary flow: new results”. In: *Proceedings of the Royal Society A: Mathematical, Physical and Engineering Sciences* 463.2088, pp. 3323–3345.

Kajishima, T. (2004). “Influence of particle rotation on the interaction between particle clusters and particle-induced turbulence”. In: *International Journal of Heat and Fluid Flow* 25.5, pp. 721–728.

Kajishima, T. and S. Takiguchi (2002). “Interaction between particle clusters and particle-induced turbulence”. In: *International Journal of Heat and Fluid Flow* 23.5, pp. 639–646.

Kane, E. D. (1951). “Sphere drag data at supersonic speeds and low Reynolds numbers”. In: *Journal of the Aeronautical Sciences* 18.4, pp. 259–270.

Keys, R. (1981). “Cubic convolution interpolation for digital image processing”. In: *IEEE Transactions on Acoustics, Speech, and Signal Processing* 29.6, pp. 1153–1160.

Kitchens, C. W. and C. C. Bush (1972). “Low Reynolds number flow past a transverse cylinder at Mach two.” In: *AIAA Journal* 10.10, pp. 1381–1382.

Knowler, A. E. and F. W. Pruden (1944). *On the drag of circular cylinders at high speeds*. HM Stationery Office.

Knudsen, V. O., J. V. Wilson, and N. S. Anderson (1948). “The attenuation of audible sound in fog and smoke”. In: *The Journal of the Acoustical Society of America* 20.6, pp. 849–857.

Koike, S. et al. (2007). “Correction method for particle velocimetry data based on the Stokes drag law”. In: *AIAA Journal* 45.11, pp. 2770–2777.

Kosinski, P. and A. C. Hoffmann (2010). “An extension of the hard-sphere particle–particle collision model to study agglomeration”. In: *Chemical Engineering Science* 65.10, pp. 3231–3239.

Krothapalli, A. et al. (2003). “Turbulence and noise suppression of a high-speed jet by water injection”. In: *Journal of Fluid Mechanics* 491, pp. 131–159.

Kurose, R. and S. Komori (1999). “Drag and lift forces on a rotating sphere in a linear shear flow”. In: *Journal of Fluid Mechanics* 384, pp. 183–206.

Kurose, R. et al. (2012). “Numerical simulation of flow past a heated/cooled sphere”. In: *Journal of Fluid Mechanics* 692, pp. 332–346.

Lang, N. (2000). “Investigation of the supersonic flow field around a delta wing using particle image velocimetry”. In: *Proceedings of the 10th International Symposium on Applications of Laser Techniques to Fluid Mechanics, Lisbon, Portugal*, pp. 10–13.

Langevin, P. (1905). *Annales de Chimie et de Physique*, p. 266.

Lau, J. C. (1981). “Effects of exit Mach number and temperature on mean-flow and turbulence characteristics in round jets”. In: *Journal of Fluid Mechanics* 105, pp. 193–218.

Lindsey, W. F. (1938). *Drag of cylinders of simple shapes*. Tech. rep. NACA-TN-3038. National Advisory Committee for Aeronautics.

Loth, E. (2008). “Compressibility and rarefaction effects on drag of a spherical particle”. In: *AIAA Journal* 46.9, pp. 2219–2228.

Luo, K. et al. (2016). “A ghost-cell immersed boundary method for simulations of heat transfer in compressible flows under different boundary conditions”. In: *International Journal of Heat and Mass Transfer* 92, pp. 708–717.

Magarvey, R. H. and R. L. Bishop (1961). “Transition ranges for three-dimensional wakes”. In: *Canadian Journal of Physics* 39.10, pp. 1418–1422.

Magnaudet, J., M. Rivero, and J. Fabre (1995). “Accelerated flows past a rigid sphere or a spherical bubble. Part 1. Steady straining flow”. In: *Journal of Fluid Mechanics* 284, pp. 97–135.

Makita, H. (2007). “Forefront of Wind-Tunnel Experiment on Turbulence Structure”. In: *Journal of Fluid Science and Technology* 2.3, pp. 525–534.

Mani, A. (2012). “Analysis and optimization of numerical sponge layers as a nonreflective boundary treatment”. In: *Journal of Computational Physics* 231.2, pp. 704–716.

Mansoorzadeh, S. et al. (1998). “Finite element simulations of incompressible flow past a heated/cooled sphere”. In: *International Journal for Numerical Methods in Fluids* 28.6, pp. 903–915.

Mao, C. et al. (2019). “Investigation of supersonic turbulent flows over a sphere by fully resolved direct numerical simulation”. In: *Physics of Fluids* 31.5, p. 056102.

Maxey, M. R. and J. J. Riley (1983). “Equation of motion for a small rigid sphere in a nonuniform flow”. In: *The Physics of Fluids* 26.4, pp. 883–889.

May, A. (1953). “Free-flight determinations of the drag coefficients of spheres”. In: *Journal of the Aeronautical Sciences* 20.9, pp. 635–638.

— (1957). “Supersonic drag of spheres at low Reynolds number in free flight”. In: *Journal of Applied Physics* 28.8, pp. 910–912.

McCarthy, J. F. and T. Kubota (1964). “A study of wakes behind a circular cylinder at M= 5.7”. In: *AIAA Journal* 2.4, pp. 629–636.

McLaughlin, J. B. (1991). “Inertial migration of a small sphere in linear shear flows”. In: *Journal of Fluid Mechanics* 224, pp. 261–274.

Mei, R. (1992). “An approximate expression for the shear lift force on a spherical particle at finite Reynolds number”. In: *International Journal of Multiphase Flow* 18.1, pp. 145–147.

Meliga, P., D. Sipp, and J.-M. Chomaz (2010). “Effect of compressibility on the global stability of axisymmetric wake flows”. In: *Journal of Fluid Mechanics* 660, pp. 499–526.

Millikan, R. A. (1923). “The general law of fall of a small spherical body through a gas, and its bearing upon the nature of molecular reflection from surfaces”. In: *Physical Review* 22.1, p. 1.

Mittal, R. et al. (2008). “A versatile sharp interface immersed boundary method for incompressible flows with complex boundaries”. In: *Journal of Computational Physics* 227.10, pp. 4825–4852.

Mizuno, Y. et al. (2015). “A simple immersed boundary method for compressible flow simulation around a stationary and moving sphere”. In: *Mathematical Problems in Engineering* 2015.

— (2016). “Direct Numerical Simulation of Shock Waves Passed by Multiple Particles by Using Immersed Boundary Method”. In: *54th AIAA Aerospace Sciences Meeting*, p. 0618.

Murthy, V. S. and W. C. Rose (1978). “Detailed measurements on a circular cylinder in cross flow”. In: *AIAA Journal* 16.6, pp. 549–550.

Nakamura, I. (1976). “Steady wake behind a sphere”. In: *The Physics of Fluids* 19.1, pp. 5–8.

Niazmand, H. and M. Renksizbulut (2003). “Surface effects on transient three-dimensional flows around rotating spheres at moderate Reynolds numbers”. In: *Computers & Fluids* 32.10, pp. 1405–1433.

Nonomura, T. et al. (2014). “Computational prediction of acoustic waves from a subscale rocket motor”. In: *Transactions of the Japan Society for Aeronautical and Space Sciences, Aerospace Technology Japan* 12.ists29, Pe_11–Pe_17.

Nonomura, T. et al. (2015). “A new technique for freestream preservation of finite-difference WENO on curvilinear grid”. In: *Computers & Fluids* 107, pp. 242–255.

Norberg, C. (2001). “Flow around a circular cylinder: aspects of fluctuating lift”. In: *Journal of Fluids and Structures* 15.3-4, pp. 459–469.

Oseen, C. W. (1927). “Neuere methoden und ergebnisse in der hydrodynamik”. In: *Leipzig: Akademische Verlagsgesellschaft mb H.*

Osnes, A. N. et al. (2019). “Particle-resolved simulations of shock-induced flow through particle clouds at different Reynolds numbers”. In: *arXiv preprint arXiv:1906.08299*.

Parmar, M., A. Haselbacher, and S. Balachandar (2010). “Improved drag correlation for spheres and application to shock-tube experiments”. In: *AIAA Journal* 48.6, pp. 1273–1276.

Pirozzoli, S. (2011). “Stabilized non-dissipative approximations of Euler equations in generalized curvilinear coordinates”. In: *Journal of Computational Physics* 230.8, pp. 2997–3014.

Poiseuille, J. L. M. (1836). “Recherches sur les causes du mouvement du sang dans les vaisseaux capillaires”. In: *Annales des Sciences Naturelles* 5.2, pp. 111–115.

Poon, E. K. W. et al. (2014). “Flow past a transversely rotating sphere at Reynolds numbers above the laminar regime”. In: *Journal of Fluid Mechanics* 759, pp. 751–781.

Pruppacher, H. R., B. P. Le Clair, and A. E. Hamielec (1970). “Some relations between drag and flow pattern of viscous flow past a sphere and a cylinder at low and intermediate Reynolds numbers”. In: *Journal of Fluid Mechanics* 44.4, pp. 781–790.

Putnam, A. (1961). “Integrable form of droplet drag coefficient”. In: *American Rocket Society Journal* 31, p. 1467.

Ragni, D. et al. (2011). “Particle tracer response across shocks measured by PIV”. In: *Experiments in Fluids* 50.1, pp. 53–64.

Ranz, W. E. and W. R. Marshall (1952). “Evaporation from drops”. In: *Chemical Engineering Progress* 48.3, pp. 141–146.

Riahi, H. et al. (2018). “A pressure-corrected Immersed Boundary Method for the numerical simulation of compressible flows”. In: *Journal of Computational Physics* 374, pp. 361–383.

Rodriguez, I. et al. (2011). “Direct numerical simulation of the flow over a sphere at Re= 3700”. In: *Journal of Fluid Mechanics* 679, pp. 263–287.

Rodriguez, O. (1984). “The circular cylinder in subsonic and transonic flow”. In: *AIAA Journal* 22.12, pp. 1713–1718.

Roos, F. W. and W. W. Willmarth (1971). “Some experimental results on sphere and disk drag”. In: *AIAA Journal* 9.2, pp. 285–291.

Roshko, A. (1954). *On the development of turbulent wakes from vortex streets*. Tech. rep. NACA-TN-2913. National Advisory Committee for Aeronautics.

Rubinow, S. I. and J. B. Keller (1961). "The transverse force on a spinning sphere moving in a viscous fluid". In: *Journal of Fluid Mechanics* 11.3, pp. 447–459.

Saffman, P. G. T. (1965). "The lift on a small sphere in a slow shear flow". In: *Journal of Fluid Mechanics* 22.2, pp. 385–400.

Saito, T., M. Marumoto, and K. Takayama (2003). "Numerical investigations of shock waves in gas-particle mixtures". In: *Shock Waves* 13.4, pp. 299–322.

Sakamoto, H. and H. Haniu (1990). "A study on vortex shedding from spheres in a uniform flow". In: *Journal of Fluids Engineering* 112.4, pp. 386–392.

Salimipour, E. and M. Anbarsooz (2019). "Surface temperature effects on the compressible flow past a rotating cylinder". In: *Physics of Fluids* 31.2, p. 023601.

Sansica, A. et al. (2018). "Three-dimensional instability of a flow past a sphere: Mach evolution of the regular and Hopf bifurcations". In: *Journal of Fluid Mechanics* 855, pp. 1088–1115.

Sauer, F. M. (1951). "Convective heat transfer from spheres in a free-molecule flow". In: *Journal of the Aeronautical Sciences* 18.5, pp. 353–354.

Schaaf, S. A. and P. A. Chambre (2017). *Flow of rarefied gases*. Princeton University Press.

Schaaf, S. A. and P. L. Chambre (1958). "Flow of Rarefied Gases, Section H". In: *Fundamentals of Gas Dynamics*, p. 689.

Schiller, L. and A. Z. Naumann (1933). "Über die Grundlegenden Berechungen bei der Schwerkraftaufbereitung". In: *Zeitschrift des Vereines Deutscher Ingenieure* 77, pp. 318–320.

Schlichting, H. and K. Gersten (1960). *Boundary layer theory*. Vol. 960. Springer.

Schneiders, L. et al. (2016). "An efficient conservative cut-cell method for rigid bodies interacting with viscous compressible flows". In: *Journal of Computational Physics* 311, pp. 62–86.

Segré, G. and A. Silberberg (1962). "Behaviour of macroscopic rigid spheres in Poiseuille flow Part 2. Experimental results and interpretation". In: *Journal of Fluid Mechanics* 14.1, pp. 136–157.

Shimada, T., Y. Daimon, and N. Sekino (2006). *Computational fluid dynamics of multiphase flows in solid rocket motors*. Tech. rep. JAXA-SP-05-035E. Japan Aerospace Exploration Agency (JAXA).

Sreekanth, A. K. (1961). *Drag measurements on circular cylinders and spheres in the transition regime at a Mach number of 2*. Tech. rep. UTIA Report, No. 74. Toronto university Downsview (Ontario) Institute for Aerospace Studies.

Stalder, J. R. and V. J. Zurick (1951). *Theoretical aerodynamic characteristics of bodies in a free-molecule-flow field*. Tech. rep. National Aeronautics and Space Administration, Langley Research Center.

Stokes, G. G. (1851). *On the effect of the internal friction of fluids on the motion of pendulums*. Vol. 9. Pitt Press Cambridge.

Sun, M. et al. (2005). "Unsteady drag on a sphere by shock wave loading". In: *Shock Waves* 14.1-2, pp. 3–9.

Sutherland, W. (1893). "LII. The viscosity of gases and molecular force". In: *The London, Edinburgh, and Dublin Philosophical Magazine and Journal of Science* 36.223, pp. 507–531.

Suzuki, T. et al. (2005). "Shock tube study of particles' motion behind a planar shock wave". In: *Measurement Science and Technology* 16.12, p. 2431.

Takahashi, S., T. Nonomura, and K. Fukuda (2014). “A numerical scheme based on an immersed boundary method for compressible turbulent flows with shocks: application to two-dimensional flows around cylinders”. In: *Journal of Applied Mathematics* 2014.

Tanaka, T., Y. Yamagata, and Y. Tsuji (1990). “Experiments on fluid forces on a rotating sphere and spheroid”. In: *Proc. Second KSME-JSME Fluids Engineering Conference, 1990*.

Taneda, S. (1956). “Experimental invstigation of the wake behind a sphere at low Reynolds numbers”. In: *Journal of the Physical Society of Japan* 11.10, pp. 1104–1108.

— (1978). “Visual observations of the flow past a sphere at Reynolds numbers between 10^4 and 10^6”. In: *Journal of Fluid Mechanics* 85.1, pp. 187–192.

Tanno, H. et al. (2003). “Interaction of a shock with a sphere suspended in a vertical shock tube”. In: *Shock Waves* 13.3, pp. 191–200.

Tchen, C.-M. (1974). “Mean value and correlation problems connected with the motion of small particles suspended in a turbulent fluid”. In: *Leipzig: Akademische Verlagsgesellschaft mb H.*

Terakado, D. et al. (2016). “Computational Analysis of Compressible Gas-Particle-Multiphase Turbulent Mixing Layer in Euler–Euler Formulation”. In: *Transactions of the Japan Society for Aeronautical and Space Sciences, Aerospace Technology Japan* 14.ists30, Po_2_25–Po_2_31.

Teymourtash, A. R. and S. E. Salimipour (2017). “Compressibility effects on the flow past a rotating cylinder”. In: *Physics of Fluids* 29.1, p. 016101.

Tiwari, S. S. et al. (2019a). “Flow past a single stationary sphere, 1. Experimental and numerical techniques”. In: *Powder Technology*.

— (2019b). “Flow past a single stationary sphere, 2. Regime mapping and effect of external disturbances”. In: *Powder Technology*.

Tomboulides, A., S. Orszag, and G. Karniadakis (1993). “Direct and large-eddy simulations of axisymmetric wakes”. In: *31st Aerospace Sciences Meeting*, p. 546.

Tomboulides, A. G. and S. A. Orszag (2000). “Numerical investigation of transitional and weak turbulent flow past a sphere”. In: *Journal of Fluid Mechanics* 416, pp. 45–73.

Torobin, L. B. and W. H. Gauvin (1959). “Fundamental aspects of solids-gas flow: Part III. Accelerated motion of a particle in a fluid”. In: *The Canadian Journal of Chemical Engineering* 37.6, pp. 224–236.

Tri, B. D., B. Oesterle, and F. Deneu (1990). “New Results Concerning the Lift of a Rotating Sphere at Intermediate Reynolds-Numbers”. In: *Comptes Rendus de L Academie des Sciences Serie II* 311.1, pp. 27–31.

Tritton, D. J. (1959). “Experiments on the flow past a circular cylinder at low Reynolds numbers”. In: *Journal of Fluid Mechanics* 6.4, pp. 547–567.

Tsuji, Y., T. Kawaguchi, and T. Tanaka (1993). “Discrete particle simulation of two-dimensional fluidized bed”. In: *Powder Technology* 77.1, pp. 79–87.

Tsuji, Y., T. Tanaka, and T. Ishida (1992). “Lagrangian numerical simulation of plug flow of cohesionless particles in a horizontal pipe”. In: *Powder Technology* 71.3, pp. 239–250.

Tsutsumi, S. et al. (2008). “Numerical study of pressure waves generated by H-IIA launch vehicle at lift-off”. In: *Proceedings of the Asian Joint Conference on Propulsion and Power*.

Tsutsumi, S. et al. (2014). “Study on acoustic prediction and reduction of Epsilon launch vehicle at liftoff”. In: *Journal of Spacecraft and Rockets* 52.2, pp. 350–361.

Udaykumar, H. S., W. Shyy, and M. M. Rao (1996). “Elafint: a mixed Eulerian–Lagrangian method for fluid flows with complex and moving boundaries”. In: *International Journal for Numerical Methods in Fluids* 22.8, pp. 691–712.

Uhlmann, M. (2005). “An immersed boundary method with direct forcing for the simulation of particulate flows”. In: *Journal of Computational Physics* 209.2, pp. 448–476.

Volkov, A. N. (2011). “Transitional flow of a rarefied gas over a spinning sphere”. In: *Journal of Fluid Mechanics* 683, pp. 320–345.

Wagner, J. L. et al. (2012). “Shock tube investigation of quasi-steady drag in shock-particle interactions”. In: *Physics of Fluids* 24.12, p. 123301.

Williams, O. J. H. et al. (2015). “Particle response analysis for particle image velocimetry in supersonic flows”. In: *Physics of Fluids* 27.7, p. 076101.

Williamson, C. H. K. (1988a). “Defining a universal and continuous Strouhal–Reynolds number relationship for the laminar vortex shedding of a circular cylinder”. In: *The Physics of Fluids* 31.10, pp. 2742–2744.

— (1988b). “The existence of two stages in the transition to three-dimensionality of a cylinder wake”. In: *The Physics of Fluids* 31.11, pp. 3165–3168.

Xia, Z. et al. (2016). “Mach Number Effect of Compressible Flow Around a Circular Cylinder”. In: *AIAA Journal*, pp. 2004–2009.

Xu, C.-Y., L.-W. Chen, and X.-Y. Lu (2009). “Numerical simulation of shock wave and turbulence interaction over a circular cylinder”. In: *Modern Physics Letters B* 23.03, pp. 233–236.

Ye, T. et al. (1999). “An accurate Cartesian grid method for viscous incompressible flows with complex immersed boundaries”. In: *Journal of Computational Physics* 156.2, pp. 209–240.

Yee, H. C., N. D. Sandham, and M. J. Djomehri (1999). “Low-dissipative high-order shock-capturing methods using characteristic-based filters”. In: *Journal of computational physics* 150.1, pp. 199–238.

You, C. F., H. Qi, and X. C. Xu (2003). “Lift force on rotating sphere at low Reynolds numbers and high rotational speeds”. In: *Acta Mechanica Sinica* 19.4, pp. 300–307.

Zarin, N. A. and J. A. Nicholls (1971). “Sphere drag in solid rockets—non-continuum and turbulence effects”. In: *Combustion Science and Technology* 3.6, pp. 273–285.

Zoppellari, E. and D. Juve (1998). “Reduction of hot supersonic jet noise by water injection”. In: *4th AIAA/CEAS Aeroacoustics Conference*, p. 2204.